On-surface Synthesis of Two-dimensional Conducting Metal-Organic Frameworks



Sisheng Shu

Mansfield College

University of Oxford

A thesis submitted for the degree of

Doctor of Philosophy

Trinity Term 2023

Abstract

This thesis focuses on the synthesis of two-dimensional metal-organic frameworks (MOFs) using on-surface methods on metal substrates. Scanning tunnelling microscopy (STM) and density-functional theory (DFT) calculations are used as the experimental and theoretical tools to study the structural and electronic properties of the frameworks.

The thesis starts with the study of hexahydroxytriphenylene (HHTP) molecules on a Au(111) substrate. Following vapour deposition from a Knudsen cell, HHTP molecules self-assemble into a near close-packed phase with two alternating molecular rows. After reacting with transition metals (Ni/Co), HHTP forms a dense structure on the surface. The metal centres adopt a three-fold coordination geometry, connecting all the molecules into a network.

Changing the ligand to hexaaminotriphenylene (HATP), single-layer MOFs with a honeycomb structure can be synthesised when metals (Ni/Co) are evaporated onto the surface containing HATP molecules. The Ni-HATP MOF has a shape of large islands, while the Co-HATP domains are long ribbons. A bimetallic MOF can also be obtained by co-depositing Ni and Co atoms. Different metal centres can be separately visualised in STM images and identified with the aid of DFT modelling.

Using a smaller ligand, hexahydroxybenzene (HHB), nonporous metal-organic coordination polymers are synthesised on the Au(111) substrate. Ni- and Co-HHB polymers have an identical structure in which each molecule is bonded with six metal atoms. The only difference is that Ni atoms are visible in STM images, while Co atoms are not evident because of their lower height.

When mixing HHTP and HHB, two phases of self-assemblies are found on the Au(111) surface. The α-phase has an HHTP : HHB ratio of 2 : 1, and the β-phase has a ratio of 6 : 1. Depositing Ni onto the α-phase mixture can create a dual-ligand MOF, where each Ni atom coordinates with one HHTP and one HHB. Besides, HHB has a stronger coordination ability than HHTP and HATP, causing ligand substitution reactions on the Au(111) surface.

Preface

The work presented in this thesis was carried out by the author from October 2019 to May 2023 at the Department of Materials, University of Oxford, under the supervision of Professor M. R. Castell. No part of this thesis has been previously submitted for a degree at this or any other university.

Acknowledgement

I would like to express my sincere gratitude to my supervisor, Professor Martin Castell, for his unwavering guidance, encouragement, and support throughout my DPhil study. He led me into the field of surface science and guided me to be a qualified scientific researcher. I have learnt so much from his knowledge, insight, and passion for science. I would also like to extend my appreciation to Dr. Christopher Patrick for his enthusiasm and assistance in the simulation work of this thesis. He kindly helped me to solve the problems I met and gave me valuable advice for modelling.

I am grateful to my colleague and collaborator, Fubiao Gu. He devoted much time to teach me how to operate instruments and perform experiments. He also shared everything he knew with me, no matter project details or other life skills. Without his help, I could not work independently and get high-quality images so quickly. After training, I worked with him for two years, which was the best time I have spent in Oxford. I would like to thank Dr. Peiyu Chen, and Dr. Yuhan Zhu, who also trained me on the instrument and gave me useful suggestions for the experiments and data processing. My thanks also go to Chris Spencer, who fixed many problems of the instrument and helped me to understand its working mechanisms.

I would like to thank my colleagues: Tairu, Yingrui, Xinze, Axel, Weishuo, Abi and Yu, who shared their knowledge, experience, and skills with me. I would also like to thank my friends: Junqing, Yuanyuan, Ganghong, Mingzhe and Yigang for their company, encouragement, and support. Finally, I would like to express my heartfelt gratitude to my parents for their love, care and understanding.

Contents

Chapter 1 Introduction 1

1.1 Background 1

1.2 Outline of the thesis 2

Chapter 2 Literature Review 4

2.1 Two-dimensional conducting MOFs 4

2.2 Conductive mechanisms and structures 5

2.2.1 Conductive mechanisms 6

2.2.2 Compositions and structures 7

2.3 On-surface synthesis of 2D c-MOFs 17

2.3.1 Synthesis methods of 2D c-MOFs 17

2.3.2 On-surface synthesis 18

2.4 Applications of 2D c-MOFs 30

2.4.1 Chemiresistive Sensing 30

2.4.2 Electrocatalysis 32

2.4.3 Electrochemical capacitors 34

2.5 Summary 36

Chapter 3 Experimental Techniques and Simulation Methods 38

3.1 Scanning tunnelling microscopy 38

3.2 Ultra-high vacuum (UHV) system 42

3.3 Sample Preparation 43

3.3.1 Materials selection 43

3.3.2 Tip etching 43

3.3.3 Substrates 44

3.3.4 Sputtering etching 45

3.3.5 E-beam evaporator 47

3.3.6 Knudsen cell (K-cell) 49

3.4 Simulation method 50

3.4.1 Density functional theory 50

3.4.2 Calculation parameters 54

3.5 STM image processing 57

Chapter 4 Self-assembly and Metal Coordination Networks of HHTP on Au(111) 59

4.1 Introduction 59

4.2 HHTP molecular self-assembly 60

4.3 HHTP metal coordination networks 65

4.4 Conclusion 70

Chapter 5 Synthesis of HATP Metal-Organic Frameworks on Au(111) and Cu(111) Substrates 72

5.1 Introduction 72

5.2 $Ni_3(HITP)_2$ MOF on Au(111) 73

5.3 $Co_3(HITP)_2$ MOF on Au(111) 80

5.4 Bimetallic $Ni_xCo_{3-x}(HITP)_2$ MOF on Au(111) 84

5.5 HATP-Cu complexes on Cu(111) 90

5.6 Conclusion 92

Chapter 6 Synthesis of HHB Coordination Polymers on Au(111) 93

6.1 Introduction 93

6.2 HHB molecular self-assembly 94

6.3 $Ni_3(HHB_{-6H})$ polymer 95

6.4 $Co_3(HHB_{-6H})$ polymer 102

6.5 Vacancy defects 106

6.6 Bimetallic $Ni_xCo_{3-x}(HHB_{-6H})$ polymer 109

6.7 Conclusion 112

Chapter 7 On-surface Reactions of Mixed Ligands on Au(111) 114

7.1 Introduction 114

7.2 HHTP-HHB molecular alloy 115

7.3 A dual-ligand Ni-coordination framework 119

7.4 Ligand substitution reactions 123

7.5 Mixture of HHTP and HATP 128

7.6 Conclusion 129

Chapter 8 Conclusion 131

8.1 Overview 131

8.2 Molecular self-assemblies on Au(111) 131

8.3 Metal-organic coordination structures on Au(111) 132

8.4 Future work 136

References 138

Chapter 1

Introduction

1.1 Background

Metal-organic frameworks (MOFs) are a class of porous materials constructed by organic ligands and metal ions or clusters. Most MOFs feature poor electrical conductivities, while this problem has been overcome since the report of two-dimensional (2D) conductive MOFs (c-MOFs).[1-2] In these c-MOFs, the extended π-d conjugation between ligands and metal ions facilitates efficient charge transport, resulting in high electrical conductivities. Owing to the variety of components and structures, 2D c-MOFs have attracted significant attention and been used in various electronic devices.[3-4] In addition to applications, 2D c-MOFs are also of interest in fundamental research as they have been reported to exhibit superconductivity and ferromagnetism.[5-7] Besides, theoretical explorations have predicted that 2D c-MOFs have exotic quantum states like non-trivial topological states, but these have not been observed in experiments.[8-11] One reason may be that the synthesised 2D c-MOFs are usually multilayers, and the quantum effects would be quenched by interlayer interactions.[12] Therefore, it is desirable to prepare single-layer 2D c-MOFs to explore their physical and chemical properties at their single-layer limit.

On-surface synthesis under ultra-high vacuum (UHV) can be utilised to fabricate single-layer 2D materials with atomic precision.[12-14] Upon depositing linker molecules and metal atoms on an atomically flat surface, they would form coordinated structures after annealing at an appropriate temperature. Through this approach, many metal-organic structures have been

successfully synthesised, including 1D chains and 2D networks.[15-20] Accordingly, the on-surface synthesis methods are also feasible for the preparation of single-layer 2D c-MOFs. So far, the growth mechanism of 2D c-MOFs has not been systematically studied. With surface-sensitive techniques, such work might be carried out during the growth of MOFs on surfaces.[21-22] These studies would provide some guidance for the controllable synthesis of 2D c-MOFs with desired structures and functionalities.

This thesis focuses on the synthesis and characterisation of 2D c-MOFs on metal substrates, extending our knowledge of single-layer 2D c-MOFs. Three main aspects are covered. Firstly, the growth processes of these metal-organic coordination networks are presented. The results suggest that the substrate affects the adsorbed layers significantly because of their strong epitaxial interactions. Other reaction conditions such as deposition order and annealing temperature have limited influences on the final product, but the growth varies slightly. Secondly, the structures of these networks and the interactions between the metal atoms and the ligands are clearly revealed. In these metal-organic coordination networks, most metal atoms adopt a square-planar coordination geometry with four functional groups to form 2D structures. Different metal centres and vacancy defects can also be visualised from high-resolution images, providing more information for structural analysis. Thirdly, the electronic properties of these networks are interpreted with the help of modelling, explaining their conductive mechanisms. All the networks exhibit typical π-d conjugation characteristics, which give them small bandgaps or even metallic characters.

1.2 Outline of the thesis

Chapter 2 reviews previous studies of 2D c-MOFs, including their components, structures, synthesis methods, and applications. An emphasis is placed on the synthesis of 2D c-MOFs on

metal substrates, which is the focus of this thesis.

Chapter 3 briefly introduces experimental techniques and theoretical simulations used in this thesis. The working principle of Scanning Tunnelling Microscopy (STM), the preparation of samples, the parameters of Density-Functional Theory (DFT) calculations, and the processing of STM images are presented.

Chapter 4 shows the self-assembly of HHTP molecules and their reactions with Ni and Co atoms on Au(111) substrates. With STM and DFT, the bonding between molecules in the assembly is revealed. Then the structure of Ni/Co-HHTP coordination networks is analysed.

Chapter 5 presents the synthesis of M-HATP MOFs. The growth processes and structures of $M_3(HITP)_2$ (M: Ni, Co) MOFs on the Au(111) substrate are described first. Following that, a bimetallic MOF with mixed Ni and Co is synthesised. The reaction between HATP molecules and Cu atoms on the Cu(111) substrate is also included in this chapter.

Chapter 6 reports the work of HHB on Au(111), from its self-assembly to metal coordination reactions. The influences of different reaction conditions on the products are studied in detail. After that, the analysis of vacancy defects and the synthesis of bimetallic polymers are presented.

Chapter 7 focuses on the mixtures of these three linkers. A molecular alloy based on mixed HHTP and HHB is discovered and studied first. Its reaction with Ni atoms is also investigated. Then the mixing behaviour between HATP and HHB is described.

Chapter 8 concludes the work presented in this thesis and provides some ideas for future studies.

Chapter 2

Literature Review

This chapter introduces basic knowledge and recent developments of 2D c-MOFs. Their conductive mechanisms, components, structures, and properties are described first. Then the studies of 2D c-MOFs on surfaces are summarised because this thesis focuses on this research field. Finally, some applications of 2D c-MOFs are presented, including chemical sensing, electrocatalysis, and energy storage.

2.1 Two-dimensional conducting MOFs

Since the isolation of graphene, a large amount of research has focused on 2D materials.[23] These materials have thin layered structures with a thickness of less than a few nanometres.[24-25] Apart from graphene, other types of 2D materials are also discovered and synthesised, like hexagonal boron nitride, black phosphorus, MXene, transition metal dichalcogenides and 2D MOFs.[26-27] Compared with their bulk material counterparts, 2D materials exhibit exceptional mechanical, optical and electrical properties, such as high carrier mobility, high surface-area-to-volume ratio and rich surface chemistry.[26, 28-29] Therefore, 2D materials have been applied in a wide range of fields, such as electronics, optoelectronics, and energy storage.[30-33]

Unlike other 2D materials, MOFs are a class of porous materials, and only a small number of them are two-dimensional. Traditional MOFs are usually three-dimensional (3D) networks composed of organic ligands and metal ions or clusters.[34-35] Because of their high porosity, enormous surface area, and high tunability, MOFs have been used in various applications, such

as gas storage and separation, catalysis, chemical sensing and luminescence.[36-42] However, the majority of MOFs feature poor electrical conductivities, limiting their utility in electrical technologies.[43]

In 2012, the Yaghi group reported a series of 2D π-conjugated MOFs with high electrical conductivities.[1] After that, research into 2D conductive MOFs (c-MOFs) has experienced a considerable expansion. In these 2D c-MOFs, the ligands and the metal nodes are connected by strong coordination bonds, while the adjacent layers are stacked through weak van der Waals interactions to form bulk crystals. Compared with other electron-conducting materials, 2D c-MOFs have some advantages over them. For example, the large number of metals and organic linkers gives MOFs a high degree of freedom to modulate their properties. This tunability makes it possible to fabricate devices with desired functionalities. Moreover, MOFs can easily be synthesised in a standard laboratory and do not require complicated procedures or expensive equipment.[44-45] With these merits, 2D c-MOFs are promising to be used in electronic devices.

2.2 Conductive mechanisms and structures

Coordination chemistry is the fundamentals of MOFs. In classical complexes, the ligand is bound to the metal through coordinate covalent bonds where the electron pairs are donated by the ligands.[46] For *d*-block transition metals, their partly filled *nd* subshells can provide nine orbitals (one *s*, three *p* and five *d*) to accommodate up to 18 electrons. Combining with the hybridisation concept, this valence bond theory has been widely used to explain the formulas and structures of coordination compounds, including MOFs. Besides, other models like crystal field theory and molecular orbital theory have also been developed to better analyse the properties of complexes.

2.2.1 Conductive mechanisms

There are four mechanisms for charge transport in c-MOFs, including through-bond, through-space, hopping and extended conjugation, as shown in Fig. 2.1.[27, 47] Through-bond means charge carriers move through covalent bonds or coordination bonds, which are formed between metal nodes and organic linkers. If the energy levels of the metals and the linkers match well, the bandgap would be small, resulting in high charge mobility.[48] Through-space pathway is formed by noncovalent interactions, especially π-π stacking between organic components. Linkers with strong π-π interactions can induce through-space charge transport and yield a high conductivity.[49] While hopping relies on the charge movement from the donor to the acceptor molecules.[50]

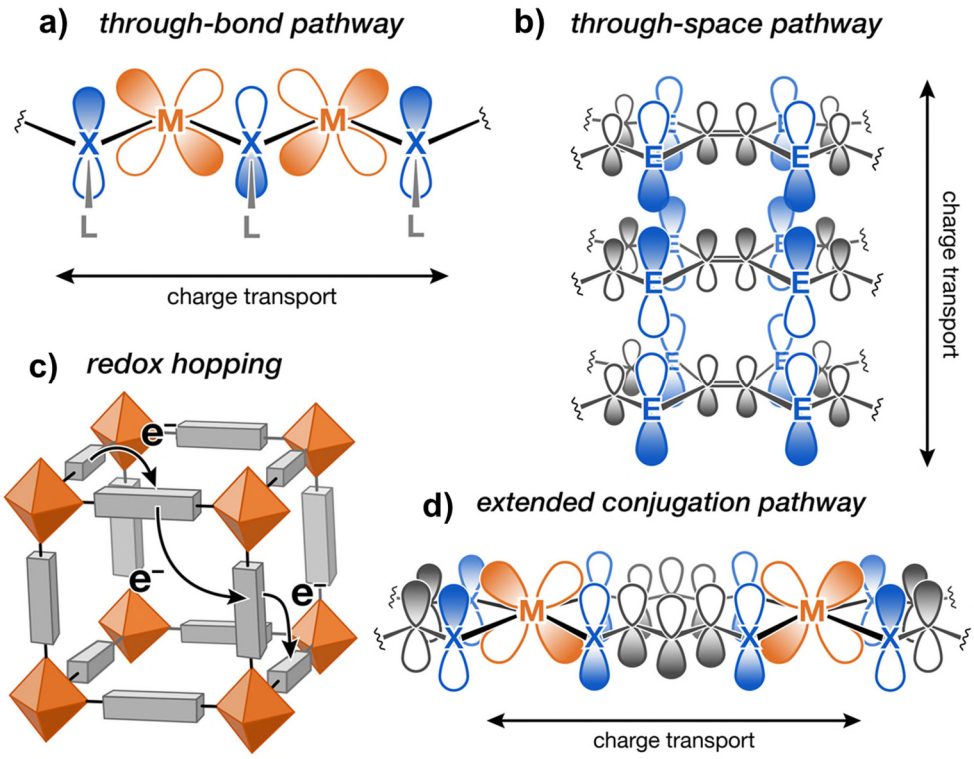


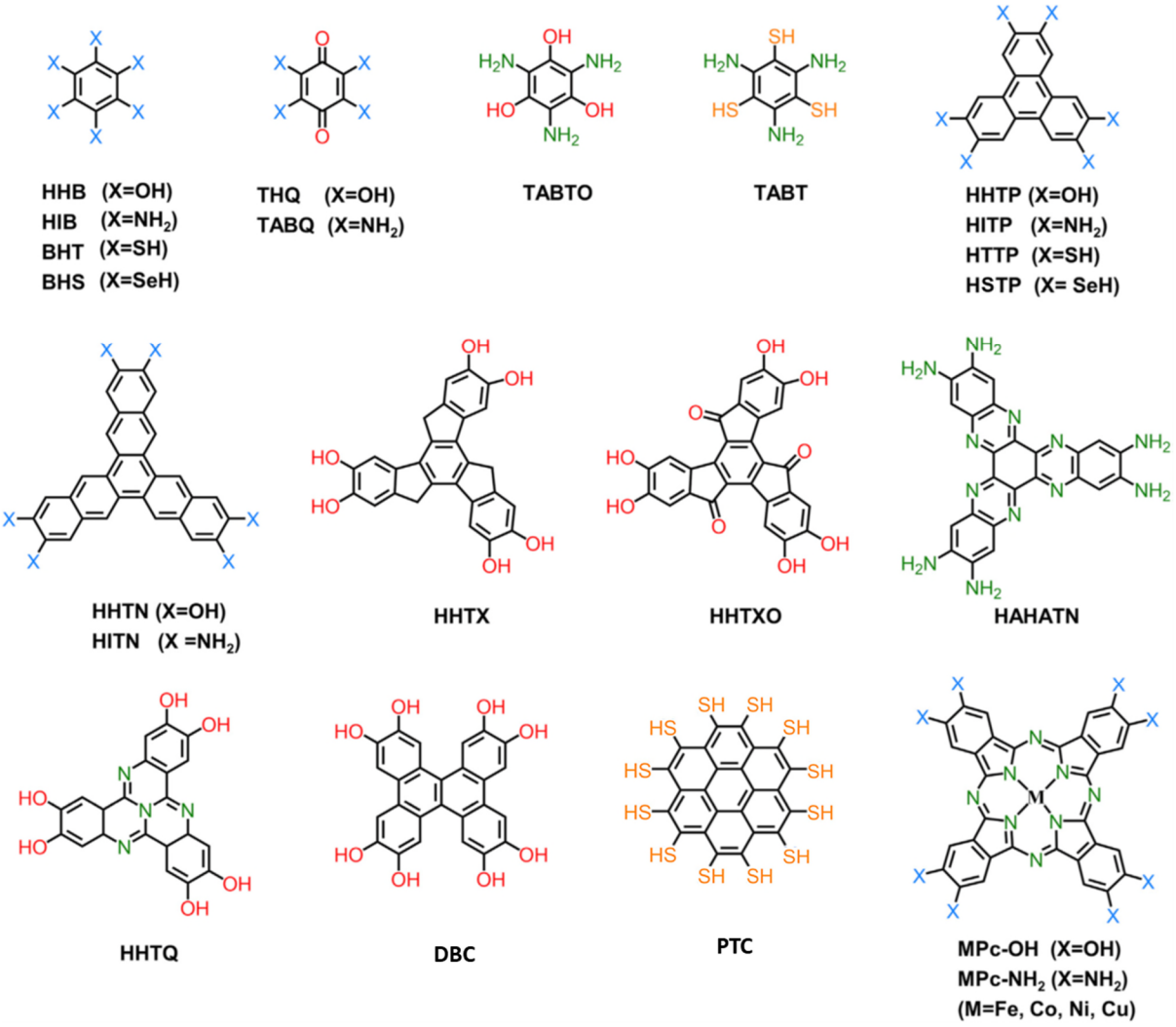
Figure 2.1: Orbital representations of charge transport pathways in c-MOFs. The p_z orbitals of the ligand atoms (X: O, N, and S) and the *d* orbitals of the metals (M) are drawn. (Taken from Ref. 47)

Extended conjugation is the main electrical conductivity mechanism for 2D c-MOFs, which depends on the delocalisation of charge carriers. More specifically, the electronic coupling between the π orbitals of the ligands and the *d* orbitals of the metal ions delocalises the electrons,

offering efficient π-d conjugation for charge transport. Because of the extended conjugation, this kind of MOFs is also known as 2D conjugated MOFs (c-MOFs). One thing that needs to be mentioned here is that 2D c-MOFs are usually stacked multilayers, so that the π-π interactions between adjacent layers also play a role in the charge transport.[51]

2.2.2 Compositions and structures

According to the conducting mechanism, selecting suitable ligands and metal nodes is important for building the extended π-d conjugation. Promising ligands should have stable radicals with unpaired electrons or redox-active sites to facilitate the charge transport. Metals are expected to have a planar coordination geometry, which is common among transition metals like Fe, Co, Ni and Cu. Scheme 2.1 and Table 2.1 summarise organic ligands used in the synthesis of 2D c-MOFs. They usually have conjugated and planar structures with -OH, -NH_2, -SH, or -SeH groups. Ligands with different symmetries, sizes and functional groups have diverse structures and properties. For instance, molecules based on benzene and triphenylene possess the C3 symmetry. After reacting with metal atoms, they form honeycomb structures with hexagonal pore channels. The pore diameters range from 0.8 to 2.4 nm, depending on the size of the ligand.[52]



Scheme 2.1: Chemical structures of various ligands used in the synthesis of 2D c-MOFs. (Taken from Ref. 51)

Table. 2.1 Full names of the listed ligands in Scheme 2.1

Family	Chemical Name	Reference
Benzene	hexahydroxybenzene/benzenehexaol (HHB/BHO)	53
	hexaiminobenzene (HIB)	54-59
	benzenehexathiol (BHT)	60-64
	benzenehexaselenol (BHS)	65
	tetrahydroxy-1,4-quinone (THQ)	53, 66
	tetraaminobenzoquinone (TABQ)	67-68
	1,3,5-triamino-2,4,6-benzenetriol (TABTO)	69
	1,3,5-triamino-2,4,6-benzenetrithiol (TABT)	70

Table 2.1 continued

Triphenylene	2,3,6,7,10,11-hexahydroxytriphenylene (HHTP)	1, 71-75
	2,3,6,7,10,11-hexaaminotriphenylene (HATP)	71, 76-80
	2,3,6,7,10,11-hexathioltriphenylene/tripheylenehexathiolate (HTTP/THT)	81-85
	2,3,6,7,10,11-hexaselenoltriphenylene (HSTP)	86
Phthalocyanine	2,3,9,10,16,17,23,24-octaamino-phthalocyaninato M(II) (MPc-$(NH_2)_8$)	87-89
	2,3,9,10,16,17,23,24-octahydroxy-phthalocyaninato M(II) (MPc-$(OH)_8$)	90-95
	3,4,12,13,21,22,30,31-octahydroxy-naphthalocyaninato M(II) (MNPc-$(OH)_8$)	90
Others	2,3,8,9,14,15-hexahydroxytrinaphthylene (HHTN)	96
	2,3,6,7,10,11-hexaiminotriphenylene (HITN)	52
	2,3,7,8,12,13-hexahydroxyl-truxene (HHTX)	97
	2,3,7,8,12,13-hexahydroxyl-truxone (HHTXO)	98
	hexahydroxyl-hexaazatrinaphthylene (HATNA)	99
	hexaimino-hexaazatrinaphthalene (HAHATN)	100
	dibenzo[g,p]chrysene-2,3,6,7,10,11,14,15-octaol (DBC)	101
	2,3,7,8,12,13-hexahydroxytricyclo-quinazoline (HHTQ)	102-103
	1,2,3,4,5,6,7,8,9,10,11,12-perthiolated coronene (PTC)	7, 104-105

2.2.2.1 Triphenylene-derived linkers

MOFs based on triphenylene backbones have attracted significant interest because of their high crystallinity, high electrical conductivity, and facile synthesis.[106] The first example is HHTP-M (Co, Ni, and Cu) reported by the Yaghi group in 2012.[1] These crystalline MOFs had a layered honeycomb structure within the *ab* plane, as shown in Fig. 2.2a. $Cu_3(HHTP)_2$ crystals showed a conductivity of 0.2 S cm^{-1}, which was the highest value of MOFs at that time. While the conductivities of Ni-HHTP and Co-HHTP were not described in this study. Later research reported the values for Ni- and Co-MOF pressed pellets were 6.8×10^{-3} and 3.2×10^{-2} S cm^{-1}, respectively.[73] After that, Day *et al.* synthesised single crystals of $Cu_3(HHTP)_2$ and investigated

their structures using high-resolution TEM (HRTEM).[71] They found that the layers were in an AA stacking mode with an offset, where the orientation was tilted around 15-23° from the perpendicular direction (Fig. 2.2b). The measured conductivities for rod and flake crystals were 1.5 S cm^{-1} (cross-plane) and 0.5 S cm^{-1} (in-plane), respectively. This result was surprising since charges in this material were assumed to transport within the plane. One possible explanation was that the π-π interactions between the layers led to a higher cross-plane conductivity.

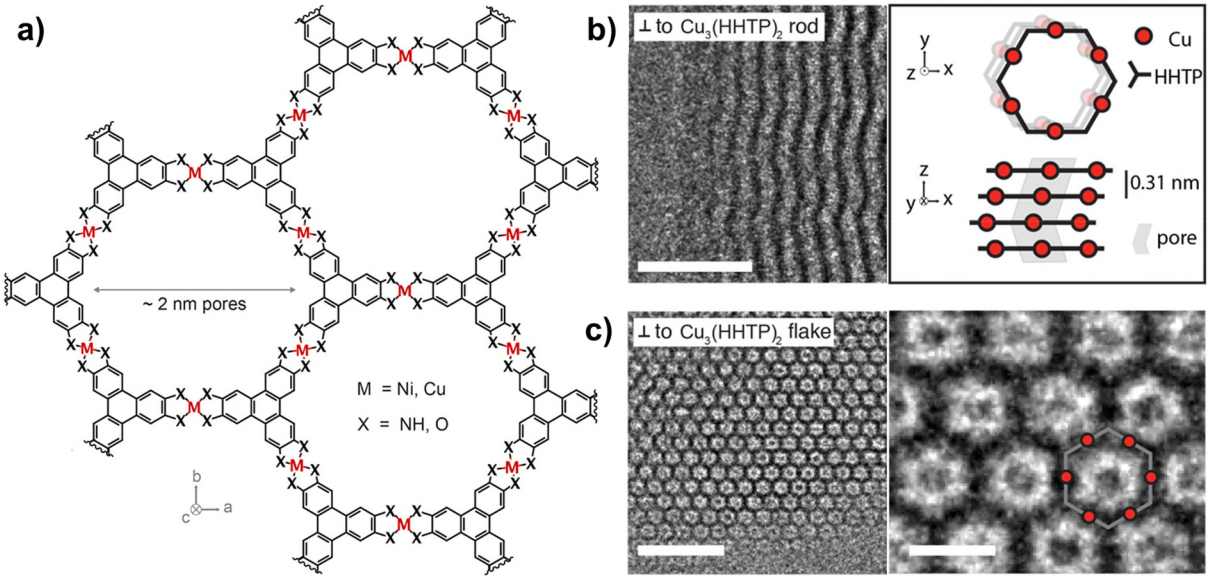


Figure 2.2: (a) General structures of 2D c-MOFs based on triphenylene ligands. (b) Left: HRTEM image of a $Cu_3(HHTP)_2$ rod. Right: Schematic of the $Cu_3(HHTP)_2$ layered structure. Scale bar: 10 nm. (c) HRTEM images of a $Cu_3(HHTP)_2$ flake. Scale bar: 10 nm (left) and 2 nm (right). (Taken from Ref. 71)

In addition to those transition metals (Ni, Co, and Cu), $Zn_3(HHTP)_2$ were also synthesised, which had the same structure as $Cu_3(HHTP)_2$.[107] Recently, both 3D and 2D structures of Fe-HHTP have been reported. The 3D Fe-HHTP MOF had a Brunauer-Emmett-Teller (BET) surface area exceeding 1400 m^2 g^{-1} and an electrical conductivity of 10^{-3} S cm^{-1}.[108] For the 2D Fe-HHTP MOF, there are two types of layers, as shown in Fig. 2.3a.[109] Type 1 is Fe coordinating with one HHTP linker and four solvent molecules. Type 2 is an extended honeycomb where Fe coordinates with two HHTP linkers and two solvent molecules. Due to large interlayer spacings and less π-π orbital overlapping, 2D Fe-HHTP had a low conductivity of 3.55×10^{-5} S cm^{-1}. Skorupskii *et al.* reported a series of lanthanide MOFs, LnHHTP, in which the lanthanide ions

were located between the layers and connected them into a 3D network (Fig. 2.3b).[72] DFT calculations showed that the contribution of lanthanide valence orbitals was small, indicating the transport was mainly through π-π interactions instead of Ln-O bonds. Because Ho-HHTP (3.01 Å) had a shorter stacking distance than La-HHTP (3.07 Å), its conductivity (0.05 S cm^{-1}) was higher than that of La-HHTP (8.2×10^{-4} S cm^{-1}).

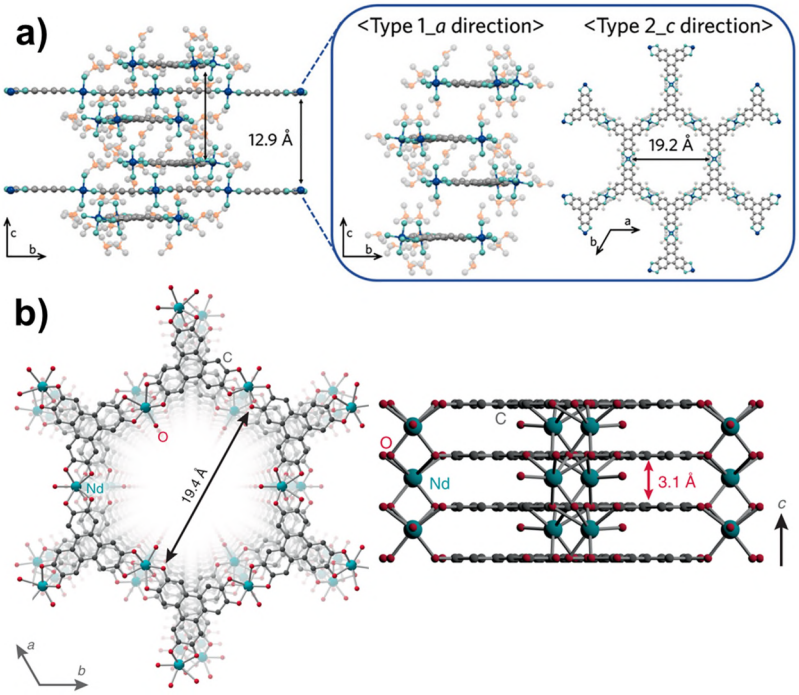


Figure 2.3: (a) Structure model of the 2D Fe-HHTP MOF. (Taken from Ref. 109) (b) Crystal structure of Nd-HHTP, showing the coordination geometry and the layer stacking. (Taken from Ref. 72)

$Ni_3(HITP)_2$, reported by Sheberla *et al.* in 2014, demonstrated a film conductivity of 40 Scm^{-1}, exceeding most c-MOFs.[76] With the increase in temperature, the conductivity increased from 25 S cm^{-1} at 100K to 50 S cm^{-1} at 400K. Later, the same group synthesised single crystals of $Ni_3(HITP)_2$ MOF and studied its crystal structure.[71] The HRTEM image in Fig. 2.4a showed periodic fringes parallel to the rod's axis, suggesting the layers were stacked in a near-eclipsed fashion (eclipsed: a zero-offset vector between consecutive layers). More importantly, the electrical conductivity of $M_3(HITP)_2$ can be modulated by varying the metal nodes. For example, $Co_3(HITP)_2$ had a lower conductivity than $Ni_3(HITP)_2$, so the mixed $Co_xNi_{3-x}(HITP)_2$ exhibited a decreasing conductivity with Co content increasing.[78] Chen *et al.* even reported a continuous

tuning of band gaps and electrical conductivities in a series of binary alloys $(M_xM'_{3-x})(HITP)_2$ (MM'=CuNi, CoNi, CoCu).[79] As shown in Fig. 2.4b, the conductivity can be improved by 4 orders of magnitude from 5.8×10^{-3} S cm^{-1} in $(Co_{2.47}Cu_{0.53})(HITP)_2$ to 55.4 S cm^{-1} in $Ni_3(HITP)_2$.

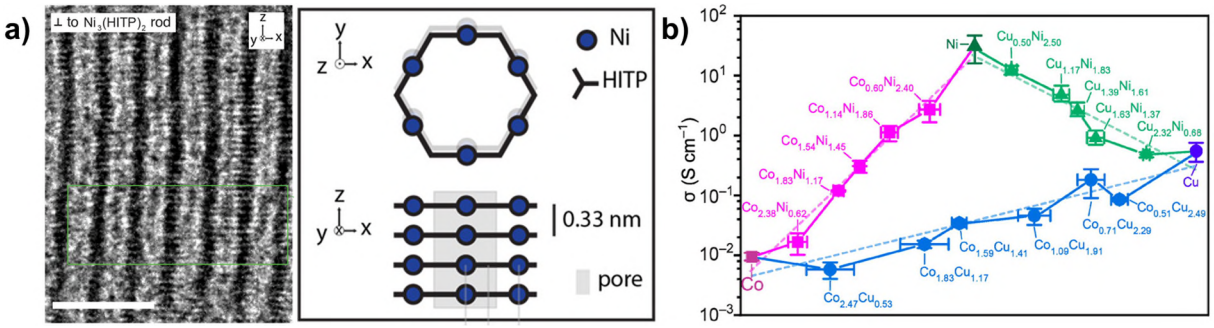


Figure 2.4: (a) Left: HRTEM image of a $Ni_3(HITP)_2$ rod. Right: Schematic of $Ni_3(HITP)_2$ layered structure. (Taken from Ref. 71) (b) Electrical conductivity data for $(M_xM'_{3-x})(HITP)_2$. Solid lines are guide to the eye; dashed lines are linear fits. (Taken from Ref. 79)

Moreover, MOFs based on sulfur-substituted triphenylene have also been studied. $Pt_3(THT)_2$ had a hexagonal structure stacked in a staggered mode and exhibited an electrical conductivity of 2.47×10^{-4} S cm^{-1}.[81] An isostructural framework, $Co_3(THT)_2$, showed a semiconducting phase between 300K and 170 K, followed by a transition to a metallic phase when the temperature was below 130 K.[82] Similarly, $Fe_3(THT)_2$ also showed a transition from semiconducting to metallic phase upon cooling.[83]

2.2.2.2 Benzene-derived linkers

Using HHB, Park *et al.* synthesised $Cu_3(HHB)_2$, which had a honeycomb structure with a low conductivity of 7.3×10^{-8} S cm^{-1}.[53] Interestingly, this $Cu_3(HHB)_2$ MOF could also be prepared by THQ, a deprotonated intermediate of HHB, as shown in Fig. 2.5a.[53, 66] In 2017, Lahiri *et al.* synthesised Cu, Ni and Co frameworks based on the HIB ligand with amino groups. [54] In this work, HIB-MOFs exhibited low conductivities because of poor crystallinity. Later research optimised the synthesis procedure and reported that the conductivity was 8 S cm^{-1} for $Ni_3(HIB)_2$ and 13 S cm^{-1} for $Cu_3(HIB)_2$ at 300K.[55] DFT calculations and UPS results suggested that these

two materials should be metallic within the *ab* plane. However, the measured conductivities increased with temperatures, which was characteristic of semiconductors (Fig. 2.5b). This was attributed to the domination of the thermally activated hopping over grain boundaries (interparticle transport).

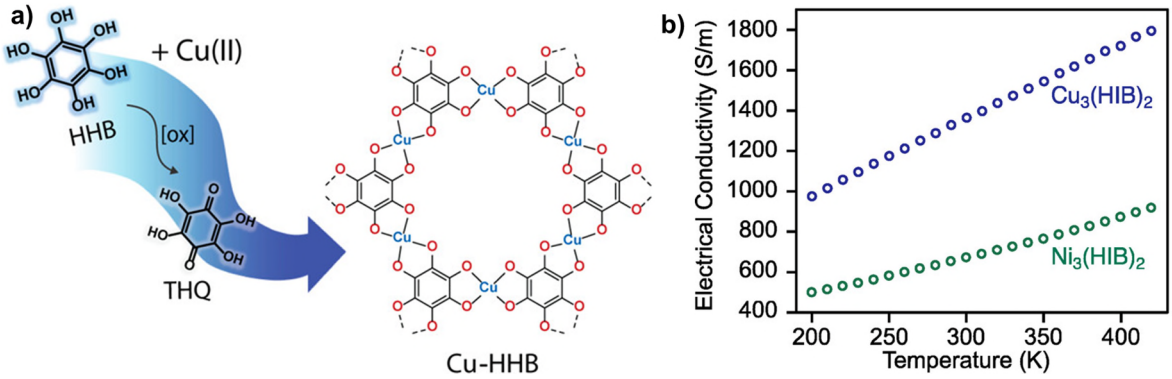


Figure 2.5: (a) Chemical structure of $Cu_3(HHB)_2$. (Taken from Ref. 53) (b) Variable-temperature electrical conductivity of pressed pellets of $M_3(HIB)_2$. (Taken from Ref. 55)

Thiolate-MOFs usually exhibit strong charge delocalisation, which can result in higher conductivities. In 2013, Kambe *et al.* synthesised a π-conjugated nanosheet of $Ni_3(BHT)_2$ with a conductivity of 0.15 S cm^{-1} (two-probe pressed pellet).[60] Later in 2014, the authors used the van der Pauw method (four-probe) to measure the conductivity of a single micro-flake and obtained a much higher value at 1.6×10^2 S cm^{-1}.[110] After that, Pd-BHT and Pt-BHT were also reported, which had the same porous honeycomb structure as $Ni_3(BHT)_2$.[61-62] When changing the metal nodes to Cu, a nonporous coordination polymer was obtained by Huang *et al.*[63] In this Cu-BHT polymer, each BHT molecule is connected with six BHT molecules through six Cu atoms, as shown in Fig. 2.6a. The Cu-BHT polymer exhibited an extremely high electrical conductivity, which could reach up to 1,580 S cm^{-1}. Later, the same group reported a higher value of 2,500 S cm^{-1} at RT for samples with improved crystallinity.[5] Moreover, the Cu-BHT showed a superconducting transition (zero resistance) below 0.25 K at ambient pressure (Fig. 2.6b). This was the first time that superconductivity was observed in a coordination polymer. In addition, Ni, Ag, and Au can also form this nonporous structure after coordinating with the

BHT linker.[64, 111-112] Ag-BHT polymer showed a higher conductivity (250 S cm^{-1}) than Ni-BHT polymer (5 S cm^{-1}) and Au-BHT polymer (10^{-4} S cm^{-1}).

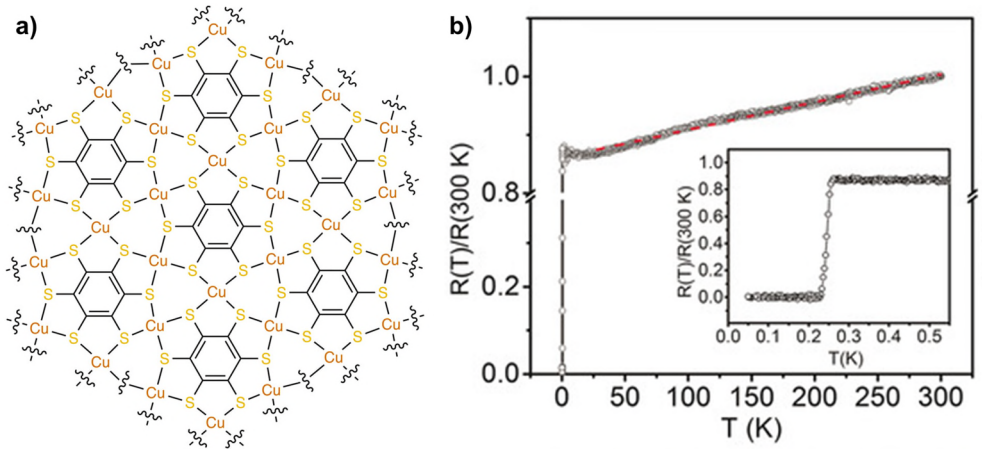


Figure 2.6: (a) Chemical structure of the Cu-BHT polymer. (Taken from Ref. 47) (b) Superconductivity of Cu-BHT. Temperature dependence of the normalised resistance R(T)/R(300) from 50 mK to 300 K. (Taken from Ref. 5)

2.2.2.3 Phthalocyanine-derived linkers

For phthalocyanine (Pc) linkers, they can form M-M'Pc or M-M'NPc MOFs where M is the metal node of the framework and M' is the central metal atom inside the Pc molecule. MOFs based on phthalocyanine ligands possess square lattices along the *ab* plane, and the pore size can be extended by changing the catechol (-Pc) to the naphthol (naphthalocyanine, -NPc) motif, as shown in Fig. 2.7. Cu-CuPc-O_8, reported by Nagatomi *et al.*, was stacked in an eclipsed mode and had a pore size of 1.4 nm.[92] The electrical conductivity of pelletised samples ranged from 9.4×10^{-8} to 1.6×10^{-6} S cm^{-1}, much lower than benzene- and triphenylene-based MOFs. Similarly, Ni-NiPc-$(NH)_8$ was also constructed in an eclipsed AA-stacking mode but had a higher conductivity of 0.2 S cm^{-1}.[87] Then, Yang *et al.* synthesised a K_3Fe_2[FePc-O_8] framework with a mixture of Fe^{II} and Fe^{III}.[94] This MOF exhibited *p*-type semiconducting behaviour with a carrier mobility of 15 ± 2 cm^2 V^{-1} s^{-1} at RT. Apart from these M-MPc frameworks, other MOFs whose metal nodes are different from the Pc-metal centres have also been studied. For example, the conductivities of Cu-NiPc-O_8 and Cu-NiNPc-O_8 were reported in the order of 10^{-2} S cm^{-1}, whereas Ni-CuPc-$(NH)_8$ had a conductivity of 10^{-3} - 10^{-4} S cm^{-1}.[88-90]

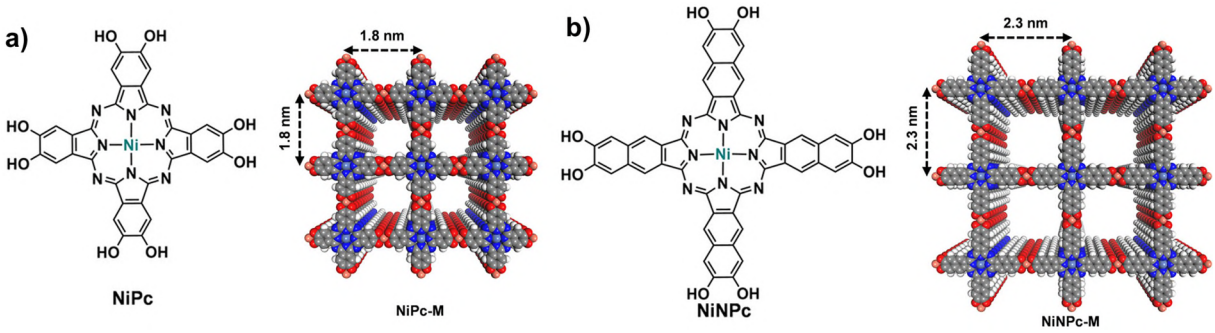


Figure 2.7: Structures of phthalocyanine and naphthalocyanine-based MOFs: (a) NiPc-M and (b) NiNPc-M. (Taken from Ref. 90)

2.2.2.4 Other linkers

To increase the acidity of the catechol groups and improve the in-plane crystallinity, Dou *et al.* designed a new electron-deficient ligand, HHTQ.[102] Single crystals of M-HHTQ (M: Cu, Ni, Co, Mg) can be grown in a rod or plate morphology with sizes ranging from 5 μm to 200 μm. Another ligand, HITN, could be used to regulate the pore size of MOFs.[52] For instance, $Ni_3(HITN)_2$ has a pore diameter of 2.39 nm, larger than $Ni_3(HITP)_2$ (1.57 nm). Chen *et al.* prepared a Cu_2(DBC) MOF with a four-fold interpenetration of distorted diamond networks. Although this material is not two-dimensional, the strong *d-π* conjugation also makes it have a decent electrical conductivity of 10^{-2} S cm^{-1}.[101] Usually, c-MOFs are synthesised using only one ligand, but Yao *et al.* reported a dual-ligand MOF, Cu_3(HHTP)(THQ), based on mixed HHTP and THQ.[113] The unit cell was in an AB slipped parallel stacking mode with a pore size between $Cu_3(HHB)_2$ and $Cu_3(HHTP)_2$. This MOF also exhibited a conductivity of 2.53×10^{-5} S cm^{-1}, higher than $Cu_3(HHB)_2$ but much lower than $Cu_3(HHTP)_2$.

Table 2.2 summarises the conductivities of the MOFs mentioned above. However, the measurement methods in each report are different, making it is difficult to compare their conductivities directly. Even for the same material, the conductivity value may vary if the measurement conditions change, for example, two-probe vs four-probe and powders vs thin films vs single crystals. A measurement standard needs to be set up in the future. Among all the

reported cases, MOFs with conductivities higher than 10^{-4} S cm^{-1} are promising to be used in electronic applications.[114] Apart from the conductivity, the performance of applications also depends on other properties, like porosity, morphology, surface area, catalysis, and stability.

Table 2.2 Conductivities of 2D c-MOFs

MOFs	Conductivity (S cm^{-1})	Measurement method	Ref.
	Triphenylene-derived linkers		
$Cu_3(HHTP)_2$	0.2	4-probe single crystal	1
	1.5	4-probe single crystal (perpendicular)	71
	0.5	2-probe single crystal (parallel)	71
	2.7×10^{-2}	van der Pauw pellet	73
$Co_3(HHTP)_2$	3.2×10^{-2}	van der Pauw pellet	73
	3.3×10^{-3}	van der Pauw film	73
$Ni_3(HHTP)_2$	6.8×10^{-3}	van der Pauw pellet	73
	1.1×10^{-3}	van der Pauw film	73
Fe-HHTP	3.55×10^{-5}	4-probe pressed pellet	109
$La_{1+x}HHTP$	8.2×10^{-4}	2-probe pressed pellet	72
$Nd_{1+x}HHTP$	8.0×10^{-4}	2-probe pressed pellet	72
$Ho_{1+x}HHTP$	5.3×10^{-2}	2-probe pressed pellet	72
$Yb_{1+x}HHTP$	1.0×10^{-2}	2-probe pressed pellet	72
$Ni_3(HITP)_2$	2	2-probe pressed pellet	76
	40	van der Pauw film	76
	150	4-probe single crystal (parallel)	71
	1.9	4-probe pressed pellet	78
$Co_3(HITP)_2$	8×10^{-4}	4-probe pressed pellet	78
$Pt_3(THT)_2$	2.47×10^{-4}	2-probe pressed pellet	81
$Co_3(THT)_2$	1.4×10^{-3}	4-probe pressed pellet	82
	Benzene-derived linkers		
$Cu_3(HHB)_2$	7.3×10^{-8}	van der Pauw pellet	53
$Cu_3(HHTP)(THQ)$	2.53×10^{-5}	2-probe pressed pellet	113
$Ni_3(HIB)_2$	8	van der Pauw pellet	55
$Cu_3(HIB)_2$	13	van der Pauw pellet	55

Table 2.2 continued

$Co_3(HIB)_2$	1.57	4-probe pressed pellet	58
$Ni_3(BHT)_2$	0.15	2-probe pressed pellet	60
	160	van der Pauw film	110
$Cu_3(BHT)$	1,580	4-probe film	63
	2,500	4-probe film	5
$Ag_3(BHT)$	250	4-probe film	64
$Au_3(BHT)$	10^{-4}	4-probe film	111
Phthalocyanine-derived linkers			
Cu-CuPc-O_8	~1×10^{-7}	2-probe pressed pellet	92
Ni-NiPc-$(NH)_8$	0.2	4-probe film	87
Ni-CuPc-$(NH)_8$	1×10^{-4}	van der Pauw film	89
Ni-NiPc-O_8	7.22×10^{-4}	4-probe pressed pellet	90
Cu-NiPc-O_8	1.43×10^{-2}	4-probe pressed pellet	90

2.3 On-surface synthesis of 2D c-MOFs

2.3.1 Synthesis methods of 2D c-MOFs

A series of methods have been developed to synthesise 2D c-MOFs, where hydro/solvothermal and interface-assisted syntheses are most popular. Hydro/solvothermal synthesis is a liquid-phase method in which reactants are sealed in autoclaves with water or other solvents under a high temperature and pressure (Fig. 2.8a and b).[115] Adjusting reaction conditions, like solvents, volume, temperature, and pressure, can modulate the crystal structures and morphologies of MOFs. After optimising the conditions, Dincă's group synthesised several single crystals (rods or flakes) of 2D c-MOFs with dimensions of more than 1 μm.[71, 102] Although this method can synthesise MOFs with a high yield and a low cost, it still has some disadvantages. For example, it is difficult to observe the growth process of the materials since the vessel is enclosed. Secondly, the synthesis is sensitive to many conditions, so it is time-consuming to optimise them and find the most suitable one. Furthermore, this method usually yields microcrystalline powders or single crystals, which are difficult to be incorporated into electronic devices.[106]

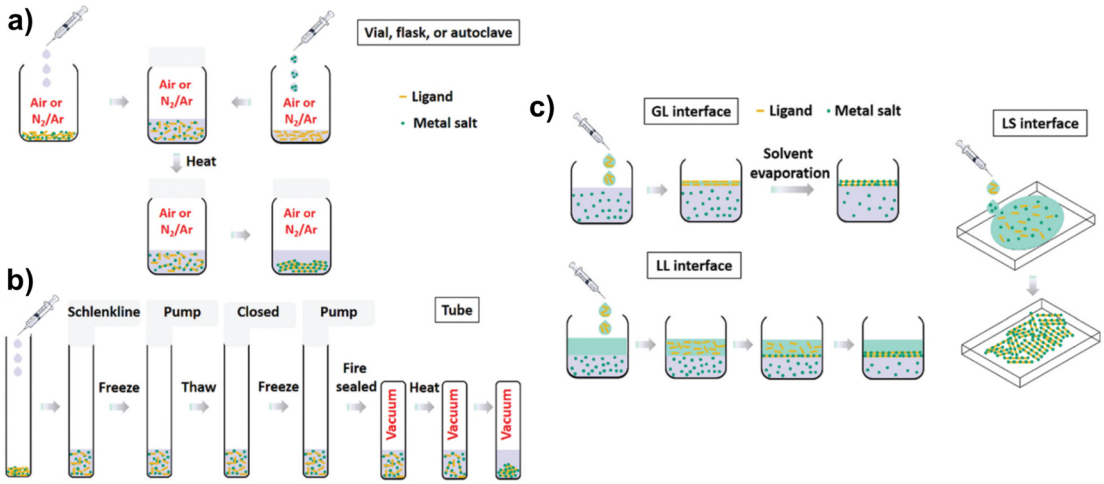


Figure 2.8: (a, b) Schematic illustration of hydro-/solvothermal syntheses methods. (a) Under ambient or inert atmosphere. (b) Under vacuum. (c) Schematic illustration of gas–liquid (GL), liquid–liquid (LL) and liquid-solid (LS) interfacial methods. (Taken from Ref. 2)

In comparison, interface-assisted synthesis methods can be used to fabricate large-scale thin films with a controllable thickness, which is beneficial for device integration.[116] Different synthetic routes have been employed to prepare 2D c-MOFs films, including gas-liquid,[60, 117-118] liquid-liquid,[84, 97, 111, 119] and liquid-solid[75, 120-121] interfacial approaches and self-assembly on solid surfaces (Fig. 2.8c).[13, 122] For example, using the liquid-liquid interfacial method, Rubio-Giménez *et al.* synthesised $Cu_3(HHTP)_2$ films with a thickness of 10 nm and Huang *et al.* obtained large continuous films (> 1 cm^2) of $Cu_3(BHT)_2$.[63, 119] More importantly, Dong *et al.* reported the fabrication of a free-standing single-layer Ni-THT sheet (0.7-0.9 nm in thickness) at an air-water interface.[123] Besides, large single crystals of $Ni_3(HHTP)_2$ with lateral dimensions exceeding 10 μm can also be grown by the liquid-solid interfacial method.[124]

2.3.2 On-surface synthesis

As a part of self-assembly methods, on-surface synthesis has been well-demonstrated for fabricating supramolecular or metal-organic structures, including 1D chains and 2D networks.[12-13] It also provides an opportunity to explore the chemical and physical properties of these low-dimensional nanostructures. The molecules adsorbed on the surfaces can be

assembled via several interactions, like van der Waals forces, dipole-dipole interactions, hydrogen bonds, and metal-organic coordinate bonds.[125-126] Table 2.3 shows some basic properties of these intermolecular interactions. Compared with other non-covalent interactions, coordinate bonds are stronger, so usually the metal-organic networks are thermally more stable than other supramolecular systems, like hydrogen bonded assemblies.

Table 2.3 Intermolecular interaction types with typical energy and bonding distance[125-126]

Interaction type	Energy range (eV)	Distance (nm)
van der Waals	0.02 – 0.1	0.5 – 1
Dipole-dipole	0.1 – 0.5	0.2 – 0.3
Hydrogen bond	0.05 – 0.7	0.15 – 0.35
Metal-ligand coordinate bond	0.5 – 3	0.15 – 0.3
Electrostatic ionic	0.05 – 3	Up to several nm

Before 2D c-MOFs, metal-organic coordination structures have been extensively investigated on surfaces using STM. Classen *et al.* reported 1D chains of TMA (1,3,5-benzenetricarboxylic acid) on a Cu(110) substrate.[127] Although the TMA molecules had a three-fold symmetry, the anisotropic geometry of the Cu(110) substrate exhibited a strong templating effect. As shown in Fig. 2.9a, the TMA molecules were coordinated with Cu dimers, forming linear [-Cu-TMA-Cu-]$_n$ chains along the [1$\bar{1}$0] direction. Using a porphyrin derivate, Heim *et al.* synthesised 1D polymers with two-fold pyridyl-Cu-pyridyl coordination units on Cu(111) and Ag(111) surfaces.[128] As shown in Fig. 2.9b, these chains exhibited a high flexibility as there were many curved segments. Boscoboinik *et al.* also prepared 1D chains of 1,4-diisocyanobenzene molecules linked via NC-Au-NC coordination motifs.[129] Apart from these straight lines, some other linear structures have also been reported. For example, Knor *et al.* studied 1,4-diaminonaphthalene molecules on Cu substrates and found that they could form zigzag chains on Cu(111) and kinked chains on Cu(110).[130] This was caused by the stereoselectivity of *trans*- and *cis*-forms of the H_2N-Cu-NH_2 coordination motifs on different substrates.

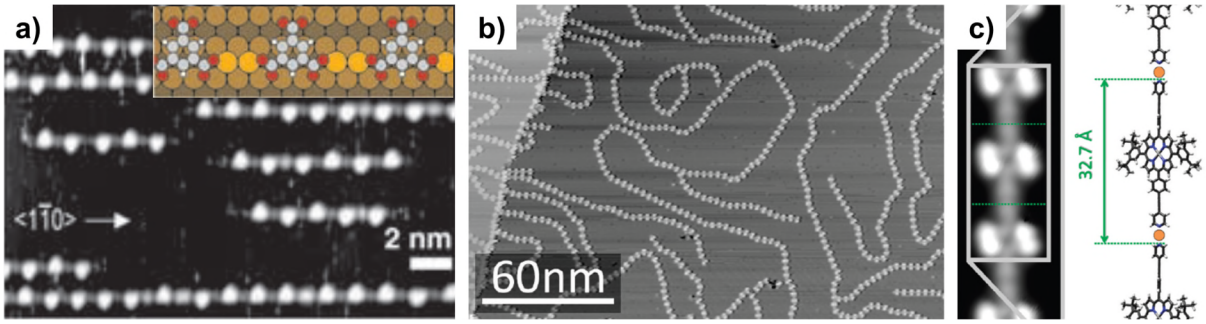


Figure 2.9: (a) STM image of [-Cu-TMA-Cu-]$_n$ chains on Cu(110). Inset: the atomistic model. (Taken from Ref. 127) (b) STM image of porphyrin-Cu chains on a Cu(111) surface. V_s = 1.0 V, I_t = 0.25 nA. (c) High-resolution STM image and model of the coordination unit in (b). V_s = −1.0 V, I_t = 77 pA. (Taken from Ref. 128)

Li *et al.* reported a 2D network of TPyP [5,10,15,20-tetra(4-pyridyl)porphyrin] molecules on a Au(111) surface.[131] The molecules were linked via two-fold pyridyl-Cu-pyridyl coordination motifs to form a square lattice. Based on the same molecule, a 2D Fe network was also synthesised by Lin *et al.*, which was constructed by four-fold Fe-(pyridyl)$_4$ motifs.[132] More importantly, Tait *et al.* prepared a robust 2D architecture with nearly identical structure on Cu(100), Ag(100) and Ag(111) substrates.[133] As shown in Fig. 2.10a, the Cu atoms coordinated with the PBP [5,5'-bis(4-pyridyl)(2,2'-bipyrimidine)] molecules in a three-fold geometry and formed a brick-wall-like pattern on these three substrates. This study demonstrated that selecting a strong metal-organic coordination motif could overcome the influences of substrates with different structures and symmetries.

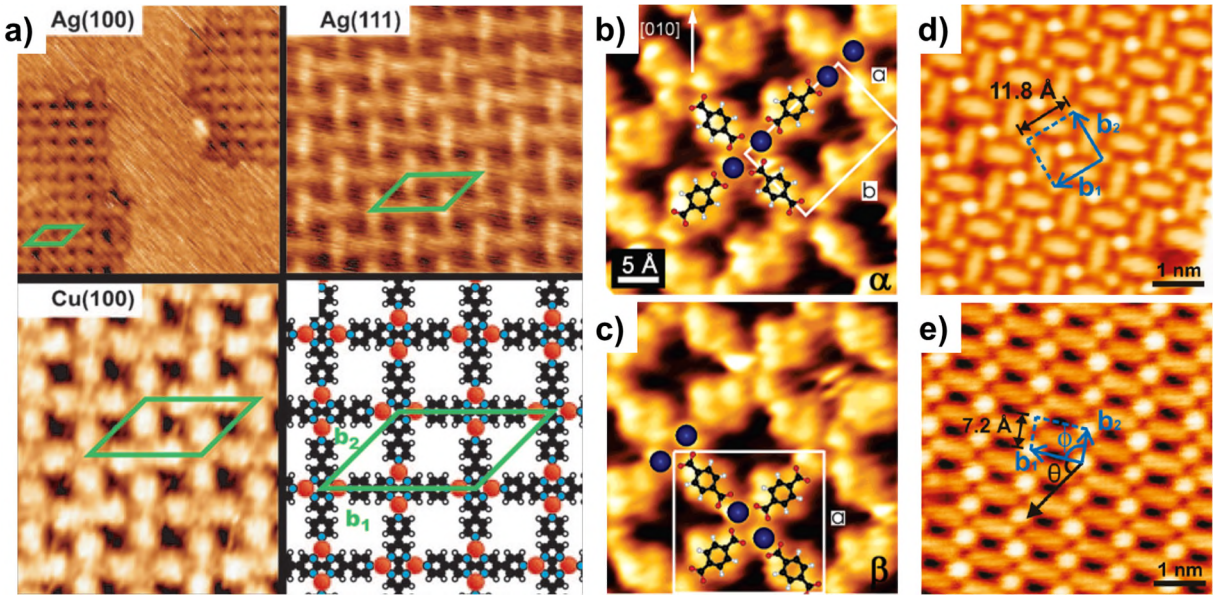


Figure 2.10: (a) STM images of PBP-Cu networks on Ag(100), Ag(111) and Cu(100) surfaces. A molecular model is also included. (Taken from Ref. 133) (b, c) STM images of the Fe-TPA networks: (b) α-phase and (c) β-phase. (Taken from Ref. 134) (d, e) STM images of TCNQ-Ni phases: (d) α-phase and (e) β-phase. (Taken from Ref. 135)

TPA (terephthalic acid) molecules could form various complexes with Fe on Cu(100) and two coordination networks are shown in Fig. 2.10b and c.[134, 136-138] The nodes of these two networks were comprised of a Fe-Fe unit surrounded by four ligands and the Fe atom was coordinated in a distorted square-planar geometry. In the first network (α-phase), all the Fe-Fe units had the same orientation, forming a rectangular lattice. The orientation of the Fe-Fe units in the second network (β-phase) rotated 90° with respect to the adjacent units, resulting in a square lattice. Tseng *et al.* studied the coordination reaction between Ni atoms and TCNQ (7,7,8,8-tetracyanoquinodimethane) molecules on a Ag(100) surface and also found two phases of coordination networks.[135] In both phases, the TCNQ molecules were bound with the Ni atom in a four-fold coordination geometry. As shown in Fig. 2.10d, the molecules rotated 90° alternatively in the α-phase, forming a square lattice. In the β-phase, the molecules were aligned in parallel, leading to a rhombic lattice (Fig. 2.10e). After that, the reaction between TCNQ and Ni on Au(111) was also studied by the authors, but only the parallel alignment was found.[139]

Hexagonal metal-organic networks of dicarbonitrile-polyphenyl linkers [NC-$(Ph)_n$-CN (n: 3-6)] have been widely studied on Ag(111) substrates.[140-142] In these networks, the molecules coordinated with the Co atoms in a three-fold geometry, resulting in the formation of hexagonal structures. As shown in Fig. 2.11a-c, the size of the pores can be tunned through extending the length of the linkers, showing the flexibility and controllability of on-surface synthesis. Matena *et al.* also reported a honeycomb network based on the reaction between dehydrogenated DPDI (4,9-diaminoperylene-quinone-3,10-diimine) molecules and Cu adatom trimers on a Cu(111) substrate.[143] Shi *et al.* used TPyB [1,3,5-tris(pyridyl)benzene] molecules and prepared a hexagonal network on Au(111).[144] Similar to previous study, the coordination in this structure was still the two-fold pyridyl-Cu-pyridyl motif, as shown in Fig. 2.11d.

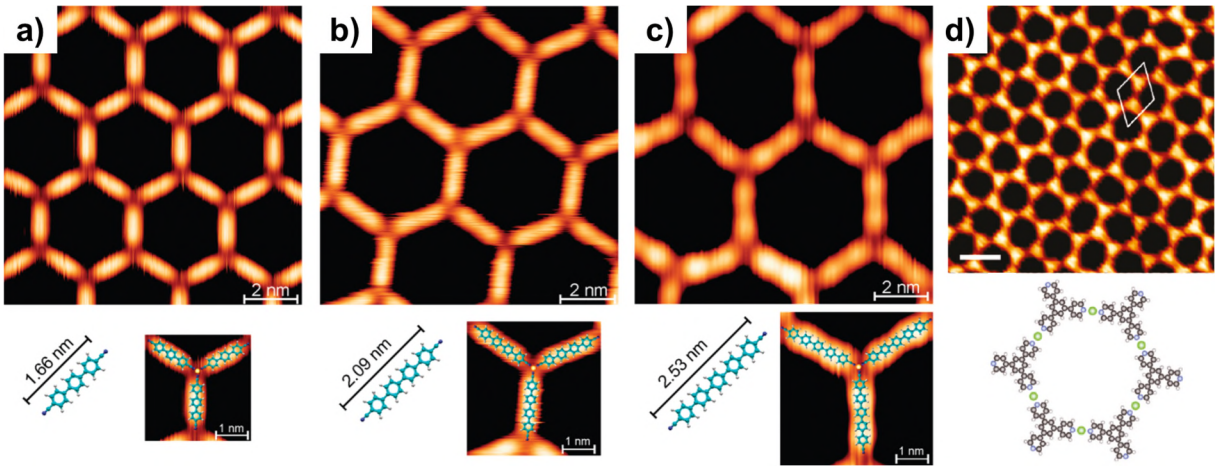


Figure 2.11: (a-c) STM images of Co coordinated honeycomb networks on Ag(111). Structure models and molecular length are included in the bottom. (a) NC-Ph_3-CN, V_s = 0.9 V, I_t = 0.1 nA. (b) NC-Ph_4-CN, V_s = 1.0 V, I_t = 0.1 nA. (c) NC-Ph_5-CN, V_s = 2.0 V, I_t = 0.1 nA. (Taken from Ref. 141) (d) STM image and structure model of the TPyB-Cu network. Scale bar: 3 nm. (Taken from Ref. 144)

When it comes to the 2D c-MOFs, the first surface study is the self-assembly of HHTP molecules on Ag(111), which was carried out by Pawlak *et al* in 2009.[145] Under STM, HHTP molecules appeared as triangles and had a flat-lying configuration on the Ag(111) surface. Depending on the substrate temperature, HHTP molecules could form three distinct phases. At room temperature, HHTP molecules faced each other and constructed rows of dimers (Fig. 2.12a).[146-147] This phase was referred as 'Zip', where the rows were aligned with the [1$\bar{1}$0]

direction of Ag(111). When the substrate temperature increased to 470 K, the molecules organised themselves into large triangular domains, and these well-ordered arrays could extend over 100 nm.[146-148] As shown in Fig. 2.12b, these triangles had a size of around 30 nm and were separated by Zip lines (domain boundaries). The hexagonal cell of the triangular domains had a constant of 1.1 ± 0.1 nm and aligned along the [1$\bar{1}$0] direction, corresponding to a superstructure of (4 × 4). Therefore, this assembly was called the (4 × 4) phase.

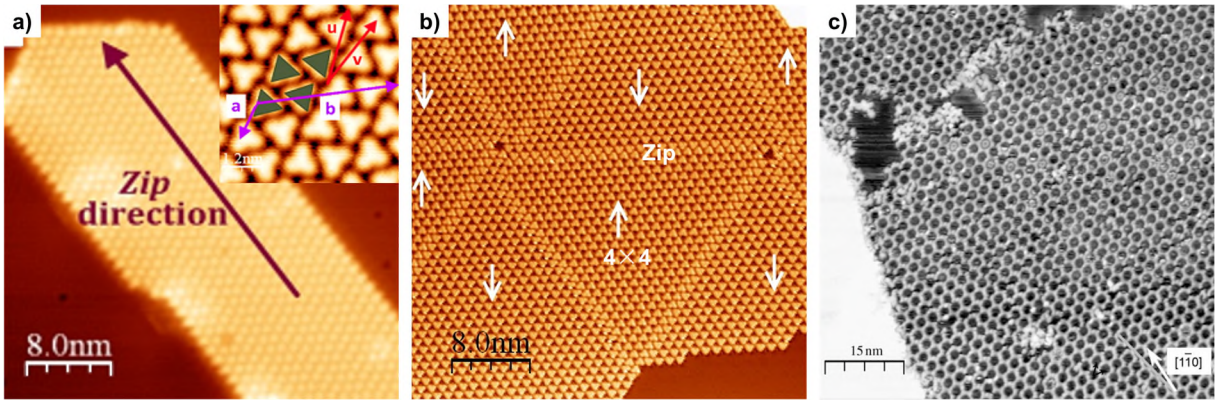


Figure 2.12: HHTP self-assemblies on Ag(111). (a) HHTP Zip phase at room temperature. Inset: higher magnification. V_s = 1.5 V, I_t = 10 pA, T = 4.5 K. (b) (4 × 4) superstructure with triangular domains. V_s = −1.2 V, I_t = 50 pA, T = 4.5 K. (Taken from Ref. 146) (c) The honeycomb network of HHTP formed after annealing at 500 K. V_s = −1.4 V, I_t = 0.4 nA, T = 298 K. (Taken from Ref. 145)

After annealing at 500K, HHTP molecules formed a network with a honeycomb structure, as shown in Fig. 2.12c.[145, 147] In this phase, the molecules were dehydrogenated di- and tetra-ketone molecules, whose carbonyl groups were transformed from original hydroxyl groups. However, Giovanelli *et al.* did XPS characterisations on these phases and found that the dehydrogenation reaction already occurred at room temperature.[147] With the increase in the deposition temperature, the rate of dehydrogenation increased. The ratios of hydroxyl to carbonyl groups were 3.0 for the Zip phase, 2.1 for the (4 × 4) phase and 1.4 for the honeycomb phase.

In 2021, Gomez-Herrero *et al.* used Cu(111) as the substrate to study the oxidation of HHTP molecules on it.[149] As illustrated in Fig. 2.13a, XPS measurements revealed that the carbonyl

groups already existed at 300K with a similar weight of hydroxyl groups, suggesting a semiquinone molecule formed. After annealing to 530K, all the groups were dehydrogenated, yielding a quinone molecule. Then, a study of 2D metal-HHTP networks on Cu(111) and Ag(111) surfaces was reported by Rochefort *et al.*[150] On Cu(111), some locally ordered lines of HHTP molecules were observed in Fig. 2.13b, resembling the 'Zip' phase on Ag(111). After annealing at 530 K, the molecular assemblies became more disordered, shown in Fig. 2.13c. There were also some dim triple dots in the domains, corresponding to Cu_3 adatom clusters. In comparison, HHTP molecules formed a homogeneous Ag-HHTP metal-organic network with Ag adatom clusters after deposition on Ag(111) at 473 K (Fig. 2.13d). DFT calculations indicated that the molecular adlayer matched with the (4 × 4) supercell of the substrate, where the HHTP molecules were on the top of Ag atoms. The simulated STM image based on the Ag_3 clusters coordinating with the molecules is shown in Fig. 2.13e, which was very similar to the experiment results, supporting the adsorption model.

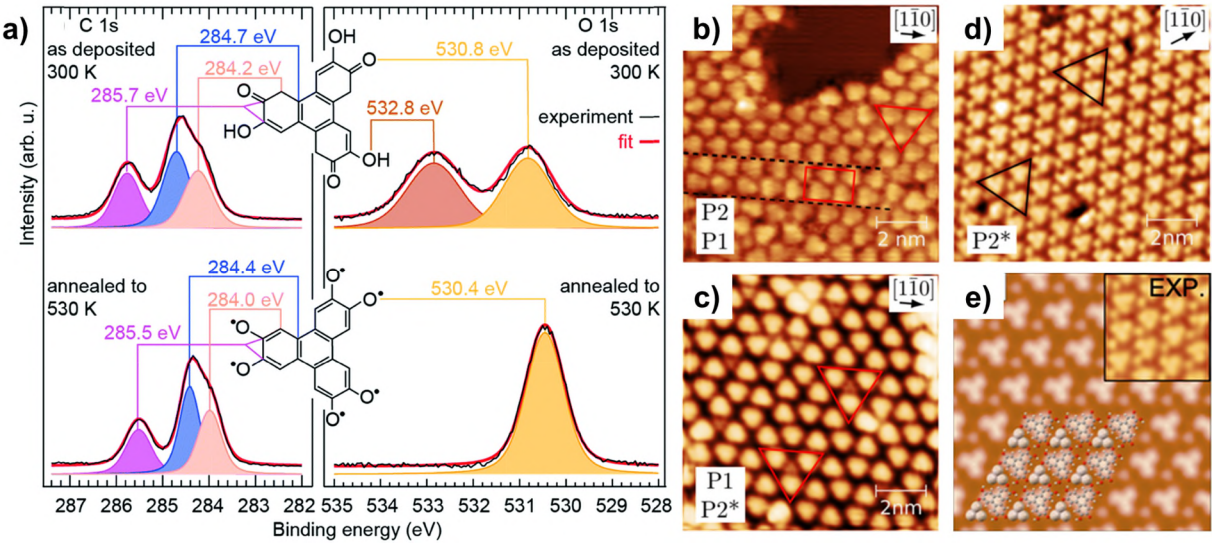


Figure 2.13: (a) High-resolution C 1s and O 1s core level spectra of a sub-monolayer HHTP deposited on Cu(111), before and after annealing to 530 K. (Taken from Ref. 149) (b, c) STM images of HHTP assemblies for adsorption at (b) 293 K and (c) 530 K on Cu(111) surfaces. (d) STM image of HHTP-Ag network after deposition at 473 K on Ag(111). (e) Simulated STM images in the constant-current mode with I_t = 0.1 nA and V_s = −1.0 V. (Taken from Ref. 150)

Apart from Ag(111) and Cu(111), three phases of HHTP molecular assemblies were also found on Au(111) substrates.[151] Phase 1 formed at room temperature, which had a hexagonal lattice with one molecule per unit cell, as shown in Fig. 2.14a. After annealing, Phase 2 ("Bow Tie") was obtained, and its structure was more complicated (Fig. 2.14b). The molecular rows in this phase can be divided into two types, '*head-to-head*' and '*head-to-tail*', where the direction of the '*head-to-tail*' rows could change. The third "Ribbons" Phase also formed after annealing but had an oblique lattice with two molecules per cell (Fig. 2.14c). This phase almost has the same structure as the 'Zip' phase of the HHTP assembly on the Ag(111) surface.

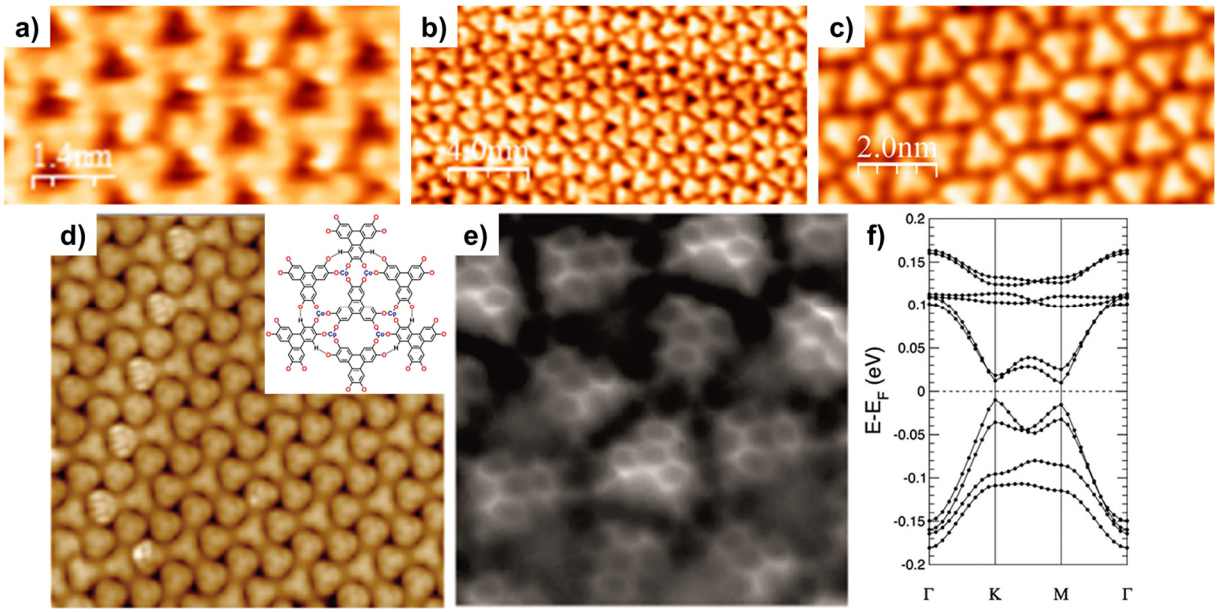


Figure 2.14: (a-c) HHTP self-assemblies on Au(111). (a) Phase 1. V_s = −0.25 V, I_t = 80 pA. (b) Phase 2. V_s = −0.98 V, I_t = 40 pA. (c) Phase 3. V_s = −0.22 V, I_t = 34 pA. (Taken from Ref. 151) (d) STM image of Co-HHTP networks on Au(111). Size: 11.7 nm × 11.7 nm, V_s = 20 mV, I_t = 120 pA, T = 4 K. (e) Constant-height frequency-shift nc-AFM image acquired with a CO-functionalised tip. Size: 3.2 nm × 3.2 nm, open feedback: V_s = 5 mV, I_t = 150 pA, Z_{offset} = 150 pm, T = 4 K. (f) Electronic band structure of the Co-HHTP network with the ground-state spin configuration. (Taken from Ref. 152)

In 2022, Martín-Fuentes *et al.* reported the reaction between HHTP and Co on Au(111).[152] As shown in Fig. 2.14d, a Co-HHTP metal-organic network was prepared after annealing at 250 °C, which had a different structure from honeycomb $Co_3(HHTP)_2$ MOFs synthesised in wet chemistry. In this structure, Co atoms adopted a three-fold coordination geometry with three HHTP molecules, demonstrated by nc-AFM in Fig. 2.14e. In the DFT-relaxed structure, the

molecules were located 3.3-3.4 Å above the Au surface, while the height of Co atoms were 2.8 and 3.2 Å. The calculation also revealed that the spin configuration of this network was the local noncollinear antiferromagnetic state with all spins in-plane. Fig. 2.14f shows the band structure of the spin ground-state network calculated by DFT + U (3.75 eV for Co), displaying an electronic gap of 30 meV at the K point.

Using the HATP linker, Gao *et al.* synthesised single-layer $Ni_3(HITP)_2$ and $Fe_3(HITP)_2$ MOFs on the Au(111) substrate.[122, 153] As shown in Fig. 2.12a and c, honeycomb networks were obtained after depositing HATP molecules and Ni/Fe atoms and post-annealing at 250 °C. Both frameworks had the same lattice constant of 2.17 ± 0.02 nm, and the orientation rotated 6.6° with respect to the $[1\bar{1}0]$ direction of Au(111), corresponding to a superstructure of $\left(\sqrt{57} \times \sqrt{57}\right)$ R 6.6°. The DFT-optimised structure of $Fe_3(HITP)_2$ on Au(111) is shown in Fig. 2.15a, where the Fe atoms were located at the bridge sites of the Au substrate. The molecular backbones were 2.68 Å above the Au atoms, and the Fe atoms dropped down around 0.2 Å off the plane. Bader charge analysis revealed that the molecule gained 0.2 *e* from the substrate, while Fe lost 0.07 *e* to the substrate. In the adsorbed model of the $Ni_3(HITP)_2$ MOF, the layer transferred 0.82 *e* per unit cell to the substrate, as illustrated in Fig. 2.15d. Moreover, DFT calculations of the $Ni_3(HITP)_2$ also showed that a non-trivial band gap of 8 meV was opened at the K point when spin-orbit coupling (SOC) interactions were included. For the $Fe_3(HITP)_2$ MOF, it had a ferromagnetic ground state with several non-trivial topological band gaps (2 gaps at the K point and 3 gaps at the Γ point). However, more experiments with higher energy resolution are needed to verify these calculation results.

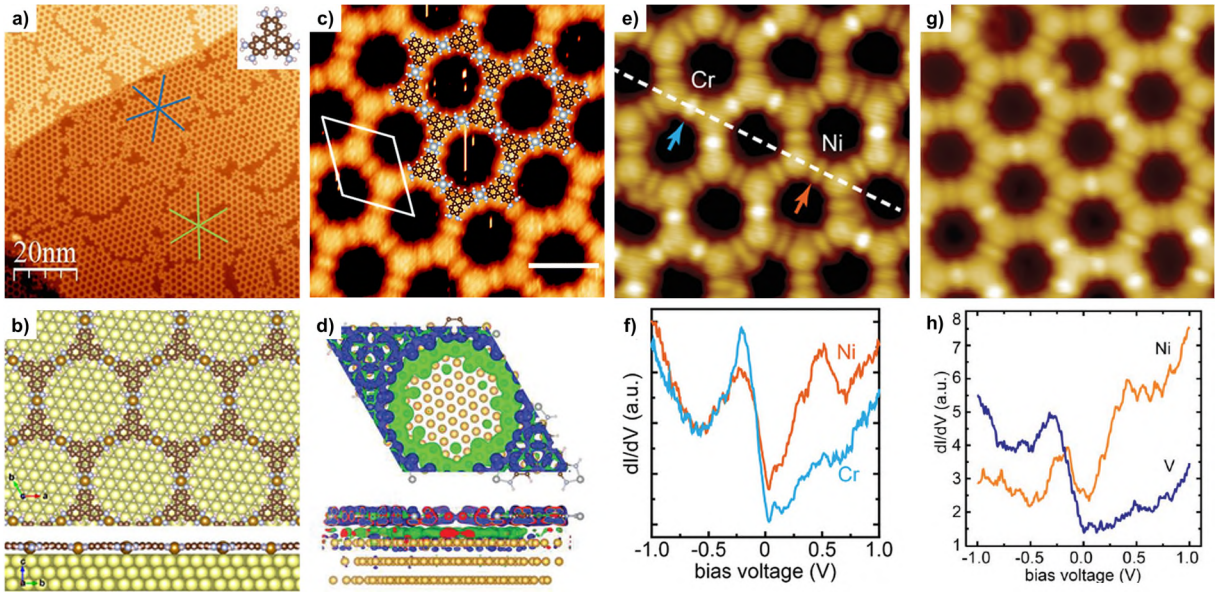


Figure 2.15: (a) $Fe_3(HITP)_2$ framework on Au(111). V_s = −1.6 V, I_t = 0.2 nA, T = 298 K. (b) DFT-optimised structure of $Fe_3(HITP)_2$ on a three-layer Au(111) slab. (Taken from Ref. 153) (c) High-resolution STM image of $Ni_3(HITP)_2$ with a molecular model overlaid. Scale bar: 2 nm. (d) Top and side views of charge transfer. Green (blue) colour represents charge accumulation (depletion), respectively. (Taken from Ref. 122) (e) Partially substituted $Ni_xCr_{3-x}(HITP)_2$ framework. Size: 8 nm × 8 nm, V_s = −1.0 V, I_t = 0.1 nA. (f) Typical dI/dV spectra measured at Ni atom (orange) and Cr atom (blue) in $(Ni_xCr_{3-x})(HITP)_2$ framework. (g) High-resolution STM images of $(Ni_xV_{3-x})(HITP)_2$ framework. Size: 8 nm × 8 nm, V_s =−1.0 V, I_t = 0.1 nA. (h) Typical dI/dV spectra of Ni and V atoms in $(Ni_xV_{3-x})(HITP)_2$ framework. (Taken from Ref. 154)

In 2023, the synthesis of $Cr_3(HITP)_2$ MOF on Au(111) was reported by Zhong *et al.*[154] Because the co-deposition of Cr atoms and HATP precursors only caused irregular branches, the crystalline $Cr_3(HITP)_2$ framework was obtained by substituting Cr for Ni in $Ni_3(HITP)_2$. The synthesised $Cr_3(HITP)_2$ had the same lattice constants and domain orientations as the $Ni_3(HITP)_2$ template. When a small amount of Cr atoms were dosed onto the $Ni_3(HITP)_2$ framework, some bright atoms appeared in the STM image (Fig. 2.15e). Site-dependent STS measurements indicated that these bright atoms were Cr, which had a main peak at -0.21 V without obvious unoccupied states (Fig. 2.15f). The authors also demonstrated that the substitution strategy could be used to synthesise bimetallic $Ni_xV_{3-x}(HITP)_2$ (Fig. 2.15g and h) and $Fe_xCr_{3-x}(HITP)_2$ MOFs. Apart from Au(111), Lischka *et al.* used Cu(111) as the substrate to investigate the coordination reaction between metals and HATP.[155] They found that HATP

molecules coordinated with Cu_3 adatom clusters and formed aggregates composed of interlinked trimers on the Cu(111) surface. After depositing more reactive Ni atoms onto the Cu(111) substrate, small patches of hexagonal Ni-HATP structures formed, but the extended honeycomb network remained elusive.

A single-layer Cu-BHO network was also prepared on the Cu(111) substrate through the on-surface method.[156] During the annealing process, BHO molecules coordinated with the substrate Cu atoms, forming a 2D network (Fig. 2.16a). The DFT-optimised structure suggested that each molecule was connected to six Cu atoms, and each Cu atom coordinated with two O atoms. The calculated band structures of the free-standing and the adsorbed Cu-BHO network are shown in Fig. 2.16b and c, respectively. The free-standing case had a direct band gap of 2.2 eV at Γ point. After adsorption, the band gap was decreased to 1.0 eV due to the shift of the bands. Fig. 2.16d is a power spectral map of the network, which manifests the band structure features and showed a band gap of 1.5 eV. Hua *et al.* used the same precursor and synthesised a Fe-BHO framework on Au(111).[157] As shown in Fig. 2.16e, the Fe-BHO network had a dense structure where each Fe atom coordinated with four O atoms, slightly different from the Cu-BHO on Cu(111). The network had a lattice constant of 7.6 ± 0.2 Å and exhibited two orientations along the $<21\bar{3}>$ directions of Au(111). DFT calculations indicated that the Fe atoms were closer to the substrate than the BHO molecules by 0.87 Å and the substrate transferred 0.55 *e* to the Fe-BHO framework. Besides, XPS data showed that the hydroxyl groups of the BHO molecules were partially dehydrogenated and transformed to carbonyl groups after adsorption on Au(111) at room temperature.

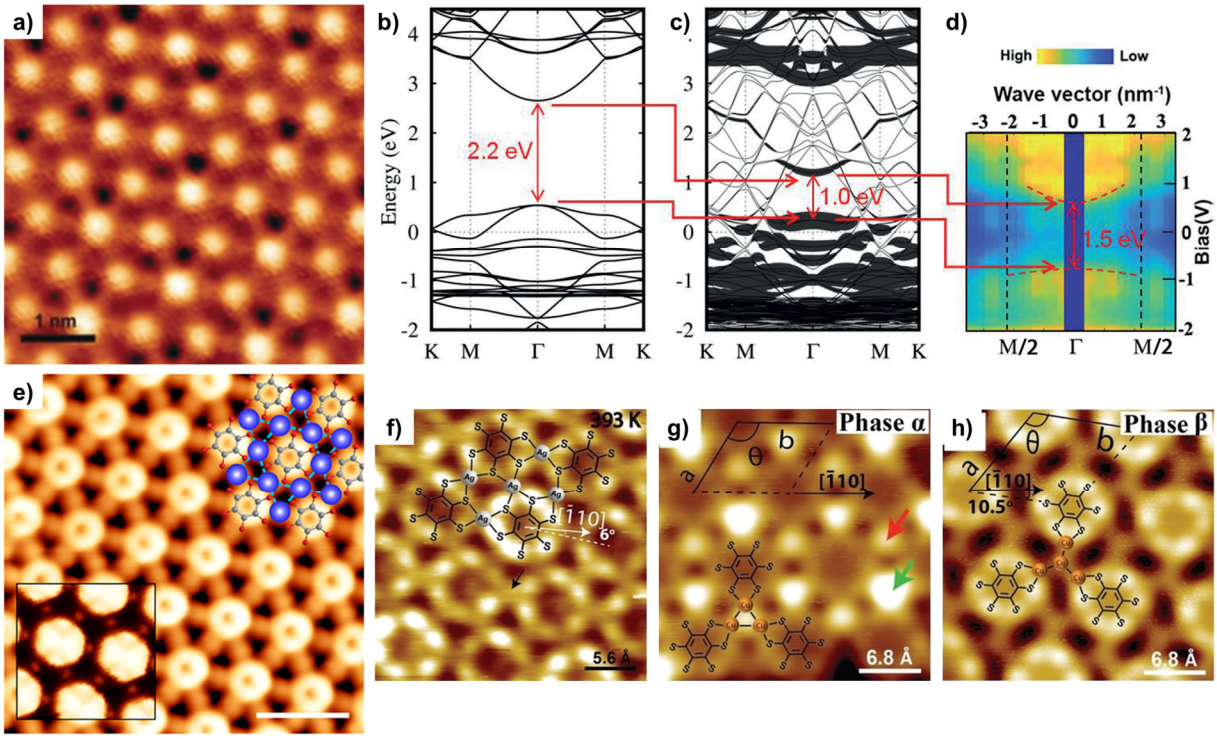
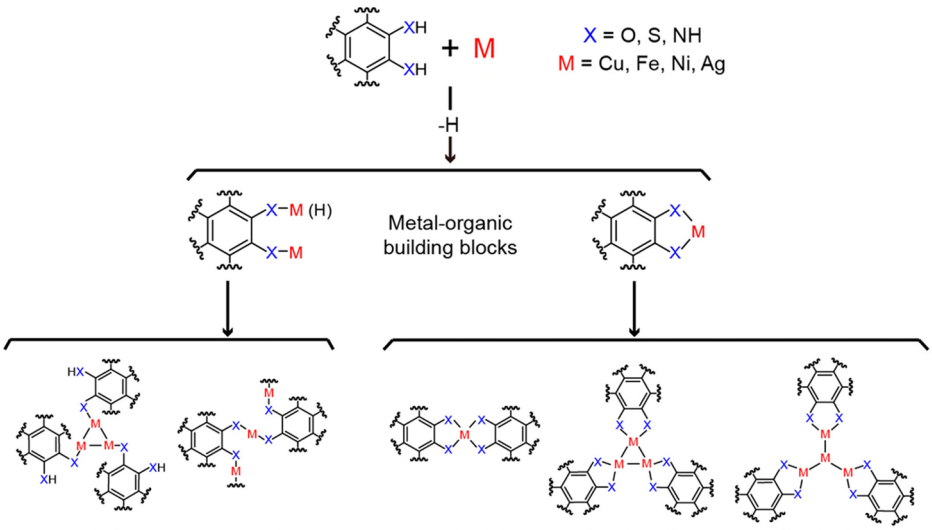


Figure 2.16: (a) Cu-BHO on Cu(111). V_s = 0.3 V, I_t = 1.0 nA. (b, c) DFT-calculated electronic band structures of a free-standing Cu-BHO network (a) and a network adsorbed on Cu(111) (b). (d) Power-spectrum map acquired at a domain of the Cu-BHO network.(Taken from Ref. 156) (e) High-resolution STM image of the $Fe_3(BHO_{-6H})$ network on Au(111). Scale bar: 1 nm. V_s = −10 mV, I_t = 1 nA, T = 5.2 K. Inset: constant-height mode STM. V_s = 10 mV, I_t = 1 nA, T = 2.6 K. (Taken from Ref. [157]) (f) STM image of the BHT-Ag after annealing at 393 K. V_s = 46 mV, I_t = 260 pA. (g, h) BHT-Cu Phase α and Phase β. V_s = −0.14 V, I_t = 0.96 nA (g); V_s = −0.2 V, I_t = 1.4 nA (h). (Taken from Ref. 158)

Meng *et al.* studied BHT-based coordination networks on Ag(111) and Cu(111) substrates.[158] Only one type of coordination network $[Ag_3(C_6S_6)]_n$ was obtained on Ag(111) (Fig. 2.16f). While two phases were observed on Cu(111): Phase α ($[Cu_6(C_6S_6)]_n$) and Phase β ($[Cu_8(C_6S_6)]_n$). As shown in Fig. 2.16g and h, the Phase α was connected by Cu_3 adatom clusters, while the Phase β had a non-coordinated Cu adatom which was metallically bonded to three adjacent coordinated Cu adatoms.

On-surface synthesis has shown promising potential to prepare single-layer 2D c-MOFs and to control their structures and properties.[12, 14] According to the studies introduced above, dihydroxyl and diamino ligands can react with transition metals (Fe, Co, Ni and Cu) to form extended coordination networks easily on the metal substrates. Dithiol linkers, which have been

widely used in wet-chemical synthesis, are rarely reported to construct metal-organic frameworks on surfaces. These results can be summarised in Scheme 2.2.



Scheme 2.2: Schematic illustration of the on-surface coordination reactions and the structures of 2D metal-organic products on surfaces. (Taken from Ref. 12)

2.4 Applications of 2D c-MOFs

2.4.1 Chemiresistive Sensing

Chemiresistive sensing devices are based on materials whose resistances change when exposed to gaseous analytes. Through monitoring the change in the resistance or current, the concentration of analytes could be measured. The first example of 2D c-MOF applied in chemical sensing was $Cu_3(HITP)_2$, shown by Campbell *et al.* (Fig. 2.17a).[77] Drop-casting of $Cu_3(HITP)_2$ onto interdigitated Au electrodes fabricated the sensing device. As shown in Fig. 2.17b, the current showed a sharp increase when exposed to the NH_3/N_2 mixture, and it could recover if the gas flow switched to pure N_2. The change in current was proportional to the NH_3 concentration, and the response could reach a sub-ppm level. After this work, the authors integrated $Cu_3(HHTP)_2$, $Cu_3(HITP)_2$ and $Ni_3(HITP)_2$ into a chemiresistive sensor array and found it could detect different volatile organic compounds (VOCs).[159] There were five categories of VOCs tested (200 ppm), including alcohols, ketones/ethers, aromatic hydrocarbons, aliphatic hydrocarbons and amines. As shown in Fig. 2.17c, $Ni_3(HITP)_2$

displayed an opposite response direction compared to Cu-based MOFs. While $Cu_3(HHTP)_2$ and $Cu_3(HITP)_2$ showed different response magnitudes to the same analyte. Principal component analysis and linear discriminant analysis showed that this MOF-based sensor array could distinguish different classes of VOCs with 90% accuracy.

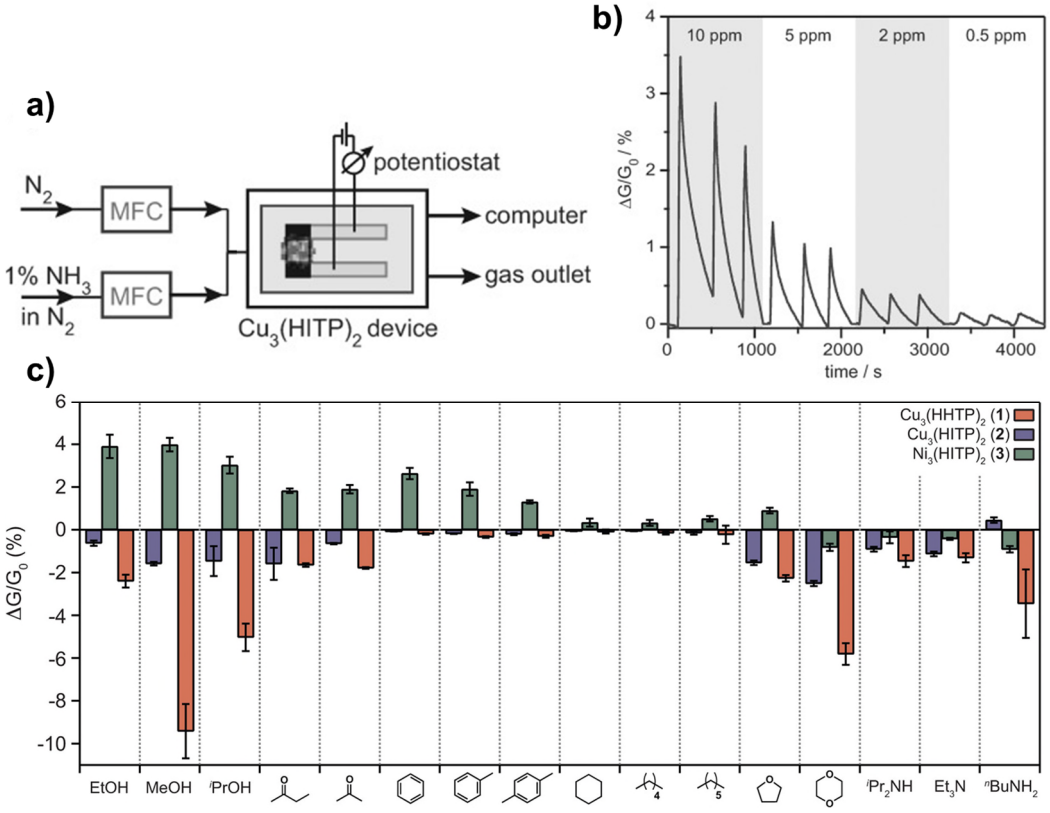


Figure 2.17: (a) Schematic of the sensor device, MFC: mass flow controller. (b) Responses of the $Cu_3(HITP)_2$ device to ammonia with different concentrations. (Taken from Ref. 77) (c) Sensing responses of different HXTP-MOFs to different VOCs (200 ppm). (Taken from Ref. 159)

An improvement in ammonia sensing was reported by Yao *et al.* using layered $Cu_3(HHTP)_2$ MOF.[160] As shown in Fig. 2.18a, the sensor based on 20 nm $Cu_3(HHTP)_2$ films exhibited good response and recovery to NH_3 with a concentration of 1 to 100 ppm. It also showed short response time (1.36 min) and recovery time (9.11 min) (Fig. 2.18b). Moreover, this device kept 88.4% response to NH_3 after 3 months, exhibiting long-term stability. The high performance might be contributed by the thin thickness (< 100 nm) and high crystallinity, which decreased the diffusion length for analytes and facilitated charge transport. Smith *et al.* fabricated conductive textiles coated with $Ni_3(HHTP)_2$ or $Ni_3(HITP)_2$ MOFs through direct self-assembly

of organic linkers and metal nodes from solution onto fabrics (Fig. 2.18c).[161] The self-organised frameworks on textiles (SOFT) device exhibited improved porosity as they combined the microporosity of the MOFs and the mesoporosity of the textile. When exposed to NO, the response of the HHTP-SOFT device decreased while that of the HITP-SOFT increased (Fig. 2.18d and e). As for H_2S, the resistances of both two SOFT devices increased after exposure. Importantly, these devices had high stability and were fully recoverable after washing in water.

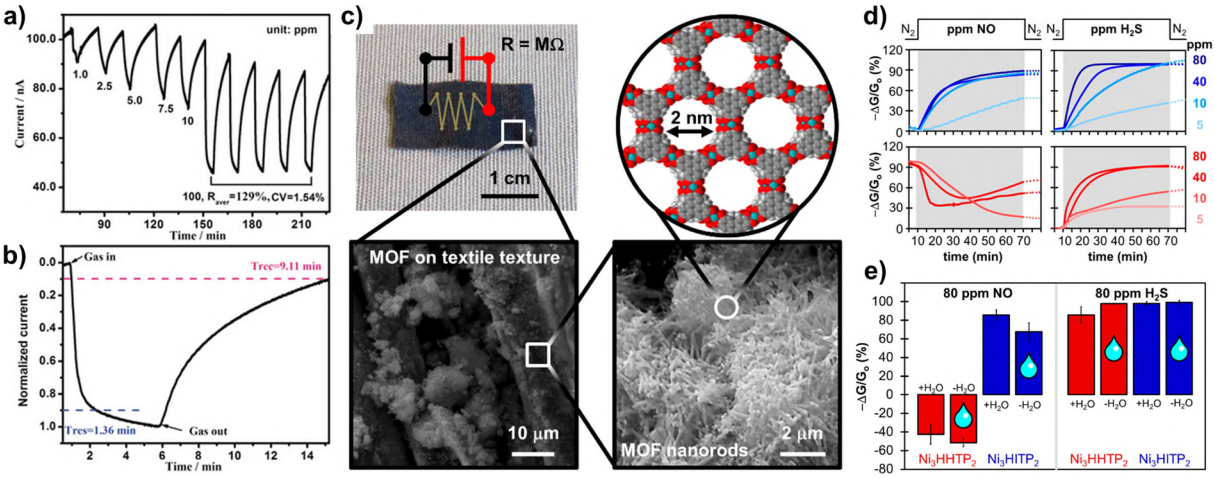


Figure 2.18: (a) The response curve of $Cu_3(HHTP)_2$ films towards NH_3 with different concentrations. (b) Response-recovery time curves of $Cu_3(HHTP)_2$ films to 100 ppm NH_3. (Taken from Ref. 160) (c) Integrating conductive MOFs onto the textiles. (d, e) Sensing responses of $Ni_3(HHTP)_2$ (red) and $Ni_3(HITP)_2$ (blue) SOFTs to NO and H_2S: (d) in dry N_2, (e) in the presence of 5000 ppm water. (Taken from Ref. 161)

2.4.2 Electrocatalysis

Hydrogen evolution reaction (HER), oxygen evolution reaction (OER), and oxygen reduction reaction (ORR) are three important reactions in electrochemical conversions.[162] Inspired by the high efficiency of cobalt dithiolene species for HER, Clough *et al.* studied the electrocatalytic HER activity for two cobalt dithiolene-based MOFs, $Co_3(BHT)_2$ and $Co_3(THT)_2$.[163] As shown in Fig. 2.19a, large current densities were observed for $Co_3(BHT)_2$ (41 mA cm^{-2}) and $Co_3(THT)_2$ (31 mA cm^{-2}) at -0.8 V vs SHE (pH = 1.3). To reach current densities of 10 mA cm^{-2}, the overpotentials for $Co_3(BHT)_2$ and $Co_3(THT)_2$ were 0.34 V and 0.53 V, respectively, at pH = 1.3. These values were much lower than other immobilised catalysts. Dong *et al.* prepared a single-

layer $Ni_3(THT)_2$ sheet and transferred it to a glassy carbon electrode.[123] With the $Ni_3(THT)_2$ catalyst, hydrogen evolution occurred at a potential of 110mV in a 0.5M H_2SO_4 solution. The operating overpotential was 333 mV to achieve a current density of 10 mA cm^{-2} (Fig. 2.19b). Except for these examples, there are also some other 2D c-MOFs exhibiting excellent electrocatalytic performance for HER, like Co-PTC,[105] Ni-TABT,[70] and Ni-HAHATN.[100]

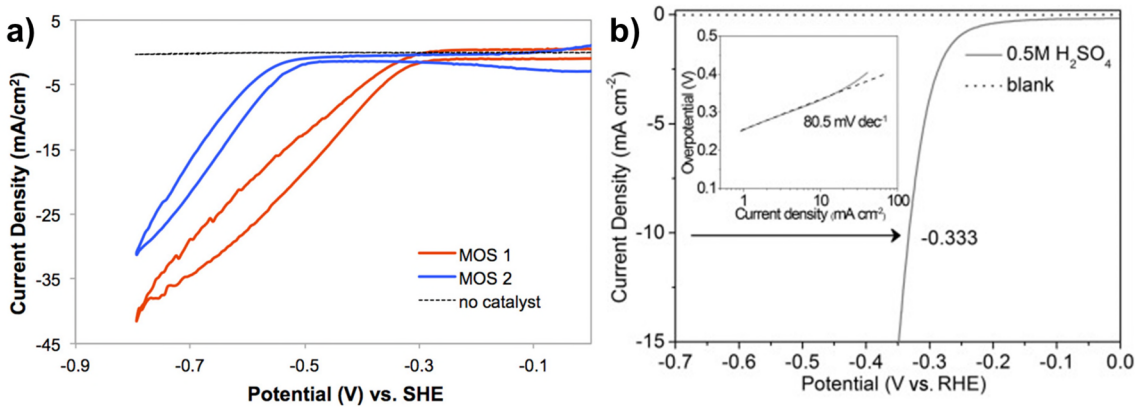


Figure 2.19: (a) Polarisation curves of $Co_3(BHT)_2$ (MOS 1) and $Co_3(THT)_2$ (MOS 2) in an H_2SO_4 solution (pH = 1.3). Scan rate: 100 mV/s. (Taken from Ref. 163) (b) Polarisation curve of $Ni_3(THT)_2$ sheet in 0.5 M H_2SO_4. Inset: Tafel plot. Scan rate: 10 mV/s. (Taken from Ref. 123)

The OER reaction is the counterpart to HER in electrochemical water splitting, so designing an efficient catalyst for OER is also necessary. Jia *et al.* grew a Ni-NiPc-$(NH)_8$ MOF (~ 300 nm) on a fluorine-doped tin oxide (FTO) substrate.[87] The Cyclic Voltammetry (CV) results showed that the OER activity of this MOF increased with the increasing pH value. In 1.0 M KOH, the onset potential was 1.48 V, corresponding to an overpotential of 0.25 V (Fig. 2.20a). Xing *et al.* reported $Co_3(HITP)_2$ as an OER catalyst with a low overpotential of 254 mV at a current density of 10 mA cm^{-2}.[164] In addition, $Co_3(HIB)_2$ nanosheets (~ 4.5 nm) also exhibited high activity for OER and high durability in alkaline electrolytes.[165] These promising results suggest the great potential of 2D c-MOFs for OER catalysts.

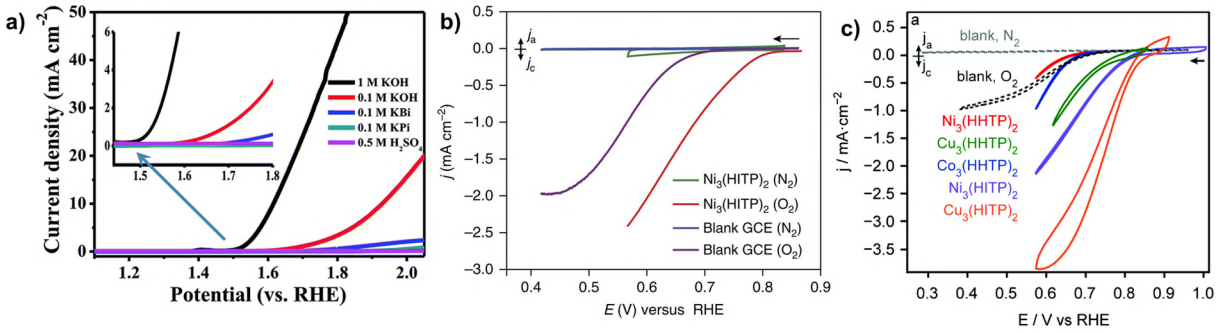


Figure 2.20: (a) The linear sweep voltammetry curves of Ni-NiPc MOF in solutions with different pH values. Scan rate: 10 mV/s. (Taken from Ref. 87) (b) Polarisation curves of $Ni_3(HITP)_2$ and blank glassy carbon electrode (GCE) under N_2 and O_2. Scan rate: 5 mV/s. (Taken from Ref. 166) (c) Cyclic voltammograms of O_2 electroreduction with the MOFs in an electrolyte (pH=13). (Taken from Ref. 167)

Miner *et al.* grew $Ni_3(HITP)_2$ thin films (~ 120 nm) on glassy carbon disk electrodes and tested their ORR activity.[166] The MOF reduced oxygen at an onset potential of 0.82 V in 0.1 M KOH (pH = 13.0), and the overpotential was 0.18 V relative to Pt (Fig. 2.20b). Then, Yoon *et al.* synthesised bimetallic Co_xNi_y-HHTP MOFs, which displayed enhanced ORR activity compared to pure Ni-HHTP and Co-HHTP.[168] Furthermore, Miner *et al.* investigated the ORR activities of various MOFs based on triphenylene ligands.[167] As shown in Fig. 2.20c, $Ni_3(HITP)_2$, $Cu_3(HITP)_2$ and $Cu_3(HHTP)_2$ exhibited excellent activity for ORR. However, $Co_3(HHTP)_2$ and $Ni_3(HHTP)_2$ showed poor performance because of the high overpotential required for oxidising an intermediate. Except for triphenylene, a phthalocyanine-based MOF Co-CuPc-O_8 was also reported to have ORR activity when mixed with carbon nanotubes.[91] These studies indicate that changing the components and structures of 2D c-MOFs can enhance their ORR activity effectively.

2.4.3 Electrochemical capacitors

In electrochemical double-layer capacitors (EDLC), the capacitance arises from the separation of charges at the electrode/electrolyte interface and it is dependent on the surface area.[27] While the reversible redox reactions are the origins of charges for the pseudocapacitors. The first supercapacitor of 2D c-MOFs was reported by Sheberla *et al.* in 2017.[169] As shown in Fig. 2.21a,

the size of the pores in $Ni_3(HITP)_2$ was around 1.5 nm, providing enough space to accommodate large electrolyte ions. The high BET surface area of $Ni_3(HITP)_2$ (630 m^2 g^{-1}) also enabled high double-layer capacitance. The gravimetric capacitance of this MOF was 111 F g^{-1} at a discharge rate of 0.05 A g^{-1}, and the specific surface area normalised capacitance was 18 μF cm^{-2}, which was higher than most carbon materials. Later, Li *et al.* directly grew $Cu_3(HHTP)_2$ nanowire arrays (NWAs) on carbon fibre paper and applied them as sole electrodes for supercapacitors.[121] This Cu-HHTP NWAs electrode exhibited an EDL capacitance of 120 F g^{-1} at a 0.5 A g^{-1} current density, with the normalised capacitance around 22 μF cm^{-2}. The direct growth of crystal nanowires on carbon fibres significantly reduced the intrinsic and charge transfer resistances, allowing effective charge/electron transport at the interface.

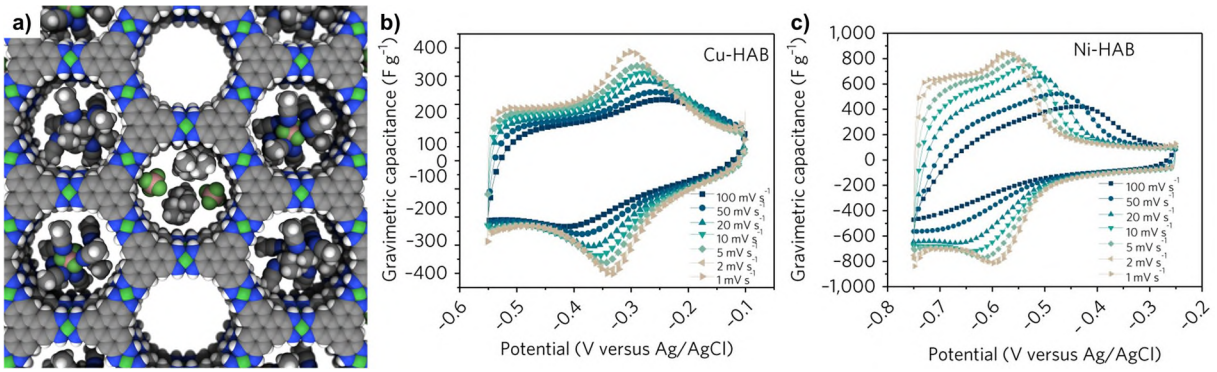


Figure 2.21: (a) Molecular structure of $Ni_3(HITP)_2$, with electrolyte ions inside the pores. (Taken from Ref. 169) (b, c) CV profiles for Cu-HIB (b) and Ni-HIB (c) at different scan rates. (Taken from Ref. 56)

Unlike the two EDLC examples described above, Feng *et al.* designed a redox-active MOF-based pseudocapacitor.[56] They chose HIB to construct the framework as its small size could increase the density of redox-active centres. The synthesised MOFs exhibited excellent chemical stability in aqueous environments, such as KOH, NH_4OH and HCl, allowing the use of low-cost aqueous electrolytes. The electrodes were prepared by mixing HIB-MOF with a binder (5% polytetrafluoroethylene) and conductive additive (5% carbon black). In Fig. 2.21b and c, the CV studies showed clear redox peaks for both Ni and Cu MOFs, and the gravimetric capacitances for Ni-HIB and Cu-HIB were 420 and 215 F g^{-1}, respectively. The authors

hypothesised that the small particle size, porosity, and intrinsic conductivity would be the reason for their high capacitances.

From these applications, it can be seen that 2D c-MOFs have several advantages over traditional electron conducting materials. For example, the large surface area and numerous active metal sites can improve the sensitivity of sensors and the catalytic activity of catalysts. As the MOF layers are usually stacked closely, there is no obvious opening along the *c* axis.[114] However, the pores within the *ab* plane can provide a channel for analyte to penetrate and interact with the active metal sites inside, maximising the efficiency. For different applications, there might be some other requirements, like the gas sensors need to endure humidity, electrocatalysts need to have high stability under acid/alkaline solutions and transistors require high mobilities of holes/electrons. Since MOFs have a high tunability of structures and components, we can modulate their properties to meet the requirements of different fields and to fabricate desired devices.

2.5 Summary

The field of 2D c-MOFs has developed tremendously over the past ten years. This chapter provides an overview of their basic knowledge and relevant studies. The strong π-*d* conjugation between the linkers and the metal centres is the main charge transport pathway in 2D c-MOFs, giving them high electrical conductivities comparable to other functional materials. Depending on the synthesis methods, different morphologies of products can be obtained, including polycrystalline powders, single crystals, multilayer thin films, and single layers. On-surface synthesis can be used to prepare single-layer MOFs with precise control, providing a possibility to investigate their growth processes and structural properties. Integrating 2D c-MOFs onto devices can realise different functionalities, such as sensing, catalysis, and energy storage.

Controlling their components, structures, and morphologies can modulate the properties of 2D c-MOFs, further influencing their performance in applications. Overall, recent developments make 2D c-MOFs more attractive and have the potential to be one of the next generation materials for electronic devices.

Chapter 3

Experimental Techniques and Simulation Methods

All experiments in this thesis were conducted in an ultra-high vacuum (UHV) system equipped with various characterisation techniques. Under UHV, surfaces can be kept clean and not contaminated by dust, water, and hydrocarbons. This chapter describes instruments and synthesis methods used in the experiments, from vacuum to sample preparation. Simulation methods and image processing are also covered.

3.1 Scanning tunnelling microscopy

Scanning tunnelling microscopy (STM) is a surface sensitive characterisation technique, which was invented by Rohrer and Binnig in 1981.[170-171] The operating principle of STM relies on the quantum tunnelling effect. This effect can be simplified to a 1D tunnelling model, as shown in Fig. 3.1. The electron described by a wavefunction $\psi(x)$ with energy E have a probability to penetrate a potential barrier $U(x)$ ($> E$), which satisfies the Schrödinger equation:

$$-\frac{\hbar^2}{2m}\frac{d^2}{dx^2}\psi(x) + U(x)\psi(x) = E\psi(x) \qquad (2.1)$$

where $\hbar$ is the reduced Planck's constant and m is the mass of the electron.

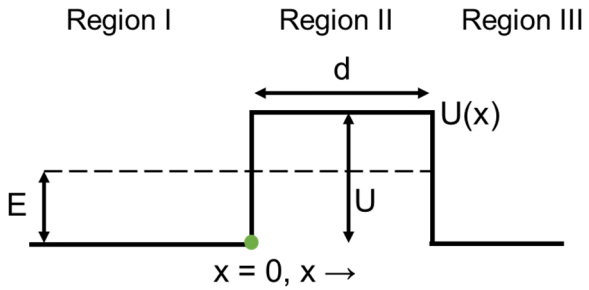


Figure 3.1: A potential barrier (width: d) with electrons incident from the left.

The general solutions of the Schrödinger equation (2.1) are:

$$\psi(x) = \begin{cases} Ae^{ikx} + Be^{-ikx} & \text{Region I} \\ Ce^{\kappa x} + De^{-\kappa x} & \text{Region II} \\ Fe^{ikx} & \text{Region III} \end{cases} \tag{2.2}$$

where

$$k = \frac{\sqrt{2mE}}{\hbar}, \qquad \kappa = \frac{\sqrt{2m(U-E)}}{\hbar} \tag{2.3}$$

The coefficients can be calculated from the boundary continuity conditions. Then, we define a transmission coefficient *T*, which is the ratio of the probability of finding the tunnelling electron on the right side of the barrier:

$$T = \frac{|\psi(d)|^2}{|\psi(0)|^2} = \frac{|F|^2}{|A|^2} = \frac{16E(U-E)}{U^2} e^{-2\kappa d} \propto e^{-2\kappa d} \tag{2.4}$$

A simple model of STM is a metal-vacuum-metal tunnelling junction between a sample and a tip, as shown in Fig. 3.2. When a bias voltage (*V*) is applied on the sample, a tunnelling current is generated. The work functions of the sample and the tip are represented by ϕ_S and ϕ_T, respectively. Then the height of the barrier *U* is approximately $(\phi_S + \phi_T)/2$. If we assume that the sample and the tip have identical work function ϕ, and the bias voltage is much smaller than the work function ($E = eV << \phi$), the decay constant can be derived as:

$$\kappa = \frac{\sqrt{2m\phi}}{\hbar} \tag{2.5}$$

The transmission coefficient can also be defined as the ratio of the tunnelling current at the tip ($x = d$) to the incoming current at the surface ($x = 0$):

$$T = \frac{I(d)}{I(0)} \propto e^{-2\kappa d} \tag{2.6}$$

The exponential dependence of the tunnelling current to the tip-sample distance gives STM an extremely high sensitivity to topographic changes. For example: if $\phi = 4.5$ eV, then $\kappa = 1.087$

$\times 10^{10}$ m^{-1}, 1 Å change of the distance d leads to a change of around 9 times ($e^{-2\kappa z} = e^{-2.174} \approx 0.11$) for the current.

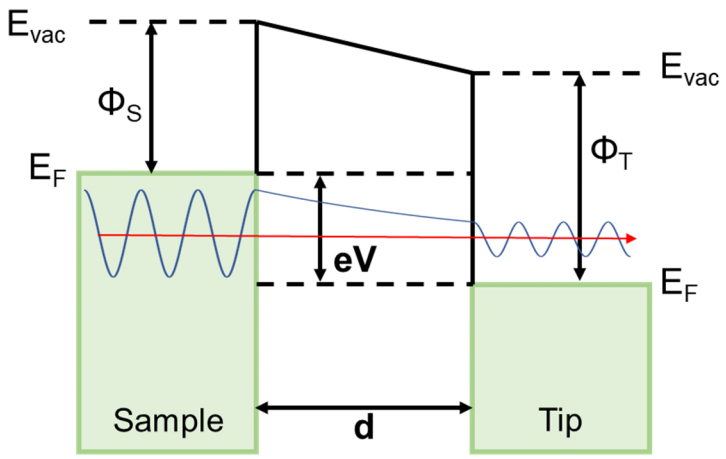


Figure 3.2: An elementary 1D model of metal-vacuum-metal tunnelling junction. By applying a negative bias on the sample, electrons can pass through the vacuum to the tip, generating a tunnelling current proportional to the bias voltage V.

The current is not only dependent on the tip-sample distance d but also the number of electronic states within the energy interval eV (V: sample bias), which can be expressed by:

$$I \propto \sum_{E_F - eV}^{E_F} |\psi(d)|^2 \tag{2.7}$$

where E_F is the fermi level of the sample. The result can also be described by the local density of states (LDOS) of the sample, ρ_S, at the Fermi level and the tip position (d):

$$I \propto V\rho_S(d, E_F) = V\rho_S(0, E_F)e^{-2\kappa d} \tag{2.8}$$

where

$$\rho_S(x, E_F) \propto \frac{1}{eV} \sum_{E_F - eV}^{E_F} |\psi(x)|^2 \tag{2.9}$$

Therefore, the tunnelling current is dependent on the tip-sample distance d and the local density of states of the sample, indicating that STM images combine the features of surface morphologies and electronic structures.

In 1983, J. Tersoff and D. R. Hamann developed a theory for tunnelling between a surface and a locally spherical tip, which is applicable to STM.[172-173] They assumed the wave function of the outmost tip atom is a simple *s*-wave function. The tunnelling current is written as:

$$I = \frac{4\pi e}{\hbar}\int_{-\infty}^{+\infty}\left[f\left(E_F^S - eV + \varepsilon\right) - f(E_F^T + \varepsilon)\right]\rho_S\left(E_F^S - eV + \varepsilon\right)\rho_T(E_F^T + \varepsilon)\left|M_{\mu\nu}\right|^2 d\varepsilon \quad (2.10)$$

where f is the Fermi-Dirac distribution function, E_F^T and E_F^S are the fermi level of the tip and the sample, respectively, V is the applied voltage, M is the tunnelling matrix element, ρ_S and ρ_T are the density of states (DOS) for the sample and tip, respectively. The DOS of the tip is assumed to be constant within the energy interval of interest. At low temperatures, the Fermi-Dirac distribution function can be replaced by a step function and the tunnelling matrix can be treated as a constant. According to these assumptions, the tunnelling current can be rewritten as:

$$I \propto \int_0^{eV}\rho_S(E_F^S - eV + \varepsilon)d\varepsilon \quad (2.11)$$

Then, the tunnelling current is proportional to the integral of the sample local density of states from the Fermi level to the bias voltage V. This method is widely used in the interpretation and simulation of STM images (also in this thesis).

The differential conductance can be derived as:

$$\frac{dI}{dV} \propto \rho_S(E_F^S - eV) \quad (2.12)$$

Therefore, the information of the sample LDOS can be revealed through measuring the differential conductance. This technique is an extended function of STM, known as scanning tunnelling spectroscopy (STS).

The general set-up of STM consists of these components: 1) a metallic tip, made of tungsten (W) or platinum-iridium (Pt-Ir); 2) a conducting substrate; 3) a feedback control system. For

scanning, the tip approaches the substrate first, driven by a coarse motor. When the tip-sample distance is close enough (usually within a nanometre), a tunnelling current is detected. The piezoelectric element in the scanner can be compressed or extended with applied voltages, which controls the movement of the tip on the surface. There are two scanning modes in STM: constant current and constant height. In the constant current mode, the tunnelling current is kept constant, and the height movement of the tip is recorded to generate the image. In the constant height mode, the tip height is fixed, and the change of the tunnelling current is recorded. This mode can run at a rapid speed but is more dangerous for tip crash. In this thesis, all the STM images were acquired using the constant current mode at room temperature (~298 K).

3.2 Ultra-high vacuum (UHV) system

The main instrument is a three-chamber UHV system, consisting of an STM chamber (JEOL JSTM 4500s), a Scanning Electron Microscopy (SEM) chamber (JEOL TM Z9043T) and a treatment chamber, as shown in Fig. 3.3. The STM and the treatment chambers operate at a base pressure of 10^{-8} Pa, while the SEM chamber is at 10^{-7} Pa. The vacuum is achieved and maintained by a rotary pump, a turbo-molecular pump (TMP) and ion pumps. Titanium sublimation pumps (TSP) are also equipped as auxiliary pumps to help the obtaining of UHV. The treatment chamber is used for sample storage and preparation, such as degassing, sputtering and annealing. The STM chamber is used for reactants deposition and STM imaging. Samples and tips are transferred into the UHV system through the exchange chamber (load lock), which can be opened to air.

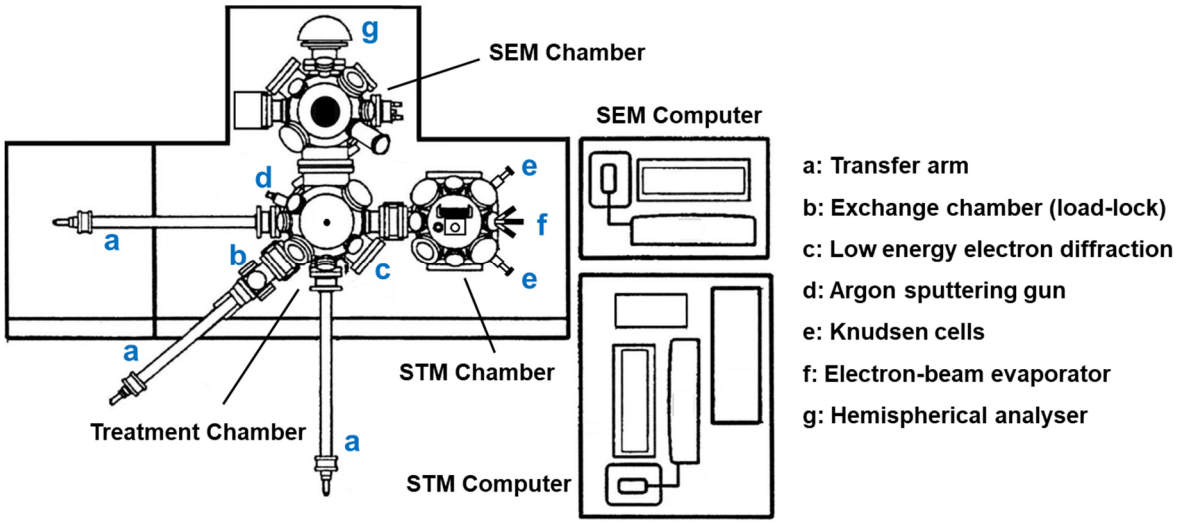


Figure 3.3: Schematic diagram of the UHV system. Adapted from Marshall, 2009.[174]

3.3 Sample Preparation

3.3.1 Materials selection

To study the self-assemblies of organic molecules and their reactions with metals, an inert surface is needed. Thus, the substrate does not significantly affect the interactions between adsorbates, and side-reactions can be prevented. Au(111) was chosen as the main substrate in this thesis because of its inertness and flatness. Additionally, a Cu(111) substrate was also used for the reactions between molecules and Cu atoms due to the Au-Cu alloying problem. For metals, they should have a planar coordination geometry and limited solubility in the Au substrate to avoid alloying. To meet these requirements, Ni and Co were chosen as the metal sources. Considering the variety of ligands, hexa-substituted triphenylene and benzene were selected since other ligands are mainly based on these two molecules.

3.3.2 Tip etching

The tip used for STM imaging was prepared by electrochemical etching of a tungsten (W) wire (diameter: 0.3 mm, 99.95%, Goodfellow) in a solution of 2.5 mol/L NaOH. The electrochemical reaction between the tungsten tip and NaOH is:

$$W + 2OH^- + 2H_2O \xrightarrow{electrolysis} WO_4^{2-} + 3H_2$$

An SEM image of an etched tip is shown in Fig. 3.4, where we can clearly see the apex of the tip is less than 100 nm.

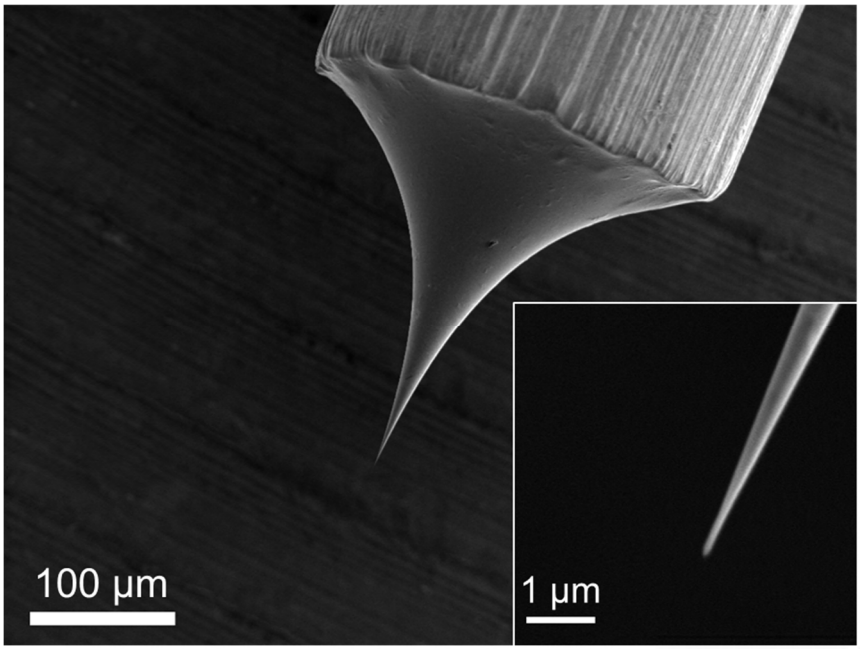


Figure 3.4: SEM images of an etched W tip. EHT = 10kV, I probe = 100 pA.

3.3.3 Substrates

The substrates used in the experiments were Au(111) thin films (300 nm) on mica, supplied by Unisoku. For heating, a strontium titanate (0.5% Nb doped $SrTiO_3$, PI-KEM) single crystal (size: 7 × 2 mm^2) was put beneath the Au substrate and used as a heater to heat the Au substrate indirectly. The substrates were mounted on a sample holder by two blades (Fig. 3.5a.) One end of the Au-mica was scratched to prevent the heating current passing through the gold films. An SEM image of the Au thin films is shown in Fig. 3.5b, where the size of grains is around several micrometres. In addition to Au(111), a Cu(111) single-crystal substrate (MTI, polished < 30 Å) was also used in the experiments.

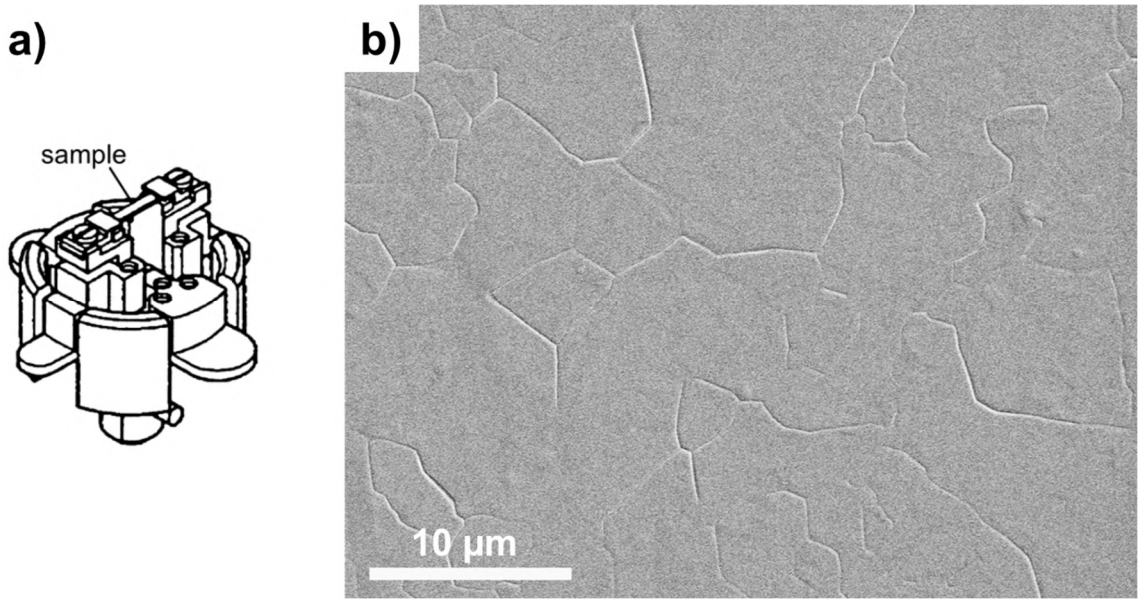


Figure 3.5: (a) JEOL-built sample holder. Adapted from JEOL Ltd., 2000.[175] (b) An SEM image of the Au(111) thin films on mica. EHT = 10kV, I probe = 100 pA.

3.3.4 Sputtering etching

After degassing, the substrate was subsequently sputtered and annealed to get a clean and flat surface. A VG Microtech EX03 ion gun was used for sputtering. Firstly, electrons generated by a filament are accelerated and collide with argon (Ar) atoms to get them ionised. Then, the Ar^+ ions are accelerated with an energy of 500 eV and bombard onto the sample surface to remove the residual materials. For the Au sample, it was sputtered for 10 to 15 minutes under an Ar pressure of 4.5×10^{-4} Pa. After sputtering, the sample was annealed at ~650 °C for 1.5h to mobilise gold atoms and make them nucleate into large terraces. Under this condition, Au(111) surface would form a $\left(22 \times \sqrt{3}\right)$ surface reconstruction, as shown in Fig. 3.6.

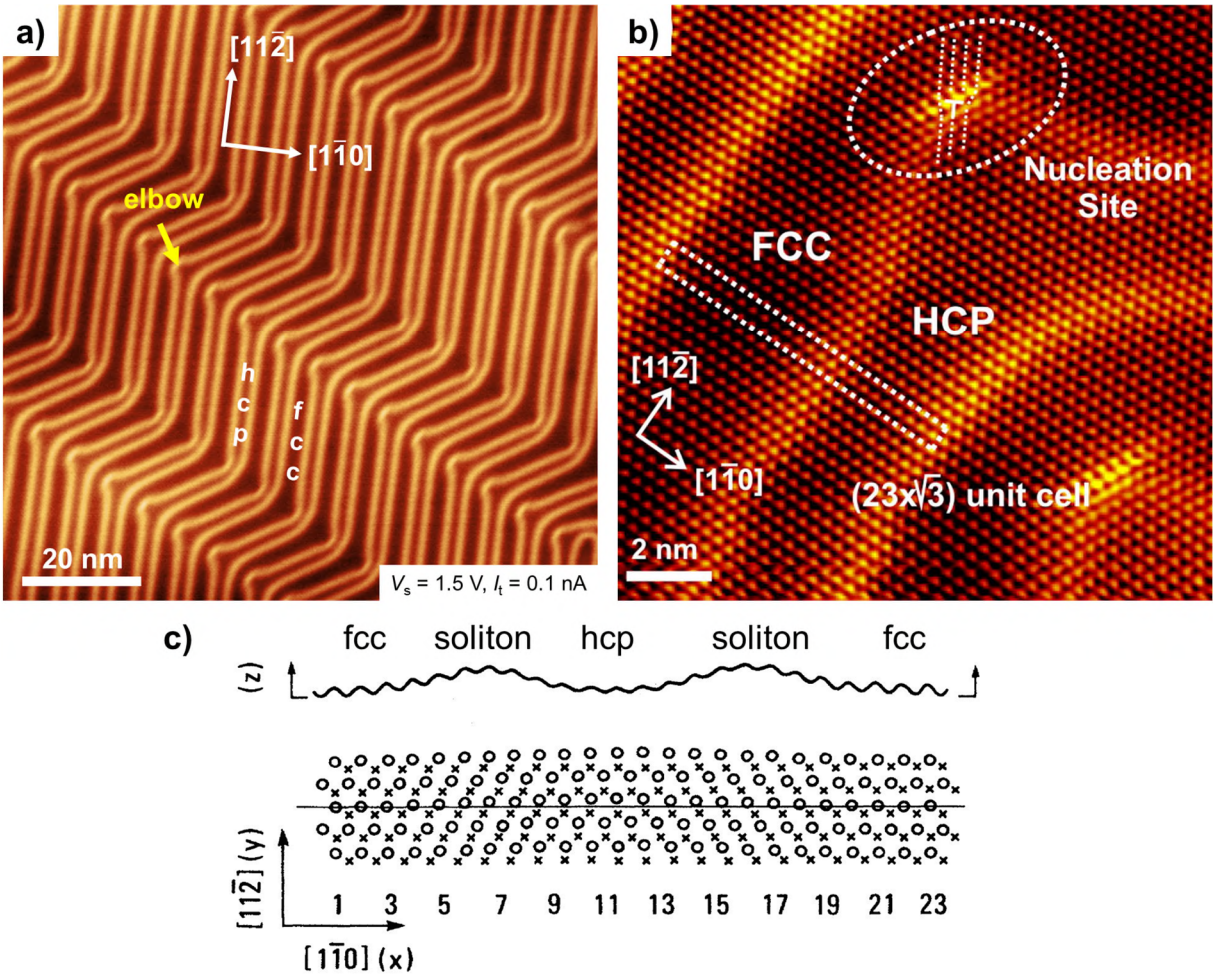


Figure 3.6: (a) STM image of $\left(22 \times \sqrt{3}\right)$ reconstructed Au(111) surface. (b) Atom-resolved STM image of the Au(111) surface. V_s = −39.1 mV, I_t = 1.55 nA. (Taken from Ref. [176]) (c) Atomic model for the reconstruction of the Au(111) surface. Bottom: the open circles denote the positions of atoms in the reconstructed top layer, whereas the crosses denote those in the second layer. Top: the displacement of the atoms from the line drawn in the [1$\bar{1}$0] direction. (Taken from Ref. [177])

In this reconstruction, 23 Au atoms of the surface layer are compressed (~4.5 %) to sit on 22 bulk lattice sites along the [1$\bar{1}$0] direction.[178] While the atoms along the [11$\bar{2}$] direction, which is perpendicular to the [1$\bar{1}$0] direction, are uncompressed. A structure model of the reconstructed surface is shown in Fig. 3.6c, where the surface atoms can be divided into three groups: fcc (face centred cubic, ABCABC… stacking), hcp (hexagonal close packed, CBCABC… stacking) and solitons.[177, 179-180] The fcc and hcp regions are separated by solitons, which appear as pairwise corrugation lines with a height of around 0.15 Å.[177-178] These solitons also bend by 120° to form a zigzag pattern, which is referred to as herringbones. At the bending

sites, the rounded elbow is free of dislocation, while the pointed one is associated with a surface dislocation, which is the preferential nucleation site of a number of metals (Fig. 3.6b).[176, 181-182]

3.3.5 E-beam evaporator

Ni and Co (99.99%, Goodfellow) were deposited onto the substrate by an e-beam evaporator (Oxford Applied Research EGCO4). Electrons emitted from a heated filament are accelerated to the metal rod, which is applied with a high voltage. Then the metal rod is heated up by the electrons bombardment and generates metal atoms vapour. After opening the shutter, these metal atoms will impinge upon the substrate. The deposition amount can be controlled by the filament current and deposition time. Usually, the flux used for deposition is around 0.02 ML/s (ML: monolayer) with a pressure of 1.5×10^{-7} Pa. Fig. 3.7 shows the deposition of Ni and Co onto the Au(111) substrate. Both metals prefer to nucleate at the elbow sites of herringbones, forming small islands.[176, 183]

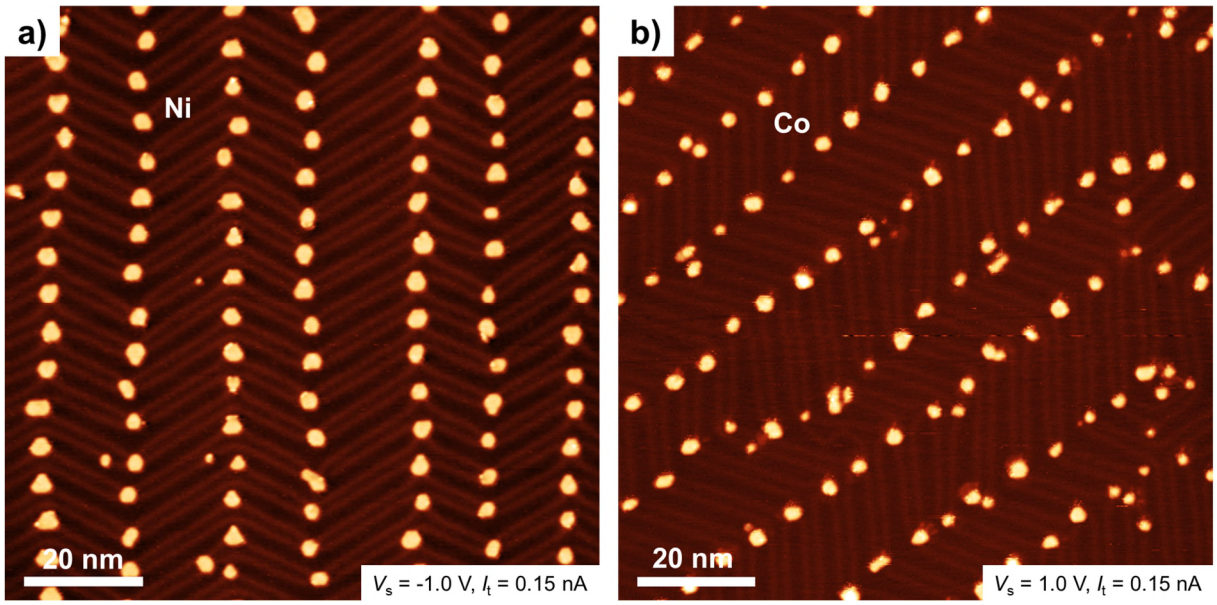


Figure 3.7: STM images of Ni (a) and Co (b) deposited onto the Au(111) substrate.

The estimation of metal coverages is shown below using the examples in Fig. 3.7. First, we need to measure the height of the metal islands to know their stacking. In Fig. 3.8a, six profiles of Ni islands are drawn on the right-hand side. All the islands have similar height, showing an

averaged value of 0.19 nm. Ni has a fcc structure with a lattice parameter of 0.352 nm and the interplanar spacing of Ni(111) is 0.20 nm.[184] Comparing the measurement and the reference, these islands are determined as monolayers. Therefore, the coverage of the Ni is equal to the area of the islands. Using the area measurement tool (by selecting a threshold) in *Image J*, the coverage of Ni was obtained as ~0.10 ML. Similarly, the profiles of Co islands are shown in Fig. 3.8b. Almost all the islands have the height of around 0.39 nm (average). However, there are two exceptions which are a little higher (0.55 nm), as marked by the red arrows. Co has a hcp structure with lattice parameters of a = 0.25 nm, c = 0.41 nm, so the spacing between Co(0001) layers is 0.20 nm.[185] Based on this information, the Co islands are actually two-layers crystals (or even three layers for those higher crystals). Consequently, the coverage of the Co is around 0.15 ML, slightly larger than the twice of the islands area (7%).

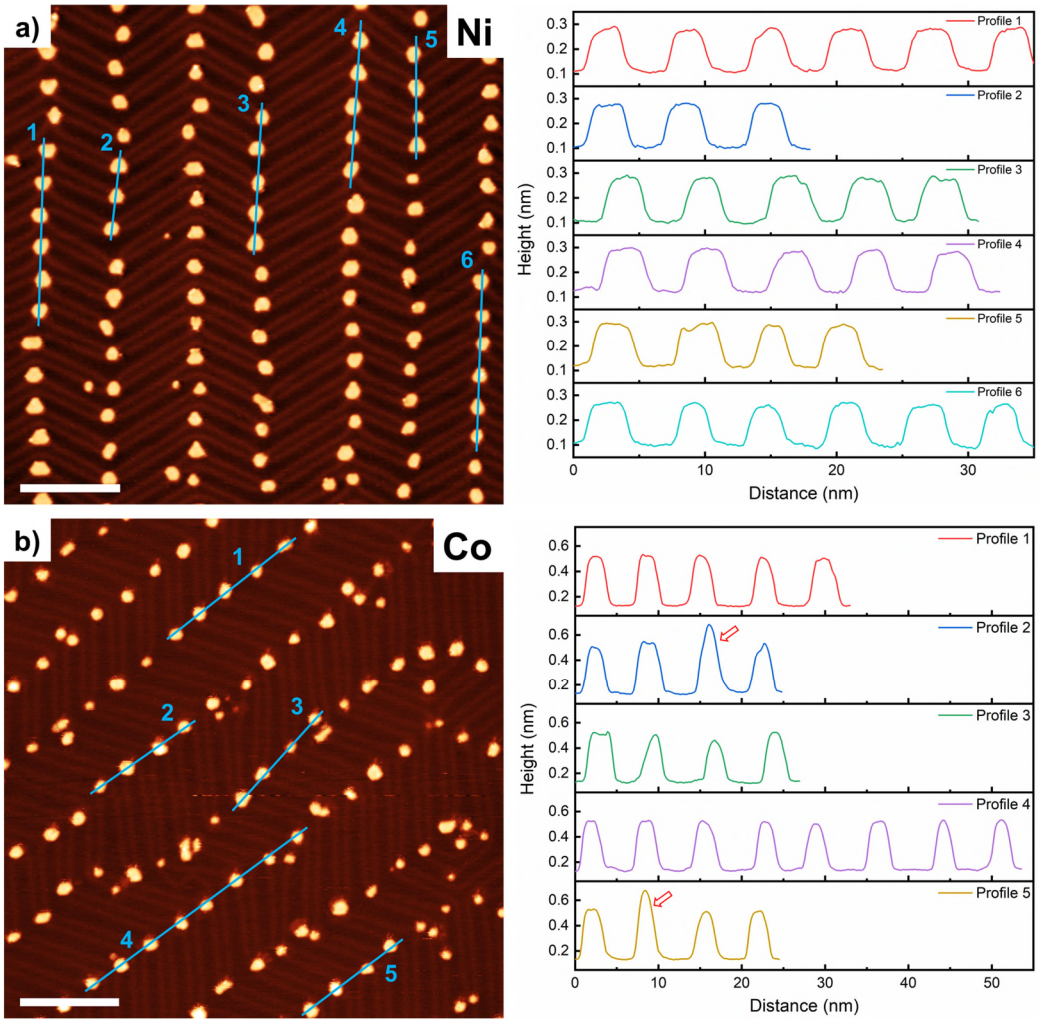
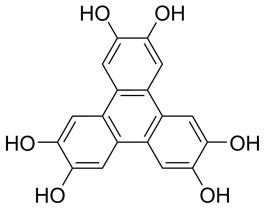
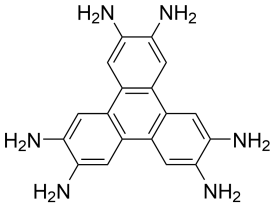
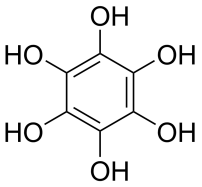


Figure 3.8: Profiles of metal islands on Au(111). (a) Ni. (b) Co. Scale bar: 20 nm.

3.3.6 Knudsen cell (K-cell)

Organic ligands were evaporated onto the substrate using a Knudsen cell (K-cell, CreaTec Single Filament effusion cell). Molecules are placed in a ceramic crucible, which can be heated by a filament coil. A thermocouple is used to monitor the temperature and control the power of heating. After reaching the deposition condition (temperature & pressure), the shutter can be opened to start the deposition. All ligands were degassed and purified in UHV for several cycles prior to depositions. Three ligands were used in this thesis, and their evaporation temperatures are listed in Table 3.1.

Table 3.1: Evaporation temperatures of organic ligands

Ligand	Chemical structure	Evaporation temperature
2,3,6,7,10,11-Hexahydroxytriphenylene (HHTP)		250 °C
2,3,6,7,10,11-Hexaaminotriphenylene (HATP)		245 °C
Hexahydroxybenzene (HHB)		135 °C

The coverages of the molecules are also estimated by measuring their areas. Here, I use HHTP as an example to show how the coverage is estimated. As shown in Fig. 3.9, a) and b) are two different regions of the same sample, showing a coverage of around 0.40 ML. Fig. 3.9c is another sample with a coverage of 0.45 ML. Through measuring different samples with different deposition amounts, the flux of HHTP is estimated to ~0.15 ML/min with a pressure of 6×10^{-7} Pa. For HHB, the flux is around 0.50 ML/min with a pressure of 3×10^{-7} Pa (due to

its low evaporation temperature). However, one problem is that HATP molecules are mobile on the surface and no area can be measured. Therefore, the coverage can only be estimated by the deposition parameters (pressure and time), like using the results of HHTP since they are very similar in structures and evaporation temperatures. More precise amounts can be calculated using the area of the products after the molecules reacting with metal atoms.

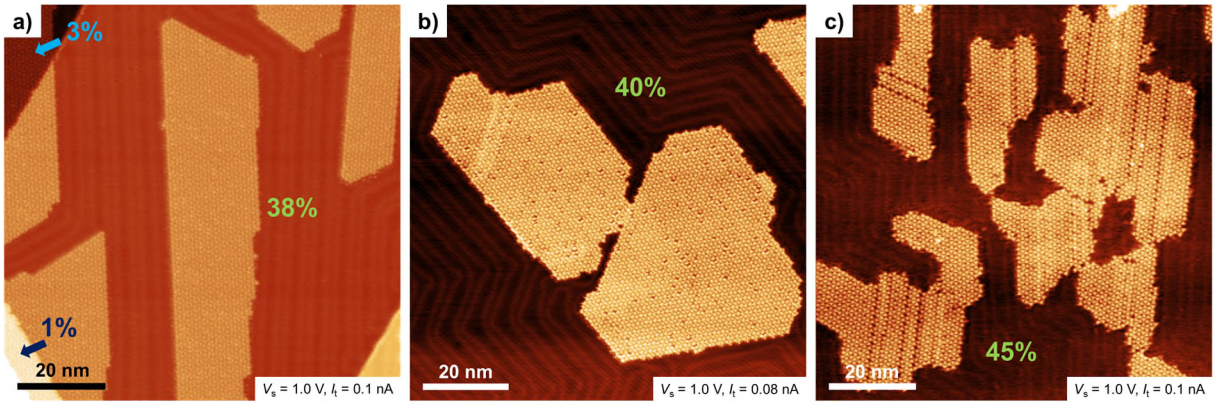


Figure 3.9: Different coverages of HHTP molecules on Au(111).

3.4 Simulation method

Density functional theory (DFT) is a quantum mechanical modelling method to investigate the electronic structures of many-body systems. It is the most popular calculation method in computational physics, chemistry, and material science.

3.4.1 Density functional theory

For a material with N electrons (positions labelled as r_N) and M nuclei (positions labelled as R_M). The many-particle wavefunction is:

$$\Psi = \Psi(r_1, r_2, \dots, r_N; R_1, R_2, \dots, R_M) \tag{2.13}$$

Then the time-independent many-body Schrödinger equation is:

$$\hat{H}\Psi = E_{total}\Psi \tag{2.14}$$

where E_{total} is the total energy of the system and $\hat{H}$ is the Hamiltonian operator which is the sum of the kinetic and potential energy operators. The kinetic energy part of the Hamiltonian is:

$$\text{Kinetic energy} = \sum_{i=1}^{N} -\frac{\hbar^2}{2m_e}\nabla_i^2 + \sum_{I=1}^{M} -\frac{\hbar^2}{2M_I}\nabla_I^2 \quad (2.15)$$

where m_e is the mass of the electron and M_I is the mass of the nucleus I. For the potential energy, the particles interact with each other through the electrostatic Coulomb force, and these interactions can be described by:

i) electrons-nuclei:

$$\text{Potential energy}_{\text{el-nuc}} = -\sum_{i,I} \frac{1}{4\pi\epsilon_0}\frac{Z_I e^2}{|r_i - R_I|} \quad (2.16)$$

where Z_I is the atomic number of the nucleus I and ϵ_0 is the electric constant.

ii) electron-electron:

$$\text{Potential energy}_{\text{el-el}} = \frac{1}{2}\sum_{i}\sum_{j\neq i} \frac{1}{4\pi\epsilon_0}\frac{e^2}{|r_i - r_j|} \quad (2.17)$$

iii) nuclei-nuclei:

$$\text{Potential energy}_{\text{nuc-nuc}} = \frac{1}{2}\sum_{I}\sum_{J\neq I} \frac{1}{4\pi\epsilon_0}\frac{Z_I Z_J e^2}{|R_I - R_J|} \quad (2.18)$$

Then, the Schrödinger equation for all the electrons and nuclei is:

$$\left[\sum_{i=1}^{N} -\frac{\hbar^2}{2m_e}\nabla_i^2 + \sum_{I=1}^{M} -\frac{\hbar^2}{2M_I}\nabla_I^2 - \sum_{i,I}\frac{1}{4\pi\epsilon_0}\frac{Z_I e^2}{|r_i - R_I|} + \frac{1}{2}\sum_{i}\sum_{j\neq i}\frac{1}{4\pi\epsilon_0}\frac{e^2}{|r_i - r_j|} + \frac{1}{2}\sum_{I}\sum_{J\neq I}\frac{1}{4\pi\epsilon_0}\frac{Z_I Z_J e^2}{|R_I - R_J|}\right]\Psi = E_{total}\,\Psi \quad (2.19)$$

Substituting the units by atomic units (Bohr radius, Hartree energy), the equation (2.19) can be simplified as:

$$\left[-\sum_{i=1}^{N}\frac{\nabla_i^2}{2} - \sum_{I=1}^{M}\frac{\nabla_I^2}{2M_I} - \sum_{i,I}\frac{Z_I}{|r_i - R_I|} + \frac{1}{2}\sum_{i\neq j}\frac{1}{|r_i - r_j|} + \frac{1}{2}\sum_{I\neq J}\frac{Z_I Z_J}{|R_I - R_J|}\right]\Psi = E_{total}\,\Psi \quad (2.20)$$

However, solving this Schrödinger equation is extremely difficult and we need to use some approximations. Because the nuclei are much heavier than the electrons, they can be regarded as stationary with infinite mass. This sets the kinetic energy of the nuclei to zero and makes nuclei-nuclei interactions constant (can be incorporated into the energy *E*).

$$\text{Set } V_n(r) = -\sum_I \frac{Z_I}{|r - R_I|} \tag{2.21}$$

The new equation is:

$$\left[-\sum_{i=1}^{N} \frac{\nabla_i{}^2}{2} + \sum_{i}^{N} V_n(r_i) + \frac{1}{2}\sum_{i \neq j} \frac{1}{|r_i - r_j|}\right] \Psi(r_1, r_2, \ldots, r_N) = E\, \Psi(r_1, r_2, \ldots, r_N) \tag{2.22}$$

If we think the electrons are independent and ignore the electron-electron interactions, the many-electron wavefunction is just a product of single-electron wavefunctions (ϕ_i).

$$\Psi(r_1, r_2, \ldots, r_N) = \phi_1(r_1)\phi_2(r_2) \ldots \phi_N(r_N) \tag{2.23}$$

$$\left[-\frac{\nabla^2}{2} + V_n(r)\right] \phi_i(\mathrm{r}) = \epsilon_i \phi_i(\mathrm{r}) \tag{2.24}$$

The probability to find an electron at point *r* is equal to the mod square of its wavefunction. With the exchange principle, the electron density *n*(*r*) can be given by:

$$n(r) = N \int |\Psi(r_1, r_2, \ldots, r_N)|^2 dr_1 dr_2 \ldots dr_N = \sum_i |\phi_i(r)|^2 \tag{2.25}$$

To partially account for the electron-electron interaction (still based on independent electrons), an averaged interaction is used to replace the individual interactions between electrons, known as the mean-field approximation. This constructs a potential called the Hartree potential $V_H(r)$:

$$V_H(r) = \int dr' \frac{n(r')}{|r - r'|} \tag{2.26}$$

Then, the single-particle equation is:

$$\left[-\frac{\nabla^2}{2} + V_n(r) + V_H(r)\right] \phi_i(\mathrm{r}) = \epsilon_i \phi_i(\mathrm{r}) \tag{2.27}$$

Based on the Hohenberg-Kohn theorem, the ground state energy *E* is a functional of the electron density only (a functional maps a function to a number).[186]

$$E = E[n] \tag{2.28}$$

Then, Kohn and Sham noted that the kinetic energy is uniquely determined by the density *n* if the electrons do not interact with each other, and the Hartree potential is also a functional of the density.[187] All the other energy which has not been considered is defined as the 'exchange-correlation' energy, $E_{xc}[n]$. The total energy can be given by:

$$E[n] = \int drn(r)V_n(r) - \sum_i \int dr\phi_i^*(r)\frac{\nabla^2}{2}\phi_i(r) + \frac{1}{2}\int \frac{n(r)n(r')drdr'}{|r-r'|} + E_{xc}[n] \tag{2.29}$$

According to the variational principle, the ground-state density, n_0, minimises the total energy:

$$\left.\frac{\delta E[n]}{\delta n}\right|_{n_0} = 0 \tag{2.30}$$

Further requiring the wavefunctions to be orthonormal, the Kohn-Sham equations are obtained:

$$\left[-\frac{\nabla^2}{2} + V_n(r) + V_H(r) + V_{xc}(r)\right]\phi_i(r) = \epsilon_i\phi_i(\mathrm{r}) \tag{2.31}$$

where

$$V_n(r) = -\sum_I \frac{Z_I}{|r-R_I|} \tag{2.32}$$

$$\nabla^2 V_H(r) = -4\pi n(r) \tag{2.33}$$

$$V_{xc}(r) = \frac{\delta E_{xc}}{\delta n(r)} \tag{2.34}$$

$$n(r) = \sum_i |\phi_i(r)|^2 \tag{2.35}$$

For the exchange-correlation energy, $E_{xc}[n]$, many approximations have been developed to calculate it. The two most popular methods are local-density approximation (LDA) and generalized-gradient approximation (GGA).[187-188]

To solve the Kohn-Sham equations, we need to use self-consistent calculations. Through giving the coordinates of the atoms, the nuclear potential can be calculated first. Then, we guess an initial electron density *n*, use it to calculate the Hartree potential and exchange-correlation potential, get the total energy, solve the equations to get ϕ_i, obtain a new density *n'* and see whether *n* = *n'*. If not, a new guess for the density is generated and another loop is performed until reaching a self-consistent solution.

3.4.2 Calculation parameters

In this thesis, DFT calculations were carried out with the QUANTUM-ESPRESSO package.[189-190] The electron-ion interaction was described by ultrasoft pseudopotentials and the electron wavefunctions and density were expanded in a plane-wave basis up to a maximum kinetic energy of 40 and 480 Ry, respectively.[191-192] Exchange and correlation were modelled using the Perdew-Burke-Ernzerhof (PBE) functional, with an empirical correction (Grimme-D3) included to account for weak van der Waals interactions.[188, 193] The Au substrate was modelled as three atomic layers using the experimental lattice constant of 4.08 Å separated by a vacuum region of 15 Å. Subsequent fixed-cell structure optimisations were performed until the forces on each atom were smaller than 0.02 eV/Å with the bottom (the 3rd) layer Au atoms fixed. The Brillouin zone was sampled using a n × n × 1 Monkhorst–Pack k-point grid for self-consistent calculations and a finer 2n × 2n × 1 grid was used for density of states (DOS) and projected density of states (PDOS) calculations.[194] STM images were simulated within the Tersoff-Hamann approximation, integrating the local DOS from the Fermi level to the set bias.[173] Structure models were drawn using XCrySDen (X-Window Crystalline Structures and Densities).[195]

The results of convergence tests are described below to provide some details for parameter selecting. Firstly, an isolated HHTP molecule and a Au(111) (4 × 4) supercell were calculated to find a suitable energy cutoff for wavefunctions. As shown in Fig. 3.10a and b, when the energy cutoff is higher than 35 Ry, the energy of the molecule/substrate is almost the same. To balance the calculation accuracy and time, 40 Ry was chosen as the energy cutoff value. Similarly, the tests of k-point grids are shown in Fig. 3.10c (Au substrate) and d (free-standing $Ni_3(HITP)_2$ MOF layer). When the grid is larger than 2 × 2 × 1, the energy is almost converged. Usually, a 4 × 4 × 1 grid was used for self-consistent calculations in this thesis, while sometimes a 3 × 3 × 1 grid was also used for large systems.

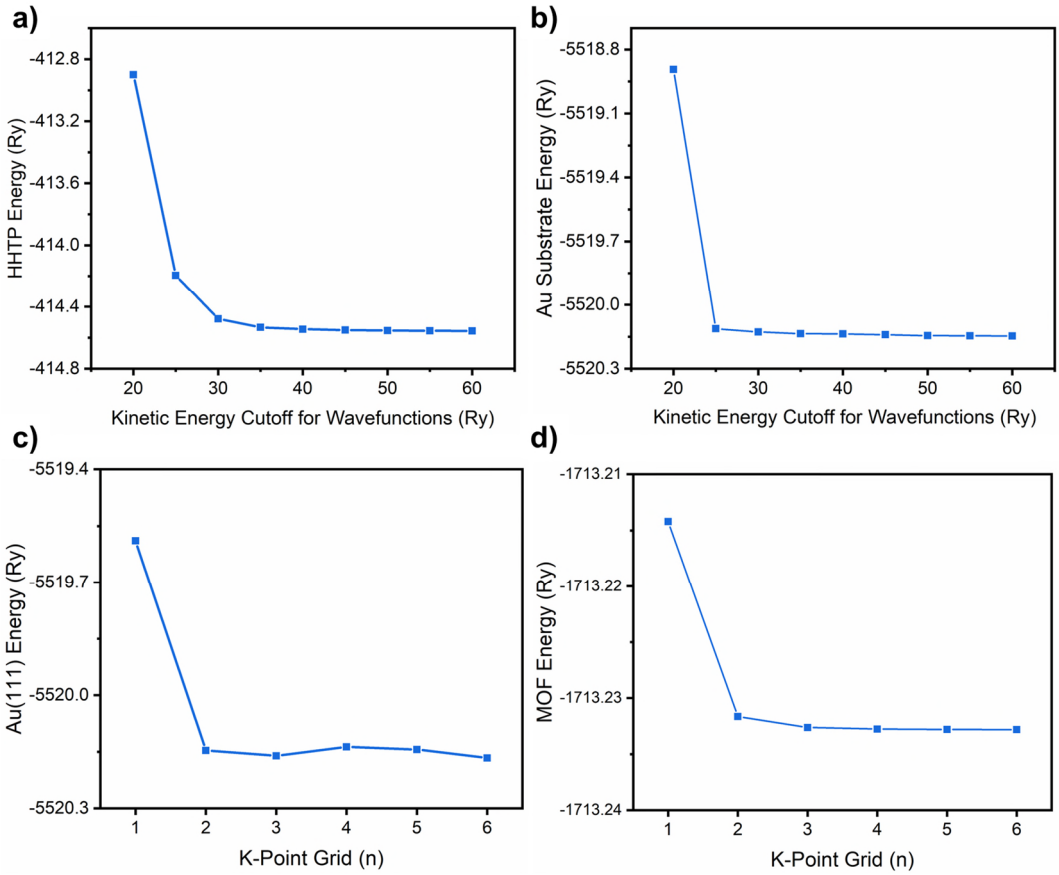


Figure 3.10: Convergence tests of some calculation parameters. (a) An isolated HHTP molecule. k-point: gamma, (b) A bare Au(111) (4 × 4) supercell (three layers). k-point: 4 × 4 × 1 grid. (c) A bare Au(111) (4 × 4) supercell (three layers). Energy cutoff: 40 Ry. (d) A free-standing $Ni_3(HITP)_2$ MOF layer. Energy cutoff: 40 Ry.

For structure optimisation, all the isolated molecules, Au(111) slabs and free-standing MOF layers were simply calculated by the 'relaxation' calculation of QUANTUM-ESPRESSO. When constructing the adsorbed system, a test was carried out first to investigate the influence of the adsorption distance. As illustrated in Fig. 3.11a, a $Ni_3(HITP)_2$ MOF layer (optimised free-standing structure) is manually put on a Au(111) slab (a fixed single-layer substrate). Through changing the height of the MOF layer, the energy with different adsorption distances can be calculated. The plot in Fig. 3.11b shows that the minimum of the system energy is located at 3.2 - 3.3 Å. Based on this result, 3.3 Å was used as the starting height (position) of the MOF layer. Then, a further 'relaxation' calculation was performed on this model and the final optimised structure is shown in Fig. 3.11c. This method was also applied in other adsorption models in this thesis, including the adsorption of isolated molecules on substrates.

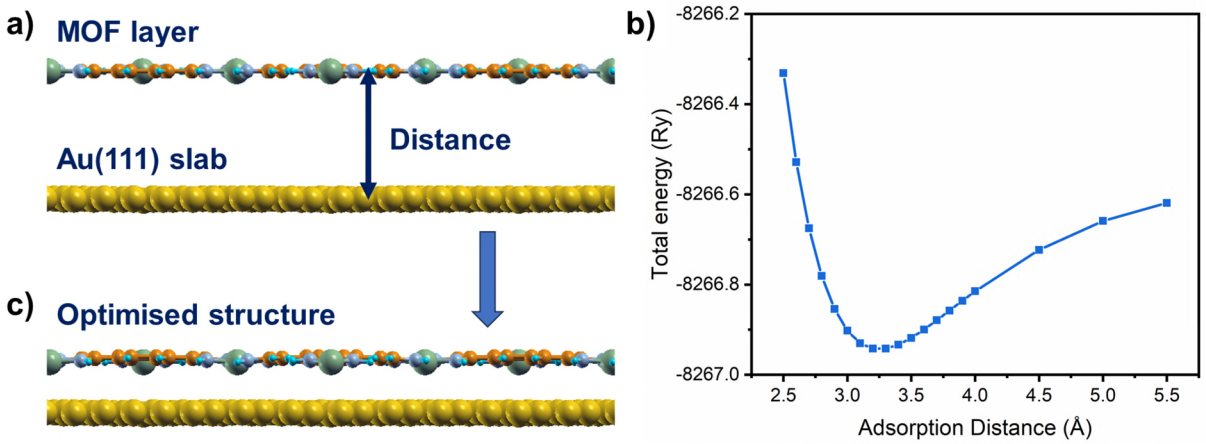


Figure 3.11: (a) Structure model of the adsorption. The $Ni_3(HITP)_2$ MOF layer is manually put on a Au(111) slab with a fixed distance. (b) The energy change of the system in (a) with the increase of the adsorption distance. (c) The final optimised structure of $Ni_3(HITP)_2$ MOF layer on Au(111).

With the optimised adsorption structure, some other properties can be calculated, like adsorption energy and charge transfer. The adsorption energy is equal to the energy difference between the adsorbed system and the sum of the isolated systems:

$$\text{Adsorption energy} = E_{adsorbed\ system} - (E_{adsorbate} + E_{substrate})$$

That usually gives a negative value because the energy of the system decreases after adsorption.

The charge analysis is based on the comparison of the charge density before and after adsorption. There are many ways to partition the total electron density into contributions from each atom. One popular method is Bader Charge Analysis, where the electron density is divided at zero flux surfaces.[196] For example, the Bader charges of free-standing $Ni_3(HITP)_2$, bare Au substrate and $Ni_3(HITP)_2$ adsorbed on the Au(111) substrate are listed in Table 3.2. Comparing the charges, we can see that 0.82 *e* has been transferred from the $Ni_3(HITP)_2$ layer to the Au(111) substrate.

Table 3.2 Bader charges of free-standing $Ni_3(HITP)_2$, Au substrate and $Ni_3(HITP)_2$ adsorbed on Au(111)

	Adsorbed system		Free-standing system	
	$Ni_3(HITP)_2$	Au(111)	$Ni_3(HITP)_2$	Au(111)
Bader charge (*e*)	281.18	1881.81	282.00	1880.99

3.5 STM image processing

Most images in this thesis were processed in two steps: multiple-frame averaging and parameters adjustment. Through continuous scanning, we can get a series of images under the same imaging conditions (size, bias voltage, tunnelling current and scanning speed). An image with significant improvements in signal-to-noise ratio and resolution can be obtained by using the *SmartAlign* package to average the serial images.[197-198] Then, the averaged image was further processed by *Gwyddion* and *Image J*, including levelling, rows alignment, scars correction, colour range selection and brightness/contrast adjustment. All these operations did not change the information of the image itself or introduce artefacts. Smoothing, sharpening and filters were not applied to the images.

An example of processing is illustrated in Fig. 3.12, where a) is a single-frame STM image. Repeating scanning for 38 times within this area under the same conditions, we got a sequence of images (38 frames). Then *SmartAlign* was used to average these images, and the averaged

one is shown in Fig. 3.12b. It is obvious that the averaged image has less noise and a higher quality than the first raw image. One thing needs to be mentioned is that the field-of-views of multiple frames are not the same because of drift. The package will correct some drift and crop a common area among all the images. This makes the size of the averaged area smaller than the raw images. After averaging, the image was processed by *Gwyddion* to adjust its parameters (Fig. 3.12c). The profiles of the Au(111) surface are also shown in the bottom of Fig. 3.12, where we can clearly see that the lines become smoother after multiple frames averaging.

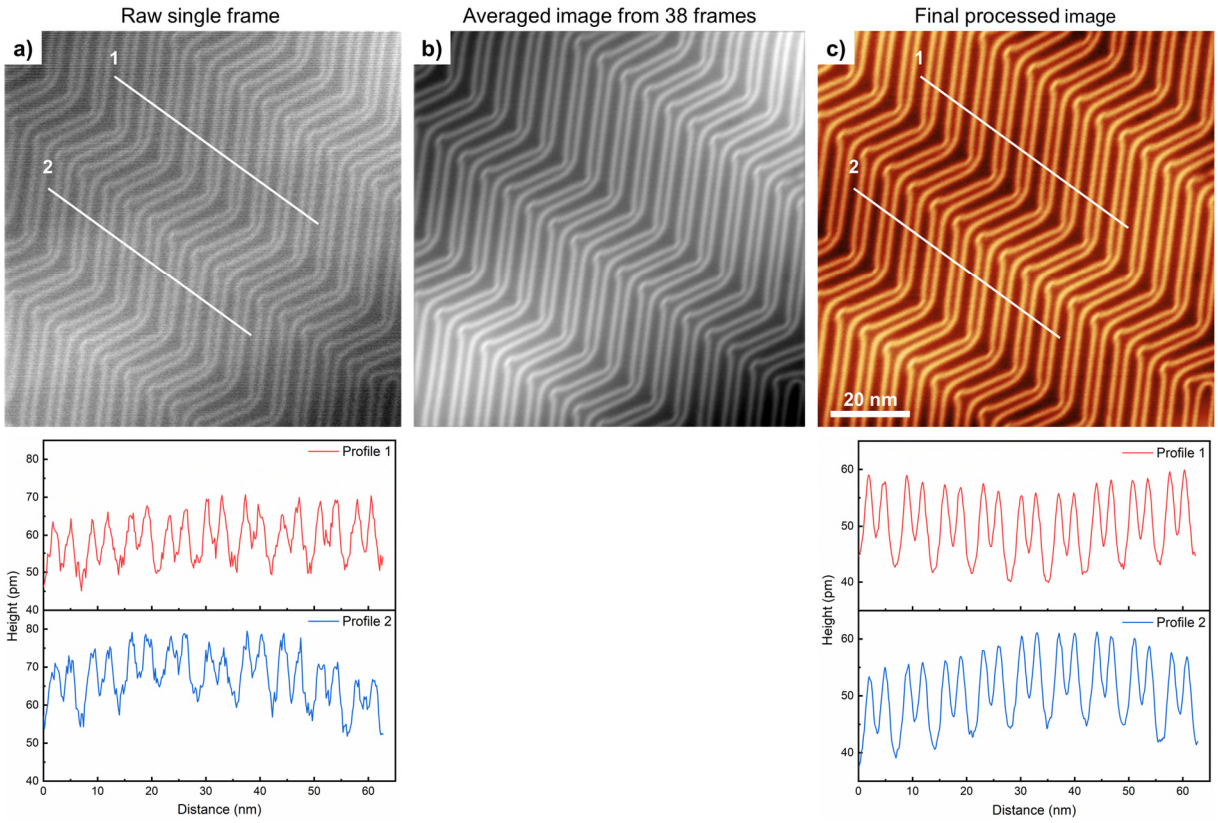


Figure 3.12: (a) Top: raw STM image of the Au(111) reconstruction. Image size: 100 nm × 100 nm, V_s = 1.5 V, I_t = 0.1 nA. Bottom: profiles of the surface. (b) Image after averaging of 38 sequential frames with *SmartAlign*. Image size: 98.05 nm × 99.32 nm. (c) Top: final processed image. Image size: 96.68 nm × 96.68 nm. Bottom: profiles of the surface.

Chapter 4

Self-assembly and Metal Coordination Networks of HHTP on Au(111)

4.1 Introduction

Hexahydroxytriphenylene (HHTP) is the most commonly used linker in 2D c-MOFs, and gas sensors based on HHTP-MOFs exhibit excellent performance with respect to sensitivity and selectivity.[159-161] However, the sensing mechanism of these MOF chemiresistive sensors is not fully understood due to the lack of in-situ characterisation techniques. Since STM has high resolution and does not damage samples, it might be possible to use STM to investigate the interactions between gas molecules and active metal centres. Before the mechanism study, we need to synthesise the HHTP-MOF first. The first STM characterisation of HHTP molecules was carried out in 2009, earlier than the report of HHTP-MOFs.[145] Following that, several studies of HHTP molecular self-assemblies on metal surfaces were published, including Au(111), Ag(111) and Cu(111) substrates.[146-151]

This chapter focuses on the reactions between HHTP molecules and transition metals as well as the synthesis of HHTP-MOFs on the Au(111) substrate. The self-assembly of HHTP molecules was investigated first, and DFT calculations were also performed to analyse the structure of this molecular phase. After that, the metal coordination reactions were carried out by depositing metal atoms and HHTP molecules together.

4.2 HHTP molecular self-assembly

When HHTP molecules were deposited onto a Au(111) substrate held at room temperature, they self-assembled into a near close-packed (NCP) phase, as shown in Fig. 4.1a. The bright stripes correspond to the underlying herringbones of the Au(111) substrate, which means the interactions between the self-assembly and the substrate are relatively weak. However, the Au(111) substrate still plays a role in the assembly formation as all the HHTP molecules align along the <112> directions of Au(111). Annealing the sample to a higher temperature (up to 350 °C) did not change this structure but eliminated some defects to get a more uniform and homogeneous phase (Fig. 4.1b). When the temperature was higher than 380 °C, the molecules decomposed on the substrate, as shown in Fig. 4.1c. Previous research reported that HHTP molecules dehydrogenated on Ag(111) and Cu(111) substrates, but the situation on Au(111) was not mentioned.[147, 149] Due to the lack of XPS, the chemical states of O atoms in the assembly cannot be determined by our instrument. In the analysis below, HHTP molecules are considered as pristine molecules without any degree of dehydrogenation because Au is more inert than Ag and Cu. A zoomed-in image in Fig. 4.1b shows that the NCP phase is constructed by two rows, labelled ‘A’ and ‘B’. HHTP molecules in Row A are aligned as ‘*head-to-head*’ or ‘*tail-to-tail*’ pairs. Row B is built by HHTP molecules with only one orientation, forming an offset ‘*head-to-tail*’ alignment.

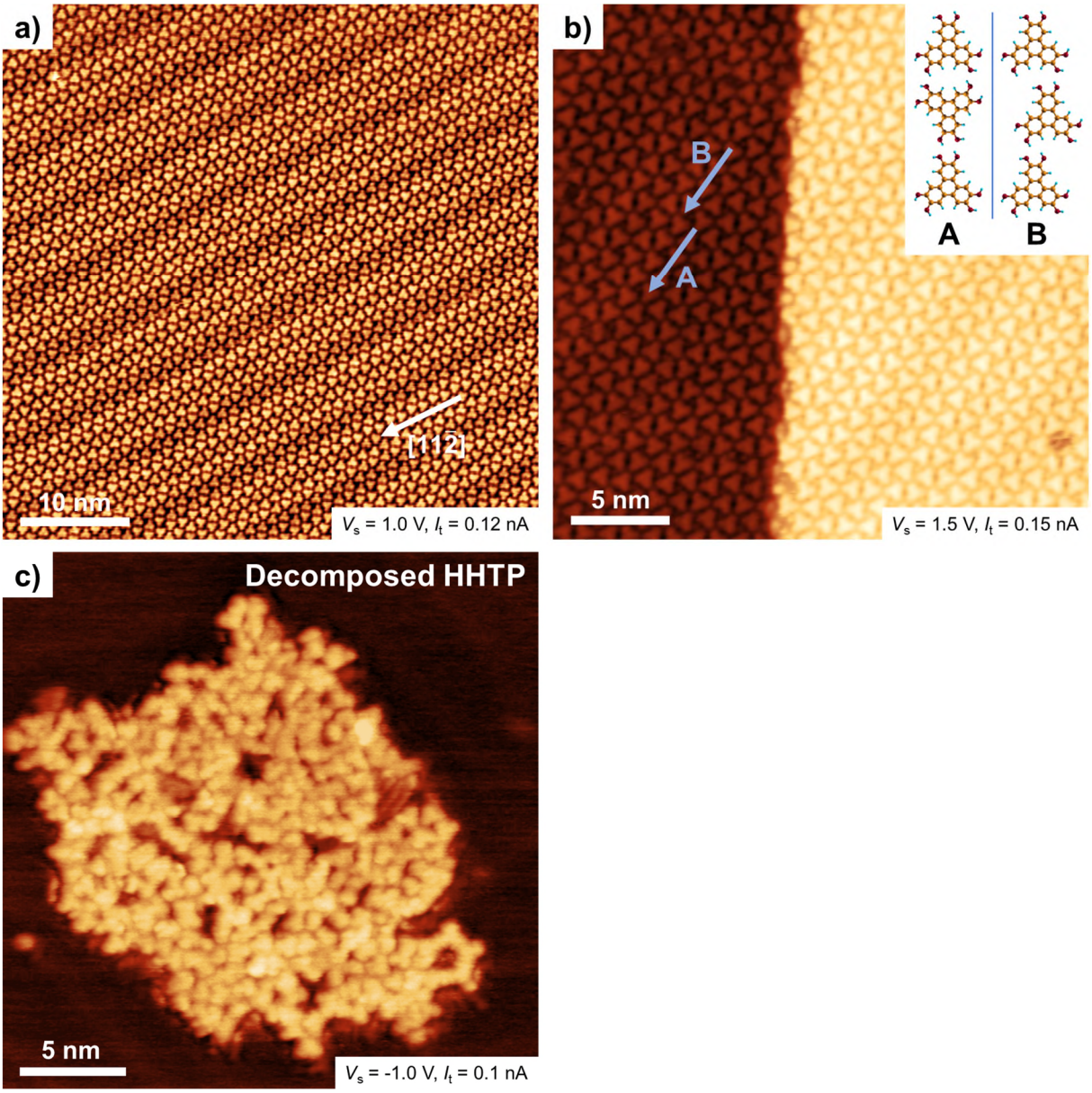


Figure 4.1: (a) STM image of HHTP molecules deposited onto Au(111) at room temperature. (b) HHTP self-assembly after annealing at 150 °C. (c) HHTP molecules decomposed after annealing at 380 °C. Images (a-c) are averaged over 5, 13 and 8 frames, respectively.

To better understand the construction of the assembly, triangles are overlaid on the molecules in Fig. 4.2a. Then we can clearly see that the AB rows are along the herringbones, corresponding to the [11$\bar{2}$] direction of Au(111). More importantly, the orientation of the B rows could change (upward or downward), such as the pure green triangle rows and the pure blue triangle rows in Fig. 4.2a. According to molecules' orientations, the rows in Fig. 4.2b are labelled A or B ($\overline{B}$), where the direction of B is right to left and $\overline{B}$ is left to right. Because of the

random direction of the B rows, this phase is not a periodic structure, and a unit cell cannot be determined. However, a basic element with four molecules in AB(A$\overline{\text{B}}$) rows is drawn by the parallelogram in Fig. 4.2b. This building element has a periodicity of 2.76 ± 0.05 nm, corresponding to a superstructure of $\left(4.5\sqrt{3} \times 4.5\sqrt{3}\right)$ R 30° - Au(111) [if we ignore the reconstruction and use the pristine surface]. Marele *et al.* reported the self-assembly of HHTP on Au(111) before, but their analysis was insufficient.[151] The unit cell they chose was just a coincidence in that local area, and they did not consider the influence of the Au substrate.

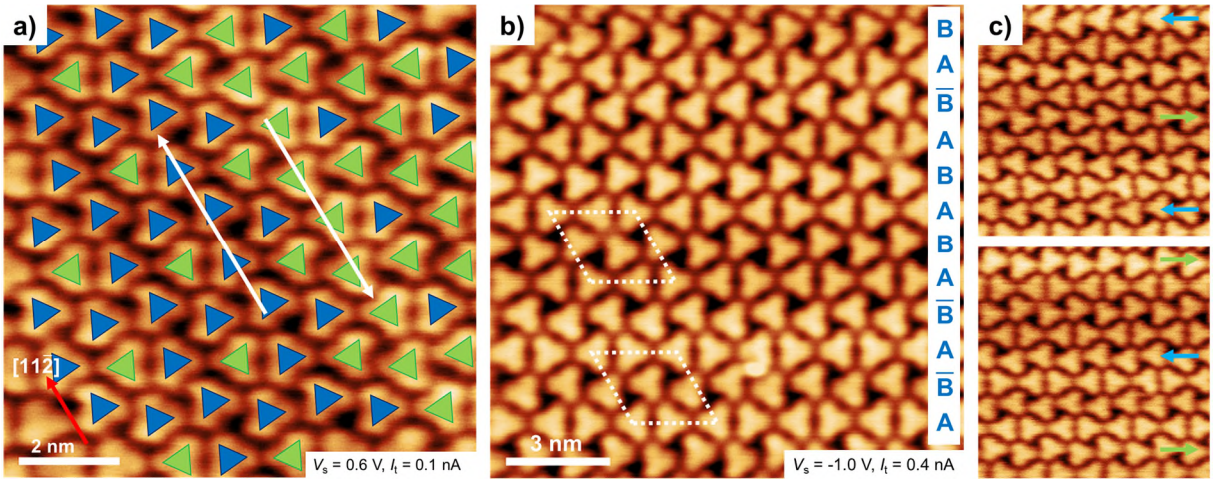


Figure 4.2: (a) The arrangement of HHTP molecules in the assembly, shown by overlaid triangles. (b) A magnified image of the NCP phase. The rows are labelled A or B ($\overline{\text{B}}$) on the right-hand side, depending on the molecular orientations. (c) Two successively scanned STM images showing the direction change of B rows. V_s = -0.5 V, I_t = 0.5 nA. Images (a, b) are averaged over 5 and 11 frames, respectively.

As described above, HHTP molecules can rotate on the surface, so the directions of the B rows can be reversed. Fig. 4.2c are two images scanned successively, where the directions of some molecular rows have changed, marked by the arrows. It is obvious that changing the direction does not affect the integrity and stability of the whole structure. This phenomenon might be caused by the thermal energy (room temperature) and the flexibility of the assembly. Sometimes, the direction of the B rows could also change back, for example, upward to downward and then upward again. There are many studies about the rotation of single molecules on surfaces, but the change of a molecular row has rarely been reported.[199-201] This

work can be further investigated in the future if the sample temperature can be well-controlled. All the images in this thesis were taken at room temperature, and using a low temperature can decrease the thermal energy, which would be helpful for this rotation study.

For modelling, DFT calculations were performed on the free-standing assembly first. The optimised structures for AB and A$\overline{B}$ rows are shown in Fig. 4.3a and b, respectively. These two structures are actually the same because we could find the A$\overline{B}$(AB) cell by rotating the original AB(A$\overline{B}$) cell. (To better understand the direction of the B rows, two images are shown here.) This AB(A$\overline{B}$) cell has an optimised constant of 22.42 Å, close to the value measured in the experiment. In this structure, one hydroxyl group connects with two adjacent hydroxyl groups, forming three-centre ring-like hydrogen bonds. There are six hydrogen-bond rings (18 hydrogen bonds) in one cell, decreasing the energy by 3.51 eV (compared with isolated molecules). The reason why the molecules in the B row can rotate might be relevant to the hydrogen bonds. The '*tail-to-tail*' alignment in Row A stabilises the base of the triangle because it has two anchor sites with two hydrogen bonds, making the entire structure firmly fixed. However, Row B does not have the '*tail-to-tail*' unit, and the '*head-to-tail*' alignment only fixes one head of the triangle through one hydrogen bond. Consequently, the molecules in Row B have some degrees of flexibility to rotate themselves. A supercell of ABA$\overline{B}$ was also shown in Fig. 4.3c, which has an optimised lattice constant of 44.83 Å.

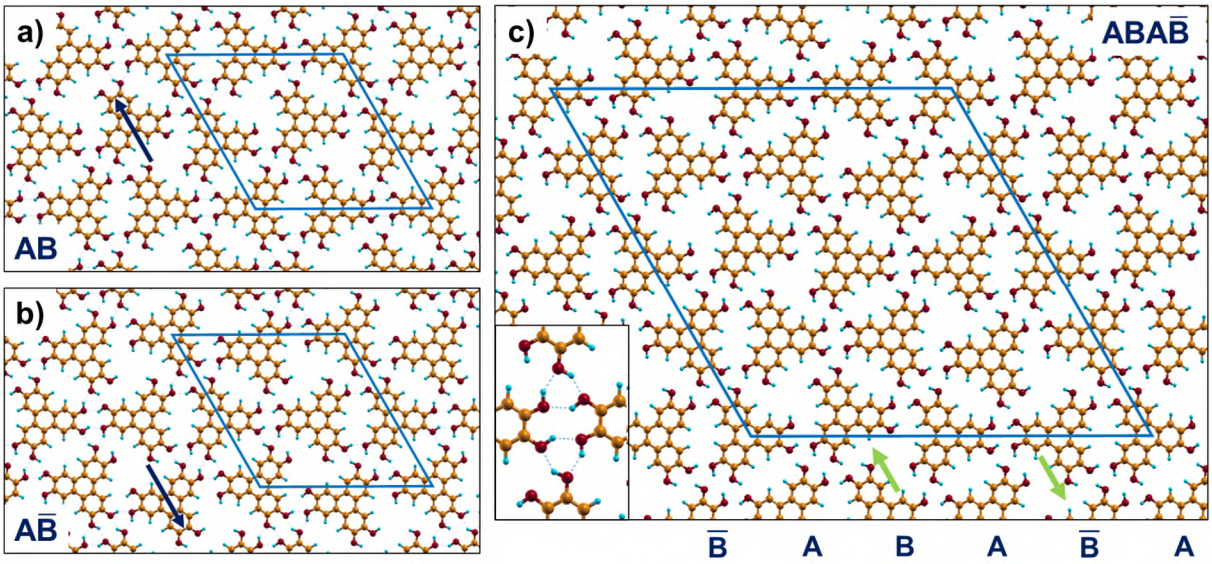


Figure 4.3: DFT relaxed structures for free-standing HHTP assembly. (a, b) Cells with pure AB(AB̄) rows. (c) A supercell with ABAB̄ rows. C: orange, O: dark red, H: light blue.

Depending on the orientation of the molecule and the position of the central aromatic ring, there are eight possibilities when an isolated HHTP molecule adsorbs on the substrate. As shown in Fig. 4.4, the molecules in the top four images are aligned to the [11$\bar{2}$] direction while the bottom ones are along the [$\bar{1}$10] direction. Their energy differences are also listed in the image, showing that the preferred adsorption position is the 'top' site along the [11$\bar{2}$] direction. In this preferred geometry, the adsorption energy of the molecule is around -1.72 eV.

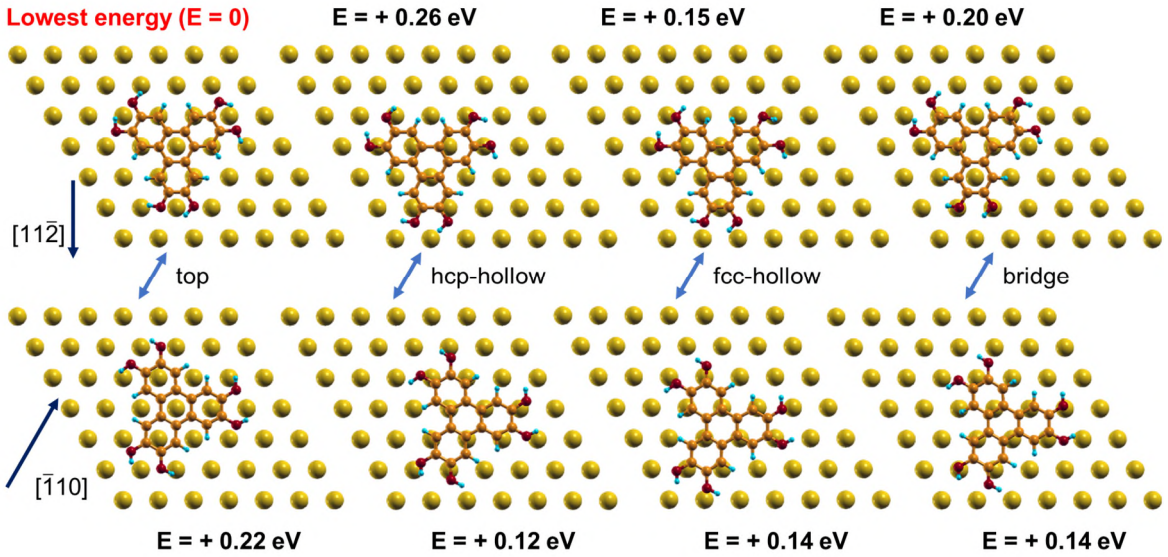


Figure 4.4: Adsorption positions for an isolated HHTP molecule on the Au(111) surface (a three-layer slab, but only the top layer is shown). C: orange, O: dark red, H: light blue and Au: yellow.

According to previous measurements, the superstructure is $\left(9\sqrt{3} \times 9\sqrt{3}\right)$ R 30° - Au(111) for the ABA$\bar{B}$ system. The problem is that this supercell contains 16 HHTP molecules and 3 layers of Au atoms (1305 atoms in total), which exceeds the ability of DFT. Using the AB cell, $\left(4.5\sqrt{3} \times 4.5\sqrt{3}\right)$, can satisfy the calculation requirement, but the Au(111) substrate cannot be created as the number of Au atoms is 60.75 per layer, which is not an integer. Therefore, DFT calculations cannot be performed on this adsorption system. The $\left(9\sqrt{3} \times 9\sqrt{3}\right)$ R 30° - Au(111) model in Fig. 4.5 is constructed manually by putting the self-assembly onto the substrate, where HHTP molecules are on the 'top' or 'bridge' sites. Based on the adsorption results of the isolated molecule (Fig. 4.4), the energy difference between the 'top' and 'bridge' sites is quite small, which should have a very limited influence on the self-assembly. However, the model here is based on the pristine Au(111) surface, and reconstruction is not considered. A more accurate model is needed in the future to study the adsorption of this system.

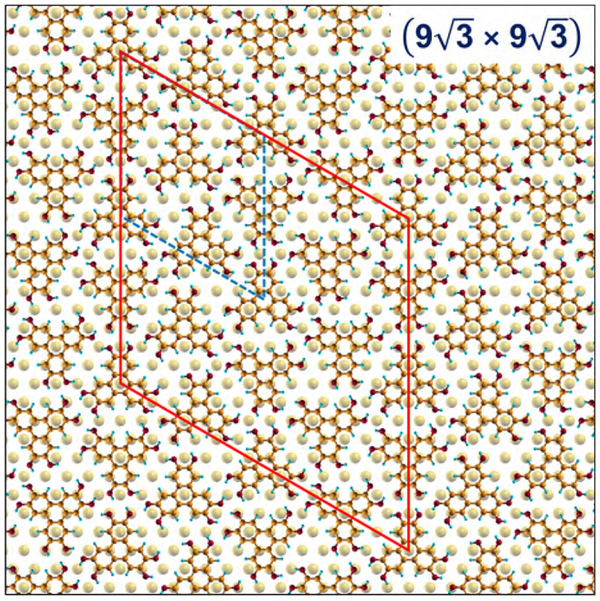


Figure 4.5: Structure models for HHTP molecules adsorbed on the Au(111) substrate (unrelaxed). The unit cells are marked by the red parallelogram. C: orange, O: dark red, H: light blue and Au: yellow.

4.3 HHTP metal coordination networks

When HHTP molecules were deposited onto the Au(111) substrate with Ni, they did not react with each other at room temperature. As shown in Fig. 4.6a, the majority of HHTP molecules

formed self-assemblies on the surface, and others surrounded the metal islands. After annealing, Ni reacted with HHTP molecules and formed a dense phase constructed by coordination complexes (Fig. 4.6b). This result is different from the wet-chemical synthesis, where the products are mainly frameworks with honeycomb structures. [1, 71, 73] Previous studies of HHTP molecules on Cu(111) and Ag(111) substrates have reported HHTP-Cu/Ag layers but they were isolated complexes or a continuous network (Fig. 2.13), also different from the HHTP-Ni obtained here. [149-150] As drawn in Fig. 4.6c, the complexes include dimers, trimers and tetramers ('Y' shape and 'Z' shape), but no higher-order multimers were observed. The white square in Fig. 4.6b is an area with a well-ordered structure built by pure Y-tetramers. This is the most periodic and uniform phase of these HHTP-Ni complexes. Usually, the coordination phase is a mixture of different multimers, as shown in Fig. 4.6d. Therefore, a unit cell cannot be determined for this phase.

Several reaction conditions were tested to investigate their influences on the synthesis. For example, switching the deposition order of the metals and molecules did not affect the reaction as they started to react after annealing. However, the deposition amount affected the yield of the products. If the amount of the metal was insufficient, most of the molecules were still in the hydrogen bonded phase and only a few complex multimers were obtained. When the amount of the metal was in excess, all the molecules were coordinated, and those unreacted metal atoms formed clusters/islands on the surface (Fig. 4.6e). As for annealing, the coordination reaction could take place at around 200 °C, while increasing the temperature (up to 350 °C) and time (> 1h) had limited influences on the synthesis. Besides, there is no obvious difference between HHTP-Ni and HHTP-Co complexes if using Co as the metal source (Fig. 4.6e).

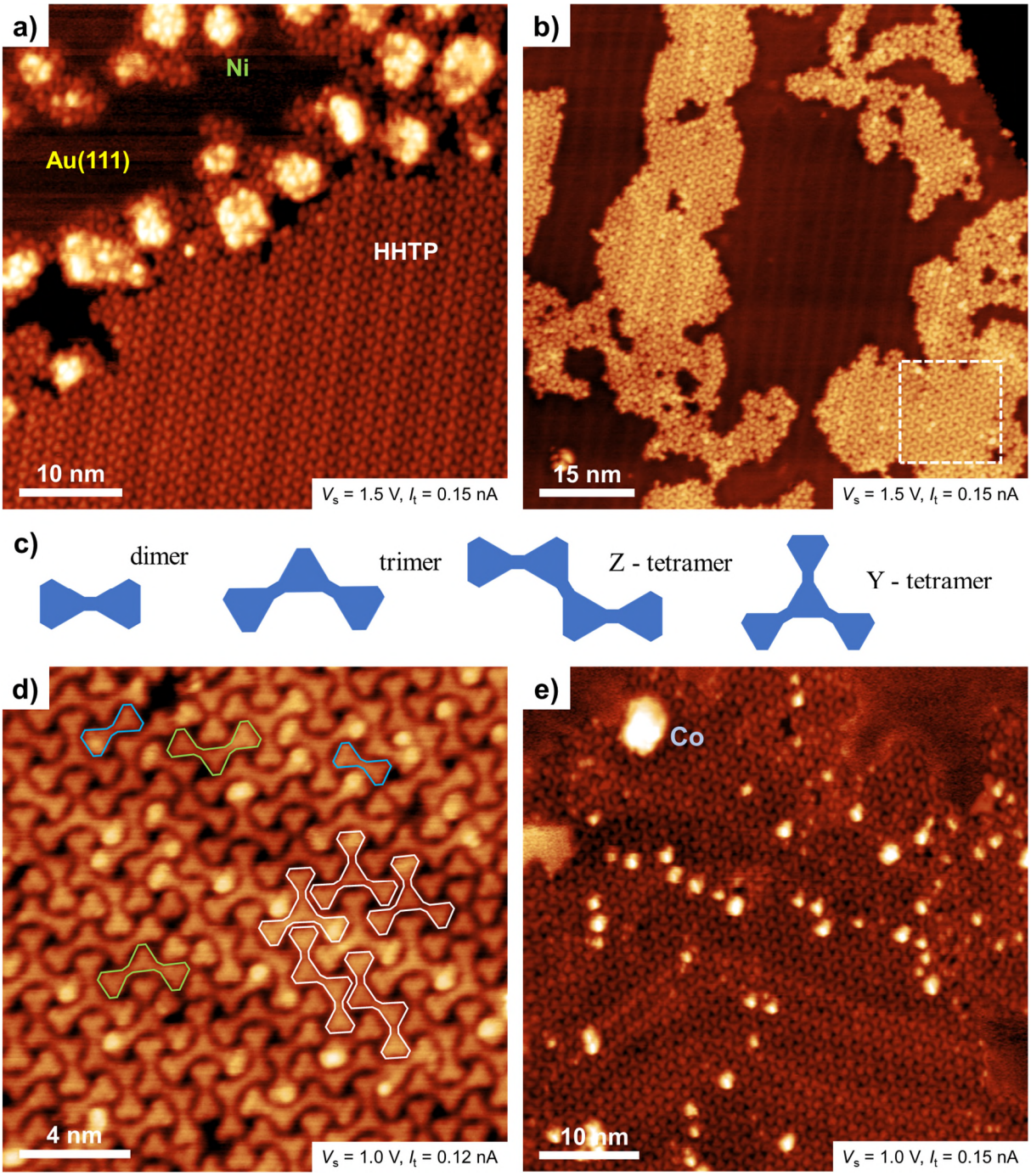


Figure 4.6: (a) Depositing HHTP molecules (0.35 ML) onto the Au(111) substrate with Ni (0.08 ML) at room temperature. (b) Annealing the sample at 250 °C. (c) Models of different multimers. (d) The dense phase constructed by HHTP-Ni multimers. (e) HHTP-Co coordination phase (0.5 ML) obtained after annealing at 280 °C. Images (a-b, d-e) are averaged over 6, 5, 10 and 5 frames, respectively.

In addition to the synthesis, another problem was that the highest resolution of the STM images was just at the molecular level, so individual atoms cannot be determined in this circumstance. No matter what the sample bias was, metal atoms could not be observed directly from the

images. This might be caused by the tip, which was not sharp enough, or the intrinsic properties of the complexes, like the metal atoms were much lower than the molecules. To investigate the coordination interactions between metal atoms and hydroxyl groups, other characterisation techniques are needed, like nc-AFM.

Fig. 4.7 illustrates several arrangements of tetramers. The formation of the Y-tetramer requires one A row and two B ($\overline{B}$) rows with the same direction, that is BAB ($\overline{B}A\overline{B}$). If the arrangement is $BA\overline{B}$, where the two B rows have opposite directions, Z-tetramers would be generated. The domains can be constructed by pure Y-tetramers or mixed Y- and Z-tetramers. For those pure Y-tetramers (Fig. 4.6b), the measured periodicity is 2.27 ± 0.05 nm, close to the value of $4.5\sqrt{3} \times a_{Au(111)}$ (2.25 nm). Therefore, the repeated supercell should still be $\left(9\sqrt{3} \times 9\sqrt{3}\right)$ R 30° - Au(111), the same as the hydrogen-bonded assembly, which indicates a strong relationship between the coordinated phase and the molecular phase.

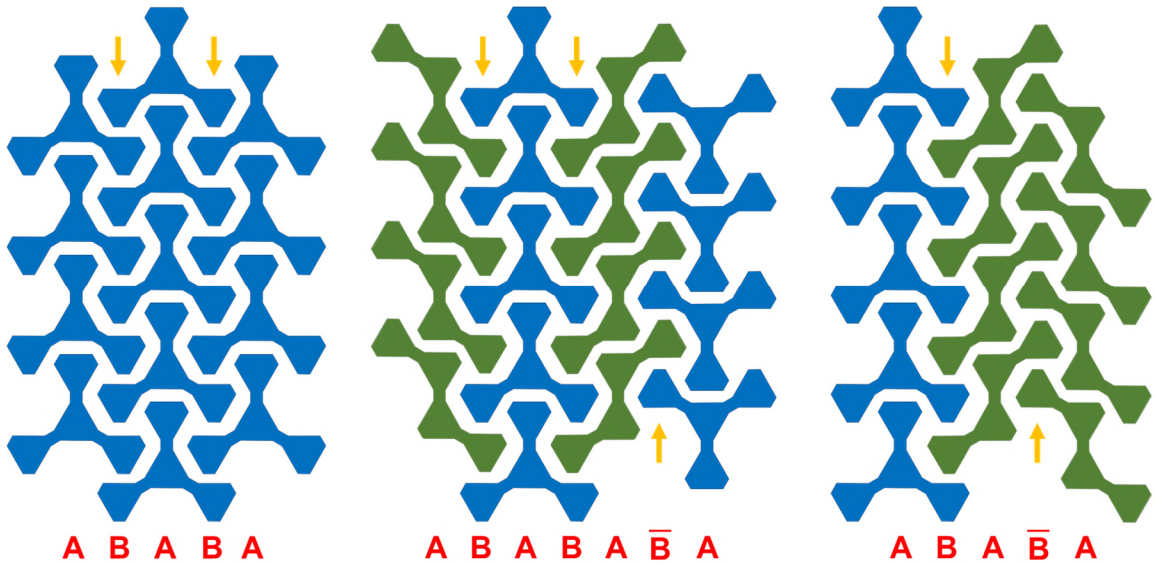


Figure 4.7: Structure models for the arrangement of tetramers.

Based on previous research, transition metal atoms in 2D c-MOFs usually coordinate with two ligands, forming a square-planar or an octahedral geometry (two solvent molecules).[1, 102] However, a recent HHTP-Co study on Au(111) (the same work, published in Aug. 2022)

reported that the Co atoms actually coordinated with three oxygen atoms, which was demonstrated by nc-AFM and STS.[152] This coordination geometry might be influenced and stabilised by the Au(111) substrate. The three-fold motif is very common for metal-organic structures on surfaces, and some examples have been shown in Chapter 2. With the help of the literature, the structure of the HHTP-M coordination phase is drawn in Fig. 4.8. Due to the three-fold coordination geometry, neighbouring HHTP molecules are bonded together by the metal atoms, making the whole structure connected. It also explains why the porous structure could not be created because the adjacent molecules are fixed and cannot move.

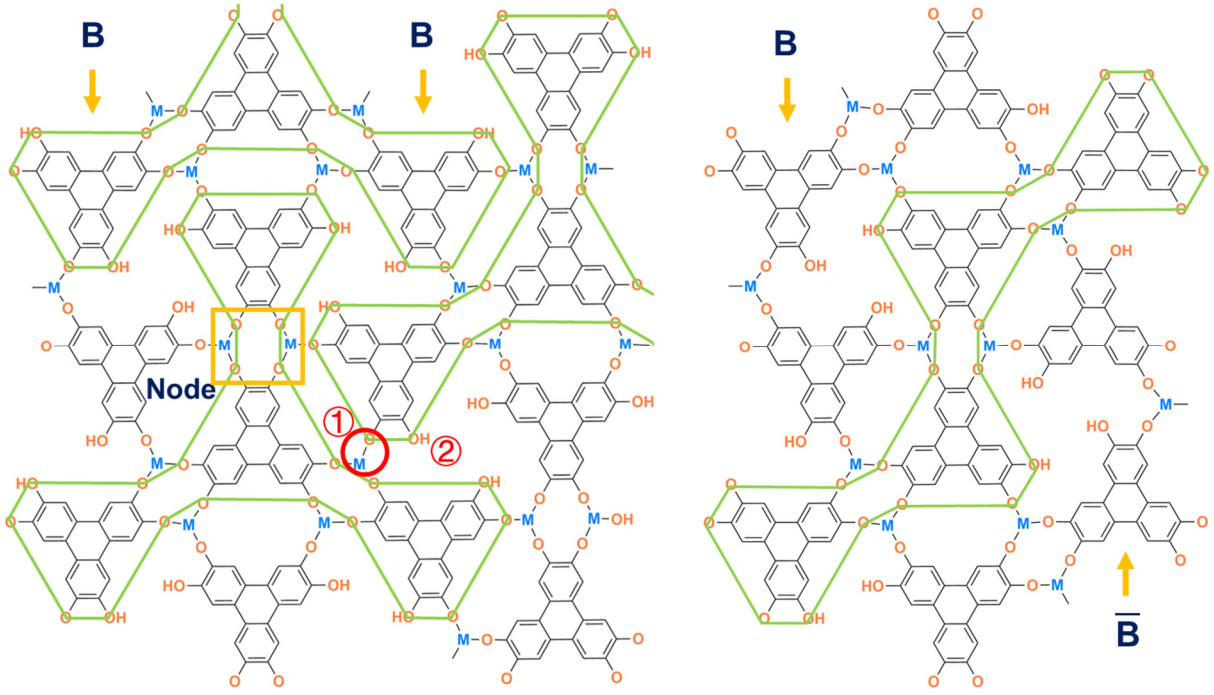


Figure 4.8: Chemical structures of the HHTP-M tetramer networks.

By comparing the structure model and the STM images, it might be possible to explain the discontinuity of the HHTP-M multimers. If both oxygen atoms at the same end are bonded with metal atoms, these M-O bonds would have a shape of a solid bridge (connection node), marked by the orange rectangle in Fig. 4.8. If there is only one coordinated oxygen atom (label '1') and the other one (label '2') is free, this M-O_1 bond will not be evident in the STM images, marked by the red circle in Fig. 4.8. As a result, the molecules did not seem to be connected in the STM

images. However, limited by the image resolution, this explanation cannot be demonstrated by the data shown here and there might be some other reasons to cause this phenomenon. From Fig. 4.6d, we could also notice that some ends of the molecules are brighter than others. This might be caused by the bonding between excessive metal atoms and the free oxygen atoms (label '2'), like adatoms on surfaces. The brightness of the central molecules is usually normal because all the oxygen atoms have been coordinated in the network.

For simulations, the optimised structures of free-standing tetramer layers were not obtained. During relaxation, HHTP molecules tended to rotate to make the metal atoms coordinate with four oxygen atoms. The reason might be that the three-fold coordination geometry is not stable without the support of the Au substrate. However, DFT calculations cannot be performed on the entire adsorbed system because of the large unit cell (the same as the self-assembly phase). In the research of the HHTP-Co, the authors used a supercell of (8 × 8) - Au(111) to study the system, but this was not correct since the true relationship is $\left(9\sqrt{3} \times 9\sqrt{3}\right)$ R 30° - Au(111).[152] Although 8 is the closest integer to $4.5\sqrt{3}$ (~7.794), it cannot be simply used to replace the real cell. This is because the orientation of HHTP molecules is along the $[1\bar{1}0]$ direction in the (8 × 8) cell, not the $[11\bar{2}]$ direction observed in the experiments. Since the positions are important in the studies of adsorptions, changing the adsorption geometry will affect their properties. Therefore, other simulation methods should be used to model this system instead of DFT, such as tight-binding (TB) modelling, which could be performed on much larger systems.

4.4 Conclusion

To summarise, HHTP molecules can self-assemble into a molecular phase on the Au(111) substrate. The formation of this phase was dominated by intermolecular hydrogen bonds, while the influence of the Au(111) substrate could not be ignored. After reacting with metal atoms

(Ni and Co), HHTP molecules formed a dense coordination phase on the surface, which appeared as multimers in the STM images. The metal atoms in this structure adopted a three-fold coordination geometry, connecting all the molecules into one network. This work extends our knowledge of molecular self-assemblies and on-surface reactions, which can provide some guidance for on-surface studies of other 2D c-MOFs linkers.

Chapter 5

Synthesis of HATP Metal-Organic Frameworks on Au(111) and Cu(111) Substrates

5.1 Introduction

HATP (hexaaminotriphenylene) is another triphenylene-derived ligand with delocalised electrons. Its coordination framework, $Ni_3(HITP)_2$ (HITP: hexaiminotriphenylene) possesses the highest electrical conductivity among porous MOFs (10^2 S/cm for single crystals).[71, 76] Apart from $Ni_3(HITP)_2$, Dincă *et al.* also studied bimetallic NiCo, NiCu and CoCu–HITP MOFs and observed a continuous tunability of bandgaps and electrical conductivities.[79] However, because of limitations in synthetic control, studies on structures and conductivities rely on polycrystalline powders or thin films. The high anisotropy and grain boundaries hinder the investigation of MOFs' intrinsic properties and limit their performance in devices. Besides, how the metals coordinate with the linkers has not yet been visualised even under high-resolution TEM (HRTEM). Therefore, synthesising a monolayer MOF and characterising it at an atomic level is crucial for the structural analysis, which will improve our understanding of this family.

In this chapter, single-layer MOFs were synthesised on metal substrates using the HATP linker under UHV. The growth processes of $Ni_3(HITP)_2$ and $Co_3(HITP)_2$ MOFs are described first, followed by the synthesis of a bimetallic $Ni_xCo_{3-x}(HITP)_2$ MOF using a mixture of Ni and Co. The structures of these MOFs were characterised by STM with high resolution and modelled by DFT. The reaction between HATP molecules and Cu is also discussed in the final section.

5.2 $Ni_3(HITP)_2$ MOF on Au(111)

The behaviour of HATP molecules was studied first when they were deposited onto the Au(111) substrate. At room temperature, HATP molecules are highly mobile on the surface, so they cannot be distinguished individually by STM.[122] Fig. 5.1a shows the surface after depositing the molecules, where only fuzzy and blurred herringbones can be observed. When Ni and HATP were deposited onto the Au(111) surface and then annealed, they reacted with each other to form complexes in the shape of polygonal strings and small hexagonal clusters, as shown in Fig. 5.1b and c. Since the amount of HATP was small and the annealing temperature was low, many Ni islands remained on the surface, surrounded or attached by the coordinated complexes. More HATP molecules were needed to consume the remaining metals. If the metal dosage is too much (> 0.1 ML), HATP molecules cannot coordinate with all the metal atoms. The critical amount should be approximately 0.06 ML for the whole layer (coverage = 1) [This estimation was calculated from the epitaxy which will be discussed in the following part. 3 Ni atoms on a surface of 57 Au atoms (Ni atomic radius ≈ Au atomic radius): 3/57 = 0.053]. However, Ni is expected to partially dissolve into the Au substrate and condense at the terrace edges, making the actual coverage a little smaller. When suitable amounts of metal atoms and HATP molecules were deposited, uniform honeycomb domains were obtained after sufficient annealing, shown in Fig. 5.1d. These networks had the same porous structure as the product synthesised by wet-chemical methods and can be regarded as a single-layer MOF.[76-77]

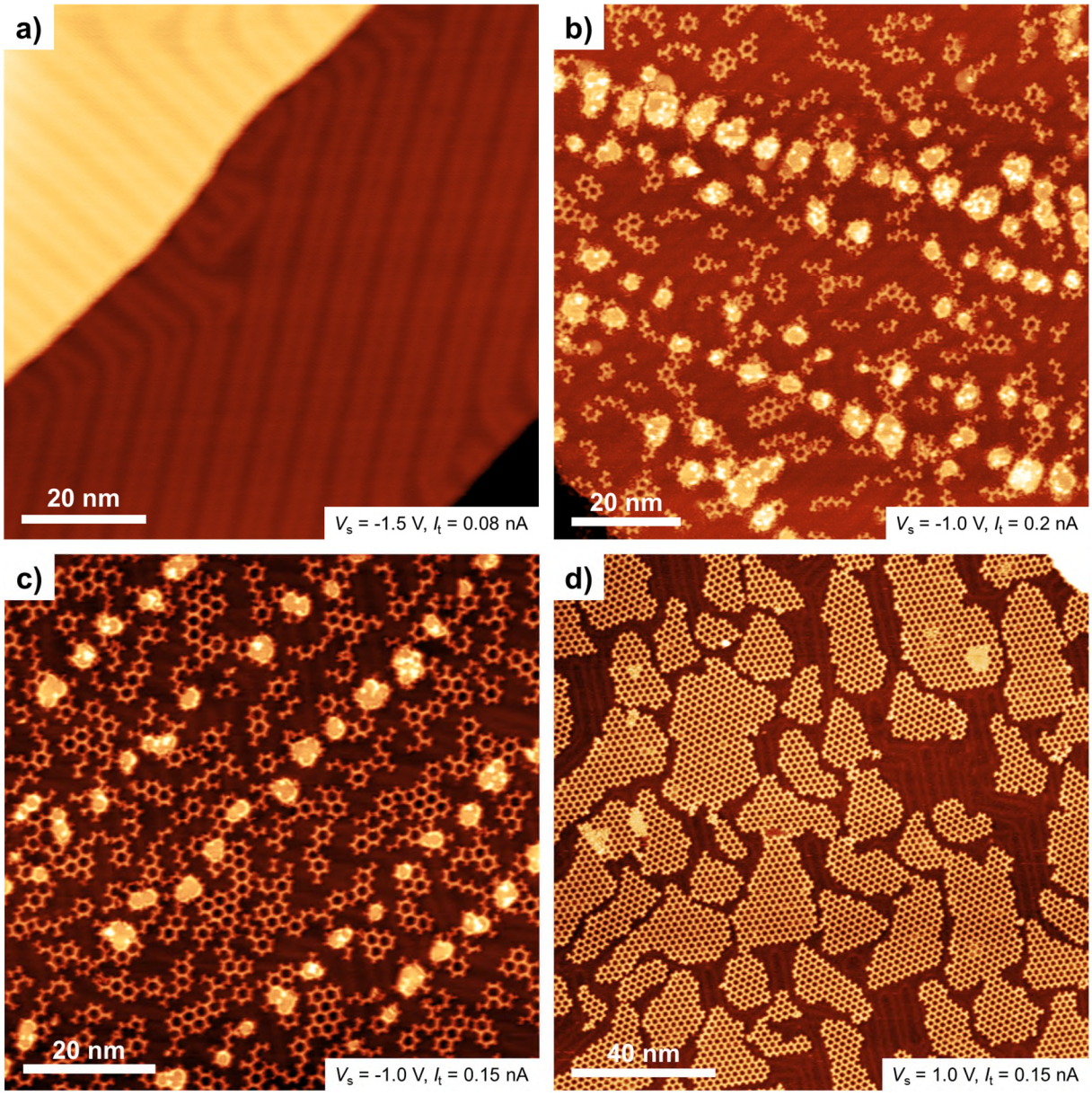


Figure 5.1: (a) Au(111) substrate after depositing HATP molecules. (b) Depositing Ni (0.12 ML) and HATP (0.1 ML) onto the Au(111) substrate then annealing at 170 °C. (c) Depositing more HATP molecules (0.15 ML) and annealing at 190 °C. (d) Mature $Ni_3(HITP)_2$ domains (0.7 ML) with honeycomb structure, obtained after annealing at 300 °C. Images (a-d) are averaged over 14, 3, 10 and 3 frames, respectively.

The average size of prepared $Ni_3(HITP)_2$ domains was around 40 × 40 nm^2 and the highest coverage was around 0.86 ML, achieved by a few cycles of deposition and annealing (Fig. 5.2a). Depositing more molecules and metals did not increase the coverage or generate multilayers. The amounts of the molecules and metals in Fig. 5.2a were over-deposited, but the second layer was not observed. This might be caused by the weak van der Waals force between

two MOF layers. I have also tried different conditions to see whether larger and continuous domains could be synthesised. The influence of the metal dosage has been discussed above, which had a very limited effect on the shape of the product. Changing the deposition order of the metals and molecules did not affect the reaction either since the reaction took place after annealing. The factor that influenced the growth most was the annealing temperature. If the annealing temperature was not high enough (below 200 °C), the main product was hexagonal clusters, like the situation in Fig. 5.1c. Usually, the annealing temperature used in the synthesis was around 250 °C (or a little higher, 300 °C), which could lead to large islands on the surface (Fig. 5.1d). However, when the temperature was higher than 550 °C, the MOF networks decomposed after annealing. Therefore, it can be concluded that adjusting the reaction parameters (mainly deposition and annealing) did not change the structure and morphology of the final MOF network, but the formation of early-stage domains was affected. To explain why the domain sizes are limited, we need to consider the influence of the substrate, that is, the relationship between the adsorbed layer and the Au(111) substrate.

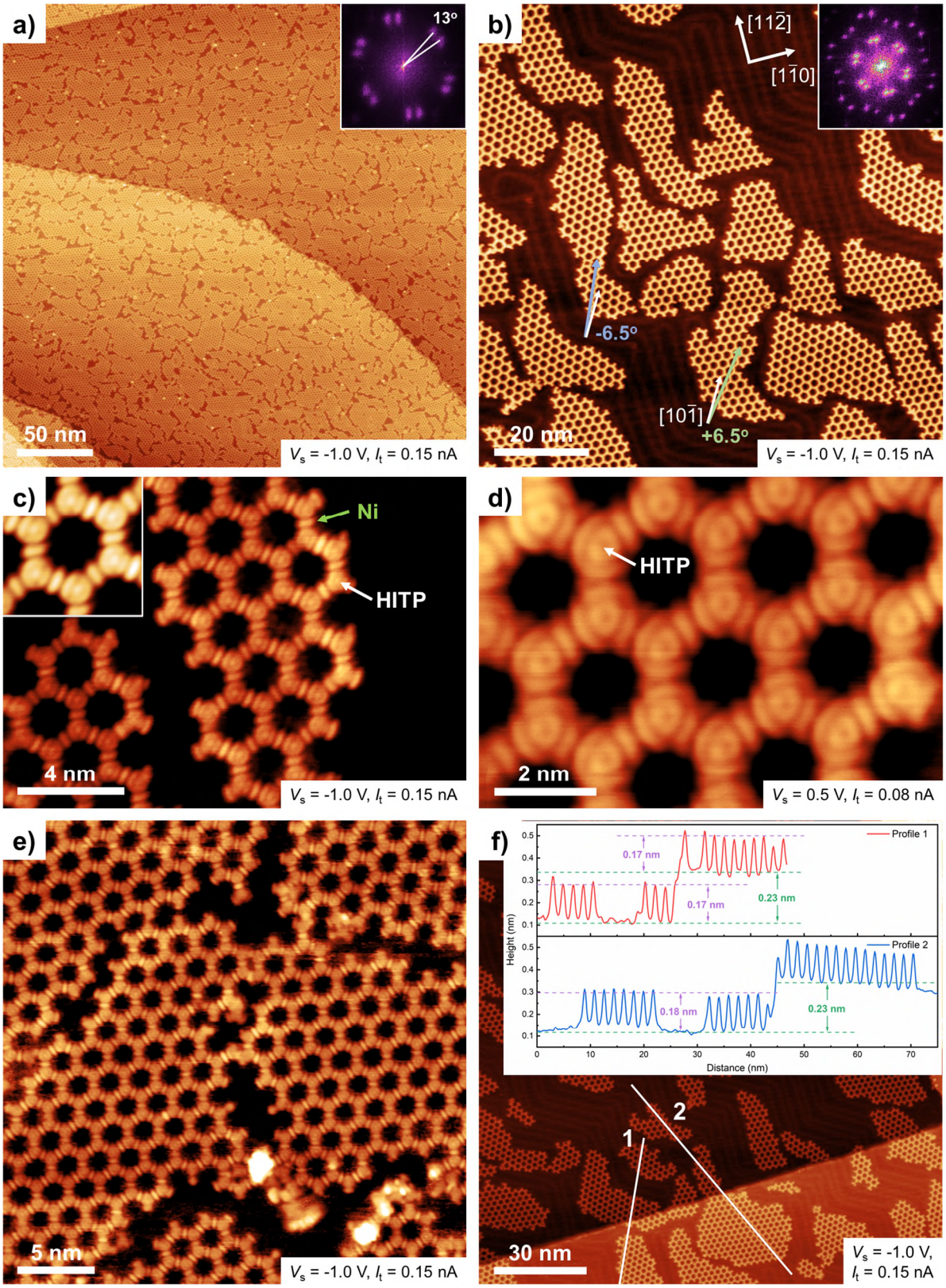


Figure 5.2: (a) High-coverage $Ni_3(HITP)_2$ MOF (0.86 ML) obtained by a few cycles of deposition and annealing. (b) Two orientations of the MOF networks: ± 6.5° with respect to the <110> directions of the Au substrate. Inset: 2D FFT of the STM image. (c - e) STM images of the MOF honeycomb with sub-molecular resolution. (c) Inset: averaged template of the hexagon. (f) Profiles of the MOF on Au(111). Images (b-f) are averaged over 13, 7, 14, 5 and 5 frames, respectively. Image (a) is a single scan.

The unit cell of the $Ni_3(HITP)_2$ network had a lattice constant of 2.16 ± 0.10 nm, close to the value reported before.[76, 122] Two lattice orientations rotated ± 6.5° with respect to the <110> directions of the Au (111) substrate were found in Fig. 5.2b. The Fourier transform of this STM image also clearly shows the existence of two orientations. Consequently, the epitaxial relationship between the $Ni_3(HITP)_2$ network and the Au(111) substrate should be $\left(\sqrt{57} \times \sqrt{57}\right)$ - R 6.6°. Because of the strong epitaxial interaction between the MOF layer and the Au(111) substrate, domains are unable to merge with others and grow into large islands. Once a domain of a particular orientation has formed, it does not readily change its orientation. Even the adjacent islands have the same orientation, they need to shift for some space to meet the registry, which is not energetically favourable. This means that agglomeration is not feasible to expand domains' sizes, leaving only ripening as a possible approach. Ripening relies on the detachment of HITP from one domain and re-attachment to another. Nevertheless, it was discovered that the molecule's detachment did not occur until the degradation of the networks. Therefore, it seems impossible to create a large single-layer MOF in this $Ni_3(HITP)_2$ - Au(111) system with our current synthesis methods.

Fig. 5.2c and e are high-resolution STM images which clearly show the metal atoms and molecules. Under negative biases, the Ni centre appears as a rounded rectangle, and the triphenylene ligand looks like a circle with a dot inside. When the bias is positive, the Ni centres become not evident or even invisible, as shown in Fig. 5.2d. Fig. 5.2f shows two profiles of the MOF domains on the surface, where the height of the Au terrace is 0.23 nm (as a reference) and the height of the MOF is around 0.17 nm.

DFT calculations were then performed to study the properties of this system. Firstly, we investigated the adsorption of an isolated HATP molecule, although we cannot see it in the

experiment. As illustrated in Fig. 5.3, there are eight possibilities for the adsorption configuration depending on orientations and positions. The molecules in the top four images are aligned to the [11$\bar{2}$] direction while the bottoms are along the [$\bar{1}$10] direction. Their energy differences are also listed in the image, where it can be concluded that the preferred adsorption position for HATP molecules on Au(111) is the 'top' site along the [11$\bar{2}$] direction. However, compared with the adsorption energy, which is around -2.4 eV, these energy differences are relatively small and may not affect the adsorption too much.

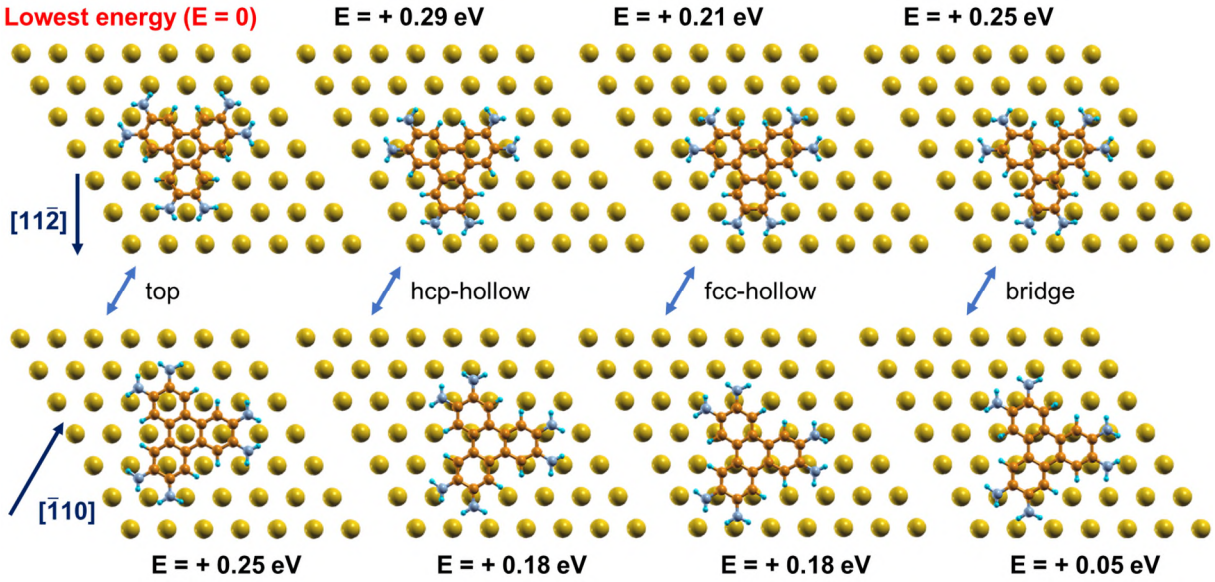


Figure 5.3: Adsorption positions for an isolated HATP molecule on the Au(111) surface (a three-layer slab, but only the top layer is shown). C: orange, N: blue-grey, H: light blue and Au: yellow. The symmetric site is determined by the position of the central aromatic ring.

For a free-standing single-layer $Ni_3(HITP)_2$ MOF, the optimised lattice constant is 21.90 Å, close to the value measured in the experiment. As shown in Fig. 5.4a, the whole layer is in the same plane without any distorted or buckled part, indicating perfectly planar coordination of Ni atoms. The band structure in Fig. 5.4b illustrates that the $Ni_3(HITP)_2$ layer is a semiconductor with a small bandgap of 0.125 eV. The maximum of valence band is located at the K point while the minimum of conduction band is located at the Γ point, indicating that the $Ni_3(HITP)_2$ layer is an indirect semiconductor. The density of states (DOS) and projected density of states (PDOS) plots in Fig. 5.4 show that the states near the Fermi level are almost fully contributed

by the p_z orbitals of C and N atoms as well as the *d* orbitals of Ni atoms, which are typical characteristics of conjugation.[202] These simulation results further suggest that the extended π-*d* conjugation is responsible for the charge transport in this conductive MOF.

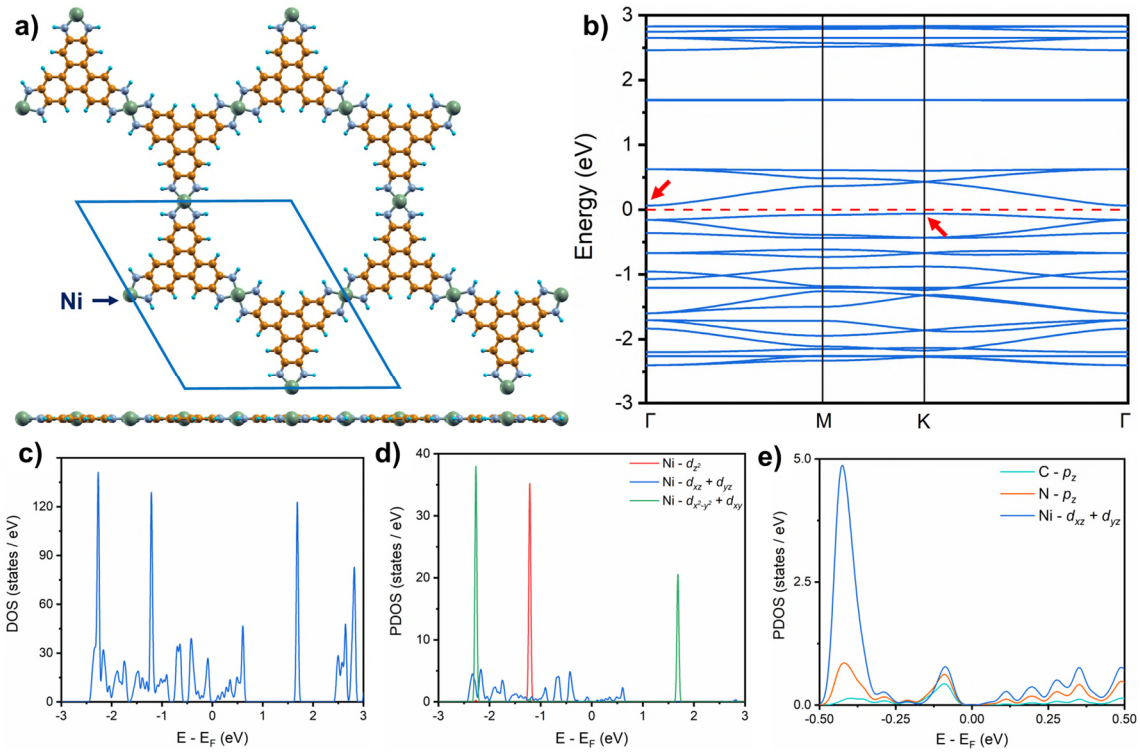


Figure 5.4: (a) DFT-relaxed structure of a free-standing $Ni_3(HITP)_2$ layer. Ni: green, C: orange, N: blue-grey and H: light blue. (b) Band structure of the single-layer $Ni_3(HITP)_2$. (c) Density of states (DOS) plot for the $Ni_3(HITP)_2$ layer. (d, e) Projected density of states (PDOS) plots for Ni, C and N atoms.

The $Ni_3(HITP)_2$ MOF adopts a superstructure of $\left(\sqrt{57} \times \sqrt{57}\right)$ - R 6.6° when adsorbed on Au(111). Fig. 5.5a is the optimised structure of the adsorbed system, but only the top layer of the Au(111) substrate is shown for clarity. In this adsorption geometry, each Ni atom locates at the 'bridge' site, and the central aromatic ring of the ligand is on the 'top' site of the Au(111) substrate. From the side view, we can see that the distance between molecules and the top-layer Au atoms is 3.13 Å, while the Ni atoms drop down about 0.19 Å off the molecular plane towards the Au substrate (2.94 Å). This breaks the flatness of the coordination, but the degree of distortion is tiny. Furthermore, Bader charge analysis shows that the $Ni_3(HITP)_2$ MOF has transferred 0.82 *e* to the Au(111) substrate compared with the free-standing layer. The

simulated STM image at -1.0 V is shown in Fig. 5.5b, which is very similar to the experiment images. The only difference is that the interior structure of the molecules is clearer in the simulated image. The PDOS of Ni atoms' *d* orbitals is plotted in Fig. 5.5c, and the PDOS near the Fermi level is enlarged in Fig. 5.5d. Compared with the free-standing case, the d_{z^2} orbital of Ni changes from a sharp peak to a lower and broader peak, while the positions and shapes of other orbitals almost keep the same. Moreover, the d_{z^2} states are located at around -1.4 eV below the Fermi level, explaining why Ni nodes are more obvious under negative biases.

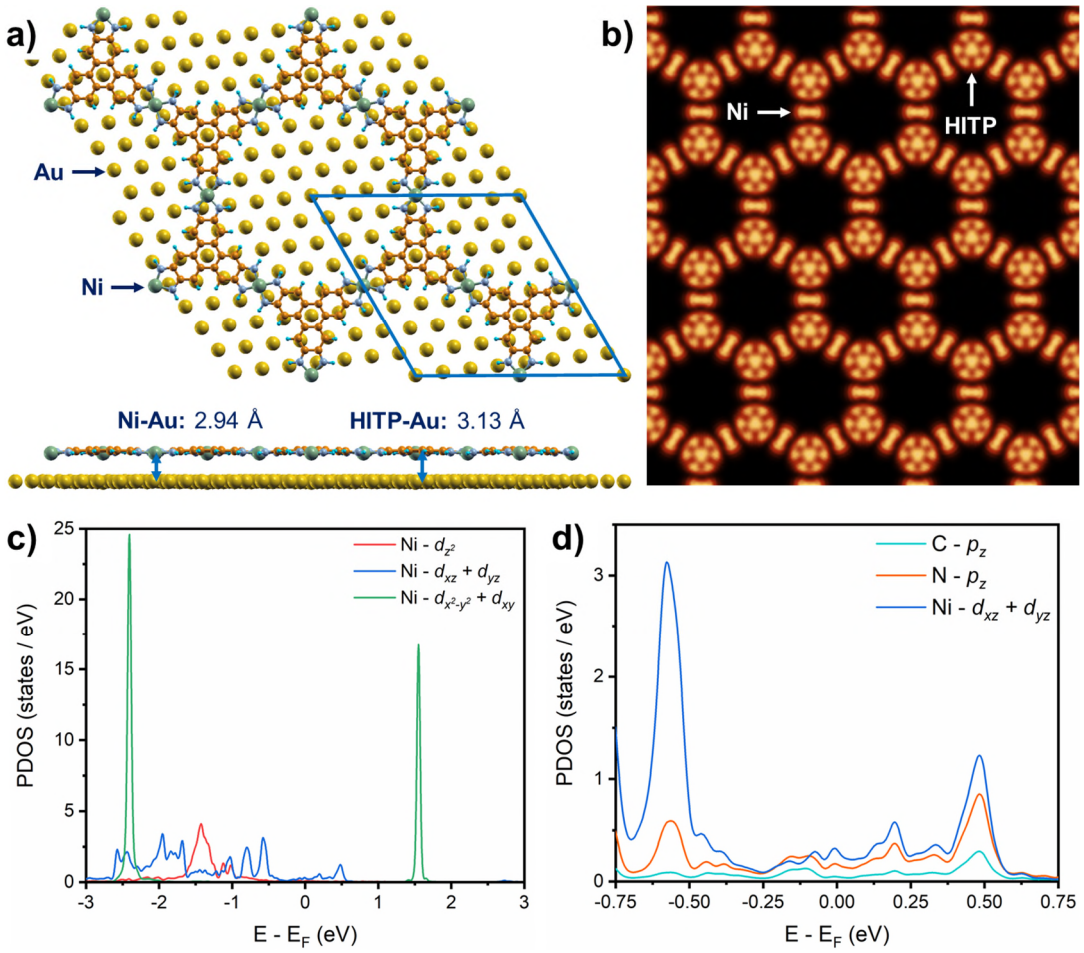


Figure 5.5: (a) DFT-relaxed structure of a $Ni_3(HITP)_2$ layer adsorbed on the Au(111) substrate (a three-layer slab, but only the top layer is shown). Ni: green, C: orange, N: blue-grey, H: light blue and Au: yellow. (b) Simulated STM image at -1.0 V. (c, d) PDOS plots for Ni, C and N atoms.

5.3 $Co_3(HITP)_2$ MOF on Au(111)

Switching from Ni to Co and following the same synthesis procedure, a distinct morphology of domains was obtained. Early-stage Co-HATP complexes were similar to Ni ones, like the

hexagonal clusters in Fig. 5.6a. However, these Co-HATP elements then developed into anisotropic nanoribbons after sufficient annealing (Fig. 5.6b). Some pentagonal and heptagonal rings were occasionally observed in these ribbons, but their amount decreased significantly if the annealing temperature and time increased. Usually, the length of the nanoribbons was around 30-40 nm but could reach up to 150 nm (Fig. 5.6c).

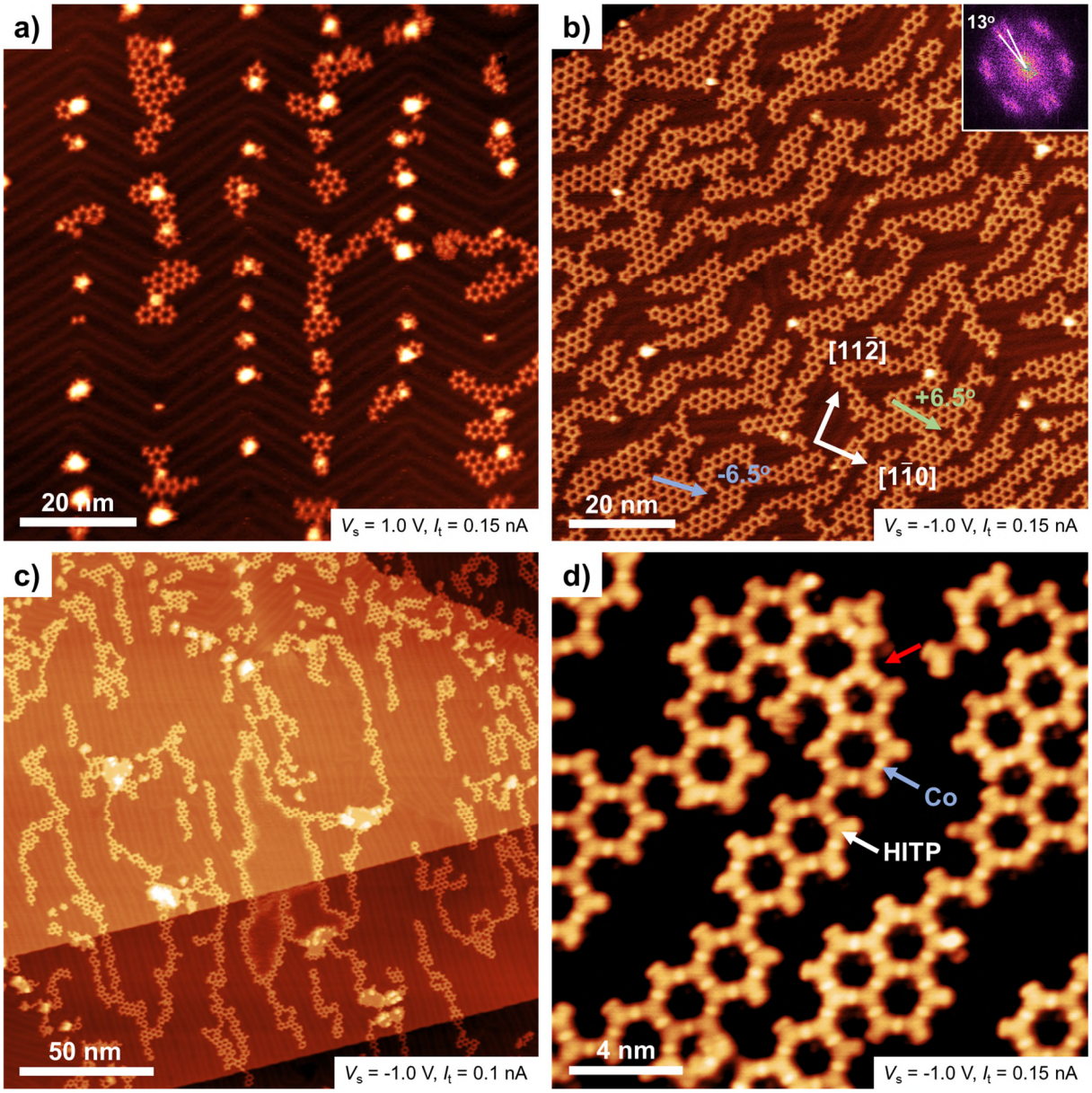


Figure 5.6: (a) Depositing Co (0.06 ML) and HATP (0.1 ML) onto the Au(111) substrate, then annealing at 160 °C. (b) Depositing more reactants and annealing at 190 °C. (MOF: 0.5 ML) Inset: 2D-FFT of the STM image. (c) A large-scale image of the $Co_3(HITP)_2$ ribbons. (d) High-resolution STM image of the $Co_3(HITP)_2$ ribbons. Images (a, c, d) are averaged over 2, 2 and 12 frames, respectively. Image (b) is a single scan.

The epitaxial relationship between Co-HATP and Au(111) is not as clear as the Ni-MOF because of their anisotropic shapes. Based on some large ribbons, two orientations were also found in these domains, marked by the blue and green arrows in Fig. 5.6b. The 2D-FFT of Fig. 5.6b shows two blurred dots next to each other, similar to the pattern in Fig. 5.2b. According to the measurements and the FFT result, the Co-MOF should follow the same epitaxy as the Ni-MOF: $\left(\sqrt{57} \times \sqrt{57}\right)$ - R 6.6°. Apart from the morphology, another difference between Ni-MOF and Co-MOF is that the Co centres are notably brighter than the ligand under some imaging conditions, as shown in Fig. 5.6d.

Although the synthesis of $Co_3(HITP)_2$ was not as successful as $Ni_3(HITP)_2$, DFT calculations were also performed on its free-standing layers to make a comparison with the Ni-MOF. The optimised structure of a free-standing $Co_3(HITP)_2$ layer is shown in Fig. 5.7a. It has a lattice constant of 21.90 Å, the same value as the $Ni_3(HITP)_2$ cell. The difference between $Ni_3(HITP)_2$ and $Co_3(HITP)_2$ is that the $Co_3(HITP)_2$ layer has a magnetic moment of 3.0 μ_B per cell, which is mainly contributed by Co atoms (0.84 μ_B per atom). Whereas there is no magnetic moment in $Ni_3(HITP)_2$ MOF. As shown in Fig. 5.7, the DOS and PDOS plots are divided into spin-up and spin-down channels, where the Co atoms behave quite differently. Similar to the Ni-case, the states near the Fermi level are mainly contributed by the p_z orbitals of C/N atoms and the *d* orbitals of Co atoms, forming an extended conjugation (Fig. 5.7d).

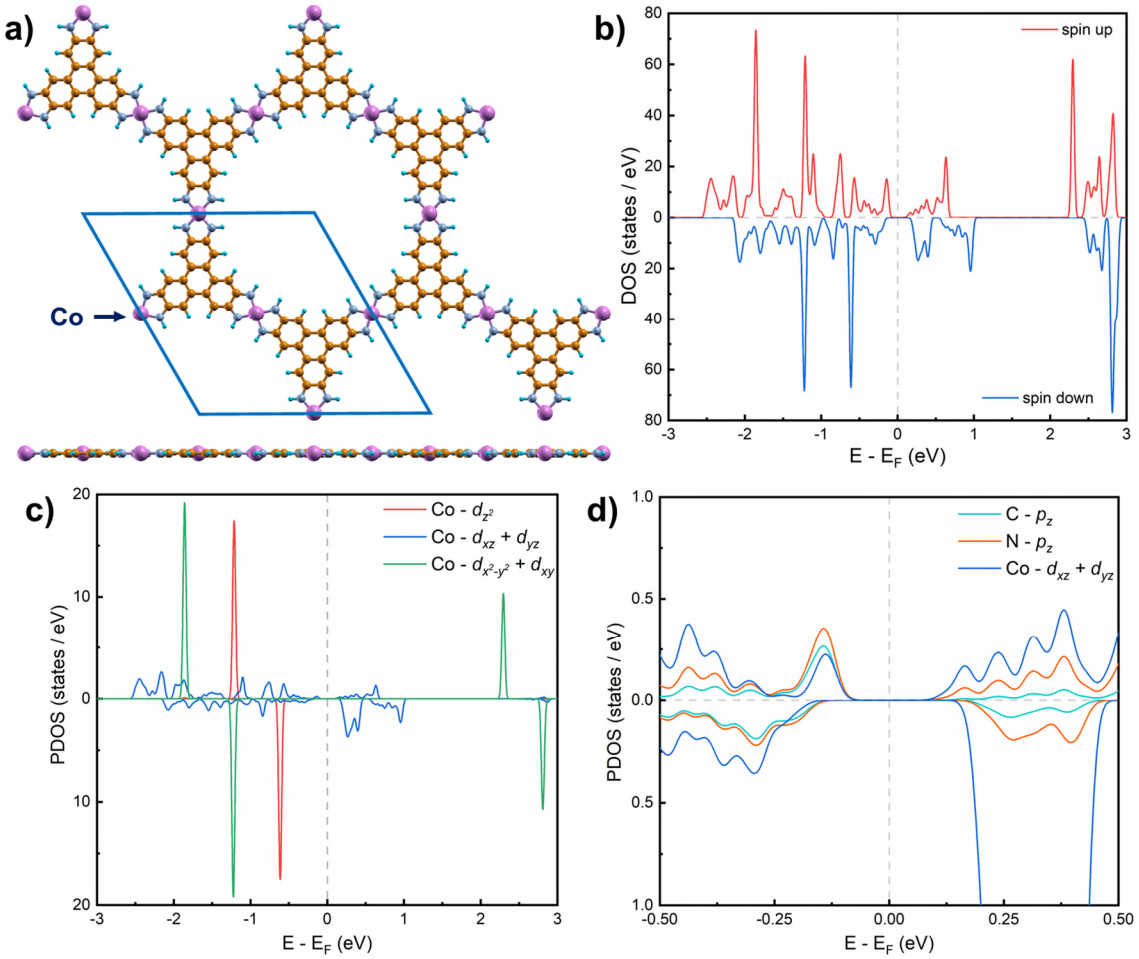


Figure 5.7: (a) DFT-relaxed structure of a free-standing $Co_3(HITP)_2$ layer. Co: purple, C: orange, N: blue-grey and H: light blue. (b) DOS plot for the $Co_3(HITP)_2$ layer. (c, d) PDOS plots for Co, C and N atoms. Top: spin up, bottom: spin down.

Co-HATP ribbons were initially grown out of the Co islands and seemed to preferentially locate on the fcc-terminated parts of the $(22 \times \sqrt{3})$ reconstruction, as shown in Fig 5.8a. This preferential adsorption effect might drive the Co-MOF to form elongated ribbons aligned with the herringbones (Fig. 5.8b). Thus, the dimension of the Co-MOF is determined by the width of the fcc regions, which limits the Co-HATP nanoribbons to widths of no more than two hexagons. I simply calculated the adsorption on an hcp-terminated Au(111) and a fcc-terminated Au(111), but there was no adsorption energy difference between these two situations. This result can be easily explained since the top layer affects the adsorption more, while the influence of deeper layers is weak and could be neglected. Further studies are needed to investigate the growth mechanism, like using a cell containing the reconstructed surface.

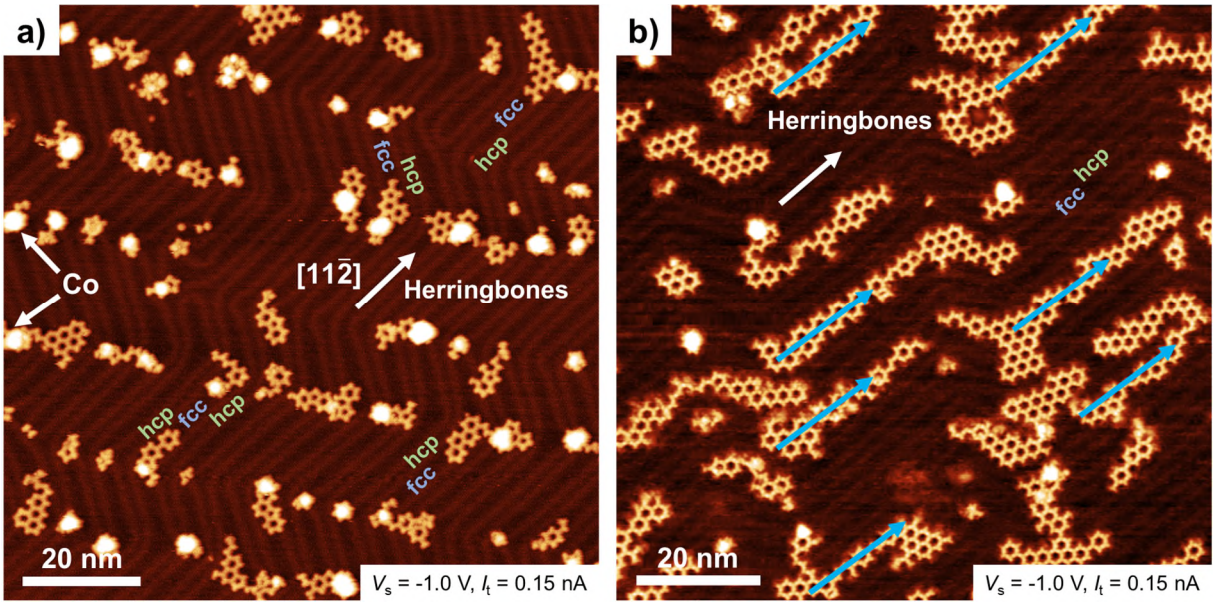


Figure 5.8 The relationship between Co-HATP ribbons and herringbones. Image (a) is a single scan. Image (b) is averaged over 7 frames.

5.4 Bimetallic $Ni_xCo_{3-x}(HITP)_2$ MOF on Au(111)

There are some studies on HATP-MOFs with mixed metals showing that their properties can be modulated by mixing different metal atoms.[78-79] Considering the different morphologies of Ni- and Co-MOF on Au(111), it is interesting to investigate the mixing behaviour between them. These two metals can be mixed by sequential deposition, that is adding one metal into the framework of the other one. For example, Fig. 5.9a shows the situation where $Ni_3(HITP)_2$ MOF was prepared first, and then Co was added. When deposited onto the sample, some Co atoms landed on the $Ni_3(HITP)_2$ MOF network, appearing as bright dots, while others on the bare Au(111) surface nucleated at the elbow sites. After depositing more HATP molecules and annealing the sample, bimetallic MOFs were obtained. The shape, size and epitaxy of the bimetallic MOF resembled those of pure Ni-MOF (Fig. 5.9b, c).

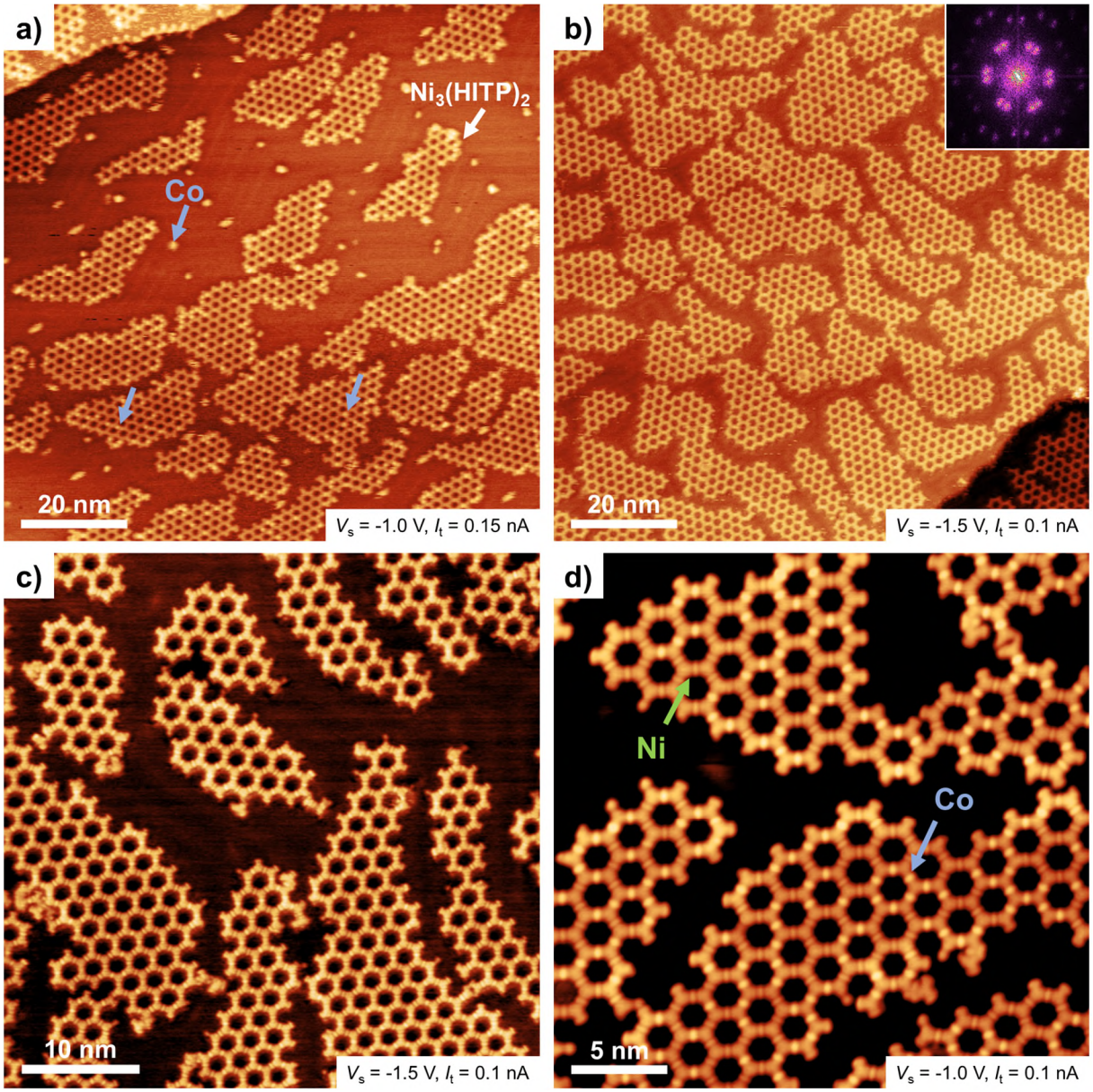


Figure 5.9: (a) Co deposited onto the substrate with $Ni_3(HITP)_2$ MOF. (b, c) STM images of the bimetallic MOF (0.7 ML). (b) inset: 2D-FFT of the STM image. (d) High-resolution STM image of the bimetallic domains, showing metal centres with different brightness. Images (a, b) are single scans. Images (c, d) are averaged over 6 and 26 frames, respectively.

The most striking part was that under certain sample biases (below -0.6 V), the metal centres in the bimetallic MOF showed different brightness, as displayed in Fig. 5.8d. According to previous results, I attribute the brighter nodes to Co atoms and those with a brightness comparable to the ligand to Ni atoms. As for the distribution of the metals, there were Co atoms both inside and outside the islands. This was caused by the deposition since some Co atoms landed on the top of the Ni-MOF and substituted the Ni atoms underneath after annealing.

Alternatively, the bimetallic MOF can also be synthesised via co-deposition of Ni and Co. Fig. 5.10 shows the evolution of the bimetallic MOF during three feeding cycles, as well as the metal distributions at each step. Comparing Fig. 5.9 and Fig. 5.10, we can see that there is no obvious difference among these domains, stating that the deposition order does not affect the morphology of the final products. Different metal centres can still be visualised from the STM images. Fig. 5.10d shows the profiles of these two metals where Co is higher than Ni and HITP. Furthermore, we can also observe that the metal distribution is random in these bimetallic MOFs, regardless of the metal dosage and ratio (Fig. 5.10a.i, b.i, and c.i). This is because the Ni- and Co-MOF have an identical structure. When forming the framework, there is no selectivity between them. These images also suggest a roughly positive correlation between the dosed Ni/Co ratio and the overall Ni/Co ratio in the well-grown MOFs, although the local deviation in adjacent domains can be high. This can inspire a phase diagram study in the future, containing a critical Ni/Co ratio for structural transformation from Ni-MOF islands to Co-MOF nanoribbons if the metal deposition can be precisely controlled.

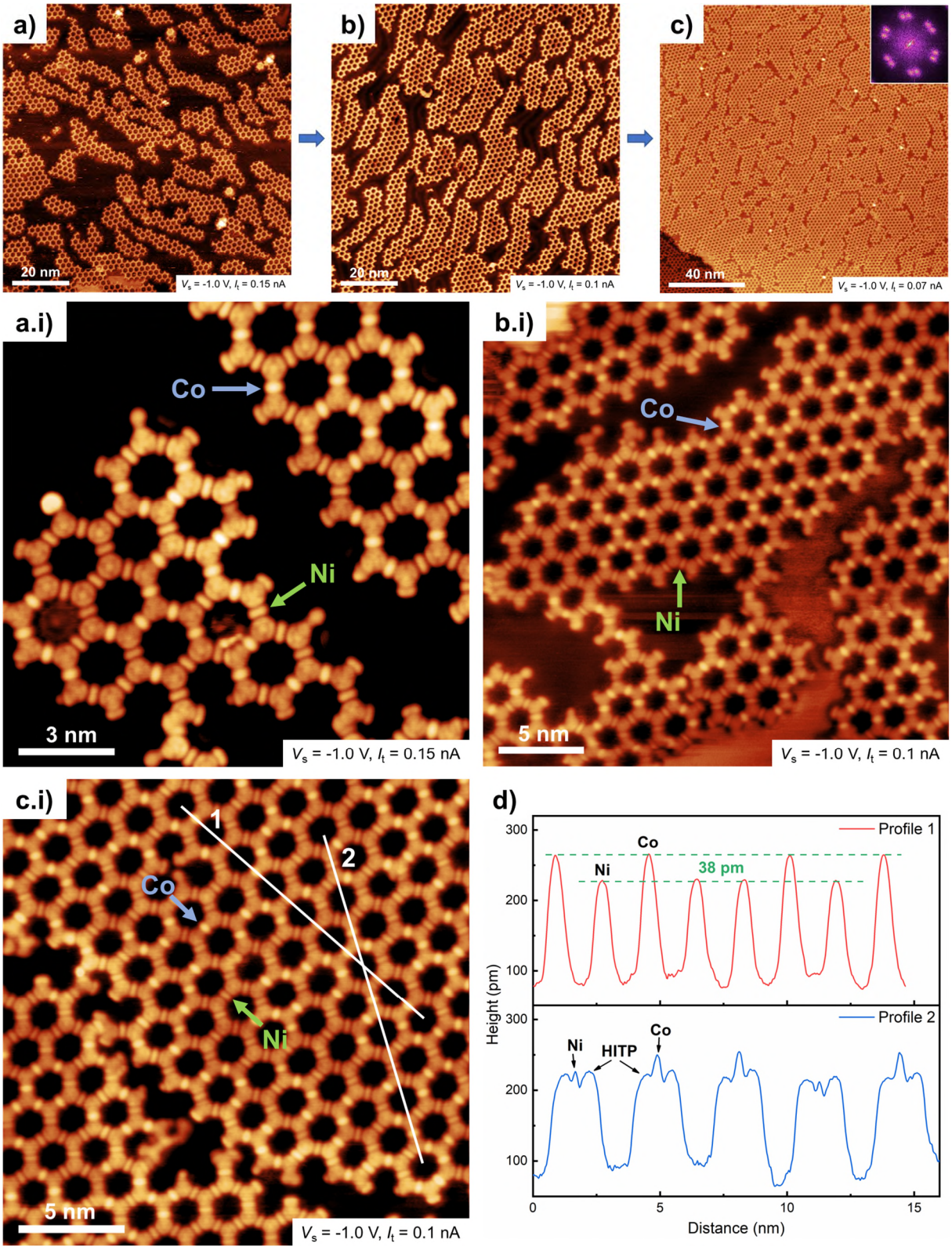


Figure 5.10: (a-c) Growth process of the $Ni_xCo_{3-x}(HITP)_2$ MOF via co-deposition of Ni and Co for three feeding cycles. Procedures for each step: depositing Ni, Co, and HATP, then post-annealing. Coverage of the MOF: (a) 0.4 ML, (b) 0.7ML, (c) 0.9 ML. Deposited amounts: (a) Ni:Co = 2:1, (b) Ni:Co = 3:1, (c) Ni:Co = 2:1. (a.i - c.i) are high-resolution STM images with identified metal centres. (d) Profiles of the two lines in (c.i). Images (b, a.i, b.i, c.i) are averaged over 7, 17, 11 and 20 frames, respectively. Images (a, c) are single scans.

To understand whether the brightness difference is caused by topographic or electronic effects, we carried out DFT calculations on this bimetallic MOF. A free-standing $Ni_2Co(HITP)_2$ layer with mixed Ni and Co is constructed in Fig. 5.11a. This cell has an optimised constant of 21.89 Å and a magnetic moment of 1.0 μ_B (Ni: 0, Co: 0.83 μ_B). These values agree well with those of previous single-metal MOFs. The DOS and PDOS plots are also displayed in Fig. 5.11b and c, where we could find that Co has a peak at around -0.6 eV but Ni does not.

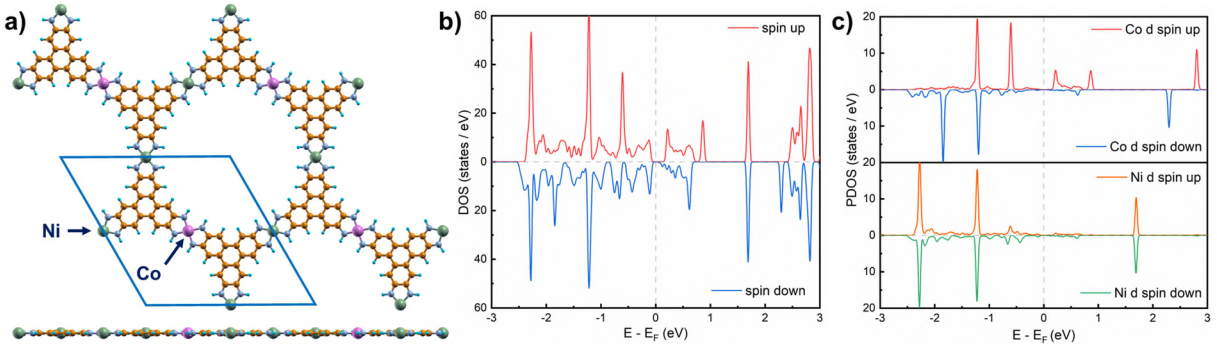


Figure 5.11: (a) DFT-relaxed structure of a free-standing $Ni_2Co(HITP)_2$ layer. Ni: green, Co: purple, C: orange, N: blue-grey and H: light blue. (b) DOS plot for the $Ni_2Co(HITP)_2$ layer. (c) PDOS plots for the *d* orbitals of Co and Ni atoms.

After adsorption on the Au(111) substrate with a $\left(\sqrt{57} \times \sqrt{57}\right)$ - R 6.6° superstructure, the optimised model in Fig. 5.12a shows that Ni atoms are located at 2.90 Å above the Au atoms, whereas the Co atom is located lower at 2.74 Å. This means that topographically the Ni atoms are 0.16 Å higher. However, in the simulated STM image (Fig. 5.12b), the Co centre appears brighter than the Ni centres at -1.0 V, consistent with the experiment results. These suggest that the brightness difference should be attributed to electronic effects instead of topography. The PDOS plots for the *d* orbitals of Ni and Co atoms are shown in Fig. 5.12c. However, the difference between these two atoms is not evident in this overall plot since both of them have states at around -1.0 eV. If we just look at the d_{z^2} orbital, which affects the STM imaging more, we can observe that the Co atom dominates the energy window from -0.6 to -1.2 eV. As a result, Co nodes become brighter than Ni nodes in this range even their heights are slightly lower.

Compared with Ni^{2+}, Co^{2+} has an unpaired electron in the unhybridized d_{z^2} orbital, which is the main contributor to the PDOS prevalence and brightness enhancement.

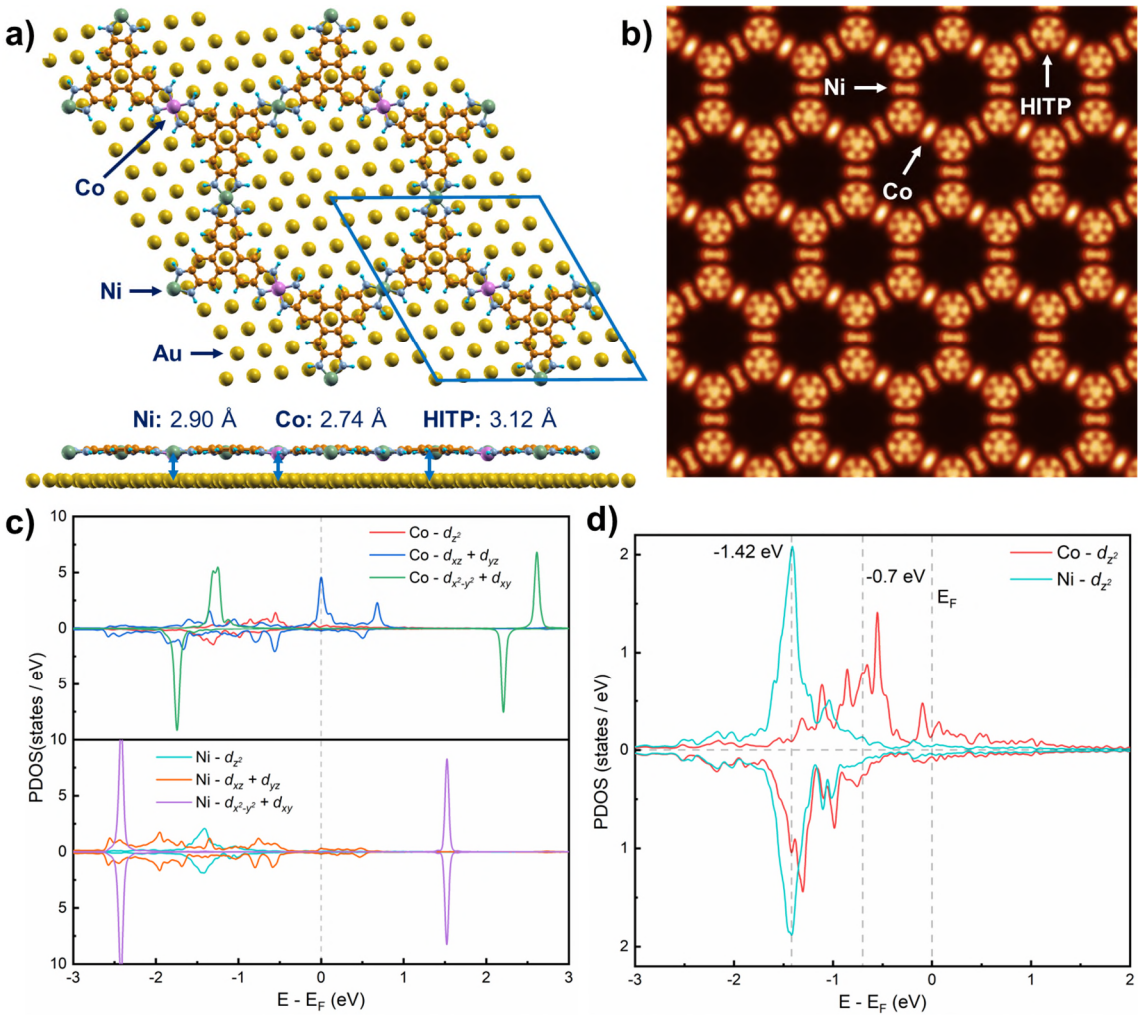


Figure 5.12: (a) DFT-optimised structure of a $Ni_2Co(HITP)_2$ layer on Au(111). Only the top-layer Au atoms are shown for clarity. Ni: green, Co: purple, C: orange, N: blue-grey, H: light blue and Au: yellow. (b) Simulated STM image at -1.0 V. (c, d) PDOS plots for Ni and Co atoms.

Fig. 5.13 contains a series of images under different sample biases, demonstrating the energy window to identify Ni and Co. When the bias is higher than -0.4 V, the metal centres almost have the same brightness. Then Co would become slightly brighter than Ni at -0.5 V, but the difference is too tiny to be observed. When the bias is lower than -0.6 V, Co atoms would be much brighter and can be easily identified from the STM images. These results agree well with the PDOS plot. This discovery provides a direct visualisation of different metals at an atomic level, which is more accurate than other characterisation techniques.

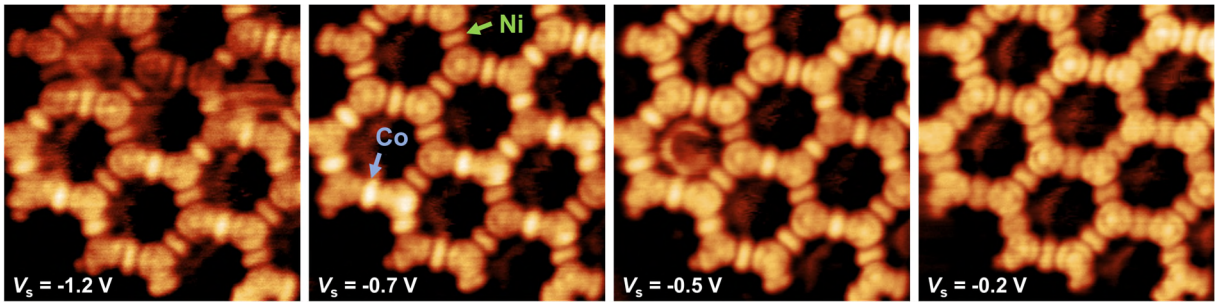


Figure 5.13: Bimetallic MOF under different sample biases. Image size: 6.05 nm × 6.05 nm. I_t = 0.15 nA. Images are averaged over 3, 6, 10 and 7 frames, respectively (left to right).

5.5 HATP-Cu complexes on Cu(111)

Due to the Au-Cu alloying problem, the reaction between ligands and Cu cannot be carried out on the Au substrate. Therefore, I used a Cu(111) substrate to conduct this experiment. Unlike the case on the Au substrate, HATP molecules can be imaged on the Cu(111) surface after deposition, as shown in Fig. 5.14a. They formed some self-assemblies as near close packing or honeycomb. The near close-packing structure was similar to the HHTP molecular phase on the Au(111) substrate, with '*head-to-head*' or '*head-to-tail*' alignments. One thing that needs to be mentioned is that HATP molecules were still mobile on the Cu surface at room temperature, as we could observe the movement of molecules and clusters during imaging. After annealing, HATP molecules reacted with the Cu substrate directly, forming complexes with hexagons and strings structures (Fig. 5.14b, c). These strings are irregular and nonperiodic, which are not suitable for further analysis.

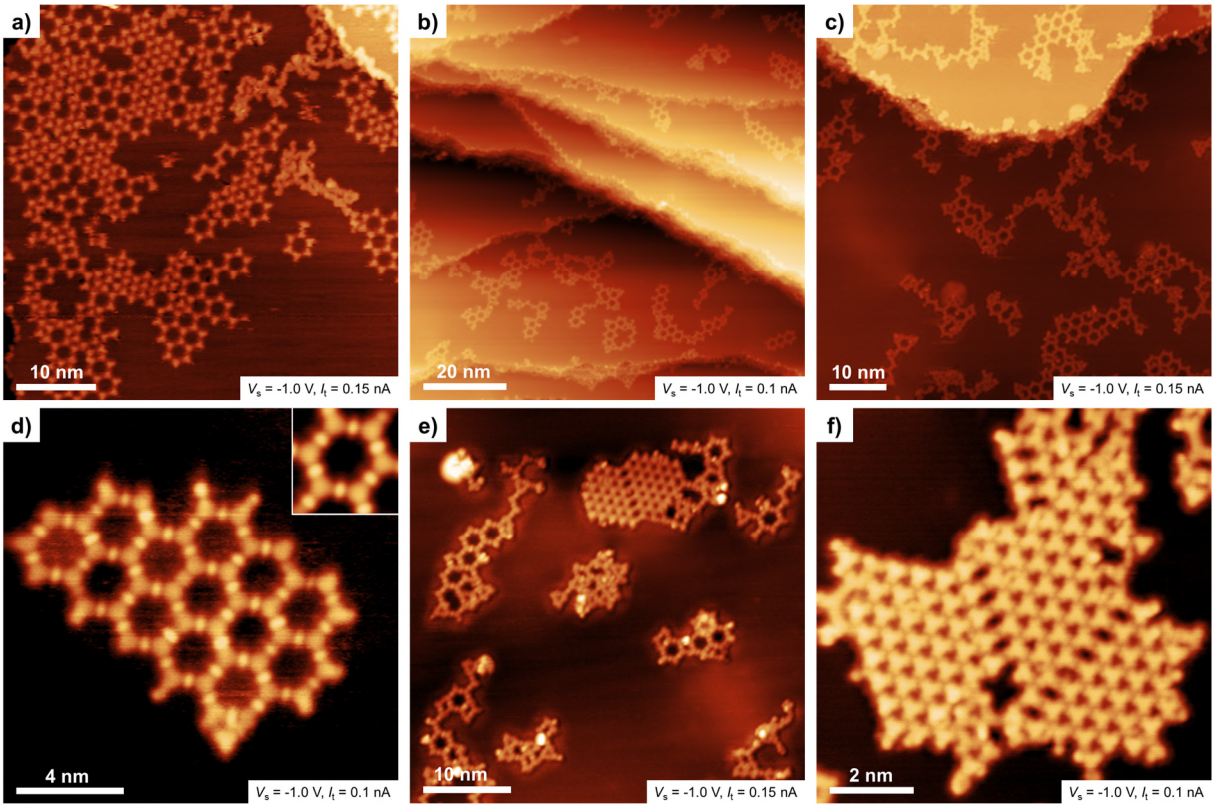


Figure 5.14: (a) HATP molecules (0.2 ML) deposited onto the Cu(111) substrate. (b, c) STM images of Cu-HATP complexes after annealing. (d) $Cu_3(HITP)_2$ MOF with honeycomb structure. Inset: averaged template. (e, f) A mixture of coordinated complexes and deprotonated molecular phase. Images (a-f) are averaged over 2, 5, 4, 15, 18 and 8 frames, respectively.

Fig. 5.14d shows a $Cu_3(HITP)_2$ MOF with a honeycomb structure. Its lattice constant is 2.10 ± 0.10 nm and the orientation is along the $[11\bar{2}]$ direction, corresponding to an epitaxial relationship of $\left(5\sqrt{3} \times 5\sqrt{3}\right)$ R 30° - Cu(111) . The problem was that the yield of this isolated honeycomb MOF was quite low, and the majority was a mixture of strings and hexagons. Except for these coordinated complexes, whose metal nodes were clear, some other structures were also discovered on the surface. For example, Fig.5.14e shows a triangular assembly coexisting with some complexes. Bright Cu centres were not found in this structure, suggesting that it could be a pure molecular phase. This phase was obtained after annealing and was obviously different from the initial molecular phase. According to previous research, this phase is assigned to deprotonated HATP molecules. Fig. 5.14f is an enlarged image of this assembly, where we can notice that the molecule's shape is not a perfect triangle. The lattice constant of

this phase is 1.24 ± 0.06 nm and the aligned direction of the molecules is along the $[11\bar{2}]$ direction. Without other characterisation techniques, like nc-AFM and XPS, the structure of this molecular phase cannot be determined just from the STM images.

5.6 Conclusion

In summary, I investigated the interactions between HATP molecules and transition metals on metal substrates using on-surface methods and demonstrated that monolayers of Ni-HATP and Co-HATP MOFs could be prepared on the Au(111) surface while Cu-HATP only formed complexes on the Cu(111) substrate. Their growth processes and structures were characterised and revealed by STM at a sub-molecular level. This knowledge can help us to understand the interactions between linkers and metals as well as the growth mechanisms of MOFs. Furthermore, the STM images also allowed direct visualisation and identification of different metal centres in the bimetallic MOF. It would benefit the interpretation of the properties of bimetallic MOFs where varying the metal ratio enables tuning their functional behaviour.

Chapter 6

Synthesis of HHB Coordination Polymers on Au(111)

6.1 Introduction

Hexa-substituted benzene (HXB) linkers are widely used in the synthesis of 2D c-MOFs. As shown in Fig. 6.1, HXB molecules can form two types of structures with transition metals: porous honeycomb frameworks (MOFs)[53-55, 58, 60] and nonporous coordination polymers (CPs)[5, 63, 111, 203]. In the framework structure, each HXB molecule coordinates with three metal atoms, while the metal number increases to six in the polymers. This structural difference makes their properties and applications distinct. For example, HXB-MOFs have been applied in battery electrodes, hydrogen evolution catalysts and supercapacitors because of their porosity, high density of redox-active sites, and excellent stability.[56, 58, 163] Polymers based on HXB exhibit much higher conductivities (up to 10^3 S/cm) than MOFs (around 10 S/cm), so they have been used in fields such as transistors and hydrogen evolution catalysis.[63, 204]

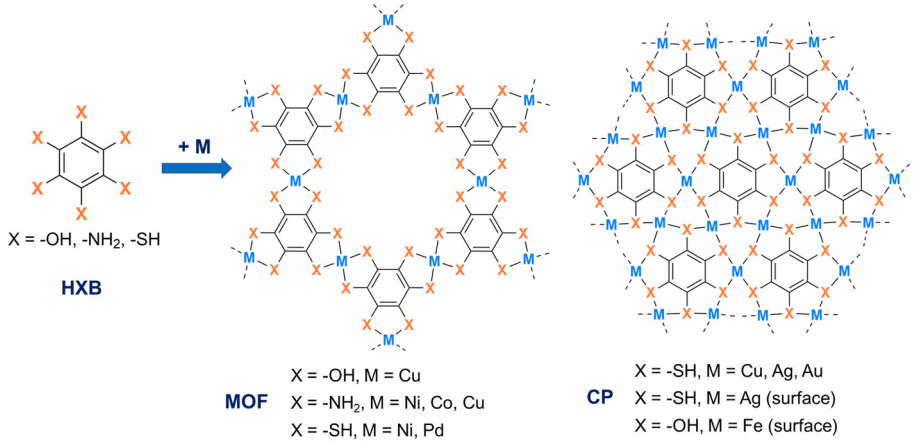


Figure 6.1: Chemical structures of HXB coordination networks.

In addition to solution-based methods, HXB ligands have also been studied in on-surface synthesis, including HHB-Cu/Fe and BHT-Ag/Cu (HHB: hexahydroxy-benzene).[156-158] All the

products obtained on the surfaces are dense polymers without any pores. This chapter focuses on the interactions between HHB molecules and Ni/Co atoms on Au(111) substrates, which have not been reported before. The growth processes and structures of the HHB-Ni/Co were characterised by STM with high resolution. The influence of different reaction conditions on the product was also investigated. After that, the emergence of vacancy defects and the synthesis of bimetallic polymers are discussed in the last section.

6.2 HHB molecular self-assembly

When HHB molecules were deposited onto a Au(111) substrate, they self-assembled into a close-packed phase (Fig. 6.2a). The preservation of Au herringbones underneath the molecular overlayer indicates weak interactions between the molecules and the Au(111) substrate. Because the molecule is a whole conjugated unit with only one aromatic ring, single atoms (C and O) cannot be identified by our STM. Therefore, the molecules still appear as discs even under high resolution (Fig. 6.2b). As marked in Fig. 6.2a, the direction of this molecular phase (the green arrow) has an angle of 11° with respect to the $[11\bar{2}]$ direction of Au(111). The unit cell is drawn by a white parallelogram with a constant of 7.4 ± 0.1 Å in Fig. 6.2b. Since the molecule-substrate interactions were weak, a simplified DFT calculation was performed on a free-standing HHB assembly. The optimised structure has a lattice constant of 7.51 Å, which is close to the measured value (Fig. 6.2b inset). In this structure, the energy per molecule is 0.93 eV lower than an isolated molecule, corresponding to the formation of intermolecular hydrogen bonds. A previous study has reported that the hydroxyl groups of HHB molecules partially dehydrogenated after adsorption on Au(111) at room temperature.[157] However, limited by the resolution, we cannot distinguish pristine and dehydrogenated molecules as both of their shapes are discs in the STM images. Moreover, HHB molecules would desorb form the Au(111) surface after annealing at a high temperature (around 170 °C).

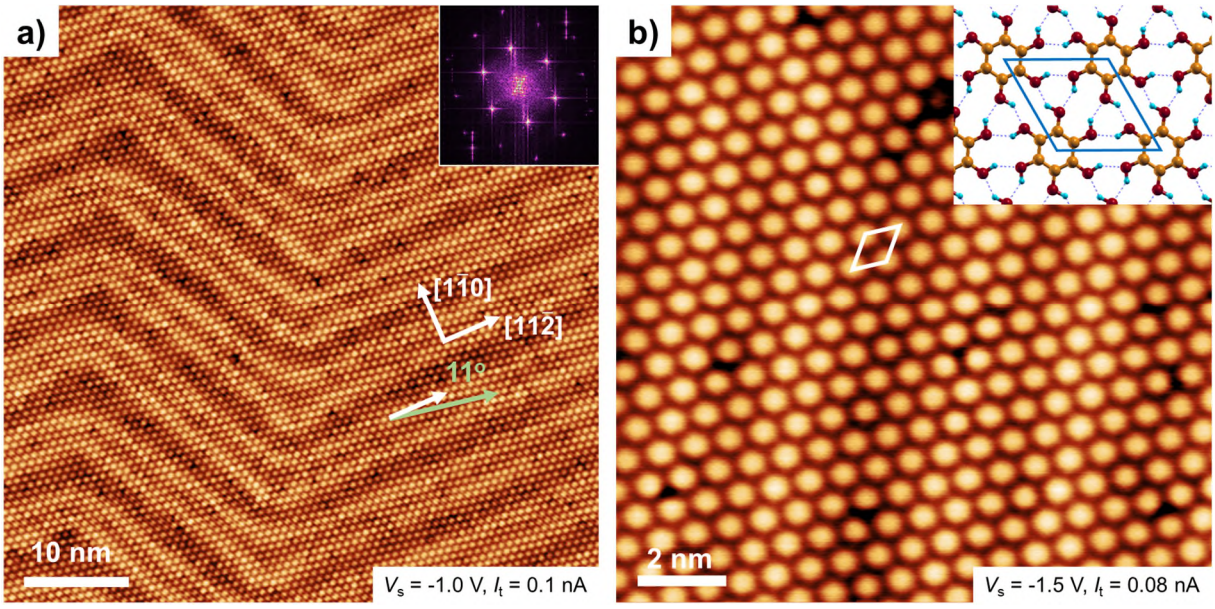


Figure 6.2: Self-assembly of HHB molecules on the Au(111) substrate at room temperature. (a) inset: 2D-FFT of the STM image. (b) inset: DFT-relaxed structure of a free-standing assembly. C: orange, O: red and H: light blue. Images (a, b) are averaged over 10 and 11 frames, respectively.

6.3 $Ni_3(HHB_{-6H})$ polymer

When Ni atoms and HHB molecules were deposited onto the substrate and then annealed at around 140 °C, they reacted with each other to form coordination polymers. This result was similar to the synthesis of HHB-Fe polymer on Au(111) published before, in which the coordination phase was obtained after annealing at 177 °C.[157] Depending on the reaction conditions, the morphology of the HHB-Ni product may change. Fig. 6.3 presents the situation where HHB molecules were deposited first, and Ni atoms were added later. As shown in Fig. 6.3a, the amount of the molecules deposited was in excess since they covered all the surface area (~1 ML). Then, Ni atoms were deposited, and they reacted directly with the molecules at this stage, shown in Fig. 6.3b. After annealing, Ni-HHB domains were obtained with shapes of small islands and narrow ribbons (Fig. 6.3c). Those molecules which did not react with Ni desorbed and the bare Au surface appeared again. When more molecules and metal atoms were deposited, the islands grew into larger networks after annealing, as displayed in Fig. 6.3d.

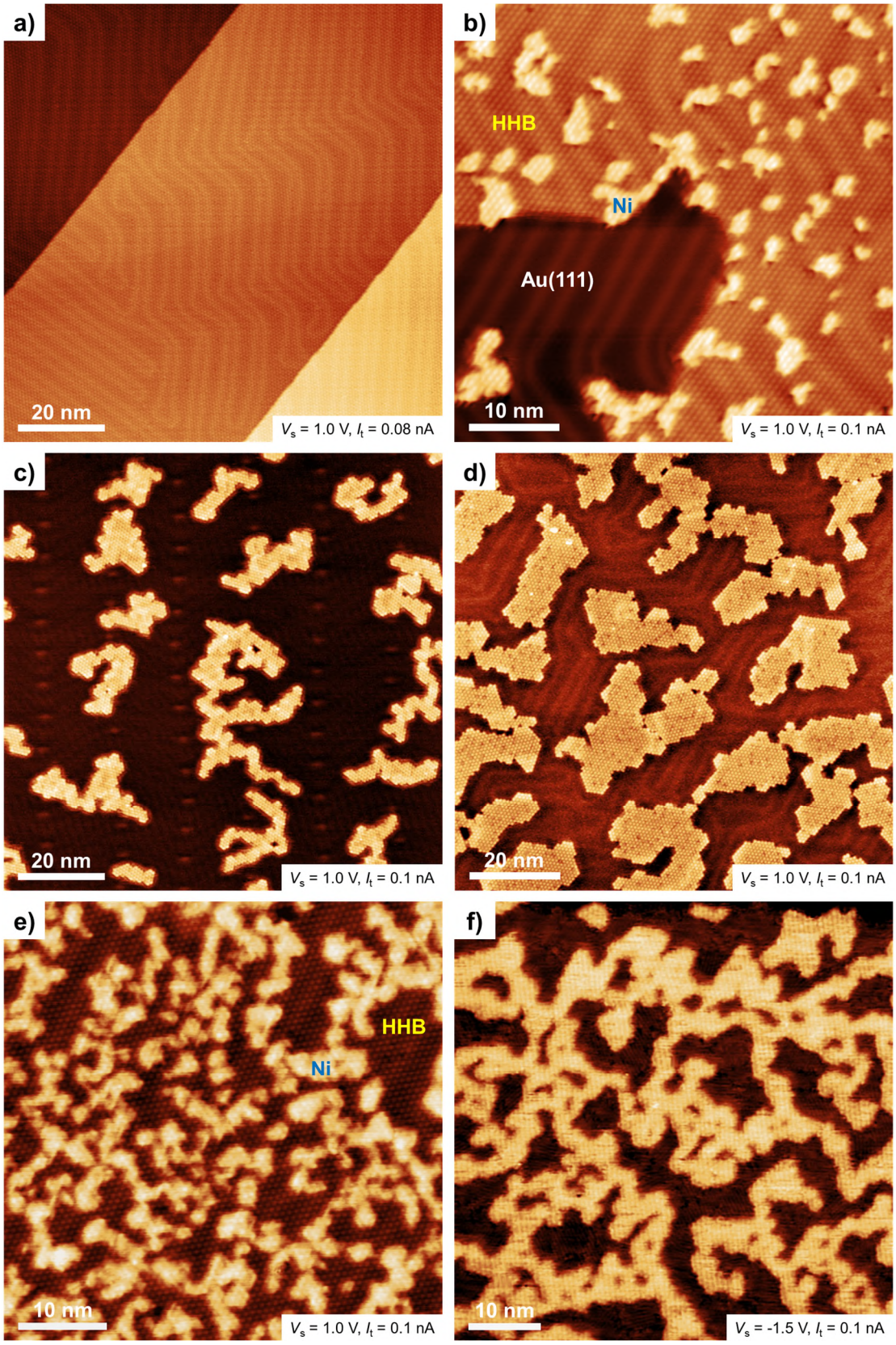


Figure 6.3: (a) HHB molecules (0.7 ML) deposited onto the Au(111) substrate. (b) Depositing Ni (0.06 ML) onto the sample with HHB. (c) Annealing the sample at 140 °C. (0.18 ML) (d) Mature domains of Ni-HHB polymers. (0.42 ML) (e) Depositing a large dosage of Ni (0.2 ML) onto the substrate pre-covered with HHB. (f) Annealing the sample at 200 °C. (0.47 ML) Images (b-e) are averaged over 10, 7, 9 and 9 frames, respectively. Images (a, f) are single scans.

By increasing the dosage of the metal, it might be possible to create large networks without depositing reactants again. However, when a large amount of metal atoms (~0.2 ML) landed on the surface and reacted with the molecules, they connected to each other and formed anisotropic ribbons (Fig. 6.3e). Post-annealing did not change their irregular shapes or uniformise the domains, as shown in Fig. 6.3f. This is because each molecule forms twelve bonds with metal atoms, making the whole system extremely stable and requiring high energy to break them. Once the bonds are formed, molecules and metal atoms are almost fixed and cannot move around. This single-dose method can still be used to generate metal-organic structures, but it may not be suitable for preparing large-network polymers.

The other order is depositing metals first and then molecules. After deposition, Ni atoms nucleated as clusters or small islands at the elbow sites of herringbones on Au(111) (Fig. 6.4a and e). Then HHB molecules were added, and it was clear that they did not react with the metal atoms at this stage (RT), as shown in Fig. 6.4b. The coordination networks were obtained after annealing, and their sizes were determined by the metal dosage (Fig. 6.4c and f). Depositing more molecules and metal atoms created larger domains with the same morphology as the product synthesised before (Fig. 6.3d). In this adding sequence, the dosage of metals did not affect the growth of polymers because Ni started to react with HHB molecules only when annealing was carried out. A slight problem with this approach was that some metal clusters would remain after annealing, especially when the dosage of Ni was high (Fig. 6.4f). Once peripheral metal atoms reacted with HHB molecules and formed stable networks, it would be difficult for internal atoms to diffuse outside as they cannot cross these obstructions. Besides, the annealing temperature was not high enough to make all the remaining Ni atoms dissolve into the Au substrate. As a result, the residual metal atoms formed bright clusters after annealing.

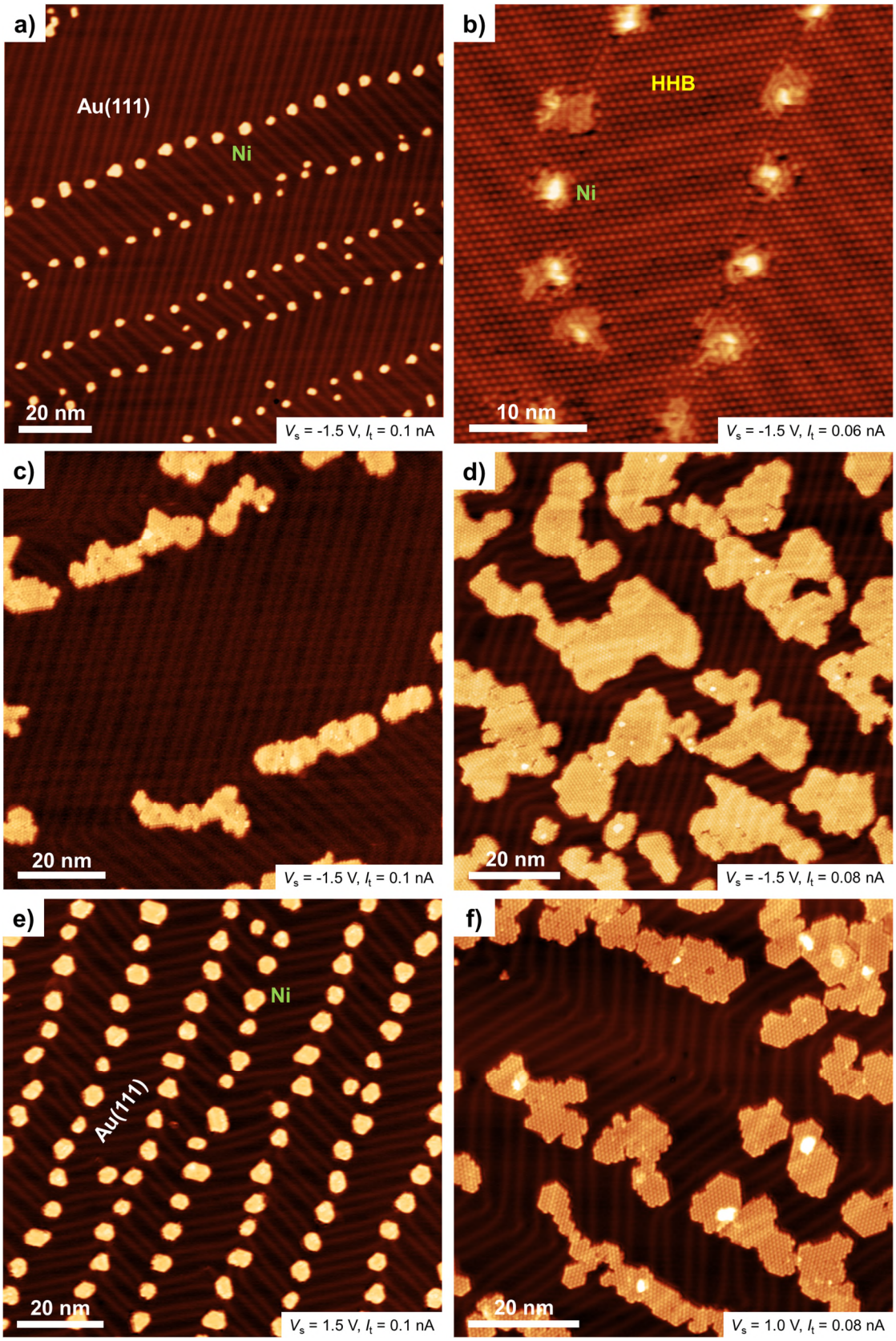


Figure 6.4: (a) Ni islands (0.05 ML) on Au(111). (b) Depositing HHB molecules (0.7 ML) onto the substrate with Ni. (c) Annealing the sample at 160 °C. (0.14 ML) (d) Adding more reactants and annealing at 160 °C. (0.42 ML) (e) Ni islands (0.16 ML) on Au(111). (f) Depositing HHB molecules (0.7 ML) and annealing the sample at 160 °C. (0.35 ML) Images (a-f) are averaged over 6, 6, 10, 11, 8 and 30 frames, respectively.

In summary, the final products synthesised by these two approaches were very similar, suggesting that the adding order did not play an important role in the synthesis. Meanwhile, multiple feeding cycles seem to be more reliable than the single-dose method. According to these findings, the best growth route should be: i) getting crystal seeds first by depositing a small amount of metals and sufficient molecules and annealing at around 160 °C; ii) adding more molecules and metals as well as post-annealing to let the seeds grow, and this step can be repeated until reaching the desired coverage. The adding sequence of metals and molecules can be switched for these two procedures, but the metal amount needs to be precisely controlled.

Although the polymers were synthesised on the Au(111) substrate, the coalescence between two neighbouring islands was not perfect (Fig. 6.5a). The 2D-FFT of the STM image reveals that the Ni-polymer exhibits two lattice orientations. This misorientation makes islands with different directions difficult to merge with each other because they need to rotate for some angles. Even when they have the same orientation, the translation of networks is also a problem for connecting. In Fig. 6.5b, the directions of the islands are drawn by the arrows, which are ±19° relative to the $[10\bar{1}]$ directions of Au(111). The unit cell of this $Ni_3(HHB_{\text{-}6H})$ polymer has a lattice constant of 7.7 ± 0.2 Å, slightly larger than the molecular phase. These features correspond to an epitaxial relationship of $\left(\sqrt{7} \times \sqrt{7}\right)$ R 19° - Au(111), the same as the reported $Fe_3(HHB_{\text{-}6H})$ polymer.[157] When reaching high resolution, it can be noticed that the molecules have three kinds of shapes: a disc shape for hydrogen-bonded molecules, a donut shape for fully coordinated ones (white circle in Fig. 6.5c), and a hamburger shape for those at domain boundaries or vacancy defects (green circle). Fig. 6.5d is an image of the $Ni_3(HHB_{\text{-}6H})$ polymer with sub-molecular resolution, clearly showing fully and partially coordinated molecules as well as Ni atoms. Fig. 6.5 e and f are two images of the same area under different sample biases, where Ni atoms appear as round dots at 0.5 V and then the shape changes to ovals at -0.5 V.

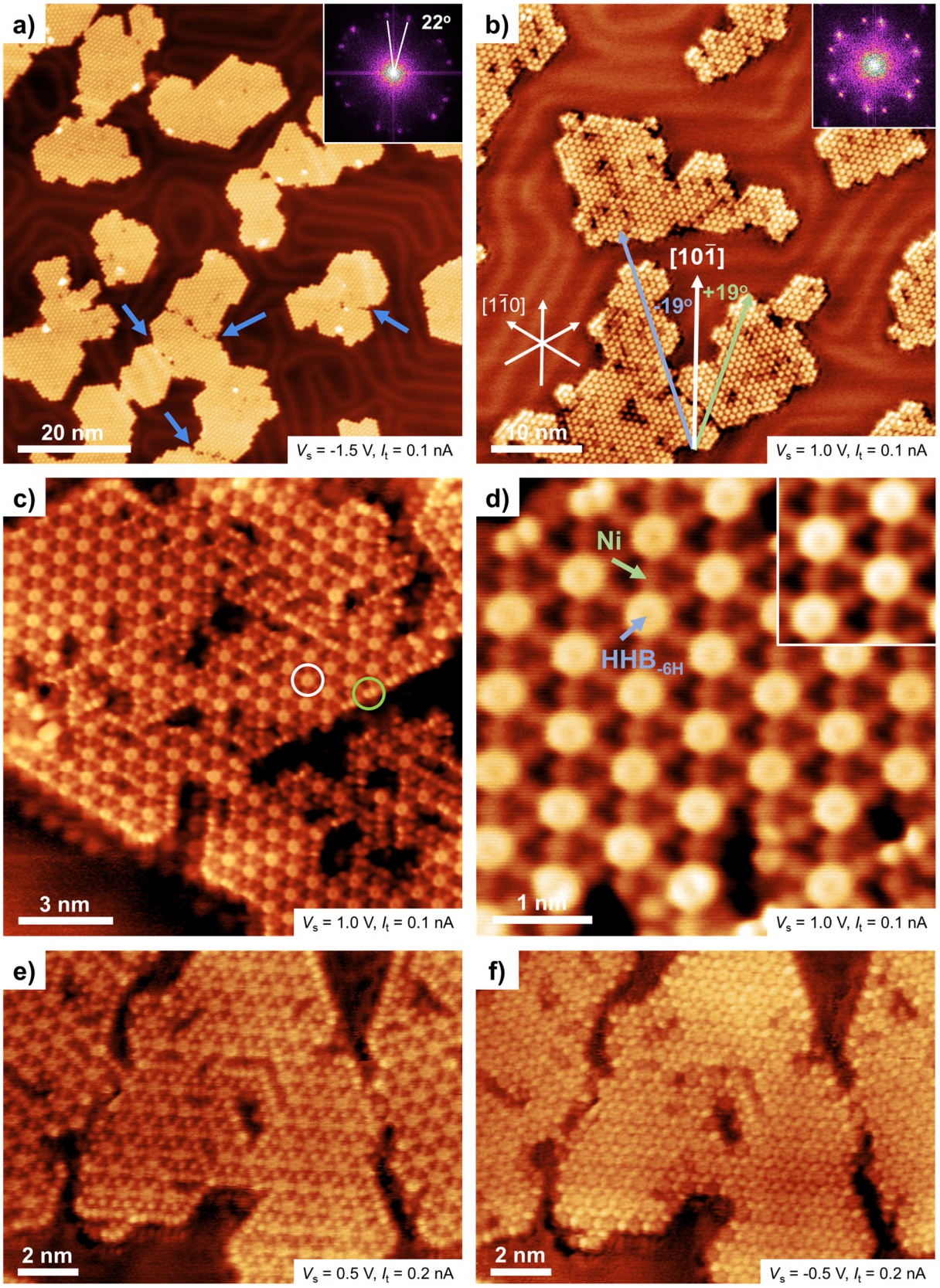


Figure 6.5: (a, b) Two orientations of $Ni_3(HHB_{-6H})$ domains. Inset: 2D-FFT of the STM image. (c, d) High-resolution STM images of the $Ni_3(HHB_{-6H})$ network. (d) inset: an averaged template for the $Ni_3(HHB_{-6H})$ unit cell. (e-f) STM images of the same area under different sample biases. Images (a-d) are averaged over 16, 9, 9 and 30 frames, respectively. Images (e-f) are single scans.

Following experiments, DFT calculations were performed to study the properties of these M-HHB polymers. For a free-standing $Ni_3(HHB_{-6H})$ layer, its lattice constant is 7.60 Å, close to the measured value. The side view in Fig. 6.6a illustrates that the whole polymer is in the same plane without any distorted part. The spin-polarised calculation reveals that this unit cell has a magnetic moment of 4.37 μ_B where each Ni atom contributes 0.99 μ_B. The band structure in Fig. 6.6c also shows that the single-layer $Ni_3(HHB_{-6H})$ is metallic without any bandgaps.

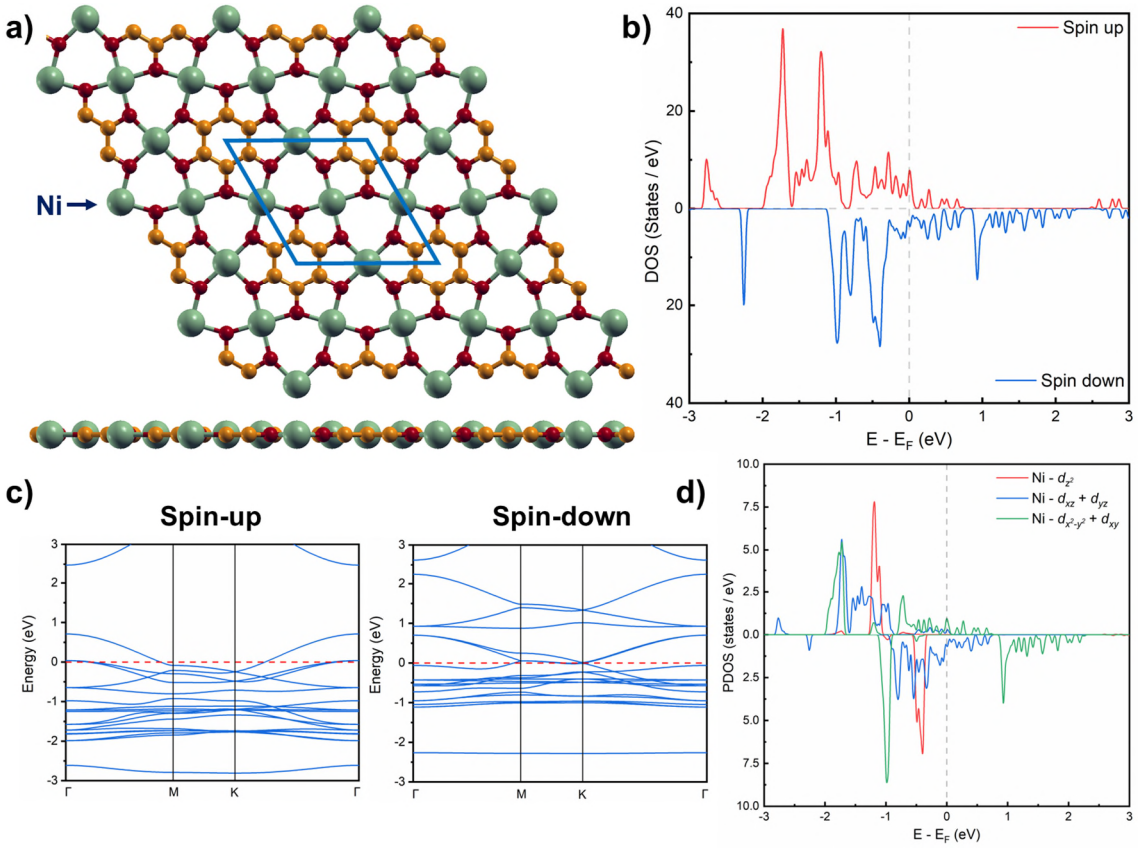


Figure 6.6: (a) DFT-relaxed structure of a free-standing $Ni_3(HHB_{-6H})$ layer. Ni: green, C: orange and O: red. (b) DOS plot for this $Ni_3(HHB_{-6H})$ layer. (c) Band structure of this $Ni_3(HHB_{-6H})$ layer. (d) PDOS plot for the *d* orbitals of Ni.

When adsorbed on the Au(111) substrate, the polymer adopts a superstructure of $\left(\sqrt{7} \times \sqrt{7}\right)$ R 19°. Fig. 6.7a is the relaxed structure of the adsorbed system, but only the first-layer Au atoms are shown for clarity. From the top view, it can be seen that each Ni atom locates at the 'bridge' site and the benzene ring is on the 'top' site of the Au(111) substrate. The distance between the molecule and the top-layer Au atoms is 3.08 Å, while the Ni atoms drop down

about 0.46 Å off the molecular plane towards the Au substrate (Ni-Au: 2.62 Å). Bader charge analysis shows that the Ni-polymer has transferred 0.11 *e* to the substrate compared with the free-standing layer. Fig. 6.7b are simulated STM images of the adsorbed system under different biases. The Ni atoms appear as ovals under negative biases and bridge lines under positive biases, matching well with the experiment images in Fig. 6.5. In the projected density of states (PDOS) plot (Fig. 6.7c), the majority of Ni-d_{z^2} states are located below the Fermi level, explaining why Ni atoms are more obvious under negative biases.

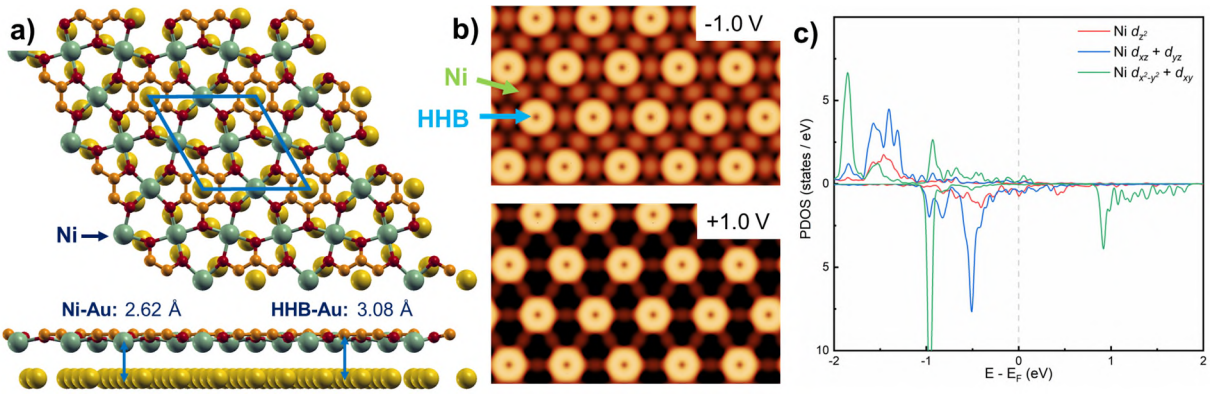


Figure 6.7: (a) DFT-relaxed structure of $Ni_3(HHB_{-6H})$ layer adsorbed on the Au(111) substrate with a supercell of $\left(\sqrt{7} \times \sqrt{7}\right)$ R19° - Au(111). Ni: green, C: orange, O: red and Au: yellow. (b) Simulated constant-current STM images under different sample biases. (c) PDOS plot for the *d* orbitals of Ni.

6.4 $Co_3(HHB_{-6H})$ polymer

The reaction between HHB molecules and Co atoms on the Au(111) substrate was also investigated. Similarly, only nonporous polymers were obtained, and the growth process is shown in Fig. 6.8a-c. The shape and size of final $Co_3(HHB_{-6H})$ networks are identical to those of $Ni_3(HHB_{-6H})$, suggesting that there is no difference among Fe, Co and Ni when reacting with HHB molecules on Au(111). If the deposition amount of Co was relatively large in the beginning, many Co crystals would remain, appearing as bright islands in Fig. 6.8d. Although Ni clusters also existed in the Ni-HHB domains, their number and sizes were much smaller.

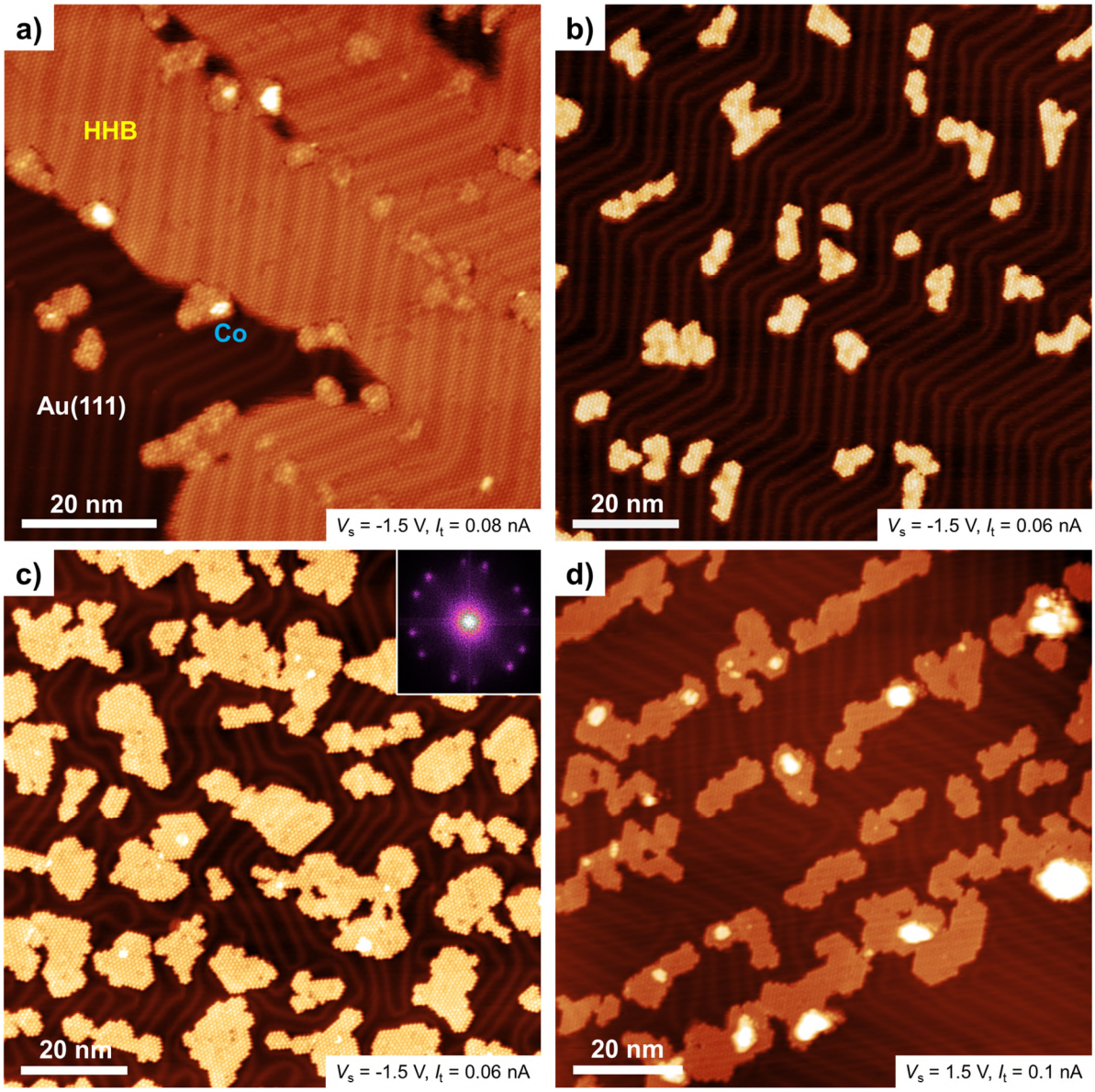


Figure 6.8: (a) Depositing HHB molecules (0.7 ML) onto the substrate with Co (0.04 ML). (b) Annealing the sample at 150°C. (0.11 ML) (c) Mature domains of $Co_3(HHB_{-6H})$. (0.4 ML) Inset: 2D-FFT of the STM image. (d) $Co_3(HHB_{-6H})$ networks with bright Co crystals. Images (a-d) are averaged over 8, 13, 13 and 8 frames, respectively.

Regarding the structure of the Co-HHB polymer, its lattice constant is 7.8 ± 0.2 Å, almost the same value as the Ni-HHB polymer. As illustrated in Fig. 6.9a, the domains also exhibit two orientations along the <21$\bar{3}$> or <12$\bar{3}$> directions of Au(111). The main difference between Ni- and Co-polymers is that Co centres are not visible in the STM images. For instance, there is nothing on the positions of Co atoms in Fig. 6.9b. As shown in Fig. 6.9 c and d, varying imaging conditions improved the resolution of the molecules but did not change the visibility of the Co

atoms. The profile in Fig. 6.9e also illustrates that there is nothing between two molecules. These findings indicate that this phenomenon was not related to electronic effects.

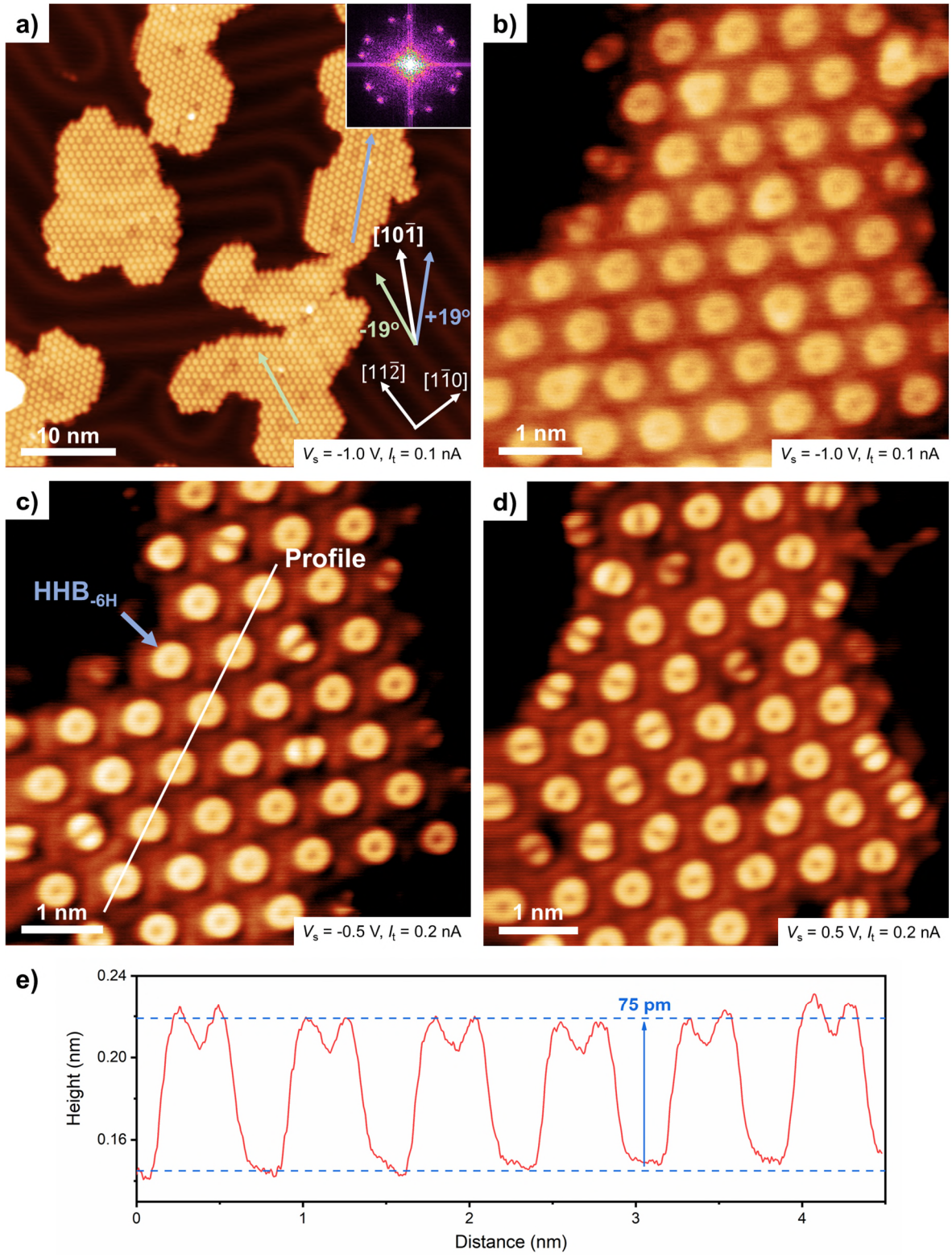


Figure 6.9: (a) $Co_3(HHB_{-6H})$ domains with two lattice orientations. Inset: 2D-FFT of the STM image. (b) A magnified image of a $Co_3(HHB_{-6H})$ network, where Co centres are not visible. (c-d) The same area under different imaging conditions. (e) Profile of the line drawn in (c). Images (a-d) are averaged over 14, 9, 18 and 20 frames, respectively.

To analyse why the Co atoms were invisible, DFT was used to model this $Co_3(HHB_{-6H})$ - Au(111) system. As shown in Fig. 6.10a, the free-standing $Co_3(HHB_{-6H})$ polymer has a planar structure with an optimised lattice constant of 7.61 Å. When adsorbed on the Au(111) substrate, Co atoms drop by 0.77 Å from the molecular backbone (HHB-Au: 3.08 Å, Co-Au: 2.31 Å). The simulated STM images in Fig. 6.10c verify that only the molecules can be observed. Although Co has many states within the energy window of -1.0 V to +1.0 V, the height drop cannot be compensated by the increase of electronic states. Ni atoms can be seen as the height difference is only 0.46 Å, but Co has a difference of 0.77 Å, much larger than Ni's. I also tested that using Ni atoms' heights to simulate the STM image of the Co-HHB polymer. As expected, Co atoms were visible in this situation, further confirming that the invisibility was a topographic effect. Besides, every Co atom has a magnetic moment of 2.35 μ_B in the adsorbed system, and the polymer layer has transferred 0.47 *e* to the Au(111) substrate.

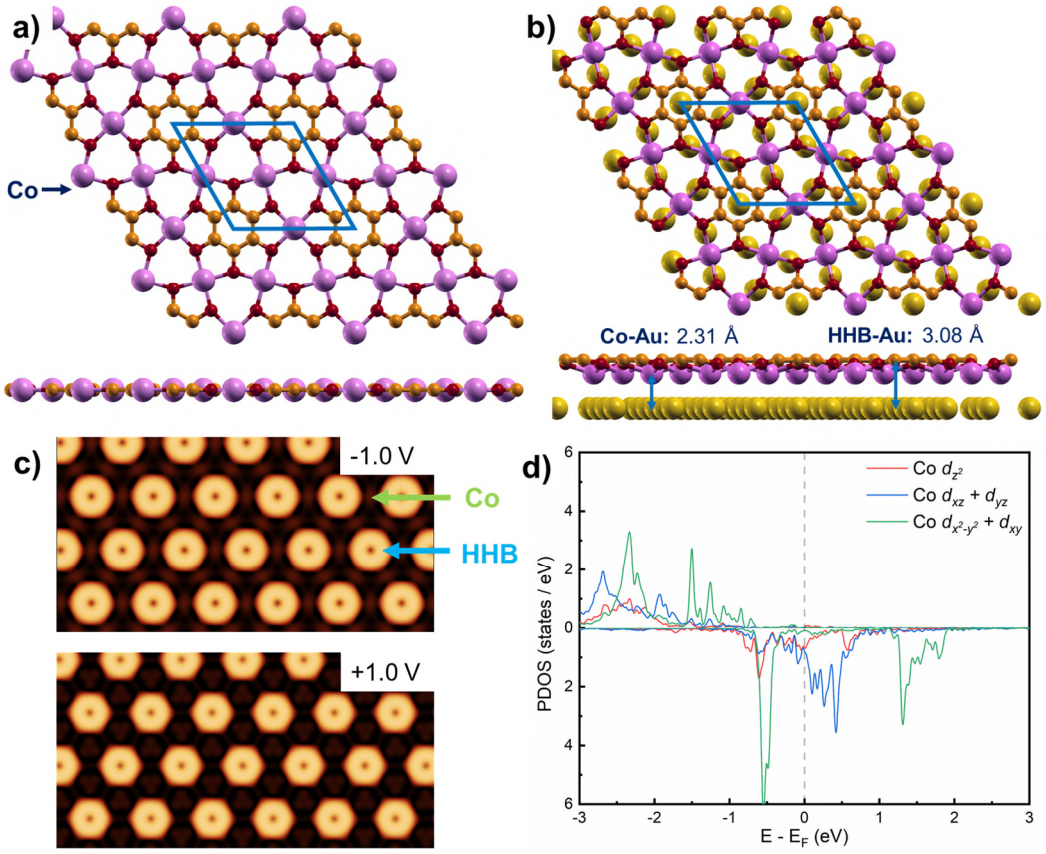


Figure 6.10: (a, b) Optimised structures of a free-standing $Co_3(HHB_{-6H})$ layer and its adsorption model on the Au(111) substrate. Co: purple, C: orange, O: red and Au: yellow. (c) Simulated constant-current STM images under different sample biases. (d) PDOS plot for the *d* orbitals of the Co atom.

6.5 Vacancy defects

The structures of all the synthesised polymers were not intact due to the existence of vacancy defects (missing metal atoms). Since these polymers are single layers, the defects might influence their stability when exfoliated from the substrate. For some applications which have a high requirement of conductivity, the electron conductivity may be limited at those vacancy areas, affecting devices' performance. Changing different reaction conditions, like the deposition order and annealing temperature (140 °C - 250 °C) did not eliminate the formation of these vacancy defects. This might be caused by the quick coordination reaction rate and the relatively slow diffusion speed of metal atoms. Before metal atoms moving to the proper position, other coordinate bonds have formed and enclosed the reaction area, causing the generation of vacancies. Finding an appropriate temperature which balances these two processes might be possible to eliminate the defects. This work could be investigated in the future with the help of in-situ characterisations.

Depending on coordination environments, the shapes of HHB molecules would change. When the HHB molecule is fully coordinated with six metal atoms, it appears as a donut (Fig. 6.5d). While the shape changes to a hamburger when there are only four metal atoms. Besides, the gap of the hamburger aligns the median of these two missing points, as shown by the dash line in Fig. 6.11a. The unique situation is that five-Ni-coordinated molecule also has the donut shape, marked by the white rectangles in Fig. 6.11b. Therefore, it seems that the coordination situation of the molecules in $M_3(HHB_{\text{-}6H})$ polymers can be estimated using these findings, especially when metal atoms are not apparent in the images. One thing needs to be mentioned is that there are some exceptions in Fig. 6.11b where the four-Ni-coordinated molecules also appear as donuts, as marked by the arrows. However, the number of these counter examples is quite limited, which does not affect the main conclusion drawn before.

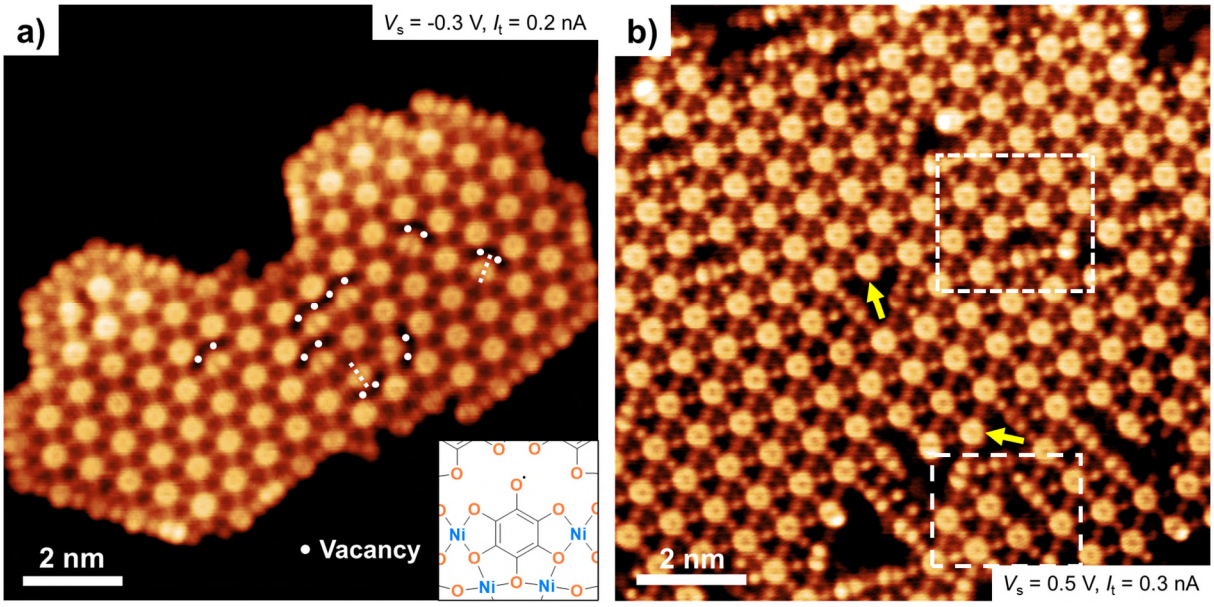


Figure 6.11: $Ni_3(HHB_{-6H})$ networks with vacancy defects. (a) inset: proposed chemical structure of the vacancy. Images (a, b) are averaged over 13 and 10 frames, respectively.

Then, a supercell with vacancies was created and calculated by DFT. The cell contains four HHB molecules: one 6-Ni-HHB, two 5-Ni-HHB and one 4-Ni-HHB. The optimised structure is shown in Fig. 6.12a, where the positions of vacancies are marked by the red dots. In the simulated STM image (Fig. 6.12b), the molecule coordinated with four Ni atoms (4-Ni-HHB) has a shape of a hamburger, while the fully coordinated molecule (6-Ni-HHB) looks like a donut. These two shapes are identical to the experiment results. For the molecule with five Ni atoms and one vacancy, its shape is very similar to a donut, but the brightness is not uniform. Such a tiny brightness difference is difficult to be distinguished in the experiments. As a consequence, the molecules with one vacancy almost have the same appearance as fully coordinated ones.

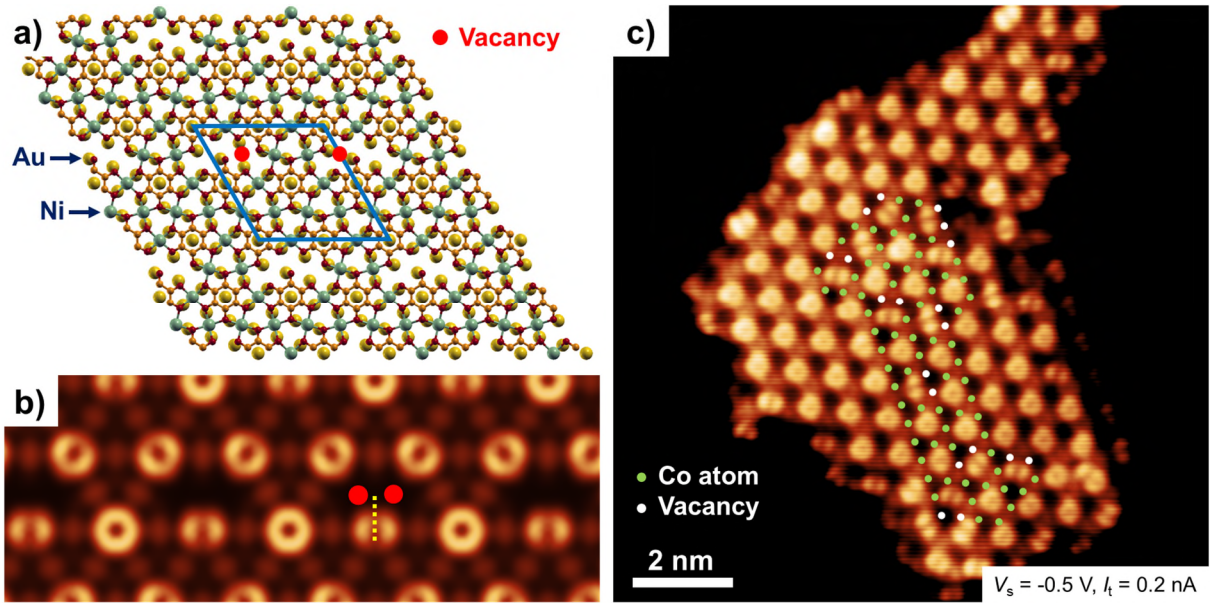


Figure 6.12: (a) DFT-relaxed structure of $Ni_3(HHB_{-6H})$ polymer with vacancies. Ni: green, C: orange, O: red and Au: yellow. (b) Simulated STM image at -1.0 V. (c) $Co_3(HHB_{-6H})$ network overlaid with some possible positions of Co atoms and vacancies. Image (c) is averaged over 16 frames.

I also tried to simulate the same cell with Co atoms to check the shapes of the molecules in Co-HHB. However, the calculation was not converged, which might be caused by the instability of this system. In Fe-HHB, Ni-HHB and Co-HHB polymers, all the molecules at the boundaries with two missing atoms appear as hamburgers, indicating that changing the metal type does not change the shape of the HHB molecules. Therefore, the rule of vacancy defects in the Ni-HHB polymer can also be used in the Co-HHB polymer.

Using this criterion, we can conjecture some possible positions of Co atoms and vacancies in $Co_3(HHB_{-6H})$ networks. As shown in Fig. 6.12c, green dots represent Co atoms and white dots correspond to vacancies. These positions are not very accurate because the vacancies are quite close or even connected. Moreover, both 5- and 6-coordination lead to the same molecular shape, making the actual environment more complicated. The estimation would be more precise when only a few isolated defects exist, like Fig. 6.11a. Nevertheless, it still provides an approach to roughly know the coordination environment of the polymers.

6.6 Bimetallic $Ni_xCo_{3-x}(HHB_{-6H})$ polymer

To systematically study this system, the synthesis of bimetallic $Ni_xCo_{3-x}(HHB_{-6H})$ polymers was also investigated, similar to the work in Chapter 5. The visibility of these two metal atoms is different, providing a possibility to identify them when mixing. Simultaneously, we can investigate whether the visibility, which is related to the atom height, is influenced by the mixing. Another factor is that Ni and Co have different magnetic moments, and mixing these two metals might be possible to modulate the magnetic properties of the polymers, which could be helpful for future application studies. The mixing was achieved by depositing metal atoms together (co-deposition) and then reacting with molecules. As shown in Fig. 6.13, the synthesis contained three feeding cycles to get more uniform domains and higher coverage. At each step, metals (Ni and Co) were deposited with the same dosage, keeping the ratio at around 1:1. Obviously, there was no morphology difference between the bimetallic and single-component polymers. The 2D-FFT in Fig. 6.13c also indicates that the bimetallic polymer follows the same epitaxy as that of Ni- or Co-polymers.

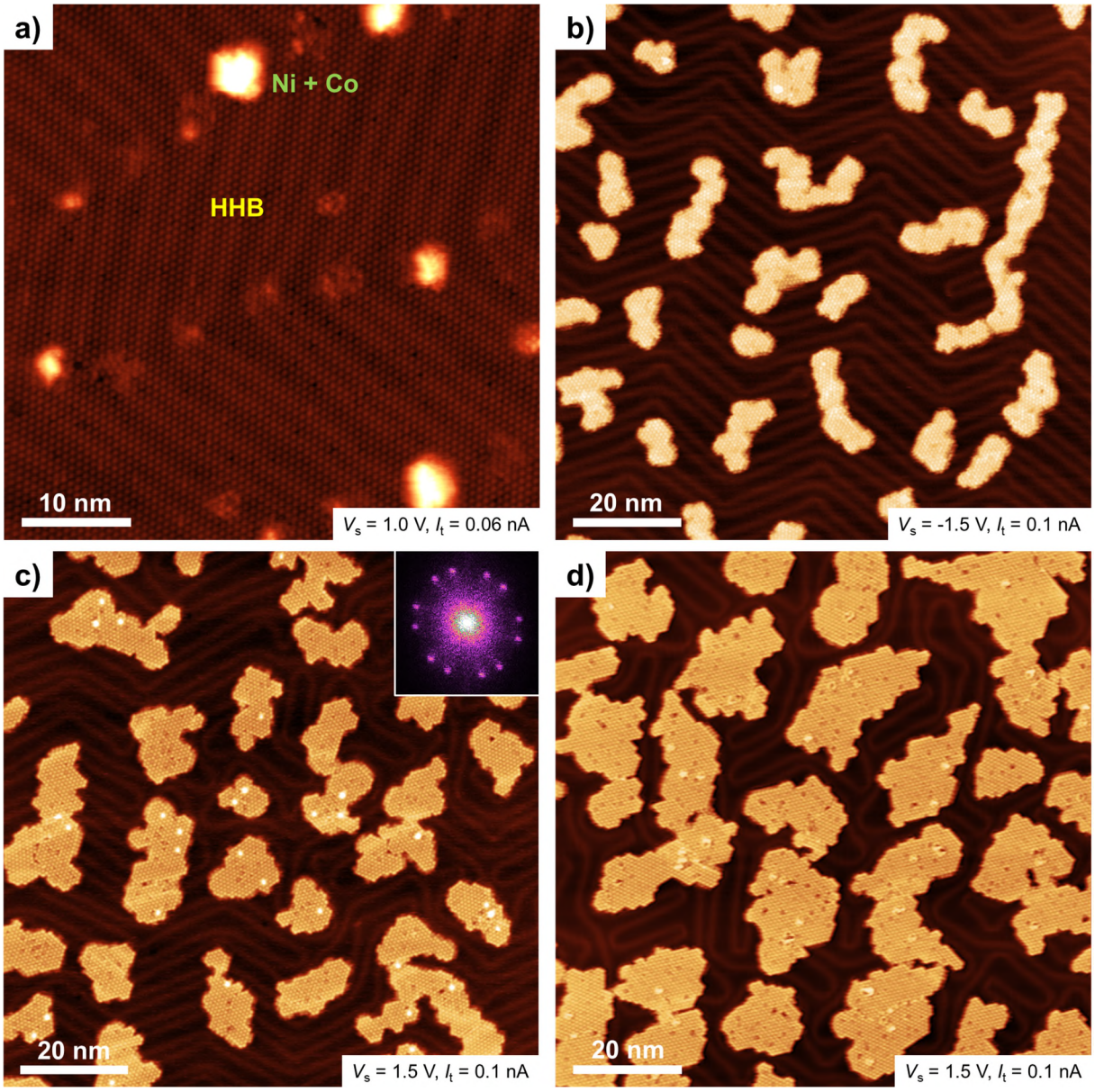


Figure 6.13: (a) Depositing HHB molecules (0.8 ML) onto the Au(111) substrate with Ni (0.03 ML) and Co (0.03 ML). (b) Annealing the sample at 220 °C. (0.18 ML) (c, d) Depositing more Ni, Co and HHB molecules, annealing at 250 °C (two cycles). (c): 0.32 ML, (d): 0.5 ML. Images (a-d) are averaged over 9, 8, 12 and 9 frames, respectively.

Fig. 6.14 shows high-resolution STM images of the bimetallic polymers. Based on the molecules' shapes, different metal atoms can be identified: visible linking bridges are Ni atoms, while other black positions should be occupied by Co atoms or vacancies. For example, the molecules in Fig. 6.14d have donuts shapes with 2 or 3 Ni bridges, which means there must be some Co atoms (blue dots) coordinated. A profile is also shown in Fig. 6.14d, which clearly illustrates the height difference of this bimetallic polymer. Although we cannot determine all

the black positions, the STM images indeed show the coexistence of two metals, demonstrating the successful synthesis of the bimetallic polymer.

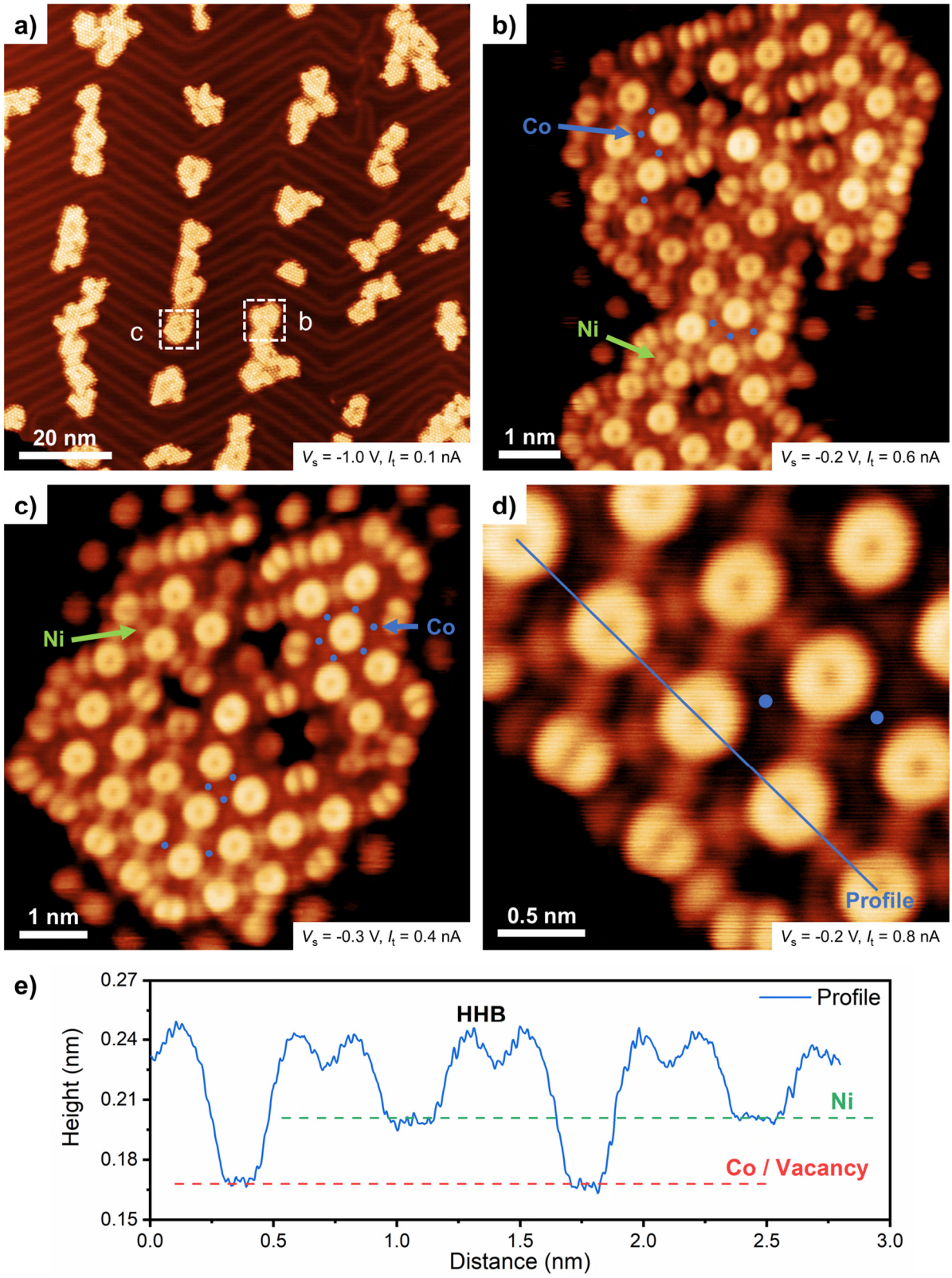


Figure 6.14: (a) Low-coverage $Ni_xCo_{3-x}(HHB_{-6H})$ polymer. (b-d) High-resolution STM images of the bimetallic polymer. (e) Profile of the line drawn in d). Images (a-d) are averaged over 12, 16, 17 and 15 frames, respectively.

After the experiments, a unit cell containing both Ni and Co atoms was constructed and modelled. The DFT optimised adsorption structure is shown in Fig. 6.15a. From the side view, it can be seen that the Co atom is lower than the Ni atoms, and the height difference is around 0.23 Å. These distance values are slightly different from those of single-component polymers, which might be caused by the breaking of the symmetry. However, the differences are less than 0.05 Å and can be neglected. Besides, the magnetic moments of Co and Ni atoms are 2.34 μ_B and 1.20 μ_B, respectively, which are almost the same value as the situation in pure Ni or Co-polymers. The simulated STM images at different biases are displayed in Fig. 6.15b, where only Ni bridges are shown, and the position of the Co atom is dark. This result agrees with both the experiment and simulation results described above.

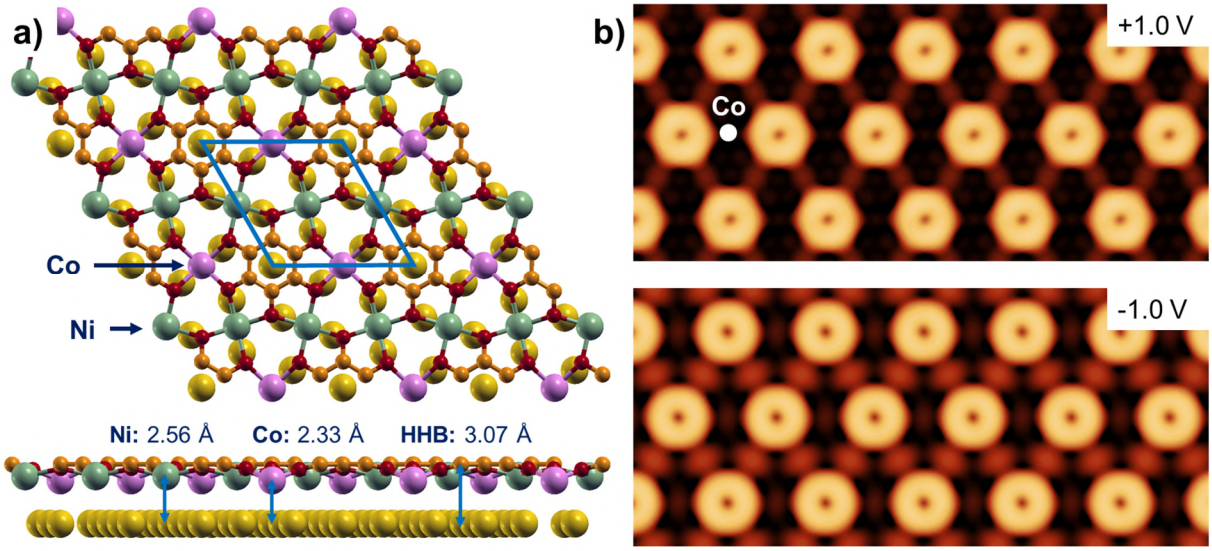


Figure 6.15: (a) Optimised structure of the $Ni_2Co(HHB_{-6H})$ bimetallic polymer adsorbed on Au(111). Ni: green, Co: purple, C: orange, O: red and Au: yellow. (b) Simulated constant-current STM images under different sample biases.

6.7 Conclusion

In conclusion, three coordination polymers based on the HHB linker were synthesised on the Au(111) surface, including Ni-HHB, Co-HHB and bimetallic Ni-Co-HHB. There was no obvious difference among these polymers in structures, shapes, and sizes. One problem was that all the synthesised networks had some vacancy defects with missing metal atoms no matter

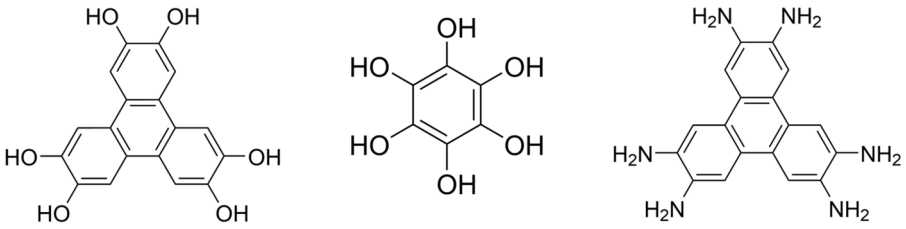
what reaction conditions were used. Combining experiment results with DFT calculations, I found a criterion which could be used to estimate the positions of metals and vacancies when they were not evident in the STM images. This project provides some details in the synthesis and structural analysis of 2D coordination polymers, which would be beneficial for future research on their properties and applications.

Chapter 7

On-surface Reactions of Mixed Ligands on Au(111)

7.1 Introduction

In addition to mixing metals, mixing ligands can also modulate the structures and properties of MOFs. Previous studies have demonstrated that it is an effective strategy to enhance the functionalities of MOFs in different areas, such as gas separation, catalysis, batteries and luminescence.[205-209] For 2D c-MOFs, a dual-ligand MOF based on mixed HHTP and THQ, Cu_3(HHTP)(THQ), has been synthesised to modulate the porosity and conductivity of MOFs.[113] It has also been reported that doping HATP into HHTP-MOF could improve the sensitivity and selectivity of gas sensors.[210] Therefore, it is necessary to explore the reactions of mixed ligands on surfaces to get a comprehensive understanding of their behaviour and to fully utilise their properties for future applications. This chapter focuses on interactions between metals and linker mixtures on the Au(111) substrate, including HHTP-HHB, HATP-HHB and HHTP-HATP. The interactions between different ligands were studied first, followed by their coordination reactions with metal atoms. According to the results in previous chapters, Ni was selected as the metal source because it had a better performance than Co in terms of acting as an intermolecular binding centre.



Schematic 7.1: Chemical structures of the ligands used in this chapter.

7.2 HHTP-HHB molecular alloy

Because HHB and HHTP molecules were visible on the Au(111) substrate, their mixture was studied first. When HHB molecules were deposited onto the substrate pre-covered with HHTP, these two molecules mixed with each other immediately and formed an assembly at room temperature. As shown in Fig. 7.1a, the surface was covered by HHB molecules and an HHTP-HHB mixture, named α-phase. The 2D Fourier transform of the STM image is shown in the inset, where the feature of pure HHB assembly is marked by the white circles and other dots correspond to the α-phase. Fig. 7.1b shows the sample after annealing at a low temperature (<100 °C), where the mixture phase became more uniform and homogenous.

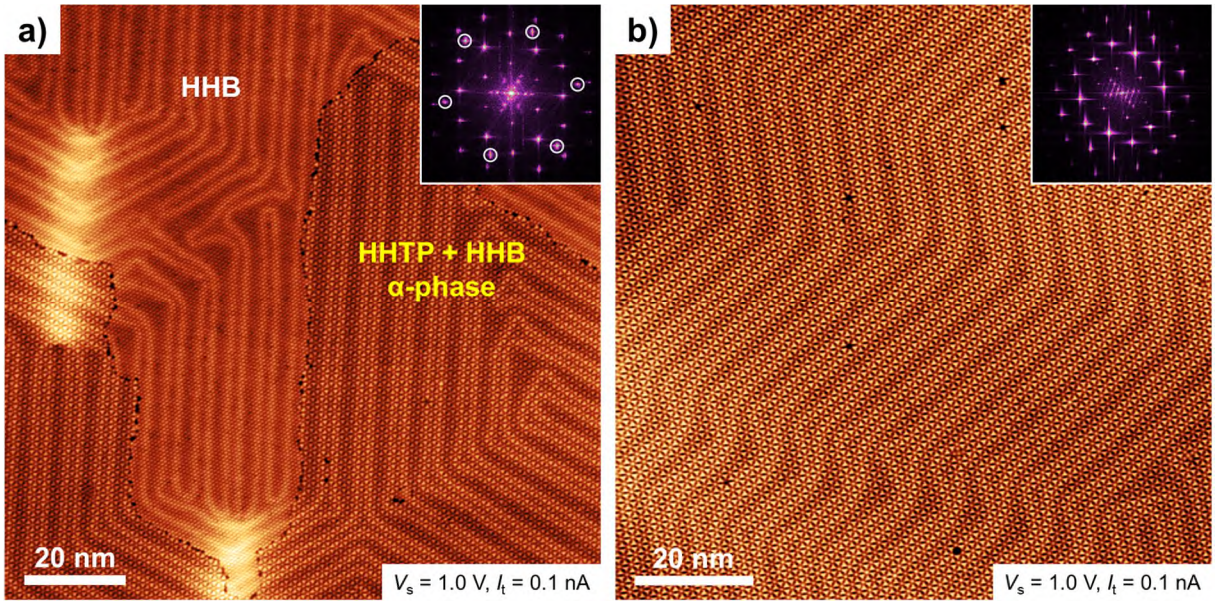


Figure 7.1: (a) Depositing HHB molecules (0.7 ML) onto the Au(111) substrate pre-covered with HHTP molecules (0.2 ML) at room temperature. (b) Annealing the sample at 80 °C. Inset: 2D Fourier transform of the STM image. Images (a, b) are averaged over 9 and 12 frames, respectively.

Under STM, HHTP molecules appear as triangles, and HHB molecules are small discs. As shown in Fig. 7.2a, each HHB is bonded with six HHTP molecules, while one HHTP molecule is connected to three HHB molecules at its vertices. The unit cell of the α-phase is drawn in the inset of Fig. 7.2a, which contains two HHTP molecules and one HHB molecule. Its lattice constant is around 1.76 ± 0.06 nm, and the direction is along the <110> directions of Au(111).

The orientation of HHTP molecules is along the [11$\bar{2}$] direction, the same as the pure HHTP assembly in Chapter 4. Fig. 7.2b is the DFT-optimised structure of a free-standing α-phase, which has a lattice constant of 17.27 Å, close to the value measured in the experiment. Due to the formation of intermolecular hydrogen bonds, the energy per cell decreases by 3.39 eV compared with isolated molecules (2 HHTP + 1 HHB). The three-centre ring-like hydrogen bonds in this phase resemble those of pure HHTP or HHB assemblies. Moreover, Fig. 7.2c shows a series of images under different sample biases, where the shapes of the molecules are almost the same in each panel.

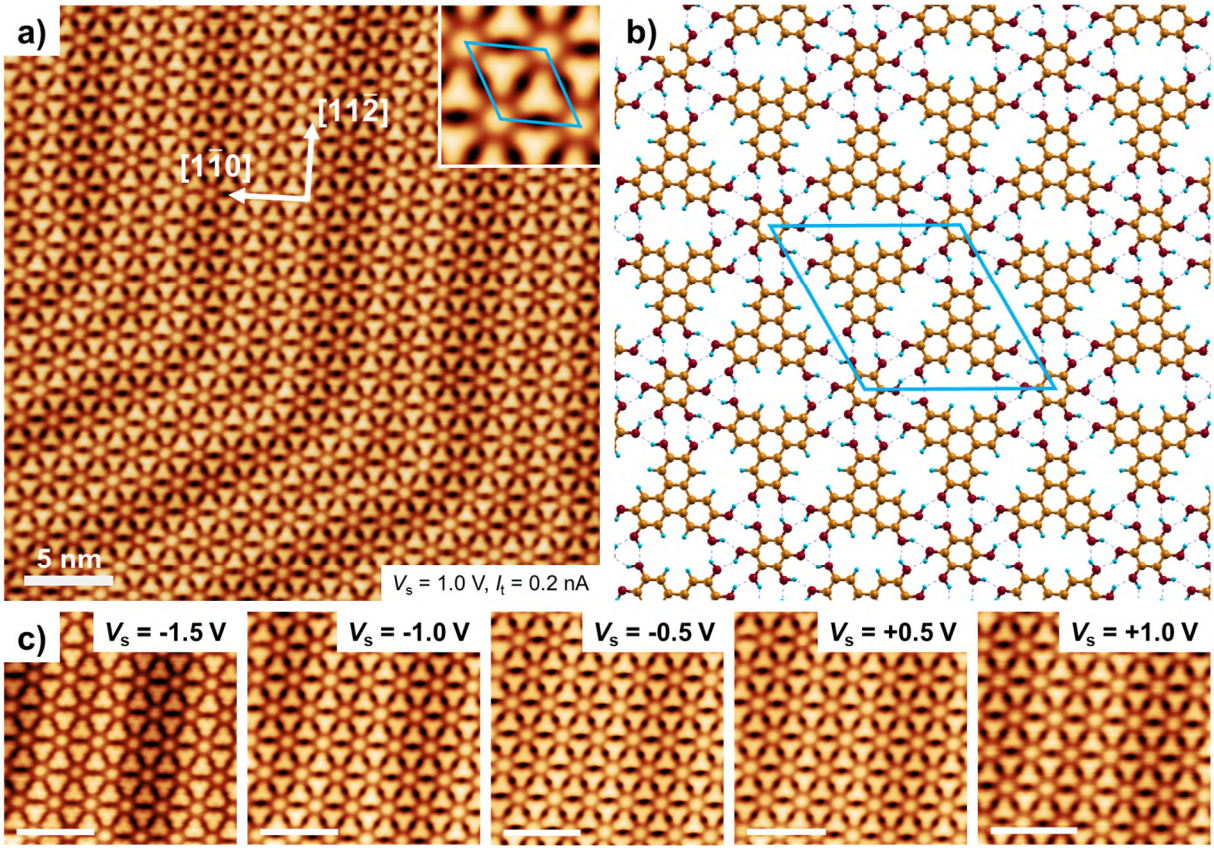


Figure 7.2: (a) A magnified image of the α-phase mixture. Inset: averaged template for the unit cell. (b) DFT-optimised structure of the free-standing mixture. C: orange, O: dark red and H: light blue. (c) The α-phase mixture at different sample biases. Scale bar: 4 nm. I_t = 0.2 nA. Image (a) is averaged over 11 frames. Images in (c) are averaged over 9, 16, 21, 15 and 14 frames, respectively (left to right).

As mentioned before, low-temperature annealing did not change the structure of the mixture. However, if the annealing temperature was increased to 150 °C (just above the evaporation temperature of HHB molecules), the mixture transformed from the α-phase to a new β-phase,

as shown in Fig. 7.3a. Because the adsorption interactions of HHB molecules are weak, they desorb from the surface during high-temperature annealing. As a comparison, HHTP molecules are highly stable on the surface and do not desorb until decomposition. Fig. 7.3b shows the structure of this HHTP-HHB β-phase, where the number of HHB molecules was apparently lower than before. In this phase, every HHB molecule is still connected to six HHTP molecules, but each HHTP molecule is bonded with only one HHB molecule. Therefore, the β-phase unit cell contains one HHB molecule and six HHTP molecules, drawn by the blue parallelogram in Fig. 7.3b. When a small amount of HHB molecules were deposited onto the sample with HHTP molecules, only the α-phase mixture and HHTP self-assembly were observed on the surface. This indicates that the β-phase mixture cannot be obtained directly by decreasing the deposition amount of HHB. Annealing the α-phase at a moderate temperature is the only approach to prepare the β-phase.

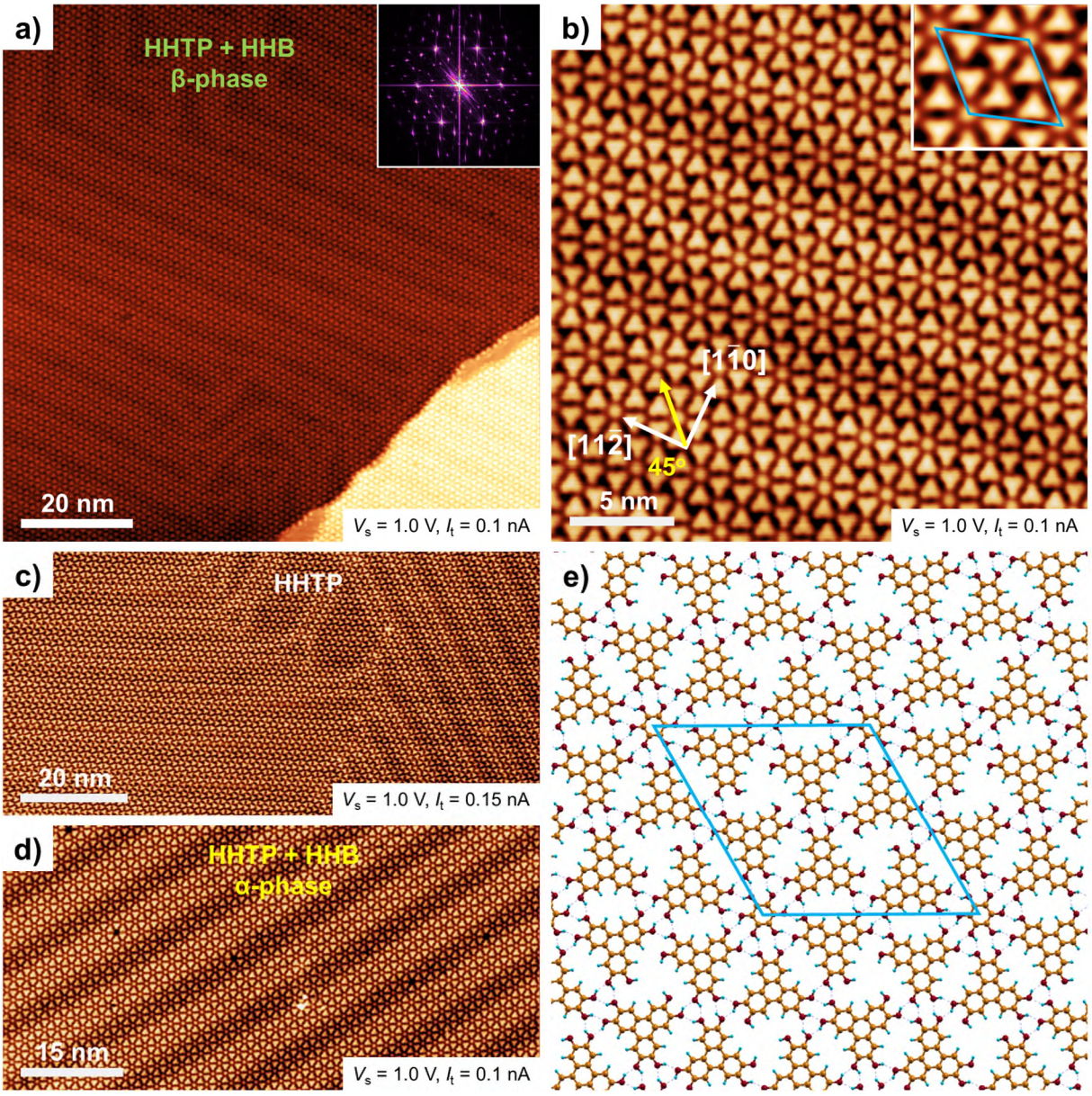


Figure 7.3: (a) HHTP-HHB β-phase transformed from the α-phase after annealing at 150 °C. Inset: 2D-FFT of the STM image. (b) A magnified image of the HHTP-HHB β-phase. Inset: averaged template for the unit cell. (c) Pure HHTP self-assembly was obtained after annealing the β-phase at 170 °C. (d) Depositing HHB molecules (0.7 ML) onto the sample in (c), the α-phase formed again. (e) DFT optimised structure for the free-standing β-phase. C: orange, O: dark red and H: light blue. Images (a-d) are averaged over 9, 17, 10 and 9 frames, respectively.

Further annealing the β-phase mixture at a higher temperature (~170 °C), all HHB molecules desorbed and only HHTP molecules were left (Fig. 7.3c). After depositing new HHB molecules onto the sample with remaining HHTP, the α-phase mixture formed again, shown in Fig. 7.3d. This cycle (HHTP – α-phase – β-phase – HHTP) can be repeated several times and does not damage the Au substrate and HHTP molecules. The unit cell of the β-phase has a lattice constant

of 2.80 ± 0.10 nm, and its orientation rotates 15° with respect to the <110> directions of Au(111) (Fig. 7.3b). The optimised structure of the free-standing β-phase is shown in Fig. 7.3e, whose lattice constant is 28.35 Å, close to the experimental value. The alignment of HHTP molecules in the β-phase is similar to that of pure HHTP assembly, having a '*head-to-head*' or '*head-to-tail*' configuration. This ensures that more hydrogen bonds can be formed to stabilise the system. Consequently, the energy per unit cell decreases by 7.05 eV compared with isolated molecules.

7.3 A dual-ligand Ni-coordination framework

After clearly knowing the mixing behaviour of these two molecules, their reaction with Ni was studied. Since the coordination complexes of close-packed HHTP molecules (β-phase) were not as organised as other linkers (Chapter 4), only the α-phase mixture was used here. Fig. 7.4a shows the situation where Ni was deposited onto the substrate covered with an HHTP-HHB α-phase mixture. After annealing, HHB-Ni polymers formed due to the excessive HHB molecules, shown in Fig. 7.4b. As for the mixture, it could be noticed that some HHB molecules were significantly brighter than others. These molecules were assumed to be Ni-coordinated since the hydrogen-bonded HHB molecules had the same brightness as HHTP molecules (Fig. 7.2c). When enlarging these areas in Fig. 7.4c, linking bridges were observed at these bright HHB molecules, while other HHB molecules were round discs without any attachments. According to the results of HHB-M polymers in Chapter 6, those bridges are likely to be Ni atoms, connecting two molecules together. Fig. 7.4d shows the boundaries between HHB-Ni polymers and HHTP molecules where the HHTP molecules are connected to the edges of the HHB-Ni islands by Ni atoms. Before reacting with Ni, all the HHTP molecules were bonded in the α-phase since the HHB molecules were in excess. The reason why these HHTP molecules did not form the coordination mixture was that HHB had a stronger coordination ability than HHTP,

and it preferred to react first. As a result, HHTP molecules were excluded from the islands and gathered at the edges. More details about the ligand activity will be discussed in the next section.

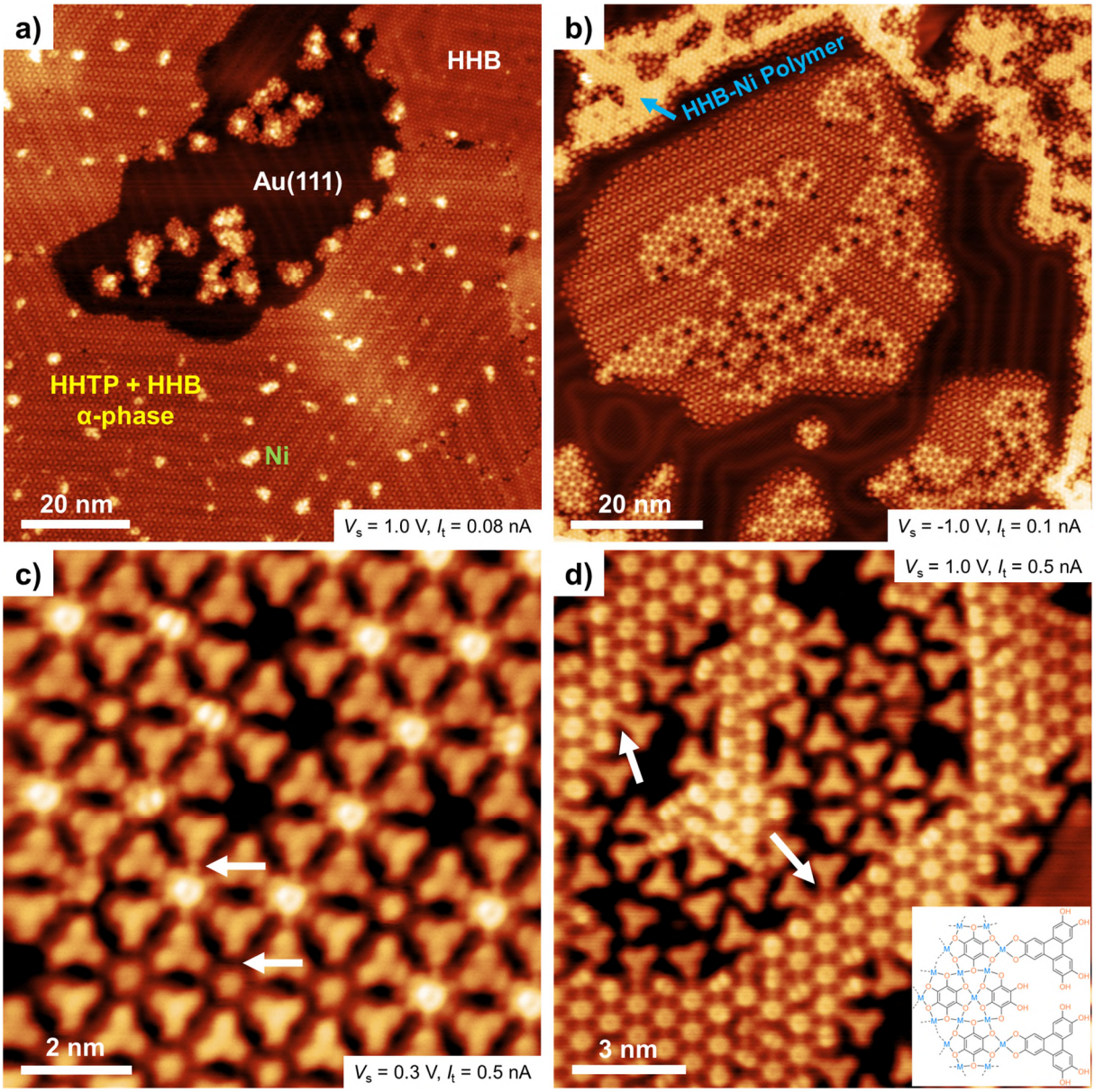


Figure 7.4: (a) Depositing Ni (0.1 ML) onto the sample with an α-phase mixture. (b) Annealing the sample at 230 °C. (c) A magnified image showing the coexistence of the hydrogen-bonded α-phase mixture and Ni-coordinated complexes. This region is the central area of (b). (d) The boundaries between HHB-Ni polymers and HHTP molecules. This image coms form another region not shown here. Inset: a proposed chemical structure. Images (a-d) are averaged over 13, 7, 15 and 11 frames, respectively.

HHTP-HHB-Ni frameworks were obtained by depositing more Ni onto the sample. As shown in Fig. 7.5a, all the HHB molecules have the same brightness, and the connection between HHTP and HHB is solid without any gap. Therefore, this domain should be the Ni-coordinated

dual-ligand framework. The lattice constant of this dual-ligand MOF is 1.75 ± 0.05 nm, and its orientation is along the <110> directions of Au(111). These parameters are similar to those of the hydrogen-bonded α-phase, indicating an epitaxial relationship of (6 × 6) - Au(111). Fig. 7.5b is an image with sub-molecular resolution, which clearly shows the positions and shapes of molecules and Ni atoms. To be more specific, the HHB molecules are slightly brighter than the HHTP molecules and appear as donuts, agreeing well with the HHB-M polymers in Chapter 6. Those small dots surrounding the HHB centres are Ni atoms. HHTP molecules in this structure have three arcs, and each arc faces a Ni atom. Based on this information, the Ni atom should adopt a four-fold coordination geometry, bonded with two oxygen atoms of the HHB molecule and two oxygen atoms of the HHTP molecule.

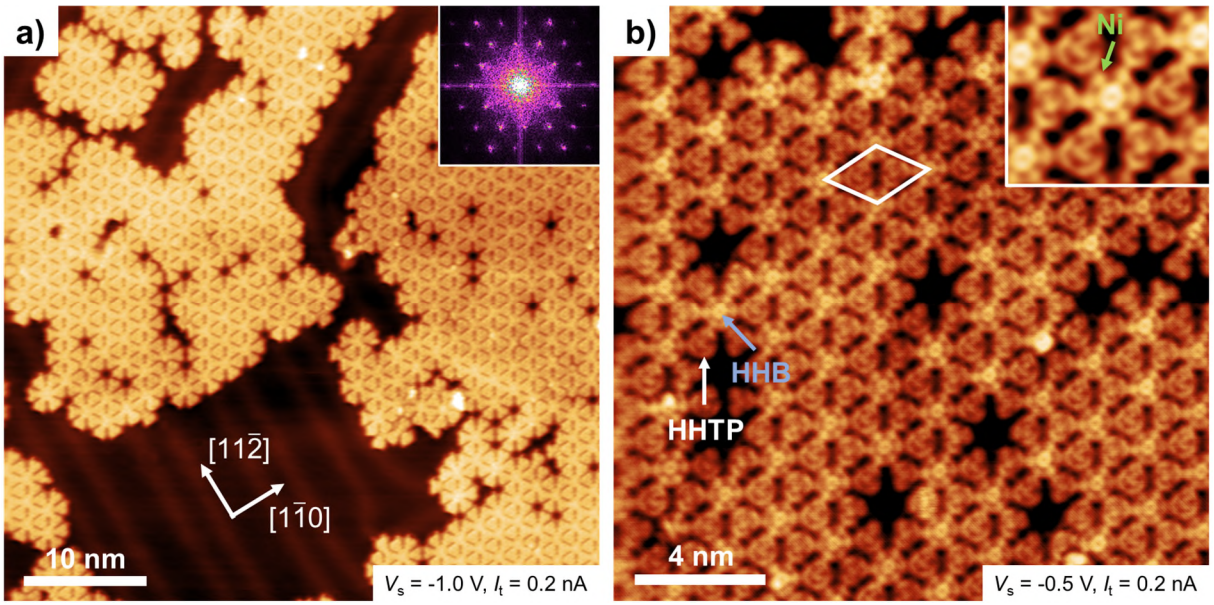


Figure 7.5: (a) HHTP-HHB-Ni coordination framework. Inset: 2D-FFT of the STM image. (b) A high-resolution STM image of the dual-ligand MOF. Inset: averaged template. Images (a, b) are averaged over 13 and 12 frames, respectively.

To verify the structural analysis, DFT calculations were performed on this system. Fig. 7.6a is the optimised structure of a free-standing MOF, which has a lattice constant of 17.23 Å. After adsorption on a (6 × 6) - Au(111) substrate, both two molecules locate at the 'top' sites, shown in Fig. 7.6b. The distance between the molecules and top-layer Au atoms is 3.05 Å while the Ni atoms drop slightly to 2.85 Å. Fig. 7.6c are simulated STM images under different sample

biases, and they match well with the experimental results. The PDOS plot in Fig. 7.6d illustrates that the peak of the Ni-d_{z^2} states locates at around -1.1 V. Therefore, the Ni atoms are more evident under negative biases due to the contribution of electronic states.

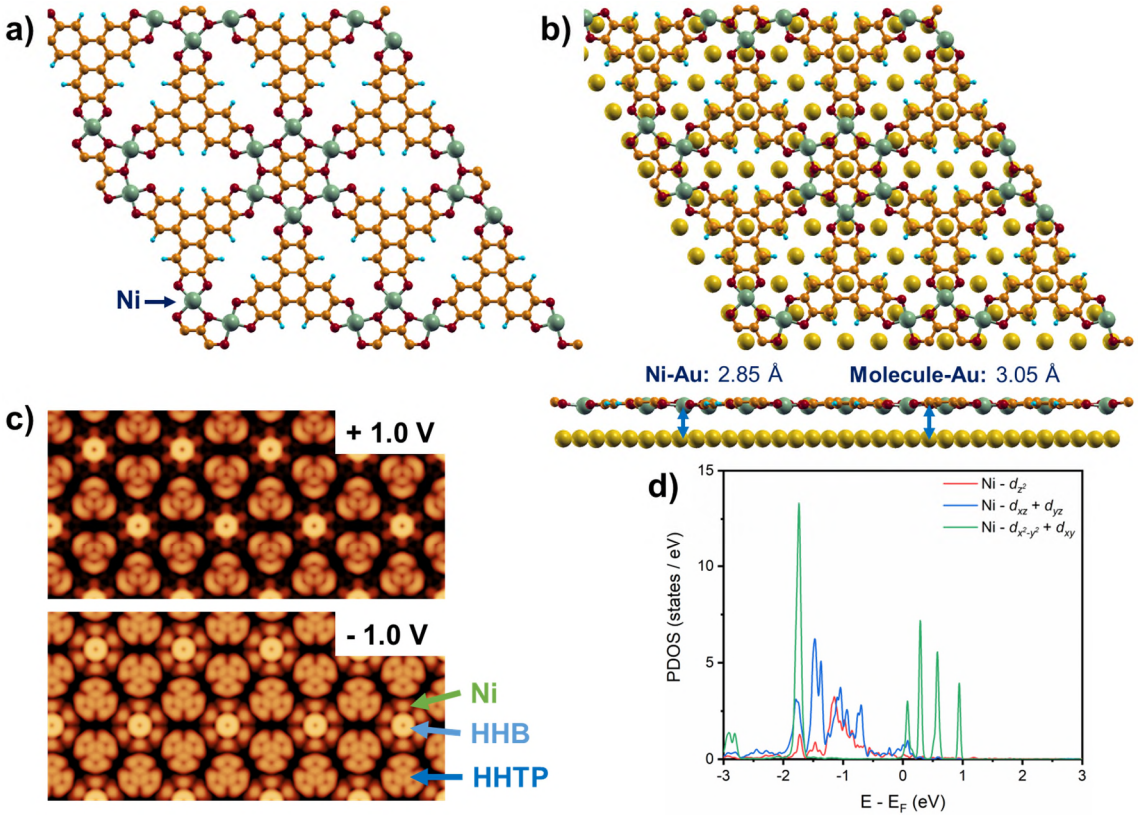


Figure 7.6: (a) DFT relaxed structure for a free-standing HHTP-HHB-Ni framework. (b) Optimised adsorption structure on the Au(111) substrate (a three-layer slab, but only the first layer is shown for clarity). C: orange, O: dark red, H: light blue, Ni: green and Au: yellow. (c) Simulated constant-current STM images at positive and negative biases. (d) PDOS plot of the Ni-*d* orbitals.

The most important thing is that this dual-ligand MOF matches well with the Au(111) substrate, and only has one orientation. All the $M_3(HITP)_2$ MOFs and $M_3(HHB)$ CPs synthesised in previous chapters had two orientations and the existence of the rotation angle made them extremely difficult to grow into continuous networks. Besides, this dual-ligand MOF is based on the α-phase mixture, which determines the size and shape of the MOF networks. The coordination reaction did not change the structure and just inserted the metal atoms into the assembly. The molecules in the hydrogen-bonded mixture can move around to meet the registry and coalesce into large assemblies. As a result, the problem of translation is avoided in this

system. If the α-phase mixture covers the whole Au terrace, the dual-ligand MOF can reach up to the same area and form an extended network. With suitable amounts of molecules and Ni atoms, a large framework was prepared in Fig. 7.7. Although there were many vacancy defects (missing HHB molecules), the domain was connected within this area. Such connection was not achieved in previous Chapters. This result demonstrates that large-scale 2D metal-organic frameworks can also be synthesised on metal surfaces.

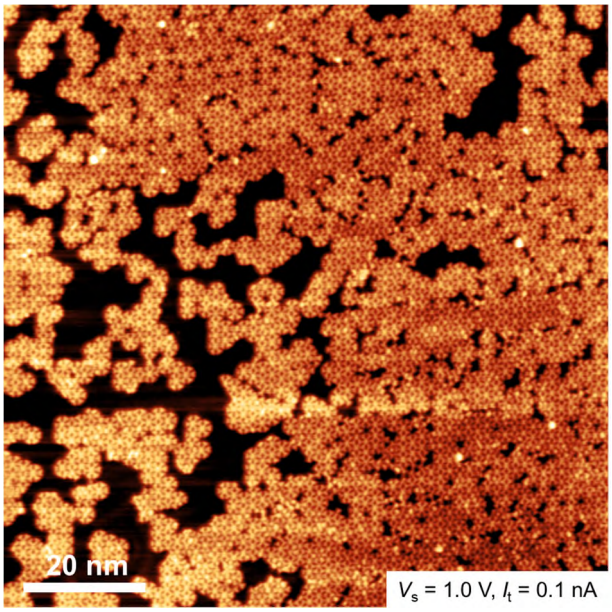


Figure 7.7: Large-scale image of the dual-ligand MOF. This image is averaged over 12 frames.

7.4 Ligand substitution reactions

When mixing HHB molecules with HATP molecules, they did not form any assembly on the Au(111) substrate. This could be ascribed to the high mobility of HATP molecules, which makes molecule-molecule interactions weak. To mix these two molecules, Ni-HHB polymers were prepared first, and then HATP molecules were deposited. In Fig. 7.8a, the triangles observed on the top of the polymers were HATP molecules and they were still moving on the islands, causing noise in the image. Fig. 7.8b shows the mixture after annealing at 160 °C. Most HATP molecules stayed on the bare Au(111) surface (invisible), while some were found to be attached to the edges of the islands. This is similar to the HHTP-Ni-HHB connection in Fig.

7.4d, where HXTP molecules are coordinated with Ni atoms at the edges. The difference is that HHTP molecules appear as triangles, but HATP molecules are closer to a 'Y' shape.

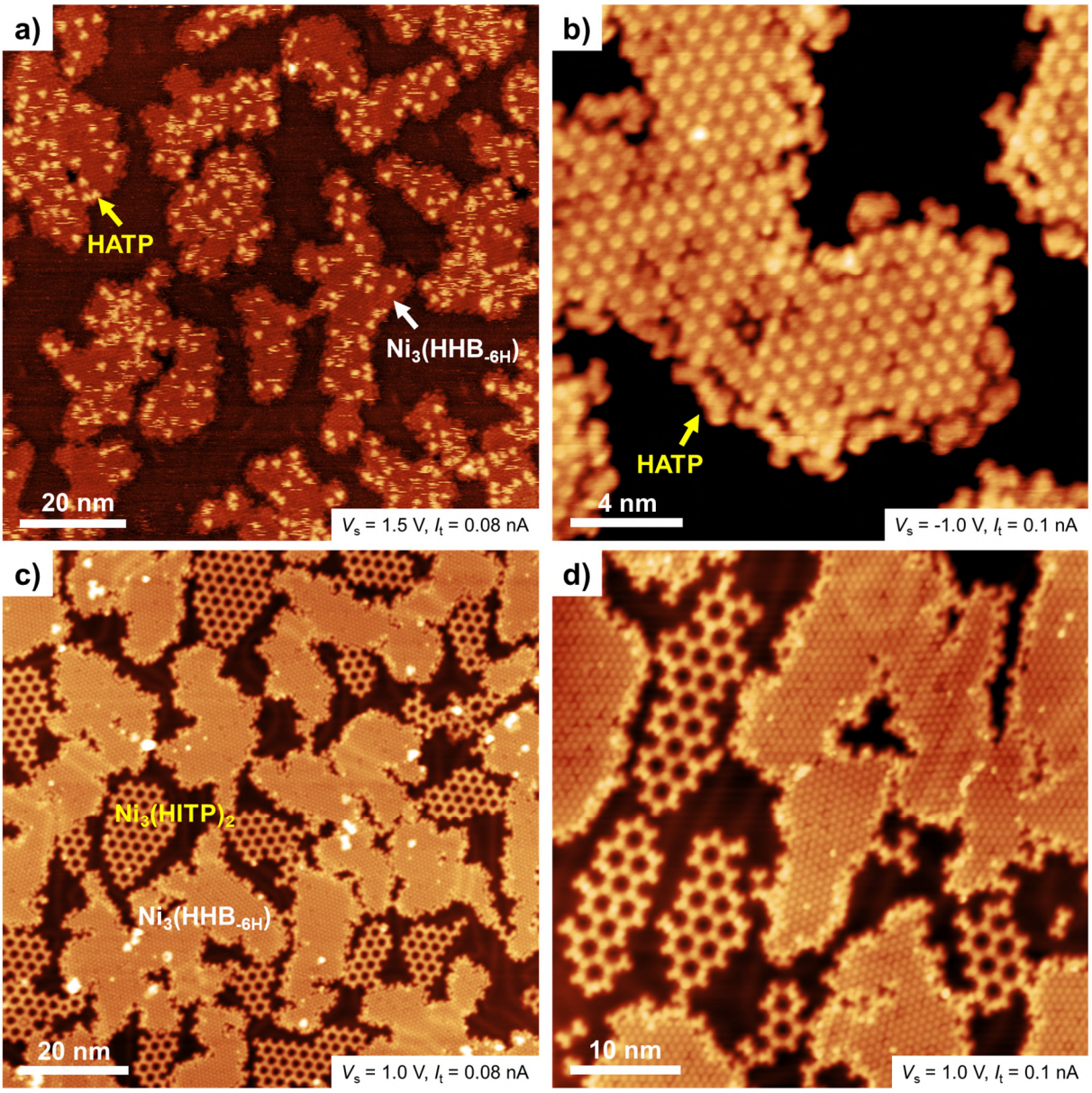


Figure 7.8: (a) Depositing HATP (0.2 ML) onto $Ni_3(HHB_{-6H})$ polymers at room temperature. (b) Annealing the mixture at 160 °C. (c, d) Mixtures of the $Ni_3(HITP)_2$ MOF and the $Ni_3(HHB_{-6H})$ polymer after annealing at 250 °C. Images (b-d) are averaged over 9, 19 and 23 frames, respectively. Image (a) is a single scan.

When Ni atoms were deposited onto the mixture sample, the remaining HATP molecules reacted with them and formed honeycomb $Ni_3(HITP)_2$ networks, shown in Fig. 7.8c. However, most $Ni_3(HITP)_2$ domains grew on the bare Au surface, away from the HHB-Ni polymer islands. Although the HHB-Ni islands were surrounded by HATP molecules, no strong connection

between MOFs and polymers was discovered in Fig. 7.8d. The difficulty in mixing should be related to their epitaxy on Au(111). These two structures have different orientations on the Au(111) surface, and connecting them requires high energy to rotate one network to the other direction, which is not favourable (HATP-MOF angle: 6.6°; HHB-CP angle: 19°). Therefore, these two structures prefer to grow separately.

If the adding order was reversed, a distinct result was found. As shown in Fig.7.9a, a $Ni_3(HITP)_2$ MOF was prepared first and then HHB molecules were deposited. After annealing the mixture, the MOF networks disappeared, and only narrow ribbons were discovered in Fig. 7.9b. These ribbons were dense HHB-Ni polymers surrounded by HATP molecules, as shown in Fig. 7.9c. Therefore, there must be a reaction happened between the HHB molecules and the $Ni_3(HITP)_2$ MOF. One possible reaction is called ligand (linker) substitution, where HHB substitutes with HATP and coordinates with Ni atoms, as illustrated in Fig. 7.9e. To prove that HATP molecules were still on the surface, Ni was deposited onto this sample. After annealing, the MOF networks appeared again (Fig. 7.9d), confirming that the HATP molecules were released from the frameworks. The occurrence of this reaction suggests that HHB has a stronger coordination ability than HATP when reacting with metals on the Au(111) substrate.

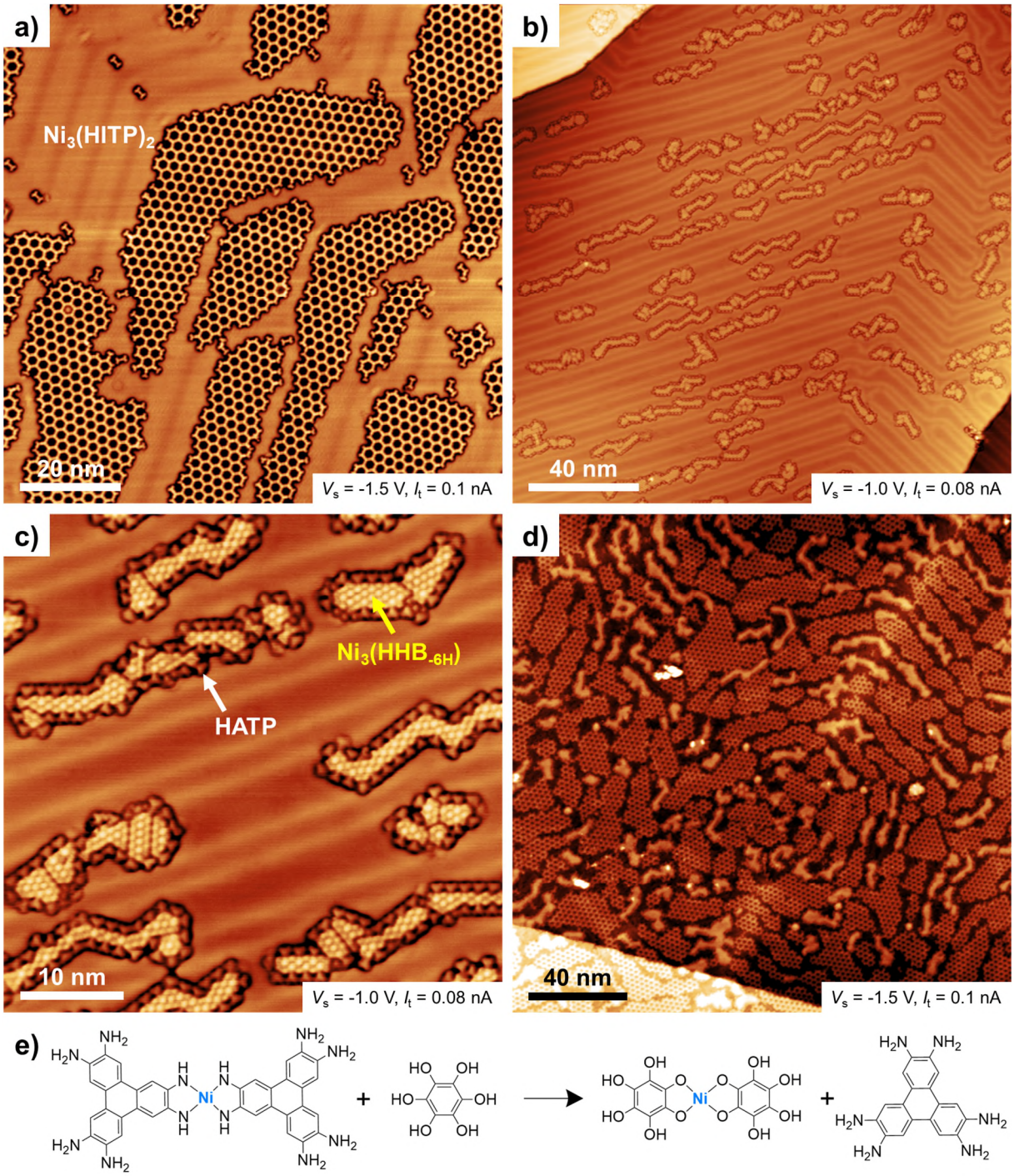


Figure 7.9: (a) $Ni_3(HITP)_2$ MOF on Au(111). (b, c) Depositing HHB molecules (0.7 ML) onto the sample with the $Ni_3(HITP)_2$ MOF and then annealing at 150 °C. (d) Depositing more Ni (0.06 ML) onto the mixture and annealing at 250 °C. (e): A simplified chemical reaction for the ligand substitution. Images (a-d) are averaged over 21, 10, 19 and 13 frames, respectively.

HHTP (-OH) has the same backbone as HATP (-NH_2) but with different functional groups. To investigate the influence of the functional groups on the ligand substitution, the reaction between HHTP-Ni networks and HHB was tested. As shown in Fig. 7.10a, all HHTP molecules

were bonded with Ni atoms. Then, HHB molecules were deposited onto this sample, and they did not react with HHTP-Ni at room temperature (Fig. 7.10b). After annealing, HHTP molecules returned to hydrogen-bonded assemblies, shown in Fig. 7.10c. At the same time, HHB molecules coordinated with Ni and formed HHB-Ni polymers. This result suggests that HHB molecules could also extract the Ni atoms from the HHTP-Ni networks and release HHTP molecules. Therefore, HHB has higher activity than both HATP and HHTP on the Au(111) surface when reacting with Ni.

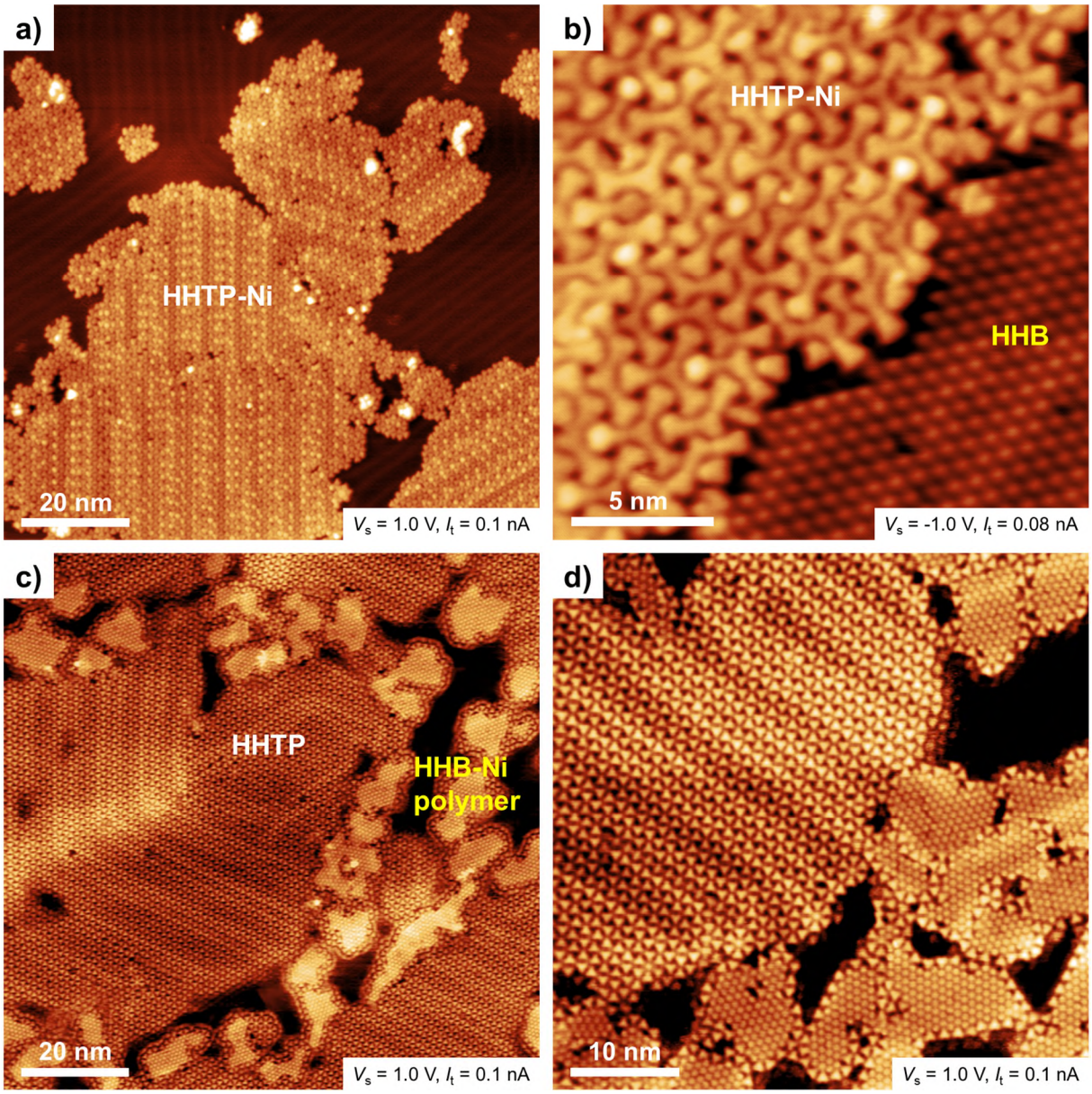


Figure 7.10: (a) HHTP-Ni domains on Au(111). (b) Depositing HHB molecules (0.5 ML) onto the substrate with HHTP-Ni networks. (c, d) Annealing the sample at 250 °C. Images (a-d) are averaged over 8, 17, 6 and 15 frames, respectively.

As described in Chapter 6, HHB molecules are partially dehydrogenated on the Au(111) surface after deposition at room temperature. Whether this affects the activity of the HHB molecules cannot be inferred from the STM images and other chemical characterisation techniques are required, like in-situ XPS. Besides, the mechanism study also needs some simulation supports from quantum chemistry, which can provide more information on transition states for this reaction. Although ligand (linker) substitution is a widely used post-synthetic modification method in MOFs, most of them are achieved in solutions.[211-214] Such substitution reaction has rarely been reported on surfaces. If this approach can be extended to other ligands or applied in wet-chemistry synthesis, it would be a useful method in applications. For example, after substitution in solution, it might be possible to remove or recycle the released ligands.

7.5 Mixture of HHTP and HATP

The last mixture is HHTP and HATP, both based on the triphenylene backbone. Fig. 7.11a shows the surface after depositions, where the observed molecules should be HHTP molecules and HATP molecules were moving on the surface. It is obvious that these two molecules did not mix with each other and just followed their own rules. Annealing the sample to 300 °C did not help the mixing, and the molecules still kept the separation. When adding metals into the mixture and annealing the sample, the molecules reacted with Ni separately, forming dense HHTP-Ni networks and porous HATP-Ni hexagons (Fig. 7.11b). However, we could notice that several hexagons were attached to the edge of the HHTP-Ni domains (Fig. 7.11c) and some molecules were trapped in the HATP-Ni hexagons (Fig. 7.11d). Since the deposited Ni was in excess, the trapped molecules should be different from the molecules in the hexagons. Otherwise, they just reacted with Ni and extended the hexagons. These findings indicate that HATP and HHTP have a very limited degree of mixing, and they behave almost the same as their isolated situations.

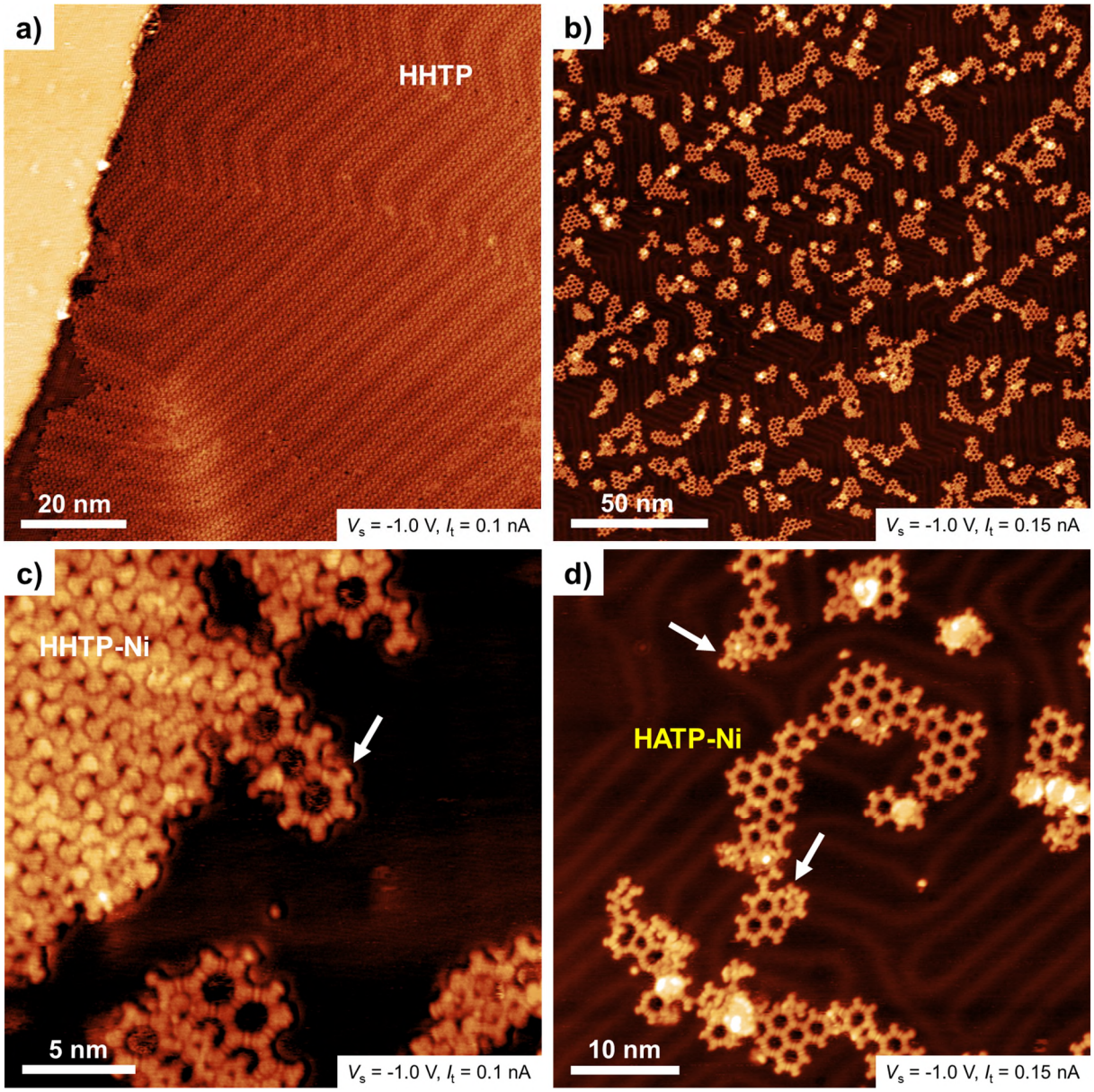


Figure 7.11: (a) Depositing HHTP and HATP together onto the Au(111) substrate at room temperature. (b-d) Mixture of HHTP-Ni and HATP-Ni products after annealing at 250 °C. Images (a) is a single scan. Images (b-d) are averaged over 2, 3 and 3 frames, respectively.

7.6 Conclusion

In conclusion, the mixture of HHTP and HHB can form a molecular alloy with two phases on the Au(111) substrate. Based on this molecular alloy, a HHTP-HHB dual-ligand framework was prepared after reacting with Ni atoms. This dual-ligand MOF matches well with the Au(111) substrate and can grow into large networks up to several hundred nanometres. Furthermore, HHB molecules can extract Ni atoms from HHTP-Ni and HATP-Ni networks, showing a

stronger coordination ability than these two triphenylene-derived ligands. These on-surface reactions broaden the applications of these linkers and make on-surface synthesis more functional and practical.

Chapter 8

Conclusion

8.1 Overview

This thesis reports the synthesis and characterisation of four metal-organic coordination structures on Au(111) substrates (HHTP-M, HATP-M, HHB-M, and HHTP-HHB-M). Combining the STM imaging and DFT modelling, their structural and electronic properties are analysed and discussed. Chapters 4 and 5 present the reactions between hexa-substituted triphenylene molecules (HHTP/HATP) and Ni/Co atoms. Chapter 6 shows coordination polymers based on HHB, and Chapter 7 focuses on the mixtures of these three ligands. These findings extend our understanding of the synthesis and growth process of 2D c-MOFs monolayers, which is underpinning knowledge of relevance to future studies on their applications.

8.2 Molecular self-assemblies on Au(111)

Before investigating the reactions between transition metals and organic linkers, it is necessary to know their individual behaviour on the substrate. Therefore, all the chapters start with the studies of molecules. HHTP in Chapter 4 and HHB in Chapter 6 can form self-assemblies on the Au(111) surface, while HATP in Chapter 5 does not because of its high mobility at room temperature. In Chapter 7, the mixture of HHTP and HHB can generate a molecular alloy, but HATP does not mix with HHB or HHTP.

HHTP molecular assembly is a near close-packed phase constructed by two alternating rows (AB) along the [11$\bar{2}$] direction of Au(111). In this phase, HHTP molecules are bonded to neighbouring molecules through a three-centre ring-like hydrogen bond. As for HHB molecules, they just form a close-packed phase on the surface. The difference between HHTP and HHB is that the assembly of HHTP is stable up to 340 °C, whereas HHB molecules desorb from the substrate at 160 °C.

The mixture of HHTP and HHB has two phases on the Au(111) substrate. At room temperature, they form an α-phase with an HHTP:HHB ratio of 2:1. Upon annealing, HHB molecules start to desorb from the surface, and the α-phase transforms to a new β-phase. The HHTP:HHB ratio of the β-phase is 6:1 due to the decrease of the HHB molecules. Annealing the β-phase to a higher temperature causes all the HHB molecules desorb, and only HHTP molecules are retained. After depositing new HHB molecules onto the sample with remaining HHTP molecules, the α-phase reappears. This 'HHTP – α-phase – β-phase – HHTP' cycle can be repeated several times and does not damage the Au substrate and HHTP molecules. There are many on-surface studies of self-assemblies using mixed molecules, but the alloy with phase transition has rarely been reported. The discovery here makes this field more attractive and provides a method to design and prepare novel nanostructures.

8.3 Metal-organic coordination structures on Au(111)

The situation for HHTP-Ni/Co is special as no long-range ordered patterns are discovered on the surface. In the coordination phase, Ni/Co adopts a three-fold coordination geometry to bond with three adjacent molecules, forming a connected network. This dense structure has not been reported before and its formation must be affected by the substrate. Specifically, the three-fold coordination of transition metals is not very stable in solutions but can be stabilised and

supported by the substrate. Because the alignment of the molecules can change, the networks appear as discontinuous multimers in STM images, including dimers, trimers, and tetramers. This finding has not been discovered or mentioned in previous publications but has been analysed and discussed in this thesis. Understanding the relationship between precursors and products can help us to improve and even control the synthesis in the future.

In comparison, the products of HATP and metals (Ni, Co) on Au(111) have the same honeycomb structure as frameworks synthesised by wet-chemical methods. The shapes of Ni-HATP and Co-HATP domains are large islands and long ribbons, respectively. This project is based on the HATP-Ni work published before, but further investigates its growth process. Because of the strong epitaxy interaction, $\left(\sqrt{57} \times \sqrt{57}\right)$ - R 6.6° - Au(111), networks are extremely difficult to coalesce with each other via rotation or translation. As a result, the size of the synthesised MOFs is limited no matter what reaction conditions are used. This is the main limitation of this on-surface synthesis approach compared with other methods. Mixing Ni and Co results in a bimetallic MOF whose metal centres can show different brightness in the STM images. The brightness difference is attributed to an electronic effect because Co has more d_{z^2} states below -0.6 V. Previous work has demonstrated that the properties of c-MOFs can be modulated by mixing different metals. Resolving different active sites, that is the direct visualisation of the metal atoms here, could provide some basic information for structure-property relationship studies on these MOF alloys.

For HHB molecules, their reactions with Ni/Co produce nonporous polymers on the Au(111) substrate. The superstructure between the coordination polymers and the substrate is $\left(\sqrt{7} \times \sqrt{7}\right)$ R 19° - Au(111). Similar to the MOFs, the rotation and translation problems still limit the size of the networks. Compared with the work of HHB-Fe on Au(111), there is no

obvious difference among these transition metals (Fe, Co, and Ni) when reacting with HHB molecules and the products have the same structure, shape and size. However, Co atoms are not visible in STM images, while Ni nodes are easy to be found. DFT calculations indicate that this phenomenon is caused by the topographic effect where Co atoms are lower than Ni atoms. This feature provides a chance to distinguish different metal atoms in a bimetallic Ni/Co-polymer. Nevertheless, the identification is not very accurate because both the vacancy defects and the Co atoms are black in the STM images. This chapter not only reveals the reactions between HHB molecules and Ni/Co atoms, but also increases the structural diversity of Ni/Co-HXB complexes as almost all the products synthesised by wet chemistry are porous frameworks.

A Ni-coordinated dual-ligand framework can be synthesised using the HHTP-HHB α-phase mixture. This framework has an identical molecular arrangement to the α-phase mixture, which differs from the Cu_3(HHTP)(THQ) honeycomb MOF synthesised before (THQ: deprotonated HHB). The epitaxial relationship of this dual-ligand MOF is (6 × 6) - Au(111), which does not have any rotation angle. The other problem of translation has been solved by the α-phase mixture as the molecules can shift to meet the matching. Benefiting from these advantages, all the islands can merge with others to form an extended network and grow as large as the Au(111) terrace. Metal-organic coordination networks with multiple molecules have been studied on surfaces for many years, but this work should be the first one based on 2D c-MOFs ligands.

Among these four structures, the HHTP-M network is the most special one as it is not perfectly periodic. The other feature is that the transition metals adopt a three-fold geometry, while the coordination is four-fold in other networks. This low coordination index brings some unique properties for the networks, like the large orbital magnetic moment of Co reported in the literature. The HATP-M MOFs and the HHB-M polymers can be classified as the same

category, and they can be easily synthesised under different reaction conditions. Both networks exhibit strong epitaxial relationships with the Au substrate, and their sizes are limited to around 40 nm. As for the HHTP-HHB-Ni MOF, its advantage is that the size can be extended as large as the Au terrace, reaching up to several hundred nanometres. However, the synthesis can only be achieved by depositing metals onto the molecular alloy (specific deposition order) because HHB molecules have a higher coordination ability than HHTP molecules. The main problem of these obtained networks is that they are not suitable for transport and device integration due to their small size (nanometre scale). Therefore, the synthesis needs to be further optimised and improved before putting into real applications.

Although on-surface methods face the difficulty in fabricating large-scale layers, they can still be used to study the mechanisms of some devices. For instance, I have tried to dose CO molecules onto the Ni-HATP MOF to investigate the adsorption mechanism relevant to chemiresistive gas sensors. To be more specific, when the active metal centres interact with gas molecules, the STM images might show some distinct features, such as bright dots. However, it is very difficult to catch this change under our STM at room temperature due to the high mobility of the gas molecules. Using low-temperature STM and combining it with other in-situ characterisation techniques, this study might be realised. As mentioned before, mixed metals could tune the properties of the MOFs. Different metals may interact with the analyte differently or show distinct binding behaviour. Such differences might be possible to be characterised by on-surface techniques, especially when different active sites are resolved.

One thing needs to be mentioned is that preparing single layers of 2D c-MOFs can help us to understand their properties within the *ab* plane (bulk surface), but the information about their stacking is lacking. Unlike other 2D materials, the stacking of 2D c-MOFs plays an important

role in their properties' determination, which cannot be ignored. For example, the π-π stacking between ligands can also provide a pathway for charge transport and some 2D c-MOFs exhibit high electrical conductivities along the *c* axis (stacking direction). In this thesis, I focus on single layers and have not studied the situation of multilayers. The stacking research can be performed in the future if multilayers of MOFs could be obtained on surfaces.

8.4 Future work

According to the results, there are three problems that can be studied in the future. The first one is the growth mechanism of Co-HATP ribbons in Chapter 5. The formation of the ribbons might be related to the $\left(22 \times \sqrt{3}\right)$ reconstruction of Au(111), but DFT calculations did not find any adsorption energy difference between the fcc-Au(111) and the hcp-Au(111). Therefore, it is necessary to build a reconstructed surface with solitons to investigate its influence on the Co-HATP MOF. Understanding the effect of the substrate is helpful for other studies on the Au(111) substrate. The second work is the vacancy defects of HHB-M polymers in Chapter 6. By optimising the synthesis conditions, it might be possible to eliminate these vacancy defects. Then, the relationship between structures and properties can be further investigated. The last one is the ligand substitution reaction in Chapter 7. To figure out how the HHB molecules extract the metals from the coordinated networks, XPS characterisations and quantum chemistry calculations are needed. With the help of these techniques, the reaction mechanism can be revealed.

Since all the experiments are carried out under the vacuum, the stability of these synthesised MOFs has not been investigated. When the layers are integrated into devices, like gas sensors, they must be stable for a long time after exposure to air or organic vapours. This work is not easy to be carried out by STM (or AFM) as it has a high requirement of the surface cleanliness.

I have tried to use SEM to study the structures after exposure to air, but nothing was resolved due to the limited resolution. TEM holds the ability to reach atomic resolution, but the high-energy beam will damage these monolayers. One possible technique is XPS, which can monitor the chemical environments of the elements. Besides, when these layers are exfoliated from the substrate, like lift-off methods for other 2D materials, whether they could keep their structures is unknown. All these stability studies need to be considered in the future.

Apart from the three ligands presented in this thesis, I have also tested another two ligands, NiPc-$(NH_2)_8$ and HHTQ. Limited by the instrument, I have not solved their evaporation problems. These two projects can be carried out in the future if the deposition is achieved. HHTQ is a similar linker to HHTP, but the acidity of its catechol groups is stronger, which can promote higher crystallinity within the plane. Using this ligand, it might be possible to overcome the disadvantages of HHTP and to synthesise more uniform porous frameworks. As for NiPc-$(NH_2)_8$, the most attractive feature is its four-fold symmetry. All the ligands described before are three-fold symmetric, so the hexagonal honeycomb is the dominant structure in their coordination networks. NiPc-$(NH_2)_8$ can form a tetragonal unit cell with metal atoms, which can broaden the structure types of MOFs. Exploring these two ligands would advance our understanding of single-layer 2D c-MOFs and strength the compatibility of on-surface synthesis.

References

1. Hmadeh, M.; Lu, Z.; Liu, Z.; Gándara, F.; Furukawa, H.; Wan, S.; Augustyn, V.; Chang, R.; Liao, L.; Zhou, F.; Perre, E.; Ozolins, V.; Suenaga, K.; Duan, X.; Dunn, B.; Yamamto, Y.; Terasaki, O.; Yaghi, O. M., New Porous Crystals of Extended Metal-Catecholates. *Chem. Mater*. **2012,** *24* (18), 3511-3513.

2. Wang, M.; Dong, R.; Feng, X., Two-dimensional conjugated metal–organic frameworks (2D c-MOFs): chemistry and function for MOFtronics. *Chem. Soc. Rev.* **2021,** *50* (4), 2764-2793.

3. Liu, J.; Song, X.; Zhang, T.; Liu, S.; Wen, H.; Chen, L., 2D Conductive Metal–Organic Frameworks: An Emerging Platform for Electrochemical Energy Storage. *Angew. Chem. Int. Ed.* **2021,** *60* (11), 5612-5624.

4. Majumder, M.; Santosh, M. S.; Viswanatha, R.; Thakur, A. K.; Dubal, D. P.; Jayaramulu, K., Two-dimensional Conducting Metal-Organic Frameworks Enabled Energy Storage Devices. *Energy Storage Mater.* **2021,** *37*, 396-416.

5. Huang, X.; Zhang, S.; Liu, L.; Yu, L.; Chen, G.; Xu, W.; Zhu, D., Superconductivity in a Copper(II)-Based Coordination Polymer with Perfect Kagome Structure. *Angew. Chem. Int. Ed.* **2018,** *57* (1), 146-150.

6. Zhang, X.; Zhou, Y.; Cui, B.; Zhao, M.; Liu, F., Theoretical Discovery of a Superconducting Two-Dimensional Metal–Organic Framework. *Nano Lett.* **2017,** *17* (10), 6166-6170.

7. Dong, R.; Zhang, Z.; Tranca, D. C.; Zhou, S.; Wang, M.; Adler, P.; Liao, Z.; Liu, F.; Sun, Y.; Shi, W.; Zhang, Z.; Zschech, E.; Mannsfeld, S. C. B.; Felser, C.; Feng, X., A coronene-based semiconducting two-dimensional metal-organic framework with ferromagnetic behavior. *Nat. Commun.* **2018,** *9* (1), 2637.

8. Wang, Z. F.; Liu, Z.; Liu, F., Organic topological insulators in organometallic lattices. *Nat. Commun.* **2013,** *4* (1), 1471.

9. Wang, Z. F.; Su, N.; Liu, F., Prediction of a Two-Dimensional Organic Topological Insulator. *Nano Lett.* **2013,** *13* (6), 2842-2845.

10. Dong, L.; Kim, Y.; Er, D.; Rappe, A. M.; Shenoy, V. B., Two-Dimensional π-Conjugated Covalent-Organic Frameworks as Quantum Anomalous Hall Topological Insulators. *Phys. Rev. Lett.* **2016,** *116* (9), 096601.

11. Zhang, X.; Wang, Z.; Zhao, M.; Liu, F., Tunable topological states in electron-doped HTT-Pt. *Phys. Rev. B* **2016,** *93* (16), 165401.

12. Liu, J.; Abel, M.; Lin, N., On-Surface Synthesis: A New Route Realizing Single-Layer Conjugated Metal–Organic Structures. *J. Phys. Chem. Lett* **2022,** *13* (5), 1356-1365.

13. Dong, L.; Gao, Z. A.; Lin, N., Self-assembly of metal–organic coordination structures on surfaces. *Prog. Surf. Sci.* **2016,** *91* (3), 101-135.

14. Liu, J.; Lin, N., On-Surface-Assembled Single-Layer Metal-Organic Frameworks with Extended Conjugation. *ChemPlusChem* **2023,** *88* (5), e202200359.

15. Santhini, V. M.; Wäckerlin, C.; Cahlík, A.; Ondráček, M.; Pascal, S.; Matěj, A.; Stetsovych, O.; Mutombo, P.; Lazar, P.; Siri, O.; Jelínek, P., 1D Coordination π–d Conjugated Polymers with Distinct

Structures Defined by the Choice of the Transition Metal: Towards a New Class of Antiaromatic Macrocycles. *Angew. Chem. Int. Ed.* **2021,** *60* (1), 439-445.

16. Denawi, H.; Nardi, E.; Koudia, M.; Siri, O.; Abel, M.; Hayn, R., Magnetic Polymer Chains of Iron and Zwitterionic Quinoidal Ligands on the Ag(111) Surface. *J. Phys. Chem. C* **2020,** *124* (2), 1346-1351.

17. Liu, J.; Gao, Y.; Wang, T.; Xue, Q.; Hua, M.; Wang, Y.; Huang, L.; Lin, N., Collective Spin Manipulation in Antiferroelastic Spin-Crossover Metallo-Supramolecular Chains. *ACS Nano* **2020,** *14* (9), 11283-11293.

18. Liu, J.; Li, J.; Chen, Q.; Xue, Q.; Wang, Y.; Di, B.; Wang, Y.; Wu, K., Lattice-Directed Stabilization of Different Spin-State Phases in Metallo-Supramolecular Chains on Au Surfaces. *Chem. Mater.* **2021,** *33* (15), 6166-6175.

19. Lin, T.; Kuang, G.; Shang, X. S.; Liu, P. N.; Lin, N., Self-assembly of metal–organic coordination networks using on-surface synthesized ligands. *Chem. Commun.* **2014,** *50* (97), 15327-15329.

20. Lyu, C.-K.; Gao, Y.-F.; Gao, Z.-A.; Mo, S.-Y.; Hua, M.-Q.; Li, E.; Fu, S.-Q.; Chen, J.-Y.; Liu, P.-N.; Huang, L.; Lin, N., Synthesis of Single-Layer Two-Dimensional Metal–Organic Frameworks M3(HAT)2 (M=Ni, Fe, Co, HAT=1,4,5,8,9,12-hexaazatriphenylene) Using an On-Surface Reaction. *Angew. Chem. Int. Ed.* **2022,** *61* (27), e202204528.

21. Sweetman, A.; Champness, N. R.; Saywell, A., On-surface chemical reactions characterised by ultra-high resolution scanning probe microscopy. *Chem. Soc. Rev.* **2020,** *49* (13), 4189-4202.

22. Mali, K. S.; Pearce, N.; De Feyter, S.; Champness, N. R., Frontiers of supramolecular chemistry at solid surfaces. *Chem. Soc. Rev.* **2017,** *46* (9), 2520-2542.

23. Novoselov, K. S.; Geim, A. K.; Morozov, S. V.; Jiang, D.; Zhang, Y.; Dubonos, S. V.; Grigorieva, I. V.; Firsov, A. A., Electric Field Effect in Atomically Thin Carbon Films. *Science* **2004,** *306* (5696), 666-669.

24. Li, J.; Wang, X.-Y.; Liu, X.-R.; Jin, Z.; Wang, D.; Wan, L.-J., Facile growth of centimeter-sized single-crystal graphene on copper foil at atmospheric pressure. *J. Mater. Chem. C* **2015,** *3* (15), 3530-3535.

25. Vlassiouk, I. V.; Stehle, Y.; Pudasaini, P. R.; Unocic, R. R.; Rack, P. D.; Baddorf, A. P.; Ivanov, I. N.; Lavrik, N. V.; List, F.; Gupta, N.; Bets, K. V.; Yakobson, B. I.; Smirnov, S. N., Evolutionary selection growth of two-dimensional materials on polycrystalline substrates. *Nat. Mater.* **2018,** *17* (4), 318-322.

26. Xu, M.; Liang, T.; Shi, M.; Chen, H., Graphene-Like Two-Dimensional Materials. *Chem. Rev.* **2013,** *113* (5), 3766-3798.

27. Ko, M.; Mendecki, L.; Mirica, K. A., Conductive two-dimensional metal–organic frameworks as multifunctional materials. *Chem. Commun.* **2018,** *54* (57), 7873-7891.

28. Meng, Z.; Stolz, R. M.; Mendecki, L.; Mirica, K. A., Electrically-Transduced Chemical Sensors Based on Two-Dimensional Nanomaterials. *Chem. Rev.* **2019,** *119* (1), 478-598.

29. Rao, C. N. R.; Sood, A. K.; Subrahmanyam, K. S.; Govindaraj, A., Graphene: The New Two-Dimensional Nanomaterial. *Angew. Chem. Int. Ed.* **2009,** *48* (42), 7752-7777.

30. Novoselov, K. S.; Fal′ko, V. I.; Colombo, L.; Gellert, P. R.; Schwab, M. G.; Kim, K., A roadmap for graphene. *Nature* **2012,** *490* (7419), 192-200.

31. Geim, A. K.; Novoselov, K. S., The rise of graphene. *Nat. Mater.* **2007,** *6* (3), 183-191.

32. Lin, Y.-M.; Dimitrakopoulos, C.; Jenkins, K. A.; Farmer, D. B.; Chiu, H.-Y.; Grill, A.; Avouris, P., 100-GHz Transistors from Wafer-Scale Epitaxial Graphene. *Science* **2010,** *327* (5966), 662-662.

33. El-Kady, M. F.; Strong, V.; Dubin, S.; Kaner, R. B., Laser Scribing of High-Performance and Flexible Graphene-Based Electrochemical Capacitors. *Science* **2012,** *335* (6074), 1326-1330.

34. James, S. L., Metal-organic frameworks. *Chem. Soc. Rev.* **2003,** *32* (5), 276-288.

35. Rowsell, J. L. C.; Yaghi, O. M., Metal–organic frameworks: a new class of porous materials. *Microporous Mesoporous Mater.* **2004,** *73* (1), 3-14.

36. Britt, D.; Furukawa, H.; Wang, B.; Glover, T. G.; Yaghi, O. M., Highly efficient separation of carbon dioxide by a metal-organic framework replete with open metal sites. *Proc. Natl. Acad. Sci.* **2009,** *106* (49), 20637-20640.

37. Yang, D.-A.; Cho, H.-Y.; Kim, J.; Yang, S.-T.; Ahn, W.-S., CO2 capture and conversion using Mg-MOF-74 prepared by a sonochemical method. *Energy Environ. Sci.* **2012,** *5* (4), 6465-6473.

38. Fu, Y.; Sun, D.; Chen, Y.; Huang, R.; Ding, Z.; Fu, X.; Li, Z., An Amine-Functionalized Titanium Metal–Organic Framework Photocatalyst with Visible-Light-Induced Activity for CO2 Reduction. *Angew. Chem. Int. Ed.* **2012,** *51* (14), 3364-3367.

39. Nickerl, G.; Senkovska, I.; Kaskel, S., Tetrazine functionalized zirconium MOF as an optical sensor for oxidizing gases. *Chem. Commun.* **2015,** *51* (12), 2280-2282.

40. Rao, X.; Song, T.; Gao, J.; Cui, Y.; Yang, Y.; Wu, C.; Chen, B.; Qian, G., A Highly Sensitive Mixed Lanthanide Metal–Organic Framework Self-Calibrated Luminescent Thermometer. *J. Am. Chem. Soc.* **2013,** *135* (41), 15559-15564.

41. Kreno, L. E.; Leong, K.; Farha, O. K.; Allendorf, M.; Van Duyne, R. P.; Hupp, J. T., Metal–Organic Framework Materials as Chemical Sensors. *Chem. Rev.* **2012,** *112* (2), 1105-1125.

42. Zhu, L.; Liu, X.-Q.; Jiang, H.-L.; Sun, L.-B., Metal–Organic Frameworks for Heterogeneous Basic Catalysis. *Chem. Rev.* **2017,** *117* (12), 8129-8176.

43. Li, P.; Wang, B., Recent Development and Application of Conductive MOFs. *Isr. J. Chem.* **2018,** *58* (9-10), 1010-1018.

44. Smith, M. K.; Angle, S. R.; Northrop, B. H., Preparation and Analysis of Cyclodextrin-Based Metal–Organic Frameworks: Laboratory Experiments Adaptable for High School through Advanced Undergraduate Students. *J. Chem. Educ.* **2015,** *92* (2), 368-372.

45. Sumida, K.; Arnold, J., Preparation, Characterization, and Postsynthetic Modification of Metal−Organic Frameworks: Synthetic Experiments for an Undergraduate Laboratory Course in Inorganic Chemistry. *J. Chem. Educ.* **2011,** *88* (1), 92-94.

46. Lawrance, G. A., Complexes. In *Introduction to Coordination Chemistry*, 2010; pp 41-82.

47. Xie, L. S.; Skorupskii, G.; Dincă, M., Electrically Conductive Metal–Organic Frameworks. *Chem. Rev.* **2020,** *120* (16), 8536-8580.

48. Sun, L.; Hendon, C. H.; Minier, M. A.; Walsh, A.; Dincă, M., Million-Fold Electrical Conductivity Enhancement in Fe2(DEBDC) versus Mn2(DEBDC) (E = S, O). *J. Am. Chem. Soc.* **2015,** *137* (19), 6164-6167.

49. Park, S. S.; Hontz, E. R.; Sun, L.; Hendon, C. H.; Walsh, A.; Van Voorhis, T.; Dincă, M., Cation-Dependent Intrinsic Electrical Conductivity in Isostructural Tetrathiafulvalene-Based Microporous Metal–Organic Frameworks. *J. Am. Chem. Soc.* **2015,** *137* (5), 1774-1777.

50. Takaishi, S.; Hosoda, M.; Kajiwara, T.; Miyasaka, H.; Yamashita, M.; Nakanishi, Y.; Kitagawa, Y.; Yamaguchi, K.; Kobayashi, A.; Kitagawa, H., Electroconductive Porous Coordination Polymer Cu[Cu(pdt)2] Composed of Donor and Acceptor Building Units. *Inorg. Chem.* **2009,** *48* (19), 9048-9050.

51. Lin, L.; Zhang, Q.; Ni, Y.; Shang, L.; Zhang, X.; Yan, Z.; Zhao, Q.; Chen, J., Rational design and synthesis of two-dimensional conjugated metal-organic polymers for electrocatalysis applications. *Chem* **2022,** *8* (7), 1822-1854.

52. Bi, S.; Banda, H.; Chen, M.; Niu, L.; Chen, M.; Wu, T.; Wang, J.; Wang, R.; Feng, J.; Chen, T.; Dincă, M.; Kornyshev, A. A.; Feng, G., Molecular understanding of charge storage and charging dynamics in supercapacitors with MOF electrodes and ionic liquid electrolytes. *Nat. Mater.* **2020,** *19* (5), 552-558.

53. Park, J.; Hinckley, A. C.; Huang, Z.; Feng, D.; Yakovenko, A. A.; Lee, M.; Chen, S.; Zou, X.; Bao, Z., Synthetic Routes for a 2D Semiconductive Copper Hexahydroxybenzene Metal–Organic Framework. *J. Am. Chem. Soc.* **2018,** *140* (44), 14533-14537.

54. Lahiri, N.; Lotfizadeh, N.; Tsuchikawa, R.; Deshpande, V. V.; Louie, J., Hexaaminobenzene as a building block for a Family of 2D Coordination Polymers. *J. Am. Chem. Soc.* **2017,** *139* (1), 19-22.

55. Dou, J.-H.; Sun, L.; Ge, Y.; Li, W.; Hendon, C. H.; Li, J.; Gul, S.; Yano, J.; Stach, E. A.; Dincă, M., Signature of Metallic Behavior in the Metal–Organic Frameworks M3(hexaiminobenzene)2 (M = Ni, Cu). *J. Am. Chem. Soc.* **2017,** *139* (39), 13608-13611.

56. Feng, D.; Lei, T.; Lukatskaya, M. R.; Park, J.; Huang, Z.; Lee, M.; Shaw, L.; Chen, S.; Yakovenko, A. A.; Kulkarni, A.; Xiao, J.; Fredrickson, K.; Tok, J. B.; Zou, X.; Cui, Y.; Bao, Z., Robust and conductive two-dimensional metal−organic frameworks with exceptionally high volumetric and areal capacitance. *Nat. Energy* **2018,** *3* (1), 30-36.

57. Shinde, S. S.; Lee, C. H.; Jung, J.-Y.; Wagh, N. K.; Kim, S.-H.; Kim, D.-H.; Lin, C.; Lee, S. U.; Lee, J.-H., Unveiling dual-linkage 3D hexaiminobenzene metal–organic frameworks towards long-lasting advanced reversible Zn–air batteries. *Energy Environ. Sci.* **2019,** *12* (2), 727-738.

58. Park, J.; Lee, M.; Feng, D.; Huang, Z.; Hinckley, A. C.; Yakovenko, A.; Zou, X.; Cui, Y.; Bao, Z., Stabilization of Hexaaminobenzene in a 2D Conductive Metal–Organic Framework for High Power Sodium Storage. *J. Am. Chem. Soc.* **2018,** *140* (32), 10315-10323.

59. Hinckley, A. C.; Park, J.; Gomes, J.; Carlson, E.; Bao, Z., Air-Stability and Carrier Type in Conductive M3(Hexaaminobenzene)2, (M = Co, Ni, Cu). *J. Am. Chem. Soc.* **2020,** *142* (25), 11123-11130.

60. Kambe, T.; Sakamoto, R.; Hoshiko, K.; Takada, K.; Miyachi, M.; Ryu, J.-H.; Sasaki, S.; Kim, J.; Nakazato, K.; Takata, M.; Nishihara, H., π-Conjugated Nickel Bis(dithiolene) Complex Nanosheet. *J. Am. Chem. Soc.* **2013,** *135* (7), 2462-2465.

61. Pal, T.; Kambe, T.; Kusamoto, T.; Foo, M. L.; Matsuoka, R.; Sakamoto, R.; Nishihara, H., Interfacial Synthesis of Electrically Conducting Palladium Bis(dithiolene) Complex Nanosheet. *ChemPlusChem* **2015,** *80* (8), 1255-1258.

62. Pal, T.; Doi, S.; Maeda, H.; Wada, K.; Tan, C. M.; Fukui, N.; Sakamoto, R.; Tsuneyuki, S.; Sasaki, S.; Nishihara, H., Interfacial transmetallation synthesis of a platinadithiolene nanosheet as a potential 2D topological insulator. *Chem. Sci.* **2019,** *10* (20), 5218-5225.

63. Huang, X.; Sheng, P.; Tu, Z.; Zhang, F.; Wang, J.; Geng, H.; Zou, Y.; Di, C.-a.; Yi, Y.; Sun, Y.; Xu, W.; Zhu, D., A two-dimensional π–d conjugated coordination polymer with extremely high electrical conductivity and ambipolar transport behaviour. *Nat. Commun.* **2015,** *6* (1), 7408.

64. Huang, X.; Li, H.; Tu, Z.; Liu, L.; Wu, X.; Chen, J.; Liang, Y.; Zou, Y.; Yi, Y.; Sun, J.; Xu, W.; Zhu, D., Highly Conducting Neutral Coordination Polymer with Infinite Two-Dimensional Silver–Sulfur Networks. *J. Am. Chem. Soc.* **2018,** *140* (45), 15153-15156.

65. Cui, Y.; Yan, J.; Chen, Z.; Zhang, J.; Zou, Y.; Sun, Y.; Xu, W.; Zhu, D., [Cu3(C6Se6)]n: The First Highly Conductive 2D π–d Conjugated Coordination Polymer Based on Benzenehexaselenolate. *Adv. Sci.* **2019,** *6* (9), 1802235.

66. Wang, Z.; Wang, G.; Qi, H.; Wang, M.; Wang, M.; Park, S.; Wang, H.; Yu, M.; Kaiser, U.; Fery, A.; Zhou, S.; Dong, R.; Feng, X., Ultrathin two-dimensional conjugated metal–organic framework single-crystalline nanosheets enabled by surfactant-assisted synthesis. *Chem. Sci.* **2020,** *11* (29), 7665-7671.

67. Xiao, Y.; Xiang, Y.; Guo, S.; Wang, J.; Ouyang, Y.; Li, D.; Zeng, Q.; Gong, W.; Gan, L.; Zhang, Q.; Huang, S., An ultralight electroconductive metal-organic framework membrane for multistep catalytic conversion and molecular sieving in lithium-sulfur batteries. *Energy Storage Mater.* **2022,** *51*, 882-889.

68. Chen, T.; Dou, J.-H.; Yang, L.; Sun, C.; Oppenheim, J. J.; Li, J.; Dincă, M., Dimensionality Modulates Electrical Conductivity in Compositionally Constant One-, Two-, and Three-Dimensional Frameworks. *J. Am. Chem. Soc.* **2022,** *144* (12), 5583-5593.

69. Jiang, Y.; Oh, I.; Joo, S. H.; Seo, Y.-S.; Lee, S. H.; Seong, W. K.; Kim, Y. J.; Hwang, J.; Kwak, S. K.; Yoo, J.-W.; Ruoff, R. S., Synthesis of a Copper 1,3,5-Triamino-2,4,6-benzenetriol Metal–Organic Framework. *J. Am. Chem. Soc.* **2020,** *142* (43), 18346-18354.

70. Sun, X.; Wu, K.-H.; Sakamoto, R.; Kusamoto, T.; Maeda, H.; Ni, X.; Jiang, W.; Liu, F.; Sasaki, S.; Masunaga, H.; Nishihara, H., Bis(aminothiolato)nickel nanosheet as a redox switch for conductivity and an electrocatalyst for the hydrogen evolution reaction. *Chem. Sci.* **2017,** *8* (12), 8078-8085.

71. Day, R. W.; Bediako, D. K.; Rezaee, M.; Parent, L. R.; Skorupskii, G.; Arguilla, M. Q.; Hendon, C. H.; Stassen, I.; Gianneschi, N. C.; Kim, P.; Dincă, M., Single Crystals of Electrically Conductive Two-Dimensional Metal–Organic Frameworks: Structural and Electrical Transport Properties. *ACS Cent. Sci.* **2019,** *5* (12), 1959-1964.

72. Skorupskii, G.; Trump, B. A.; Kasel, T. W.; Brown, C. M.; Hendon, C. H.; Dincă, M., Efficient and tunable one-dimensional charge transport in layered lanthanide metal–organic frameworks. *Nat. Chem.* **2020,** *12* (2), 131-136.

73. Mähringer, A.; Jakowetz, A. C.; Rotter, J. M.; Bohn, B. J.; Stolarczyk, J. K.; Feldmann, J.; Bein, T.; Medina, D. D., Oriented Thin Films of Electroactive Triphenylene Catecholate-Based Two-Dimensional Metal–Organic Frameworks. *ACS Nano* **2019,** *13* (6), 6711-6719.

74. Sun, L.; Yang, L.; Dou, J.-H.; Li, J.; Skorupskii, G.; Mardini, M.; Tan, K. O.; Chen, T.; Sun, C.; Oppenheim, J. J.; Griffin, R. G.; Dincă, M.; Rajh, T., Room-Temperature Quantitative Quantum Sensing of Lithium Ions with a Radical-Embedded Metal–Organic Framework. *J. Am. Chem. Soc.* **2022,** *144* (41), 19008-19016.

75. Song, X.; Wang, X.; Li, Y.; Zheng, C.; Zhang, B.; Di, C.-a.; Li, F.; Jin, C.; Mi, W.; Chen, L.; Hu, W., 2D Semiconducting Metal–Organic Framework Thin Films for Organic Spin Valves. *Angew. Chem. Int. Ed.* **2020,** *59* (3), 1118-1123.

76. Sheberla, D.; Sun, L.; Blood-Forsythe, M. A.; Er, S.; Wade, C. R.; Brozek, C. K.; Aspuru-Guzik, A.; Dincă, M., High Electrical Conductivity in Ni3(2,3,6,7,10,11-hexaiminotriphenylene)2, a Semiconducting Metal–Organic Graphene Analogue. *J. Am. Chem. Soc.* **2014,** *136* (25), 8859-8862.

77. Campbell, M. G.; Sheberla, D.; Liu, S. F.; Swager, T. M.; Dincă, M., Cu3(hexaiminotriphenylene)2: An Electrically Conductive 2D Metal–Organic Framework for Chemiresistive Sensing. *Angew. Chem. Int. Ed.* **2015,** *54* (14), 4349-4352.

78. Lian, Y.; Yang, W.; Zhang, C.; Sun, H.; Deng, Z.; Xu, W.; Song, L.; Ouyang, Z.; Wang, Z.; Guo, J.; Peng, Y., Unpaired 3d Electrons on Atomically Dispersed Cobalt Centres in Coordination Polymers Regulate both Oxygen Reduction Reaction (ORR) Activity and Selectivity for Use in Zinc–Air Batteries. *Angew. Chem. Int. Ed.* **2020,** *59* (1), 286-294.

79. Chen, T.; Dou, J.-H.; Yang, L.; Sun, C.; Libretto, N. J.; Skorupskii, G.; Miller, J. T.; Dincă, M., Continuous Electrical Conductivity Variation in M3(Hexaiminotriphenylene)2 (M = Co, Ni, Cu) MOF Alloys. *J. Am. Chem. Soc.* **2020,** *142* (28), 12367-12373.

80. Mariano, R. G.; Wahab, O. J.; Rabinowitz, J. A.; Oppenheim, J.; Chen, T.; Unwin, P. R.; Dincă, M., Thousand-fold increase in O2 electroreduction rates with conductive MOFs. *ACS Cent. Sci.* **2022,** *8* (7), 975-982.

81. Cui, J.; Xu, Z., An electroactive porous network from covalent metal–dithiolene links. *Chem. Commun.* **2014,** *50* (30), 3986-3988.

82. Clough, A. J.; Skelton, J. M.; Downes, C. A.; de la Rosa, A. A.; Yoo, J. W.; Walsh, A.; Melot, B. C.; Marinescu, S. C., Metallic Conductivity in a Two-Dimensional Cobalt Dithiolene Metal–Organic Framework. *J. Am. Chem. Soc.* **2017,** *139* (31), 10863-10867.

83. Clough, A. J.; Orchanian, N. M.; Skelton, J. M.; Neer, A. J.; Howard, S. A.; Downes, C. A.; Piper, L. F. J.; Walsh, A.; Melot, B. C.; Marinescu, S. C., Room Temperature Metallic Conductivity in a Metal–Organic Framework Induced by Oxidation. *J. Am. Chem. Soc.* **2019,** *141* (41), 16323-16330.

84. Dong, R.; Han, P.; Arora, H.; Ballabio, M.; Karakus, M.; Zhang, Z.; Shekhar, C.; Adler, P.; Petkov, P. S.; Erbe, A.; Mannsfeld, S. C. B.; Felser, C.; Heine, T.; Bonn, M.; Feng, X.; Cánovas, E., High-mobility band-like charge transport in a semiconducting two-dimensional metal–organic framework. *Nat. Mater.* **2018,** *17* (11), 1027-1032.

85. Mendecki, L.; Ko, M.; Zhang, X.; Meng, Z.; Mirica, K. A., Porous Scaffolds for Electrochemically Controlled Reversible Capture and Release of Ethylene. *J. Am. Chem. Soc.* **2017,** *139* (48), 17229-17232.

86. Cui, Y.; Yan, J.; Chen, Z.; Xing, W.; Ye, C.; Li, X.; Zou, Y.; Sun, Y.; Liu, C.; Xu, W.; Zhu, D., Synthetic Route to a Triphenylenehexaselenol-Based Metal Organic Framework with Semi-conductive and Glassy Magnetic Properties. *iScience* **2020,** *23* (1), 100812.

87. Jia, H.; Yao, Y.; Zhao, J.; Gao, Y.; Luo, Z.; Du, P., A novel two-dimensional nickel phthalocyanine-based metal–organic framework for highly efficient water oxidation catalysis. *J. Mater. Chem. A* **2018,** *6* (3), 1188-1195.

88. Zhang, P.; Wang, M.; Liu, Y.; Yang, S.; Wang, F.; Li, Y.; Chen, G.; Li, Z.; Wang, G.; Zhu, M.; Dong, R.; Yu, M.; Schmidt, O. G.; Feng, X., Dual-Redox-Sites Enable Two-Dimensional Conjugated Metal–Organic Frameworks with Large Pseudocapacitance and Wide Potential Window. *J. Am. Chem. Soc.* **2021,** *143* (27), 10168-10176.

89. Wang, M.; Shi, H.; Zhang, P.; Liao, Z.; Wang, M.; Zhong, H.; Schwotzer, F.; Nia, A. S.; Zschech, E.; Zhou, S.; Kaskel, S.; Dong, R.; Feng, X., Phthalocyanine-Based 2D Conjugated Metal-Organic Framework Nanosheets for High-Performance Micro-Supercapacitors. *Adv. Funct. Mater.* **2020,** *30* (30), 2002664.

90. Meng, Z.; Aykanat, A.; Mirica, K. A., Welding Metallophthalocyanines into Bimetallic Molecular Meshes for Ultrasensitive, Low-Power Chemiresistive Detection of Gases. *J. Am. Chem. Soc.* **2019,** *141* (5), 2046-2053.

91. Zhong, H.; Ly, K. H.; Wang, M.; Krupskaya, Y.; Han, X.; Zhang, J.; Zhang, J.; Kataev, V.; Büchner, B.; Weidinger, I. M.; Kaskel, S.; Liu, P.; Chen, M.; Dong, R.; Feng, X., A Phthalocyanine-Based Layered Two-Dimensional Conjugated Metal–Organic Framework as a Highly Efficient Electrocatalyst for the Oxygen Reduction Reaction. *Angew. Chem. Int. Ed.* **2019,** *58* (31), 10677-10682.

92. Nagatomi, H.; Yanai, N.; Yamada, T.; Shiraishi, K.; Kimizuka, N., Synthesis and Electric Properties of a Two-Dimensional Metal-Organic Framework Based on Phthalocyanine. *Chem. Eur.* **2018,** *24* (8), 1806-1810.

93. Yi, J.-D.; Si, D.-H.; Xie, R.; Yin, Q.; Zhang, M.-D.; Wu, Q.; Chai, G.-L.; Huang, Y.-B.; Cao, R., Conductive Two-Dimensional Phthalocyanine-based Metal–Organic Framework Nanosheets for Efficient Electroreduction of CO2. *Angew. Chem. Int. Ed.* **2021,** *60* (31), 17108-17114.

94. Yang, C.; Dong, R.; Wang, M.; Petkov, P. S.; Zhang, Z.; Wang, M.; Han, P.; Ballabio, M.; Bräuninger, S. A.; Liao, Z.; Zhang, J.; Schwotzer, F.; Zschech, E.; Klauss, H.-H.; Cánovas, E.; Kaskel, S.; Bonn, M.; Zhou, S.; Heine, T.; Feng, X., A semiconducting layered metal-organic framework magnet. *Nat. Commun.* **2019,** *10* (1), 3260.

95. Wang, Z.; Walter, L. S.; Wang, M.; Petkov, P. S.; Liang, B.; Qi, H.; Nguyen, N. N.; Hambsch, M.; Zhong, H.; Wang, M.; Park, S.; Renn, L.; Watanabe, K.; Taniguchi, T.; Mannsfeld, S. C. B.; Heine, T.; Kaiser, U.; Zhou, S.; Weitz, R. T.; Feng, X.; Dong, R., Interfacial Synthesis of Layer-Oriented 2D Conjugated Metal–Organic Framework Films toward Directional Charge Transport. *J. Am. Chem. Soc.* **2021,** *143* (34), 13624-13632.

96. Meng, Z.; Mirica, K. A., Two-dimensional d-π conjugated metal-organic framework based on hexahydroxytrinaphthylene. *Nano Res.* **2021,** *14* (2), 369-375.

97. Zhao, Q.; Li, S.-H.; Chai, R.-L.; Ren, X.; Zhang, C., Two-Dimensional Conductive Metal–Organic Frameworks Based on Truxene. *ACS Appl. Mater. Interfaces* **2020,** *12* (6), 7504-7509.

98. Zhao, Q.; Jiang, J.; Zhao, W.; Li, S.-H.; Mi, W.; Zhang, C., Truxone-Based Conductive Metal–Organic Frameworks for the Oxygen Reductive Reaction. *J. Phys. Chem. C* **2021,** *125* (23), 12690-12698.

99. Liu, Y.; Li, S.; Dai, L.; Li, J.; Lv, J.; Zhu, Z.; Yin, A.; Li, P.; Wang, B., The Synthesis of Hexaazatrinaphthylene-Based 2D Conjugated Copper Metal-Organic Framework for Highly Selective and Stable Electroreduction of CO2 to Methane. *Angew. Chem. Int. Ed.* **2021,** *60* (30), 16409-16415.

100. Huang, H.; Zhao, Y.; Bai, Y.; Li, F.; Zhang, Y.; Chen, Y., Conductive Metal–Organic Frameworks with Extra Metallic Sites as an Efficient Electrocatalyst for the Hydrogen Evolution Reaction. *Adv. Sci.* **2020,** *7* (9), 2000012.

101. Liu, J.; Zhou, Y.; Xie, Z.; Li, Y.; Liu, Y.; Sun, J.; Ma, Y.; Terasaki, O.; Chen, L., Conjugated Copper–Catecholate Framework Electrodes for Efficient Energy Storage. *Angew. Chem. Int. Ed.* **2020,** *59* (3), 1081-1086.

102. Dou, J.-H.; Arguilla, M. Q.; Luo, Y.; Li, J.; Zhang, W.; Sun, L.; Mancuso, J. L.; Yang, L.; Chen, T.; Parent, L. R.; Skorupskii, G.; Libretto, N. J.; Sun, C.; Yang, M. C.; Dip, P. V.; Brignole, E. J.; Miller, J. T.; Kong, J.; Hendon, C. H.; Sun, J.; Dincă, M., Atomically precise single-crystal structures of electrically conducting 2D metal–organic frameworks. *Nat. Mater.* **2021,** *20* (2), 222-228.

103. Liu, J.; Yang, D.; Zhou, Y.; Zhang, G.; Xing, G.; Liu, Y.; Ma, Y.; Terasaki, O.; Yang, S.; Chen, L., Tricycloquinazoline-Based 2D Conductive Metal–Organic Frameworks as Promising Electrocatalysts for CO2 Reduction. *Angew. Chem. Int. Ed.* **2021,** *60* (26), 14473-14479.

104. Chen, Z.; Cui, Y.; Jin, Y.; Liu, L.; Yan, J.; Sun, Y.; Zou, Y.; Sun, Y.; Xu, W.; Zhu, D., Nanorods of a novel highly conductive 2D metal–organic framework based on perthiolated coronene for thermoelectric conversion. *J. Mater. Chem. C* **2020,** *8* (24), 8199-8205.

105. Chen, Z.; Cui, Y.; Ye, C.; Liu, L.; Wu, X.; Sun, Y.; Xu, W.; Zhu, D., Highly Conductive Cobalt Perthiolated Coronene Complex for Efficient Hydrogen Evolution. *Chem. Eur.* **2020,** *26* (56), 12868-12873.

106. Li, W.-H.; Deng, W.-H.; Wang, G.-E.; Xu, G., Conductive MOFs. *EnergyChem* **2020,** *2* (2), 100029.

107. Misumi, Y.; Yamaguchi, A.; Zhang, Z.; Matsushita, T.; Wada, N.; Tsuchiizu, M.; Awaga, K., Quantum Spin Liquid State in a Two-Dimensional Semiconductive Metal–Organic Framework. *J. Am. Chem. Soc.* **2020,** *142* (39), 16513-16517.

108. Mähringer, A.; Döblinger, M.; Hennemann, M.; Gruber, C.; Fehn, D.; Scheurle, P. I.; Hosseini, P.; Santourian, I.; Schirmacher, A.; Rotter, J. M.; Wittstock, G.; Meyer, K.; Clark, T.; Bein, T.; Medina, D. D., An Electrically Conducting Three-Dimensional Iron–Catecholate Porous Framework. *Angew. Chem. Int. Ed.* **2021,** *60* (33), 18065-18072.

109. Stodolka, M.; Choi, J. Y.; Flood, J.; Pham, H. T. B.; Park, J., Iron-Based 2D Conductive Metal–Organic Framework Nanostructure with Enhanced Pseudocapacitance. *ACS Appl. Nano Mater.* **2022,** *5* (2), 2156-2162.

110. Kambe, T.; Sakamoto, R.; Kusamoto, T.; Pal, T.; Fukui, N.; Hoshiko, K.; Shimojima, T.; Wang, Z.; Hirahara, T.; Ishizaka, K.; Hasegawa, S.; Liu, F.; Nishihara, H., Redox Control and High Conductivity of Nickel Bis(dithiolene) Complex π-Nanosheet: A Potential Organic Two-Dimensional Topological Insulator. *J. Am. Chem. Soc.* **2014,** *136* (41), 14357-14360.

111. Chen, I.-F.; Lu, C.-F.; Su, W.-F., Highly Conductive 2D Metal–Organic Framework Thin Film Fabricated by Liquid–Liquid Interfacial Reaction Using One-Pot-Synthesized Benzenehexathiol. *Langmuir* **2018,** *34* (51), 15754-15762.

112. Banda, H.; Dou, J.-H.; Chen, T.; Zhang, Y.; Dincă, M., Dual-Ion Intercalation and High Volumetric Capacitance in a Two-Dimensional Non-Porous Coordination Polymer. *Angew. Chem. Int. Ed.* **2021,** *60* (52), 27119-27125.

113. Yao, M.-S.; Zheng, J.-J.; Wu, A.-Q.; Xu, G.; Nagarkar, S. S.; Zhang, G.; Tsujimoto, M.; Sakaki, S.; Horike, S.; Otake, K.; Kitagawa, S., A Dual-Ligand Porous Coordination Polymer Chemiresistor with Modulated Conductivity and Porosity. *Angew. Chem. Int. Ed.* **2020,** *59* (1), 172-176.

114. Borysiewicz, M. A.; Dou, J.-H.; Stassen, I.; Dincă, M., Why conductivity is not always king – physical properties governing the capacitance of 2D metal–organic framework-based EDLC supercapacitor electrodes: a Ni3(HITP)2 case study. *Faraday Discuss.* **2021,** *231* (0), 298-304.

115. Feng, S.; Xu, R., New Materials in Hydrothermal Synthesis. *Acc. Chem. Res.* **2001,** *34* (3), 239-247.

116. Dong, R.; Zhang, T.; Feng, X., Interface-Assisted Synthesis of 2D Materials: Trend and Challenges. *Chem. Rev.* **2018,** *118* (13), 6189-6235.

117. Yuan, K.; Song, T.; Zhu, X.; Li, B.; Han, B.; Zheng, L.; Li, J.; Zhang, X.; Hu, W., Construction of Large-Area Ultrathin Conductive Metal–Organic Framework Films through Vapor-Induced Conversion. *Small* **2019,** *15* (12), 1804845.

118. Wu, G.; Huang, J.; Zang, Y.; He, J.; Xu, G., Porous Field-Effect Transistors Based on a Semiconductive Metal–Organic Framework. *J. Am. Chem. Soc.* **2017,** *139* (4), 1360-1363.

119. Rubio-Giménez, V.; Galbiati, M.; Castells-Gil, J.; Almora-Barrios, N.; Navarro-Sánchez, J.; Escorcia-Ariza, G.; Mattera, M.; Arnold, T.; Rawle, J.; Tatay, S.; Coronado, E.; Martí-Gastaldo, C., Bottom-Up Fabrication of Semiconductive Metal–Organic Framework Ultrathin Films. *Adv. Mater.* **2018,** *30* (10), 1704291.

120. Zhou, S.; Kong, X.; Zheng, B.; Huo, F.; Strømme, M.; Xu, C., Cellulose Nanofiber @ Conductive Metal–Organic Frameworks for High-Performance Flexible Supercapacitors. *ACS Nano* **2019,** *13* (8), 9578-9586.

121. Li, W.-H.; Ding, K.; Tian, H.-R.; Yao, M.-S.; Nath, B.; Deng, W.-H.; Wang, Y.; Xu, G., Conductive Metal–Organic Framework Nanowire Array Electrodes for High-Performance Solid-State Supercapacitors. *Adv. Funct. Mater.* **2017,** *27* (27), 1702067.

122. Gao, Z. A.; Hsu, C.-H.; Liu, J.; Chuang, F.-C.; Zhang, R.; Xia, B.; Xu, H.; Huang, L.; Jin, Q.; Liu, P. N.; Lin, N., Synthesis and characterization of a single-layer conjugated metal–organic structure featuring a non-trivial topological gap. *Nanoscale* **2019,** *11* (3), 878-881.

123. Dong, R.; Pfeffermann, M.; Liang, H.; Zheng, Z.; Zhu, X.; Zhang, J.; Feng, X., Large-Area, Free-Standing, Two-Dimensional Supramolecular Polymer Single-Layer Sheets for Highly Efficient Electrocatalytic Hydrogen Evolution. *Angew. Chem. Int. Ed.* **2015,** *54* (41), 12058-12063.

124. Ha, D.-G.; Rezaee, M.; Han, Y.; Siddiqui, S. A.; Day, R. W.; Xie, L. S.; Modtland, B. J.; Muller, D. A.; Kong, J.; Kim, P.; Dincă, M.; Baldo, M. A., Large Single Crystals of Two-Dimensional π-Conjugated Metal–Organic Frameworks via Biphasic Solution-Solid Growth. *ACS Cent. Sci.* **2021,** *7* (1), 104-109.

125. Kühnle, A., Self-assembly of organic molecules at metal surfaces. *Current Opinion in Colloid & Interface Science* **2009,** *14* (2), 157-168.

126. Barth, J. V., Molecular Architectonic on Metal Surfaces. *Annu. Rev. Phys. Chem.* **2007,** *58* (1), 375-407.

127. Classen, T.; Fratesi, G.; Costantini, G.; Fabris, S.; Stadler, F. L.; Kim, C.; de Gironcoli, S.; Baroni, S.; Kern, K., Templated Growth of Metal–Organic Coordination Chains at Surfaces. *Angew. Chem. Int. Ed.* **2005,** *44* (38), 6142-6145.

128. Heim, D.; Écija, D.; Seufert, K.; Auwärter, W.; Aurisicchio, C.; Fabbro, C.; Bonifazi, D.; Barth, J. V., Self-Assembly of Flexible One-Dimensional Coordination Polymers on Metal Surfaces. *J. Am. Chem. Soc.* **2010,** *132* (19), 6783-6790.

129. Boscoboinik, J. A.; Calaza, F. C.; Habeeb, Z.; Bennett, D. W.; Stacchiola, D. J.; Purino, M. A.; Tysoe, W. T., One-dimensional supramolecular surface structures: 1,4-diisocyanobenzene on Au(111) surfaces. *Phys. Chem. Chem. Phys.* **2010,** *12* (37), 11624-11629.

130. Knor, M.; Gao, H.-Y.; Amirjalayer, S.; Studer, A.; Gao, H.; Du, S.; Fuchs, H., Stereoselective formation of coordination polymers with 1,4-diaminonaphthalene on various Cu substrates. *Chem. Commun.* **2015,** *51* (54), 10854-10857.

131. Li, Y.; Xiao, J.; Shubina, T. E.; Chen, M.; Shi, Z.; Schmid, M.; Steinrück, H.-P.; Gottfried, J. M.; Lin, N., Coordination and Metalation Bifunctionality of Cu with 5,10,15,20-Tetra(4-pyridyl)porphyrin: Toward a Mixed-Valence Two-Dimensional Coordination Network. *J. Am. Chem. Soc.* **2012,** *134* (14), 6401-6408.

132. Lin, T.; Kuang, G.; Wang, W.; Lin, N., Two-Dimensional Lattice of Out-of-Plane Dinuclear Iron Centers Exhibiting Kondo Resonance. *ACS Nano* **2014,** *8* (8), 8310-8316.

133. Tait, S. L.; Langner, A.; Lin, N.; Chandrasekar, R.; Fuhr, O.; Ruben, M.; Kern, K., Assembling Isostructural Metal-Organic Coordination Architectures on Cu(100), Ag(100) and Ag(111) Substrates. *ChemPhysChem* **2008,** *9* (17), 2495-2499.

134. Stepanow, S.; Lin, N.; Barth, J. V.; Kern, K., Surface-Template Assembly of Two-Dimensional Metal−Organic Coordination Networks. *J. Phys. Chem. B* **2006,** *110* (46), 23472-23477.

135. Tseng, T.-C.; Abdurakhmanova, N.; Stepanow, S.; Kern, K., Hierarchical Assembly and Reticulation of Two-Dimensional Mn- and Ni–TCNQx (x = 1, 2, 4) Coordination Structures on a Metal Surface. *J. Phys. Chem. C* **2011,** *115* (20), 10211-10217.

136. Lingenfelder, M. A.; Spillmann, H.; Dmitriev, A.; Stepanow, S.; Lin, N.; Barth, J. V.; Kern, K., Towards Surface-Supported Supramolecular Architectures: Tailored Coordination Assembly of 1,4-Benzenedicarboxylate and Fe on Cu(100). *Chem. Eur.* **2004,** *10* (8), 1913-1919.

137. Seitsonen, A. P.; Lingenfelder, M.; Spillmann, H.; Dmitriev, A.; Stepanow, S.; Lin, N.; Kern, K.; Barth, J. V., Density Functional Theory Analysis of Carboxylate-Bridged Diiron Units in Two-Dimensional Metal−Organic Grids. *J. Am. Chem. Soc.* **2006,** *128* (17), 5634-5635.

138. Stepanow, S.; Lingenfelder, M.; Dmitriev, A.; Spillmann, H.; Delvigne, E.; Lin, N.; Deng, X.; Cai, C.; Barth, J. V.; Kern, K., Steering molecular organization and host–guest interactions using two-dimensional nanoporous coordination systems. *Nat. Mater.* **2004,** *3* (4), 229-233.

139. Abdurakhmanova, N.; Tseng, T. C.; Langner, A.; Kley, C. S.; Sessi, V.; Stepanow, S.; Kern, K., Superexchange-Mediated Ferromagnetic Coupling in Two-Dimensional Ni-TCNQ Networks on Metal Surfaces. *Phys. Rev. Lett.* **2013,** *110* (2), 027202.

140. Stepanow, S.; Lin, N.; Payer, D.; Schlickum, U.; Klappenberger, F.; Zoppellaro, G.; Ruben, M.; Brune, H.; Barth, J. V.; Kern, K., Surface-Assisted Assembly of 2D Metal–Organic Networks That Exhibit Unusual Threefold Coordination Symmetry. *Angew. Chem. Int. Ed.* **2007,** *46* (5), 710-713.

141. Schlickum, U.; Decker, R.; Klappenberger, F.; Zoppellaro, G.; Klyatskaya, S.; Ruben, M.; Silanes, I.; Arnau, A.; Kern, K.; Brune, H.; Barth, J. V., Metal−Organic Honeycomb Nanomeshes with Tunable Cavity Size. *Nano Lett.* **2007,** *7* (12), 3813-3817.

142. Kühne, D.; Klappenberger, F.; Decker, R.; Schlickum, U.; Brune, H.; Klyatskaya, S.; Ruben, M.; Barth, J. V., High-Quality 2D Metal−Organic Coordination Network Providing Giant Cavities within Mesoscale Domains. *J. Am. Chem. Soc.* **2009,** *131* (11), 3881-3883.

143. Matena, M.; Björk, J.; Wahl, M.; Lee, T.-L.; Zegenhagen, J.; Gade, L. H.; Jung, T. A.; Persson, M.; Stöhr, M., On-surface synthesis of a two-dimensional porous coordination network: Unraveling adsorbate interactions. *Phys. Rev. B* **2014,** *90* (12), 125408.

144. Shi, Z.; Liu, J.; Lin, T.; Xia, F.; Liu, P. N.; Lin, N., Thermodynamics and Selectivity of Two-Dimensional Metallo-supramolecular Self-Assembly Resolved at Molecular Scale. *J. Am. Chem. Soc.* **2011,** *133* (16), 6150-6153.

145. Pawlak, R.; Clair, S.; Oison, V.; Abel, M.; Ourdjini, O.; Zwaneveld, N. A. A.; Gigmes, D.; Bertin, D.; Nony, L.; Porte, L., Robust Supramolecular Network on Ag(111): Hydrogen-Bond Enhancement through Partial Alcohol Dehydrogenation. *ChemPhysChem* **2009,** *10* (7), 1032-1035.

146. Coratger, R.; Calmettes, B.; Abel, M.; Porte, L., STM observations of the first polymerization steps between hexahydroxy-tri-phenylene and benzene-di-boronic acid molecules. *Surf. Sci.* **2011,** *605* (7), 831-837.

147. Giovanelli, L.; Ourdjini, O.; Abel, M.; Pawlak, R.; Fujii, J.; Porte, L.; Themlin, J.-M.; Clair, S., Combined Photoemission Spectroscopy and Scanning Tunneling Microscopy Study of the Sequential Dehydrogenation of Hexahydroxytriphenylene on Ag(111). *J. Phys. Chem. C* **2014,** *118* (27), 14899-14904.

148. Clair, S.; Abel, M.; Porte, L., Mesoscopic Arrays from Supramolecular Self-Assembly. *Angew. Chem. Int. Ed.* **2010,** *49* (44), 8237-8239.

149. Gómez-Herrero, A. C.; Sánchez-Sánchez, C.; Chérioux, F.; Martínez, J. I.; Abad, J.; Floreano, L.; Verdini, A.; Cossaro, A.; Mazaleyrat, E.; Guisset, V.; David, P.; Lisi, S.; Martín Gago, J. A.; Coraux, J., Copper-assisted oxidation of catechols into quinone derivatives. *Chem. Sci.* **2021,** *12* (6), 2257-2267.

150. Rochefort, A.; Vernisse, L.; Gómez-Herrero, A. C.; Sánchez-Sánchez, C.; Martín-Gago, J. A.; Chérioux, F.; Clair, S.; Coraux, J.; Martínez, J. I., Role of the Structure and Reactivity of Cu and Ag Surfaces in the Formation of a 2D Metal–Hexahydroxytriphenylene Network. *J. Phys. Chem. C* **2021,** *125* (31), 17333-17341.

151. Marele, A. C.; Corral, I.; Sanz, P.; Mas-Ballesté, R.; Zamora, F.; Yáñez, M.; Gómez-Rodríguez, J. M., Some Pictures of Alcoholic Dancing: From Simple to Complex Hydrogen-Bonded Networks Based on Polyalcohols. *J. Phys. Chem. C* **2013,** *117* (9), 4680-4690.

152. Martín-Fuentes, C.; Parreiras, S. O.; Urgel, J. I.; Rubio-Giménez, V.; Muñiz Cano, B.; Moreno, D.; Lauwaet, K.; Valvidares, M.; Valbuena, M. A.; Gargiani, P.; Kuch, W.; Camarero, J.; Gallego, J. M.; Miranda, R.; Martínez, J. I.; Martí-Gastaldo, C.; Écija, D., On-Surface Design of a 2D Cobalt-Organic Network Preserving Large Orbital Magnetic Moment. *J. Am. Chem. Soc.* **2022,** *144* (35), 16034-16041.

153. Gao, Z. A.; Gao, Y.; Hua, M.; Liu, J.; Huang, L.; Lin, N., Design and Synthesis of a Single-Layer Ferromagnetic Metal–Organic Framework with Topological Nontrivial Gaps. *J. Phys. Chem. C* **2020,** *124* (49), 27017-27023.

154. Zhong, W.; Zhang, T.; Chen, D.; Su, N.; Miao, G.; Guo, J.; Chen, L.; Wang, Z.; Wang, W., Synthesizing Cr-Based Two-Dimensional Conjugated Metal-Organic Framework Through On-Surface Substitution Reaction. *Small* **2023,** *19* (21), 2207877.

155. Lischka, M.; Dong, R.; Wang, M.; Martsinovich, N.; Fritton, M.; Grossmann, L.; Heckl, W. M.; Feng, X.; Lackinger, M., Competitive Metal Coordination of Hexaaminotriphenylene on Cu(111) by Intrinsic Copper Versus Extrinsic Nickel Adatoms. *Chem. Eur.* **2019,** *25* (8), 1975-1983.

156. Zhang, R.; Liu, J.; Gao, Y.; Hua, M.; Xia, B.; Knecht, P.; Papageorgiou, A. C.; Reichert, J.; Barth, J. V.; Xu, H.; Huang, L.; Lin, N., On-surface Synthesis of a Semiconducting 2D Metal–Organic Framework Cu3(C6O6) Exhibiting Dispersive Electronic Bands. *Angew. Chem. Int. Ed.* **2020,** *59* (7), 2669-2673.

157. Hua, M.; Xia, B.; Wang, M.; Li, E.; Liu, J.; Wu, T.; Wang, Y.; Li, R.; Ding, H.; Hu, J.; Wang, Y.; Zhu, J.; Xu, H.; Zhao, W.; Lin, N., Highly Degenerate Ground States in a Frustrated Antiferromagnetic Kagome Lattice in a Two-Dimensional Metal–Organic Framework. *J. Phys. Chem. Lett* **2021,** *12* (15), 3733-3739.

158. Meng, X.; Kolodzeiski, E.; Huang, X.; Timmer, A.; Schulze Lammers, B.; Gao, H.-Y.; Mönig, H.; Liu, L.; Xu, W.; Amirjalayer, S.; Zhu, D.; Fuchs, H., Tunable Thiolate Coordination Networks on Metal Surfaces. *ChemNanoMat* **2020,** *6* (10), 1479-1484.

159. Campbell, M. G.; Liu, S. F.; Swager, T. M.; Dincă, M., Chemiresistive Sensor Arrays from Conductive 2D Metal–Organic Frameworks. *J. Am. Chem. Soc.* **2015,** *137* (43), 13780-13783.

160. Yao, M.-S.; Lv, X.-J.; Fu, Z.-H.; Li, W.-H.; Deng, W.-H.; Wu, G.-D.; Xu, G., Layer-by-Layer Assembled Conductive Metal–Organic Framework Nanofilms for Room-Temperature Chemiresistive Sensing. *Angew. Chem. Int. Ed.* **2017,** *56* (52), 16510-16514.

161. Smith, M. K.; Mirica, K. A., Self-Organized Frameworks on Textiles (SOFT): Conductive Fabrics for Simultaneous Sensing, Capture, and Filtration of Gases. *J. Am. Chem. Soc.* **2017,** *139* (46), 16759-16767.

162. Downes, C. A.; Marinescu, S. C., Electrocatalytic Metal–Organic Frameworks for Energy Applications. *ChemSusChem* **2017,** *10* (22), 4374-4392.

163. Clough, A. J.; Yoo, J. W.; Mecklenburg, M. H.; Marinescu, S. C., Two-Dimensional Metal–Organic Surfaces for Efficient Hydrogen Evolution from Water. *J. Am. Chem. Soc.* **2015,** *137* (1), 118-121.

164. Xing, D.; Wang, Y.; Zhou, P.; Liu, Y.; Wang, Z.; Wang, P.; Zheng, Z.; Cheng, H.; Dai, Y.; Huang, B., Co3(hexaiminotriphenylene)2: A conductive two-dimensional π–d conjugated metal–

organic framework for highly efficient oxygen evolution reaction. *Appl. Catal. B: Environ.* **2020,** *278*, 119295.

165. Li, C.; Shi, L.; Zhang, L.; Chen, P.; Zhu, J.; Wang, X.; Fu, Y., Ultrathin two-dimensional π–d conjugated coordination polymer Co3(hexaaminobenzene)2 nanosheets for highly efficient oxygen evolution. *J. Mater. Chem. A* **2020,** *8* (1), 369-379.

166. Miner, E. M.; Fukushima, T.; Sheberla, D.; Sun, L.; Surendranath, Y.; Dincă, M., Electrochemical oxygen reduction catalysed by Ni3(hexaiminotriphenylene)2. *Nat. Commun.* **2016,** *7* (1), 10942.

167. Miner, E. M.; Wang, L.; Dincă, M., Modular O2 electroreduction activity in triphenylene-based metal–organic frameworks. *Chem. Sci.* **2018,** *9* (29), 6286-6291.

168. Yoon, H.; Lee, S.; Oh, S.; Park, H.; Choi, S.; Oh, M., Synthesis of Bimetallic Conductive 2D Metal–Organic Framework (CoxNiy-CAT) and Its Mass Production: Enhanced Electrochemical Oxygen Reduction Activity. *Small* **2019,** *15* (17), 1805232.

169. Sheberla, D.; Bachman, J. C.; Elias, J. S.; Sun, C.-J.; Shao-Horn, Y.; Dincă, M., Conductive MOF electrodes for stable supercapacitors with high areal capacitance. *Nat. Mater.* **2017,** *16* (2), 220-224.

170. Binnig, G.; Rohrer, H.; Gerber, C.; Weibel, E., Surface Studies by Scanning Tunneling Microscopy. *Phys. Rev. Lett.* **1982,** *49* (1), 57-61.

171. Binnig, G.; Rohrer, H., Scanning tunneling microscopy. *Surf. Sci.* **1983,** *126* (1), 236-244.

172. Tersoff, J.; Hamann, D. R., Theory and Application for the Scanning Tunneling Microscope. *Phys. Rev. Lett.* **1983,** *50* (25), 1998-2001.

173. Tersoff, J.; Hamann, D. R., Theory of the scanning tunneling microscope. *Phys. Rev. B* **1985,** *31* (2), 805-813.

174. Marshall, M. S. J. Nanostructured Strontium Titanate Surfaces. University of Oxford, 2009.

175. Ltd., J., JEOL Instruction Manual: JSPM-4500S/TM-51021 Ultrahigh Vacuum Scanning Tunneling Microscope. **2000**.

176. Morgenstern, K.; Kibsgaard, J.; Lauritsen, J. V.; Lægsgaard, E.; Besenbacher, F., Cobalt growth on two related close-packed noble metal surfaces. *Surf. Sci.* **2007,** *601* (9), 1967-1972.

177. Wöll, C.; Chiang, S.; Wilson, R. J.; Lippel, P. H., Determination of atom positions at stacking-fault dislocations on Au(111) by scanning tunneling microscopy. *Phys. Rev. B* **1989,** *39* (11), 7988-7991.

178. Harten, U.; Lahee, A. M.; Toennies, J. P.; Wöll, C., Observation of a Soliton Reconstruction of Au(111) by High-Resolution Helium-Atom Diffraction. *Phys. Rev. Lett.* **1985,** *54* (24), 2619-2622.

179. Barth, J. V.; Brune, H.; Ertl, G.; Behm, R. J., Scanning tunneling microscopy observations on the reconstructed Au(111) surface: Atomic structure, long-range superstructure, rotational domains, and surface defects. *Phys. Rev. B* **1990,** *42* (15), 9307-9318.

180. Fujita, D.; Amemiya, K.; Yakabe, T.; Nejoh, H.; Sato, T.; Iwatsuki, M., Observation of two-dimensional Fermi contour of a reconstructed Au(111) surface using Fourier transform scanning tunneling microscopy. *Surf. Sci.* **1999,** *423* (2), 160-168.

181. Voigtländer, B.; Meyer, G.; Amer, N. M., Epitaxial growth of thin magnetic cobalt films on Au(111) studied by scanning tunneling microscopy. *Phys. Rev. B* **1991,** *44* (18), 10354-10357.

182. Meyer, J. A.; Baikie, I. D.; Kopatzki, E.; Behm, R. J., Preferential island nucleation at the elbows of the Au(111) herringbone reconstruction through place exchange. *Surf. Sci.* **1996,** *365* (1), L647-L651.

183. Chambliss, D. D.; Wilson, R. J.; Chiang, S., Nucleation of ordered Ni island arrays on Au(111) by surface-lattice dislocations. *Phys. Rev. Lett.* **1991,** *66* (13), 1721-1724.

184. Song, G.; Lin, J. Y. Y.; Bilheux, J. C.; Xie, Q.; Santodonato, L. J.; Molaison, J. J.; Skorpenske, H. D.; M. Dos Santos, A.; Tulk, C. A.; An, K.; Stoica, A. D.; Kirka, M. M.; Dehoff, R. R.; Tremsin, A. S.; Bunn, J.; Sochalski-Kolbus, L. M.; Bilheux, H. Z., Characterization of Crystallographic Structures Using Bragg-Edge Neutron Imaging at the Spallation Neutron Source. *Journal of Imaging* **2017,** *3* (4), 65.

185. Lahtinen, J.; Vaari, J.; Vaara, T.; Kauraala, K.; Kaukasoina, P.; Lindroos, M., LEED investigations on Co(0001): the clean surface and the (2×2)-K overlayer. *Surf. Sci.* **1999,** *425* (1), 90-100.

186. Hohenberg, P.; Kohn, W., Inhomogeneous Electron Gas. *Phys. Rev.* **1964,** *136* (3B), B864-B871.

187. Kohn, W.; Sham, L. J., Self-Consistent Equations Including Exchange and Correlation Effects. *Phys. Rev.* **1965,** *140* (4A), A1133-A1138.

188. Perdew, J. P.; Burke, K.; Ernzerhof, M., Generalized Gradient Approximation Made Simple. *Phys. Rev. Lett.* **1996,** *77* (18), 3865-3868.

189. Giannozzi, P.; Baroni, S.; Bonini, N.; Calandra, M.; Car, R.; Cavazzoni, C.; Ceresoli, D.; Chiarotti, G. L.; Cococcioni, M.; Dabo, I.; Dal Corso, A.; de Gironcoli, S.; Fabris, S.; Fratesi, G.; Gebauer, R.; Gerstmann, U.; Gougoussis, C.; Kokalj, A.; Lazzeri, M.; Martin-Samos, L.; Marzari, N.; Mauri, F.; Mazzarello, R.; Paolini, S.; Pasquarello, A.; Paulatto, L.; Sbraccia, C.; Scandolo, S.; Sclauzero, G.; Seitsonen, A. P.; Smogunov, A.; Umari, P.; Wentzcovitch, R. M., QUANTUM ESPRESSO: a modular and open-source software project for quantum simulations of materials. *J. Phys.: Condens. Matter* **2009,** *21* (39), 395502.

190. Giannozzi, P.; Andreussi, O.; Brumme, T.; Bunau, O.; Buongiorno Nardelli, M.; Calandra, M.; Car, R.; Cavazzoni, C.; Ceresoli, D.; Cococcioni, M.; Colonna, N.; Carnimeo, I.; Dal Corso, A.; de Gironcoli, S.; Delugas, P.; DiStasio, R. A.; Ferretti, A.; Floris, A.; Fratesi, G.; Fugallo, G.; Gebauer, R.; Gerstmann, U.; Giustino, F.; Gorni, T.; Jia, J.; Kawamura, M.; Ko, H. Y.; Kokalj, A.; Küçükbenli, E.; Lazzeri, M.; Marsili, M.; Marzari, N.; Mauri, F.; Nguyen, N. L.; Nguyen, H. V.; Otero-de-la-Roza, A.; Paulatto, L.; Poncé, S.; Rocca, D.; Sabatini, R.; Santra, B.; Schlipf, M.; Seitsonen, A. P.; Smogunov, A.; Timrov, I.; Thonhauser, T.; Umari, P.; Vast, N.; Wu, X.; Baroni, S., Advanced capabilities for materials modelling with Quantum ESPRESSO. *J. Phys.: Condens. Matter* **2017,** *29* (46), 465901.

191. Vanderbilt, D., Soft self-consistent pseudopotentials in a generalized eigenvalue formalism. *Phys. Rev. B* **1990,** *41* (11), 7892-7895.

192. Garrity, K. F.; Bennett, J. W.; Rabe, K. M.; Vanderbilt, D., Pseudopotentials for high-throughput DFT calculations. *Comput. Mater. Sci.* **2014,** *81*, 446-452.

193. Grimme, S.; Antony, J.; Ehrlich, S.; Krieg, H., A consistent and accurate ab initio parametrization of density functional dispersion correction (DFT-D) for the 94 elements H-Pu. *J. Phys. Chem.* **2010,** *132* (15), 154104.

194. Monkhorst, H. J.; Pack, J. D., Special points for Brillouin-zone integrations. *Phys. Rev. B* **1976,** *13* (12), 5188-5192.

195. Kokalj, A., Computer graphics and graphical user interfaces as tools in simulations of matter at the atomic scale. *Comput. Mater. Sci.* **2003,** *28* (2), 155-168.

196. Tang, W.; Sanville, E.; Henkelman, G., A grid-based Bader analysis algorithm without lattice bias. *J. Phys.: Condens. Matter* **2009,** *21* (8), 084204.

197. Jones, L.; Yang, H.; Pennycook, T. J.; Marshall, M. S. J.; Van Aert, S.; Browning, N. D.; Castell, M. R.; Nellist, P. D., Smart Align—a new tool for robust non-rigid registration of scanning microscope data. *Adv. Struct. Chem. Imaging* **2015,** *1* (1), 8.

198. Jones, L.; Wang, S.; Hu, X.; Rahman, S. U.; Castell, M. R., Maximising the resolving power of the scanning tunneling microscope. *Adv. Struct. Chem. Imaging* **2018,** *4* (1), 7.

199. Simpson, G. J.; García-López, V.; Daniel Boese, A.; Tour, J. M.; Grill, L., How to control single-molecule rotation. *Nat. Commun.* **2019,** *10* (1), 4631.

200. Li, Q.; Yamazaki, S.; Eguchi, T.; Hasegawa, Y.; Kim, H.; Kahng, S.-J.; Feng Jia, J.; Xue, Q. K., Adsorption, manipulation and self-assembling of TBrPP-Co molecules on a Ag/Si(111) surface by scanning tunnelling microscopy. *Nanotechnology* **2008,** *19* (46), 465707.

201. Tierney, H. L.; Calderon, C. E.; Baber, A. E.; Sykes, E. C. H.; Wang, F., Understanding the Rotational Mechanism of a Single Molecule: STM and DFT Investigations of Dimethyl Sulfide Molecular Rotors on Au(111). *J. Phys. Chem. C* **2010,** *114* (7), 3152-3155.

202. Chen, S.; Dai, J.; Zeng, X. C., Metal–organic Kagome lattices M3(2,3,6,7,10,11-hexaiminotriphenylene)2 (M = Ni and Cu): from semiconducting to metallic by metal substitution. *Phys. Chem. Chem. Phys.* **2015,** *17* (8), 5954-5958.

203. Takenaka, T.; Ishihara, K.; Roppongi, M.; Miao, Y.; Mizukami, Y.; Makita, T.; Tsurumi, J.; Watanabe, S.; Takeya, J.; Yamashita, M.; Torizuka, K.; Uwatoko, Y.; Sasaki, T.; Huang, X.; Xu, W.; Zhu, D.; Su, N.; Cheng, J. G.; Shibauchi, T.; Hashimoto, K., Strongly correlated superconductivity in a copper-based metal-organic framework with a perfect kagome lattice. *Sci. Adv. 7* (12), eabf3996.

204. Huang, X.; Yao, H.; Cui, Y.; Hao, W.; Zhu, J.; Xu, W.; Zhu, D., Conductive Copper Benzenehexathiol Coordination Polymer as a Hydrogen Evolution Catalyst. *ACS Appl. Mater. Interfaces* **2017,** *9* (46), 40752-40759.

205. Bae, Y.-S.; Mulfort, K. L.; Frost, H.; Ryan, P.; Punnathanam, S.; Broadbelt, L. J.; Hupp, J. T.; Snurr, R. Q., Separation of CO2 from CH4 Using Mixed-Ligand Metal−Organic Frameworks. *Langmuir* **2008,** *24* (16), 8592-8598.

206. Kim, M.; Oh, J. S.; Kim, B. H.; Kim, A. Y.; Park, K. C.; Mun, J.; Gupta, G.; Lee, C. Y., Enhanced Photocatalytic Performance of Nanosized Mixed-Ligand Metal–Organic Frameworks through Sequential Energy and Electron Transfer Process. *Inorg. Chem.* **2020,** *59* (17), 12947-12953.

207. Rui, K.; Zhao, G.; Chen, Y.; Lin, Y.; Zhou, Q.; Chen, J.; Zhu, J.; Sun, W.; Huang, W.; Dou, S. X., Hybrid 2D Dual-Metal–Organic Frameworks for Enhanced Water Oxidation Catalysis. *Adv. Funct. Mater.* **2018,** *28* (26), 1801554.

208. Sharma, N.; Szunerits, S.; Boukherroub, R.; Ye, R.; Melinte, S.; Thotiyl, M. O.; Ogale, S., Dual-Ligand Fe-Metal Organic Framework Based Robust High Capacity Li Ion Battery Anode and Its Use in a Flexible Battery Format for Electro-Thermal Heating. *ACS Appl. Energy Mater.* **2019,** *2* (6), 4450-4457.

209. Zhu, D.; Zhang, Y.; Bao, S.; Wang, N.; Yu, S.; Luo, R.; Ma, J.; Ju, H.; Lei, J., Dual Intrareticular Oxidation of Mixed-Ligand Metal–Organic Frameworks for Stepwise Electrochemiluminescence. *J. Am. Chem. Soc.* **2021,** *143* (8), 3049-3053.

210. Wu, A.-Q.; Wang, W.-Q.; Zhan, H.-B.; Cao, L.-A.; Ye, X.-L.; Zheng, J.-J.; Kumar, P. N.; Chiranjeevulu, K.; Deng, W.-H.; Wang, G.-E.; Yao, M.-S.; Xu, G., Layer-by-layer assembled dual-ligand conductive MOF nano-films with modulated chemiresistive sensitivity and selectivity. *Nano Res.* **2021,** *14* (2), 438-443.

211. Karagiaridi, O.; Bury, W.; Mondloch, J. E.; Hupp, J. T.; Farha, O. K., Solvent-Assisted Linker Exchange: An Alternative to the De Novo Synthesis of Unattainable Metal–Organic Frameworks. *Angew. Chem. Int. Ed.* **2014,** *53* (18), 4530-4540.

212. Burnett, B. J.; Barron, P. M.; Hu, C.; Choe, W., Stepwise Synthesis of Metal–Organic Frameworks: Replacement of Structural Organic Linkers. *J. Am. Chem. Soc.* **2011,** *133* (26), 9984-9987.

213. Zhao, X.; Zhang, Z.; Cai, X.; Ding, B.; Sun, C.; Liu, G.; Hu, C.; Shao, S.; Pang, M., Postsynthetic Ligand Exchange of Metal–Organic Framework for Photodynamic Therapy. *ACS Appl. Mater. Interfaces* **2019,** *11* (8), 7884-7892.

214. Liu, L.; Li, L.; Ziebel, M. E.; Harris, T. D., Metal–Diamidobenzoquinone Frameworks via Post-Synthetic Linker Exchange. *J. Am. Chem. Soc.* **2020,** *142* (10), 4705-4713.